SIZE AND SHAPE CONTROLLED SYNTHESIS AND SUPERPARAMAGNETIC PROERTIES OF SPINEL FERRITES NANOCRYSTALS

A Dissertation
Presented to
The Academic Faculty

By

Qing Song

In Partial Fulfillment
Of the Requirements for the Degree
Doctor of Philosophy in Chemistry

Georgia Institute of Technology

December 2005

SIZE AND SHAPE CONTROLLED SYNTHESIS AND SUPERPARAMAGNETIC PROERTIES OF SPINEL FERRITES NANOCRYSTALS

Approved by:

Dr Z. John Zhang, Advisor
School of Chemistry and Biochemistry
Georgia Institute of Technology

Dr. Mostafa A. El-Sayed
School of Chemistry and Biochemistry
Georgia Institute of Technology

Dr. Kent E. Barefield
School of Chemistry and Biochemistry
Georgia Institute of Technology

Dr. Zhong Lin Wang
Material Science and Engineering
Georgia Institute of Technology

Dr. Angus P. Wilkinson
School of Chemistry and Biochemistry
Georgia Institute of Technology

Date Approved: August 26, 2005

To My Family

ACKNOWLEDGEMENTS

First, I would like to thank Dr. Z. John Zhang, my advisor, for his support, encouragement and allowing me the research freedom in my doctoral projects. Perhaps, it is a bonus that I have also learned a great deal of both American and Chinese history from him. I am very grateful to my committee members, Dr. Mostafa A. El-Sayed, Dr. E. Kent Barefield, Dr. Angus P. Wilkinson and Dr. Zhong Lin Wang for their suggestions, comments and information over the past years, and especially their strong solid support in my recent job hunting. Special thanks go to Dr. Z. L. Wang, for his generous assistance and insightful discussions in HRTEM studies.

I would also like to thank Dr. Chris Jones for allowing me access to his TGA and DSC instruments, Dr. Leslie T. Gelbaum for his assistance in NMR and He for SQUID, and Ms. Yolanda Berta for her help and training in TEM. The cutting-edge TEM facilities at the Georgia Institute of Technology Microscopy Center have been most appreciated, as TEM is one of essential tools in my research. Also, Drs. Yong Ding, Xiangyang Kong, Mr. Puxian Gao, and many other people who are willing to give me their hands whenever I need them. I highly appreciate their friendship and support.

I am also grateful for the help, assistance and friendship of the past and current group members. In particular, I greatly thank Dr. Chao Liu, Dr. Anna C. Samia, and Dr. Christy A. Vestal for their helpful assistance, discussions and suggestions.

By no means, I could fully appreciate the value of my entire families. Their love and care are the prime source of incentive for me to accomplish more. I have the greatest parents in the world as they teach me, whenever and wherever to be tough to face the

hard time in your life. My parents and in-laws, they provide their continuing encouragement, indispensable understanding and tremendous support not only for me but also for my child. I am a luck man as well. My beautiful, talented and dedicated wife, Dr. Xin Ai, she not only successfully defended her Ph. D in Chemistry last year, but she also pumps her love, energy, time and inspiration in science in supporting me. Without her, I might not ever have a chance to be here and get what I have so far. I may say sorry to my loved daughter, Avery Song, because I could not spend a littler bit more time to play with her as I searched and indulged myself in the ‘ Nano Jungle’ world. I wish she could appreciate what I have done in the past few years when she is growing up and I believe she will.

Last, but certainly not least, tons of thanks are extended to my close friends for their encouragement and support.

TABLE OF CONTENTS

LIST OF TABLES

LIST OF FIGURES

SUMMARY

The correlationship between magnetic properties and magnetic couplings is established by investigations of various cubic spinel ferrite nanocrystals. The results of this thesis contribute to the knowledge of size and shape controlled synthesis of various spinel ferrites and core shell architectured nanocrystals as well as the nanomagnetism in spinel ferrites by systematically investigating the effects of spin – orbital coupling, magnetocrystalline anisotropy, exchange coupling, shape and surface anisotropy upon superparamagnetic properties of spinel ferrites nanocrystals. In **Chapter 3**, a general synthetic method for size and shape control metal oxide nanocrystals is described by taking $CoFe_2O_4$ nanocrystals as an example. The size and shape dependent superparamagnetic properties are discussed. These results are the first experiment that report the synthesis of spinel ferrite nanocrystals with shape control capability. **Chapter 4** describes the relationship between spin – orbital coupling and magnetocrystalline anisotropy by comparative studies on variable sized spherical $CoFe_2O_4$ and Fe_3O_4 nanocrystals. **Chapter 5** details the effect of exchange coupling between magnetic hard phase $CoFe_2O_4$ and soft phase, either $MnFe_2O_4$ or Fe_3O_4, upon magnetic properties in core shell structured spinel ferrites nanocrystals. **Chapter 6** is about the role of anisotropic shapes of nanocrystals upon self assembled orientation ordered superstructures and the shape effect upon magnetic properties of Fe_3O_4 nanocrystals. These studies are the first experiments that address the shape as a key factor in the structures of self assembly superlattices. **Chapter 7** addresses the thermal stability of

molecular precursors upon size controlled synthesis of $MnFe_2O_4$ nanocrystals and the size dependent superparamagnetic properties is described.

CHAPTER 1

INTRODUCTION TO SUPERPARAMAGNETISM AND LITERATURE REVIEW

1.1 Introduction

It is well known that a bulk magnetic material consists of many magnetic domains, and the magnetic properties are determined by the formation, structures and movements of these magnetic domains under a variation of temperature and/or magnetic field.

What happens if the physical dimension of a bulk magnetic material is reduced to be comparable to or smaller than a magnetically critical size such as the magnetic domain wall width in nanoscopic regime? This would lead the magnetic particle to possess only a single-domain and show superparamagnetic behaviors. The magnetization reversal can be agitated by thermal fluctuation and become sensitive to the size and shape of the magnetic nanoparticles, which differs dramatically from the magnetic properties of their bulk counterparts.

The potential of using these novel size and shape dependent magnetic properties in new technological applications has been demonstrated in many new and traditional fields, such as ultrahigh density magnetic data storage, giant magnetoresistance (GMR) sensor, magnetocaloric refrigerator, magnetoelectrics, magnetic resonance imaging (MRI) contrast enhancement agents, magnetically guided target-specific drug delivery systems, cells, DNAs and genes sorting and delivery, and ferrofluids. [1-17]

In this chapter, a general introduction of fundamentals on magnetism is first overviewed and followed by a discussion of some important issues on nanomagnetism – single domain theory, superparamagnetism and magnetic anisotropy mechanisms.

1.2 Fundamentals of Magnetism[18-24]

The magnetic properties of a matter are fundamentally the result of the electrons of the atom, which have a magnetic moment by means of the electron motion. At the atomic level, there are two types of electron motion, spin and orbital, and each has a magnetic moment associated with it. Since the response of a material to a magnetic field (**H**) is characteristic of the magnetic induction or the flux density (**B**) and the effect that a material has upon the magnetic induction in a magnetic field is represented by the magnetization (**M**). Thus, a universal equation relating these three magnetic quantities, magnetic field, magnetic induction and magnetization, can be established by

$$\mathbf{B} = \mu_0 (\mathbf{H} + \mathbf{M}) \qquad (1.1)$$

$$\mathbf{B} = \mu \mathbf{H} \qquad (1.2)$$

where μ_0 is a universal constant of permeability in a free space and μ is the permeability of a material. From equation (1.1), one can see that $\mu_0\mathbf{H}$ is the magnetic induction generated by the field alone and $\mu_0\mathbf{M}$ is the additional magnetic induction contributed by a material.

The magnetic susceptibility (χ) is defined as the ratio of magnetization to magnetic field

$$\chi = \mathbf{M} / \mathbf{H} \qquad (1.3)$$

Therefore, from the above equations, the permeability and susceptibility of a material are correlated with respect to each other by

$$\mu = \mu_0 (1+ \chi) \qquad (1.4)$$

The susceptibility is a major parameter in characterization of magnetic properties of a material. The magnitude of the susceptibility and its temperature and field dependencies provide a measure of magnetic behavior of different types of magnetic materials. Therefore, the magnetic behavior of a material is classified into diamagnetism, paramagnetism, ferromagnetism, antiferromagnetism and ferrimagnetism. The varieties of magnetic orderings are schematically depicted in Figure 1.1.

Diamagnetic material has a negative susceptibility with typical values on the order of 10^{-5} to 10^{-6}. Most materials are diamagnetic, including Cu, B, S, N_2, and most organic compounds. If a magnetic field is applied to a diamagnetic material, the induced magnetic moment is small and opposite to the field direction. Diamagnetism obeys Lenz's law, which states that when a conducting loop is acted upon by an applied magnetic field a current is induced in the loop that counteracts the change in the field.

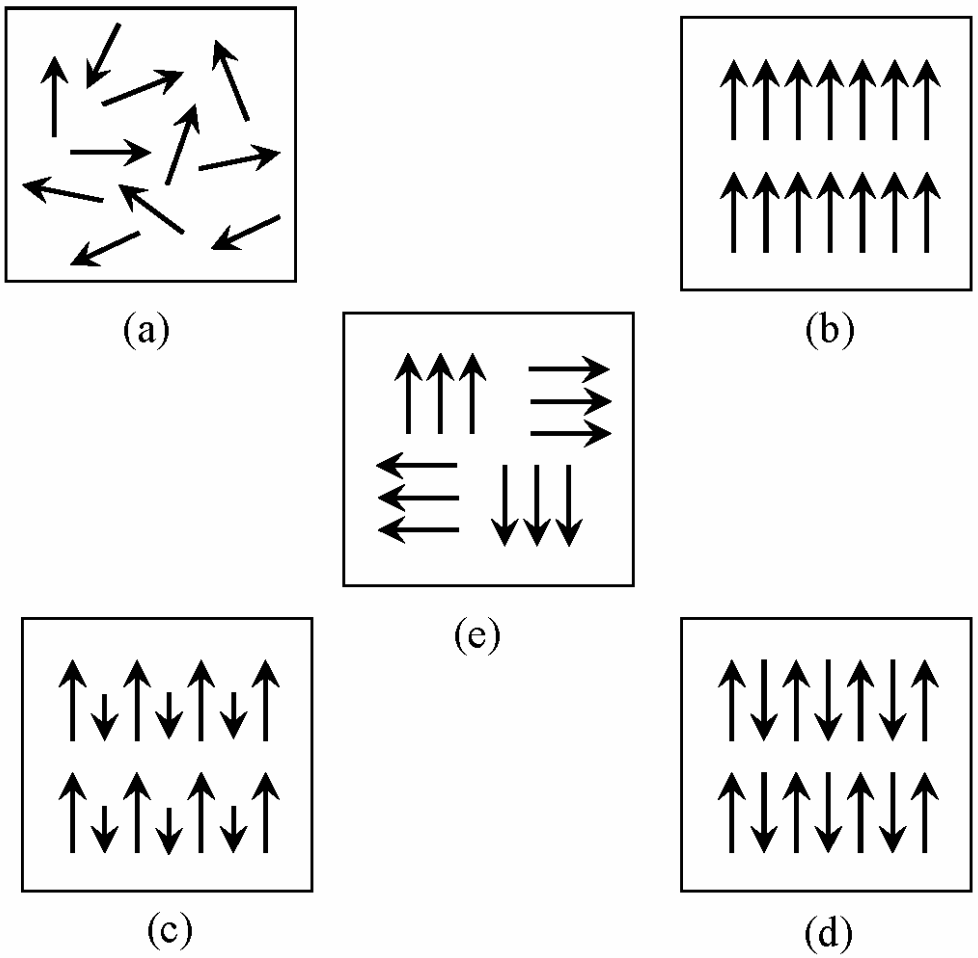

Figure 1.1 Varieties of magnetic orderings (a) paramagnetic, (b), ferromagnetic, (c) ferrimagnetic, (d) antiferromagnetic, and (e) superparamagnetic.

rding a simple Langevin theory, the susceptibility of diamagnetic material is expressed as:

$$\chi = - NZe^2r^2 / (mc^2) \qquad (1.5)$$

where N is the number of atoms per unit volume, Z is the number of electron, e is the charge of electron, r is the orbital radius and c is the speed of light. The temperature independence is the characteristic of diamagnetic materials.

Paramagnetic material possesses nonzero magnetic moment due to unpaired electrons. The magnetic moments can be oriented along an applied field to give rise to a positive susceptibility, and yet the values of susceptibility are very small with the order of 10^{-5} to 10^{-3}. O_2, NO, Cr and Mn are just a few examples of the paramagnetic materials. The susceptibility of a paramagnetic material is inversely dependent on temperature, which is known as Curie law (Figure1.2a)

$$\chi = C / T \qquad (1.6)$$

where C is the Curie constant.

Ferromagnetic material differs from diamagnetic and paramagnetic materials in many different ways. In a ferromagnetic material, the exchange coupling between neighboring moments leads the moments to align parallel with each other. Therefore, the ferromagnetic materials generally can acquire a large magnetization in a relatively weak magnetic field, since all magnetic moments are easily aligned together. Also, the

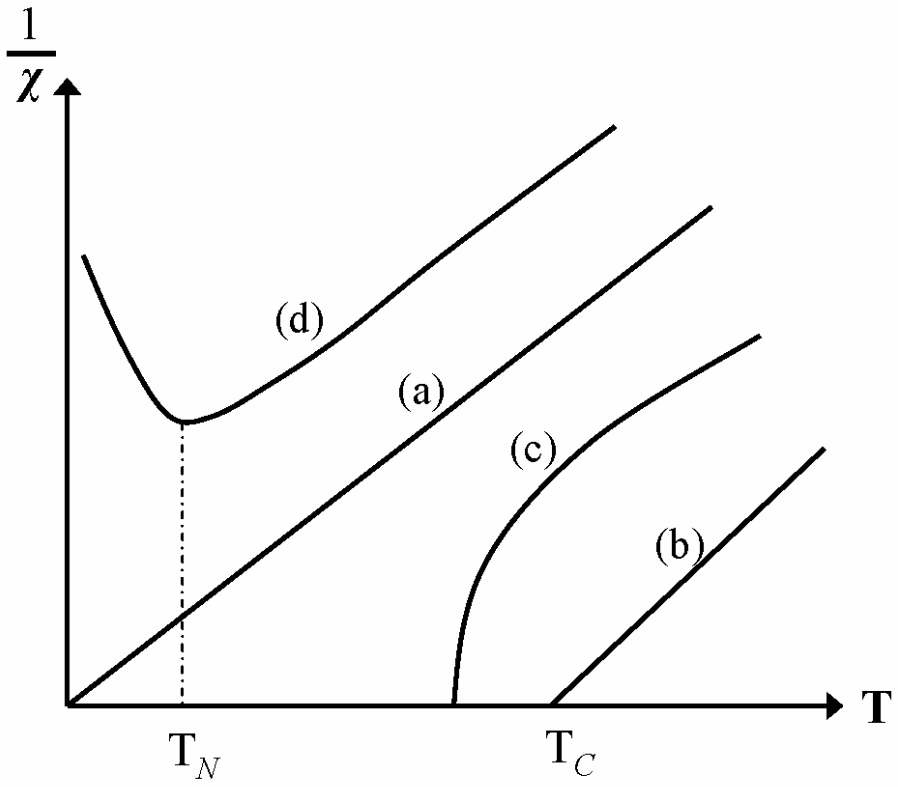

Figure 1.2 The inverse susceptibility varies with T for (a) paramagnetic, (b) ferromagnetic, (c) ferrimagnetic, (d) antiferromagnetic materials. T_N and T_C are Néel temperature and Curie temperature, respectively.

susceptibility of a ferromagnetic material does not follow the Curie law, but displayed a modified behavior defined by Curie-Weiss law (Figure 1.2b)

$$\chi = C / (T - \theta) \qquad (1.7)$$

where C is a constant and θ is called Weiss constant. For ferromagnetic materials, the Weiss constant is almost identical to the Curie temperature (T_C). At temperature below Curie temperature, the magnetic moments are ordered, whereas above Curie temperature, material loses magnetic ordering and shows paramagnetic character. The common ferromagnetic materials are Fe, Co, and Ni transitional metals.

Antiferromagnetic material aligns the magnetic moments in a way that all moments are antiparallel to each other, which is totally opposite to ferromagnetic ordering. The antiferromagnetic susceptibility is followed the Curie-Weiss law with a negative θ as in equation (1.7). The inverse susceptibility as a function of temperature is given in Figure 1.2d. Common examples of materials with antiferromagnetic ordering include MnO, FeO, CoO and NiO.

Ferrimagnetic material has the same antiparallel alignment of magnetic moments as an antiferromagnetic material does. However, the magnitude of magnetic moment in one direction differs from that of the opposite direction. As a result, a net magnetic moment remains in the absence of external magnetic field. The behavior of susceptibility of a ferrimagnetic material obeys Curie-Weiss law and has a negative θ as well in Figure 1.2c. Cubic spinel ferrites probably are the most common ferrimagnetic materials.

1.3 Superparamagnetism of Magnetic Nanomaterial

1.3.1 Exchange Interaction and Magnetic Anisotropy

The fundamental basis for the magnetic behavior of magnetic materials relies on two mechanisms, exchange interaction and anisotropy. The quantum origin of exchange interaction derives from the combination of electrostatic coupling between electron orbitals and the necessity to satisfy the Pauli Exclusion Principle, leading to spin – spin interactions that favor long range spin ordering over macroscopic range. The spin – spin interaction can be expressed universally in terms of Heisenberg Hamiltonian

$$H = - \Sigma J_{ij} \boldsymbol{S}_i \cdot \boldsymbol{S}_j \qquad (1.8)$$

where $\boldsymbol{S}_i$ is the spin angular momentum located at *i*th site of a particular lattice, and the exchange integral J_{ij} represents the strength of the exchange coupling between the spin angular momentum i and j. If J_{ij} is positive, the parallel spin configuration will minimize the system total energy and all spins aligned to each other is the ground state. Therefore, a magnetic material is ferromagnetic. On the other hand, a negative J_{ij} favors the antiparallel alignment of spins and consequently gives rise to antiferromagnetic ordering.

The exchange interactions are isotropic relative to any externally fixed spatial direction. In reality, the exchange spherical symmetry is always broken, because the electron orbitals interact with the potential created by the hosting crystal lattice. As a result of the potential symmetry is characterized in the symmetry of the lattice, spin orientation along certain spatial direction becomes energetically favorable. The

macroscopic behavior of a magnetic material will eventually depend on the spatial direction in which it is measured. Such a phenomenon is called *magnetic anisotropy*.

There are several causes from which the magnetic anisotropy may occur, including the *magnetocrystalline anisotropy* and *shape anisotropy*, *magnetostriction* and *stress anisotropy*. In case of magnetic nanomaterials, *surface anisotropy* and/or other kinds of anisotropy can be of the same magnitude as these usual anisotropies. A brief description of three important magnetic anisotropies responsible for the magnetic properties of magnetic nanomaterials is outline here.

Magnetocrystalline anisotropy depends on spin – orbital coupling and shows various symmetries. The two most common cases are uniaxial and cubic forms. For uniaxial symmetry, the magnetocrystalline anisotropy constant (K_u) is given by

$$K_u = K_0 + K_1\sin^2\theta + K_2\sin^4\theta + \cdots \qquad (1.9)$$

where K_0, K_1, and K_2 are anisotropy constants. While for cubic symmetry, the magnetocrystalline anisotropy constant (K_c) is

$$K_c = K_0 + [K_1(\sin^4\theta\sin^2 2\varphi + \sin^2 2\theta)]/4 + (K_2\sin^2 2\theta\sin^2 2\varphi)/16 + \cdots \quad (1.10)$$

The magnetocrystalline anisotropy is intrinsic and its magnitude determines the magnetization in response of the magnetic field. Large magnetocrystalline anisotropy energy of a magnetic material is called hard magnetic material and shows a large

coercivity in hysteresis measurement. A magnetic material with small magnetocrystalline anisotropy energy is referred to soft magnetic material and has a small value of coercivity.

Shape anisotropy is induced from magnetostatic energy and is an extrinsic property. For a prolate spheroid with major axis c greater than the other two and equal axes length a, the shape anisotropy constant (K_s) is

$$K_s = M_S^2(N_a - N_c)/2 \qquad (1.11)$$

where M_S is the saturation magnetization, N_a and N_c are demagnetization factors. For nonspherical magnetic materials such as a long rod, the shape anisotropy can be very predominant.

Surface anisotropy is caused by the existence of a surface that represents a discontinuity for magnetic interactions. Such surface effects become more significant as the size of magnetic nanomaterials decrease, because the increasing numbers of atoms are on the surface layer of a particle. In order to take into account surface effect, Néel first proposed the surface anisotropy.[25] Recent theoretical studies indicated that spins at surface are dictated by the local crystal field, a lower coordination number and a broken magnetic exchange bond. Thus, surface spins are often canted and/or disordered.[26-28]

Judging from the surface effect is dependent on the size and often correlated to the nanoparticle size effect, an effective anisotropy constant ($K_{eff.}$), which includes the surface anisotropy constant, is used to describe surface effect. For a spherical particle, $K_{eff.}$ is given by

$$K_{eff.} = K + (6/d)K_s \qquad (1.12)$$

where K_s is surface anisotropy constant, K is magnetocrystalline anisotropy constant, and d is the diameter of the particle. Surface anisotropy generally leads the surface to be magnetically harder than the core of the particle.

1.3.2 Single Domain Theory and Superparamagnetism

It is well known that a bulk magnetic material is comprised of magnetic domains. The magnetization inside each domain is uniform, but varies from domain to domain as they are separated by an interface layer known as the domain wall. By reducing the dimension of a magnetic material, the size of the domains is accordingly decreased and their structures may change in terms of domain wall width and wall structures. As far as the energy is concerned, when the size reaches a critical length, the magnetic material only possesses a 'single domain', since the energy cost for the formation of domain walls becomes energetically unfavorable, that is, the energy gain from the formation of domain walls is higher than the energy reduction by dividing the single domain into even smaller domains. The critical size (radius R_C) for domain formation has been estimated by Kittle, which depends on spontaneous magnetization (Ms), the anisotropy constant (K), and the exchange energy density or constant (A) as given in equation 1.13.

$$R_C = 36(KA)^{1/2} / \mu_0 M_S^2 \qquad (1.13)$$

The critical size for typical magnetic materials is in the range of 10 ~ 800 nm. A small magnetic particle less than critical size prefers to be uniformly magnetized along

one of its anisotropy easy axes, and is accompanied by a strong enhancement in coercivity.

If the size of magnetic materials is below the critical size, magnetic materials can only acquire a single domain. On still reduction in size, the magnetic anisotropy energy further deceases and may become so low as to be comparable to or even lower than the thermal energy (k_BT, as k_B being Boltzmann constant). As a result, the energy barrier for magnetization reversal may be thermally overcome, and the magnetic moment is thermally fluctuated, like a single spin in a paramagnetic material. A result of the spins within a single-domain particle remain magnetically coupled to each other is the formation of a 'superspin' with a relative enormous moment per particle, and this phenomenon is called *superparamagnetism*.[29,30] (see Figure 1.3e)

In a simple model described by Stoner-Wohlfarth,[31] for a noninteracting single-domain spherical particle with uniaxial anisotropy in zero magnetic field, the magnetic anisotropy energy is given by an expression of the type

$$E_A = KV \sin^2\theta \qquad (1.14)$$

where E_A is the energy barrier, K is the magnetocrystalline anisotropy constant, V is the volume of the particle, and θ is the angle between magnetization and ease axis of the particle. The dependency of anisotropy energy on θ is depicted schematically in Figure 1.3. Clearly, either θ = 0 or π is a direction of minimum energy and these directions are symmetrically separated by an energy barrier as high as KV. The magnetic field can also be a form of energy that can lower the magnetic anisotropy energy barrier for

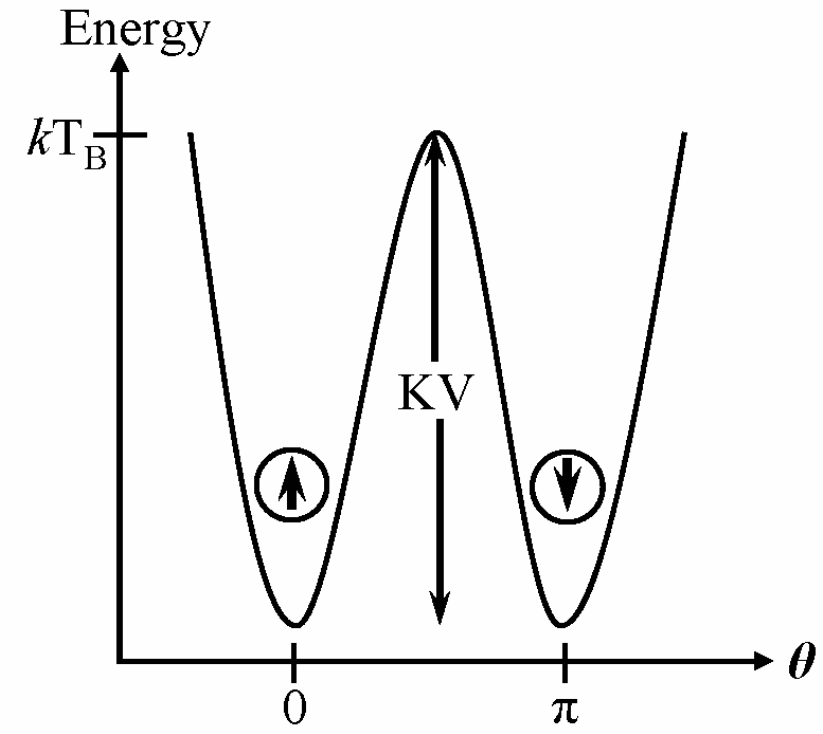

Figure 1.3 Schematic of Stoner-Wohlfarth anisotropy energy barrier for magnetization reversal.

magnetization reversal. When a magnetic field is applied along the easy axis, the anisotropy energy will be as

$$E_A = KV \sin^2\theta - HVM_{nr} \cos\theta \qquad (1.15)$$

where M_{nr} is the nonrelaxing magnetization.

Superparamagnetism is also characterized by a relaxation time (τ) and thus the actual magnetic behavior depends on the value of measuring time (t_m) in a particular experimental technique. Now, the magnetic anisotropy serves as an energy barrier to the total spin reorientation. In a bistable system as shown in Figure 1.3, the probability for such magnetic moment thermally overcoming energy barrier is proportional to Boltzmann factor as derived by Néel as

$$\tau = \tau_0 \exp(- KV/k_BT) \qquad (1.16)$$

where τ_0 is an attempt frequency factor equal to approximately 10^{-9} s, and depends on several factors such as temperature, gyromagnetic ratio, magnetic field, magnetization, particle size and damping constant, and yet is treated as a constant. At given temperature, if the measurement time is much longer than relaxation time, the moment is rapidly relaxed by thermal fluctuation, and consequently the entire system is in superparamagnetic state. On the contrary, as the measurement time is much shorter than the relaxation time, the moment relaxes so slow that it seems to be blocked. The *blocking temperature* is thus defined as the temperature at which the magnetic moment relaxation

time is equal to the measurement time, or the temperature where the moment is able to overcome the energy barrier into the superparamagnetic state at a certain measurement time.

Some typical instrument measurement times are 100 s for DC SQUID, $10^{-7} \sim 10^{-9}$ s for Mössbauer spectroscopy, and $10^{-8} \sim 10^{-12}$ s for neutron diffraction, respectively.

1.4 Review of Size and Shape Controlled Synthesis of Magnetic Nanocrystals

The literature review of size and shape controlled synthesis of magnetic nanocrystals in this section focuses entirely on solution phase "bottom-up" synthetic methodologies with size and shape control capability. Other preparation routes such as mechanical ball-milling and gas phase aerosol processes have been published in literature.[32,33] In addition, as suggested by Murray *et al.*[34] the term nanocrystals refers to as nanostructures with well-characterized crystalline cores and nanoparticles is a more general term denoted to amorphous or inherently multidomain inorganic cores. The following literature review on the synthesis of magnetic nanocrystals is restricted to the procedures that can reproducibly prepare a homologous size and shape series of magnetic nanocrystals with rational adjustments of the experimental conditions.

The chemical synthesis of nanomaterials inevitably is related to the crystallization of solid phase from a solution. A general synthetic scheme for preparing monodispersed nanocrystals relies on rapidly inducing a short nucleation step followed by a slower growth on the formed nuclei.[34,35] To achieve the control on reaction nucleation and growth and consequently the size, size distribution and shapes of nanocrystals, a rapid addition or a direct dissolution of reagents at high temperature is commonly utilized to

increase the active molecular precursor concentration over the nucleation threshold at a short period of reaction time. As the formation of nuclei is over and the precursor concentration is not exceeded the supersaturation threshold, the growth of nanocrystals starts. At this stage, the additional reagents can only accumulate on the existing nuclei and the smaller nanocrystals grow faster than the larger ones, because the free energy of smaller nanocrystals is higher than that of larger ones, which is the so-called "focusing of the size distribution" stage.[35,36]Moreover, due to the fact that the growth of any nanocrystal is similar and homogeneous, the size distribution will be narrow if the reaction is arrested at size focusing stage. On the other hand, if keep the nanocrystal growth for a longer period of time, the depletion of active precursor will cause the concentration decreased and the relative smaller nanocrystals dissolved, as a result, the size distribution of nanocrystal will be broader. This has been known as "Ostwald ripening".[37]

In general, the nanocrystal size is dependent on a set of reaction parameters such as temperature, time, and precursor concentration. The longer the reaction time and the higher the reaction temperature typically result in the formation of larger nanocrystals. The nanocrystal size is also strongly determined by some other parameters including the types of solvent, coordinate or non-coordinate, and the characteristic of surfactants such as strong or weak binding capability and the steric hindrance. For example, a stronger binding or a bulky surfactant can retard the rate of precursor addition to the nanocrystals, leading to a smaller nanocrystal size. Finally, size-selective precipitation or size sorting has become a practical procedure and is frequently used to further narrow the size distribution of as-synthesized nanocrystals to monodispersity (standard deviation $\sigma < 5\%$).

Remarkable progress in the shape-controlled synthesis of nanocrystals has been made over the past years. A variety of shapes, rod, branched rod, disk, cube, star, and polyhedral shapes have been successfully produced. For most of shape-controlled synthesis of colloidal semiconductor nanocrystals, the growth mechanism on shape evolution has been investigated by Peng and co-workers based on II-VI semiconductor nanocrystals. A monomer-concentration-dependence model has been proposed to account for the mechanism of shape evolutions of semiconductor nanocrystals.[36,38] In the case of metal and metal oxides nanocrystals, no general shape evolution mechanism has been established so far. However, it has been demonstrated in many cases that the surfactant plays a key role on the shape evolutions, because the binding of surfactant on a specific facet of crystal will vary the surface energy and consequently change the rate growth from one facet to another. An effective strategy on shape control involves the application of a pair of surfactants, whereby one coordinates tightly on the nanocrystal surface, slowing the growth rate, and the other binds weakly, allowing rapid growth. By adjusting the ratio of these surfactants, the growth rate and therefore the shape of nanocrystals can be controlled.

1.4.1 Preparation of Magnetic Metal and Metal Alloy Nanocrystals

The synthesis of magnetic metal nanocrystals of Fe, Co, Ni and metal alloys of FePt and CoPt is of great interest. Numerous synthetic procedures have been developed to control the size and shapes of magnetic metal and metal alloy nanocrystals. In the synthesis of Fe nanocrystals,[39] as shown in Figure 1.4a. Thermal decomposition of precursor $Fe(CO)_5$ in the presence of trioctylphospine oxide (TOPO) at 340 °C results in

the formation of spherical Fe nanocrystals. When using these spherical Fe nanocrystals as seeds and in the presence of pyridine and surfactant of didodecylmethylammonium bromide (DDAB), the shape of Fe nanocrystals changed to rods. This morphology variation from sphere to rod has been attributed to the irreversible binding of DDAB surfactant on the center region of nanocrystals and the fusion of spherical Fe nanocrystals. The cubic Fe nanocrystals have also been synthesized recently by thermal decomposition of $[Fe\{N(SiMe_3)_2\}_2]$ with H_2 in the presence of oleic acid (OA) and hexadecylamine (HDA) after 48 hours reaction at 150 °C in Figure 1.4b. The quality of Fe nanocubes is very high in terms of the uniformity on both size and shape. Large self assembled orientation ordered superlattices formed by these cubic Fe nanocrystals were observed.[40] Although other alkylamines and carboxylic acids with different carbon chain length as well as the variation in their ratios have been examined, only limited effect on shape of Fe nanocrystals was observed. By contrast, the reaction time can dramatically influence the shape of Fe nanocrystals. For example, if the reaction was stopped after 3 hours, a mixture of spherical and cubic nanocrystals with a polydispersed size distribution was found. However, if the reaction time was extended to 18 hours, smaller cubic Fe nanocrystals were the final product. These results lead the authors to conclude that the crystal structure of Fe (bcc) might involve in the shape control of nanocrystals under thermodynamic conditions. Also, the success on the preparation of Fe nanocubes suggests that the hydrogen atmosphere is important, as it provides a reduction condition and likely prevents the oxidation problems that may otherwise be caused by the formation of water by the acid and amine.

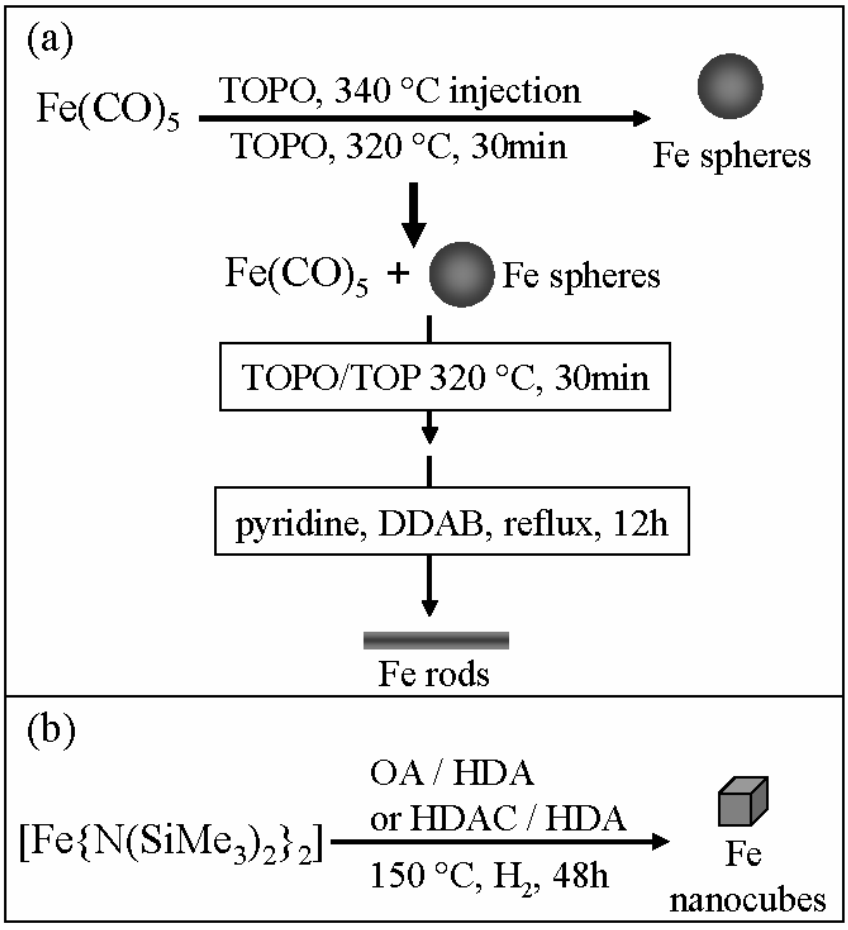

Figure 1.4 Some examples of shape controlled synthesis of Fe nanocrystals. (see text)

The synthetic methods for Co nanocrystals are similar to those of Fe nanocrystals, a range of crystal structures and shapes, however, have been observed in different procedures. Figure 1.5 shows the shape evolutions of Co nanocrystals prepared by different routes. After the injection of $Co_2(CO)_8$ into a hot (182 °C) solvent *o*-dichlorobenzene (DCB) with oleic acid and TOPO, the disk-like Co nanocrystals were formed at initial course of reaction (<10 seconds). As the reaction was kept for a sufficient period of time, not only the disk Co nanocrystals transformed into more thermodynamically stable spheres,[41] but the crystal phases also vary from hexagonal-close-packing, hcp-Co to ε-Co, as shown in Figure 1.5a. As the substitution of the surfactant of linear chain alkylamine for TOPO, the formation of hcp-Co nanodisks becomes easier and can survive for longer period of time, due to amine surfactant is a stronger binding ligand to Co relative to bulky TOPO ligand.

Co nanorods can be produced by thermal decomposition of organometallic precursor, $[Co(\eta^3\text{-}C_8H_{13})(\eta^4\text{-}C_8H_{12})]$ in the presence of H_2, oleic acid and amine at 150 °C.[42,43] The aspect ratios of nanorods are strongly dependent on the different combinations of carboxylic acids and alkylamines, as shown in Figure 1.5b. An interesting result is that in addition to the reaction time, H_2 is an essential component on the rod formation in Figure 1.5c. If there is no H_2 presented in reaction, only spherical Co nanocrystals were formed, even though the reaction was kept for 48 hours. This is very similar with the formation of Fe nanocubes. However, as the precursor of Co varying from $[Co(\eta^3\text{-}C_8H_{13})(\eta^4\text{-}C_8H_{12})]$ to $Co_2(CO)_8$, instead of the formation of Co nanorods, only polydispersed spherical Co nanocrystals are made, indicating the chemical nature of precursor is also an important parameter on shape evolution of Co nanocrystals.

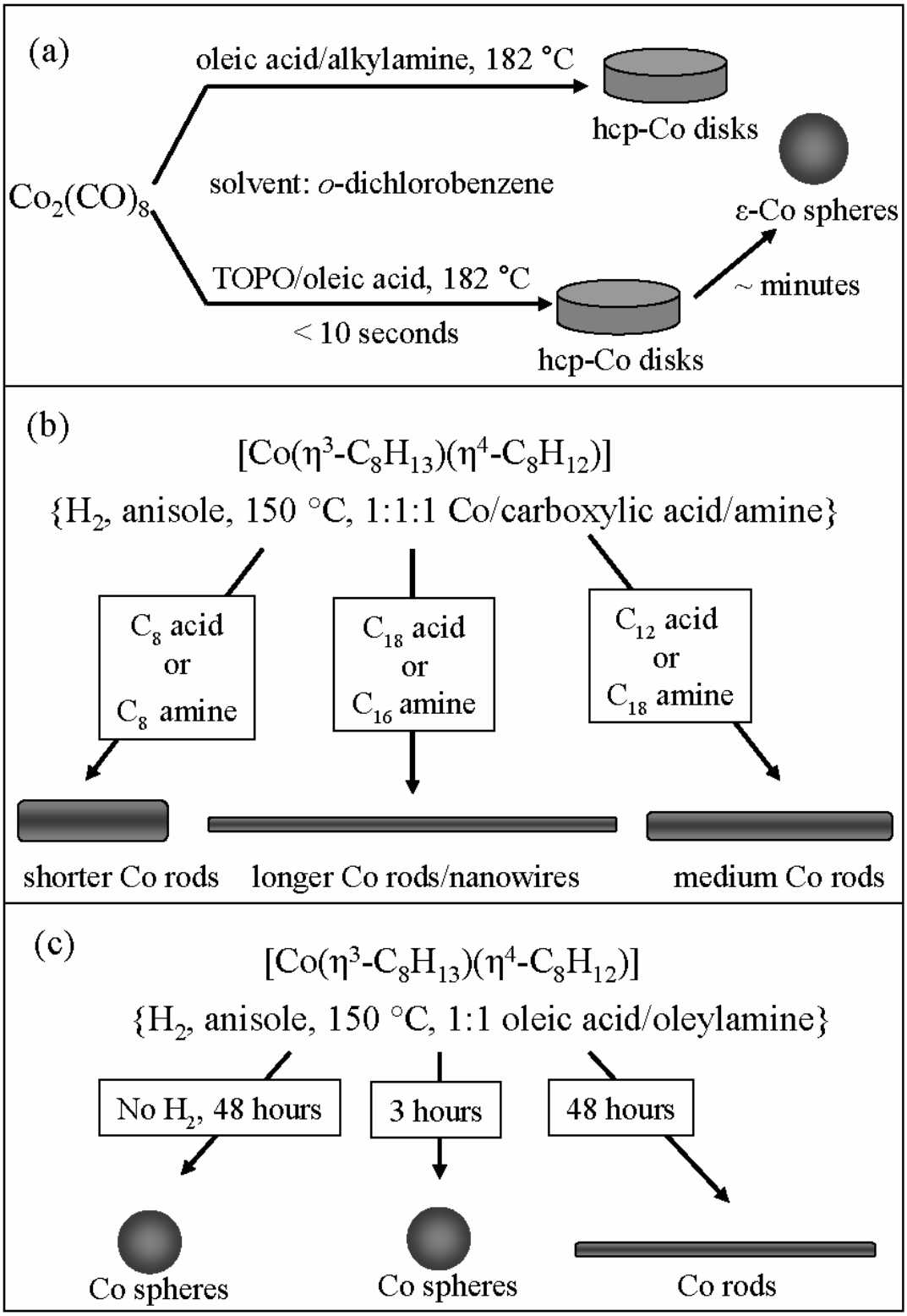

Figure 1.5 Examples of shape controlled synthesis of Co nanocrystals. (see text)

Spherical Co nanocrystals have also been produced by the reduction of cobalt salts by polyalcohols (polyol process) or reduction reagents at temperature ranging from 100 °C to 300 °C in the presence of surfactants.[44,45] The size of Co nanocrystals can be tailored by the precursor concentration and the surfactants. For example, the substitution of tributylphospine (TBP) for trioctylphospine (TOP) allows the larger spherical Co nanocrystals to be produced, due to the less steric hindrance effect of TBP.

It is intriguing that the crystal structure of Co nanocrystals varies from hcp, fcc to ε-Co under different reaction conditions, as presented in Figure 1.6. ε-Co is a cubic crystal phase (space group $P4_132$), which contains 20 cobalt atoms in two subgroups: 12 cobalt atoms of Type I and 8 atoms of Type II.[44,46] This ε-Co is a metastable phase and can be transformed into more thermodynamically stable hcp or fcc structures upon heat treatment at 300 °C or 500 °C, respectively. A recent report by Samia *et al.*[47] showed the existence of clusters of Co_2 and Co_3 carboxylic acid complexes in the preparation of ε-Co nanocrystals, which provides the direct experimental evidence on the formation of ε-Co crystal structure, due to Co_2 and Co_3 clusters being the basic unit in ε-Co structure.

The preparation of Ni nanocrystals resembles the procedure of reduction formation of Co nanocrystals, as long as replacing the Co precursor by Ni precursor as shown in Figure 1.7a.[45] The Ni nanorods have been synthesized under reaction condition similar to the preparation of Co nanorods in Figure 1.7b.[48]

Last, Fe, Co and Ni nanoparticles have also been produced by the reduction of metal salts in aqueous solution. To better control the size of nanoparticles, reverse microemulsion method has been used.[49] The only lanthanide magnetic metal nanoparticle produced in solution is Gd nanoparticles.[50] Under strictly anaerobic and anhydrous

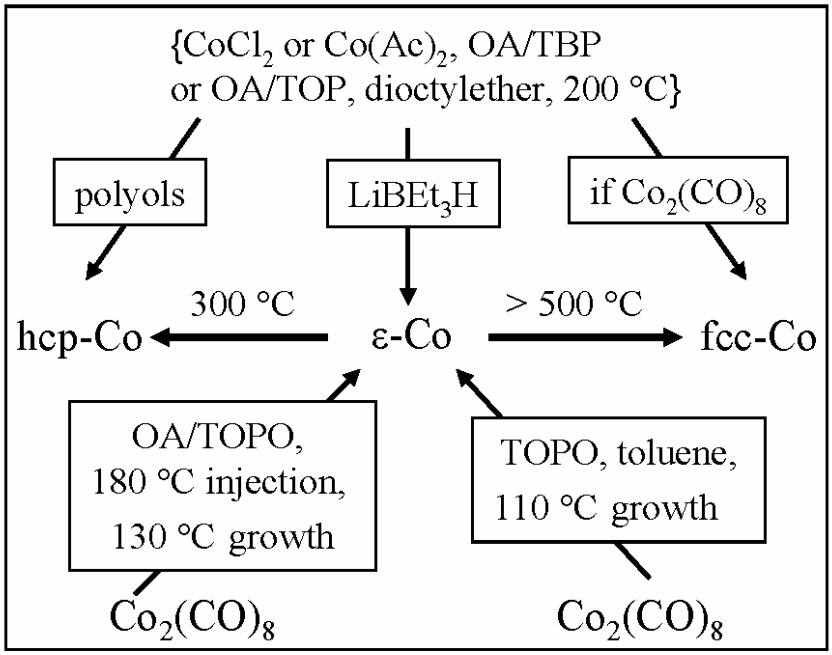

Figure 1.6 Crystal structure evolutions of Co nanocrystals in different synthetic methods.

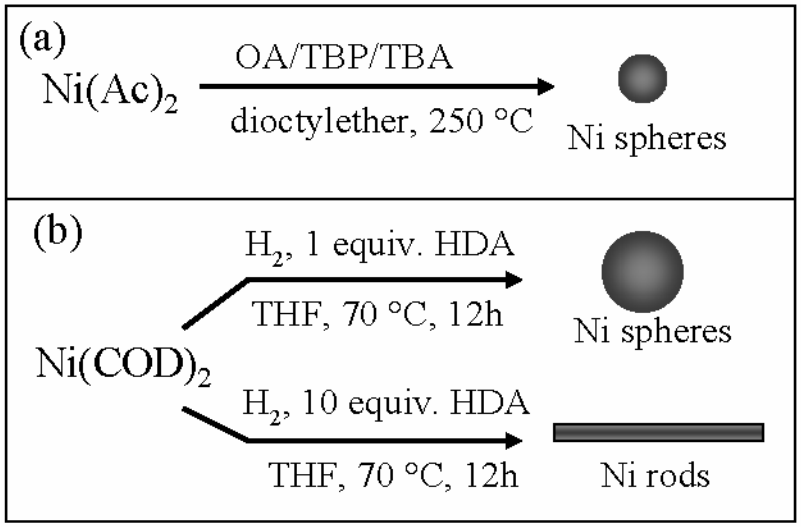

Figure 1.7 Examples of shape controlled synthesis of Ni nanocrystals.(see text)

conditions, the $GdCl_3$ was reduced by alkalide ($K^+(15\text{-crown-}5)_2Na^-$) to yield Gd nanoparticles.

The synthesis of magnetic metal alloy nanocrystals with a high uniaxial anisotropy and a large coercivity is of great interest, since they are the most attractive candidates of the next-generation of ultrahigh density magnetic recording media.[2] FePt nanocrystal is among one of the most investigated systems. Several procedures have been developed to prepare monodispersed FePt nanocrystals.[3,51-54] A typical preparation of FePt nanocrystals is conducted by simultaneous reduction of $Pt(acac)_2$ and thermal decomposition of $Fe(CO)_5$ in high boiling organic octyl ether solvent as given in Figure 1.8. Other precursors such as $Fe(acac)_2$ and $FeCl_2$ have also been successfully used to make FePt nanocrystals.[51,53] The crystal structure of as-synthesized FePt nanocrystals is face-center cubic and they are magnetically soft. To form magnetically hard phase FePt, the crystal structure must be transformed from face center cubic to face center tetragonal (fct) (see Figure 1.8 bottom). Such phase transition is typically conducted at temperatures more than 550 °C under a reducing atmosphere (H_2 or CO). However, this heat treatment process gives rise to a serious aggregation of small FePt nanocrystals and completely destroys the assemble arrays, because the organic surfactant protection layers can not survive from such high temperature treatment.[55] On an attempt to overcome this problem, the fabrication of core-shell structured $FePt@Fe_3O_4$ nanocrystals has recently been studied. Another synthetic method for solving this problem is by sequential formation of a core of Pt nanocrystals first and *in situ* overcoating Fe_2O_3 to make a $Pt@Fe_2O_3$ core shell structure. After the later high temperature annealing under a reducing atmosphere,

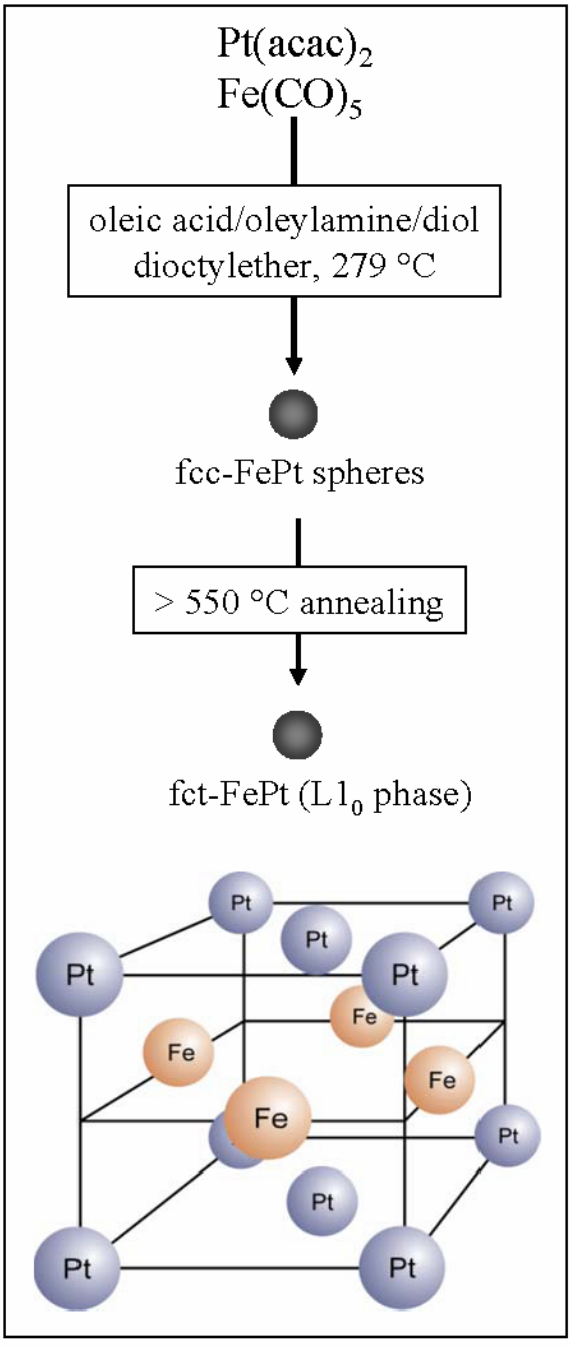

Figure 1.8 A general synthetic procedure of FePt nanocrystals. The inset is the crystal model of fct $L1_0$ phase of FePt.

the desired fct-FePt nanocrystals are formed.[54,56] Additionally, the variation in the size of fct-FePt nanoparticles is not difficult by this synthetic procedure. Last, except for a very recent report by Sun and coworkers,[57] the progress in the shape controlled synthesis of FePt nanocrystals is still limited.

CoPt magnetic nanocrystals can be prepared by several different routes. Simultaneous reaction of $[Co(\eta^3\text{-}C_8H_{13})(\eta^4\text{-}C_8H_{12})]$ and $Pt(dba)_3$ with H_2 and polymer PVP surfactant results in the production of polymer coated CoPt nanocrystals.[58,59] The chemical composition can be adjusted between Co_3Pt, CoPt and $CoPt_3$ by varying the ratios of precursors. Simultaneous thermal decomposition of $Co_2(CO)_8$ and reduction of $Pt(acac)_2$ in the 1-adamantanecarboxylic acid and various coordinating solvents gives rise to the formation of monodispersed $CoPt_3$ nanocrystals.[60-62]

1.4.2 Preparation of Magnetic Metal Oxides Nanocrystals

The above mentioned preparation methods can be potentially indirect routes for the synthesis of metal oxides nanocrystals. Herein, the focus is on the direct size and shape controlled synthesis of magnetic metal oxide nanocrystals. In general, the crystallization of metal oxides can be from both aqueous and nonaqueous solutions. The preparation of monodispersed metal oxides nanoparticles frequently requires a surfactant as stabilizer to prevent agglomeration in the course of synthesis.

In case of the synthesis in aqueous solution, different sized metal oxides nanoparticles have been produced by various methods including coprecipitation, microemulsion, forced hydrolysis, sonochemical and hydrothermal process *etc*.[63-81] The nanoparticle size range varies from 5 nm to 30 nm with a typical size distribution ranging

from 10% to 30 %. Many of these procedures can be applied to the preparation of different doped metal oxide nanoparticles such as spinel ferrites $CoCrFeO_4$, and $Co_{0.85}Zn_{0.15}Fe_2O_4$, $CoLn_{0.12}Fe_{1.88}O_4$ (Ln = Ce, Sm, Eu, Gd, Dy, Er),[82-85] and binary metal oxide nanoparticles including Co_3O_4.[86,87]

Nonhydrolytic procedures for the synthesis of iron oxides nanoparticles rely on the thermal decomposition of an appropriate iron precursor in hot surfactants. A rapid injection of iron cupferon ($Fe(Cup)_3$) octylamine solution into hot trioctylamine leads to the formation of γ-Fe_2O_3 nanoparticles coated with an amine monolayer.[88] By controlling the reaction temperature or by performing sequential addition of $Fe(Cup)_3$, the size of these γ-Fe_2O_3 nanoparticles can be varied between 5 and 10 nm. Thermal decomposition of $Fe(CO)_5$ in octyl ether containing oleic acid and trimethylamine oxide (TMO) results in the production of oleate γ-Fe_2O_3 coated nanocrystals.[89] The size distribution of γ-Fe_2O_3 nanocrystals is very narrow, less than 5%. Fe_3O_4 nanocrystals can be prepared by the reaction of $Fe(acac)_3$ in phenyl ether solution with oleic acid, oleylamine, 1,2-hexdecandiol at reflux. The size of Fe_3O_4 nanocrystals can be tuned from 4 nm to 20 nm by a seed-mediated growth process.[90] Fe_3O_4 nanocrystals have also been prepared by directly using iron carboxylate such as iron oleate at high temperature.[91-93] The iron carboxylate can be prepared separately or *in situ* formation by dissolving either elemental iron or inorganic iron salts at high boiling non-coordinating solvent. By changing the reaction time or the concentration of carboxylic acid, the size of Fe_3O_4 nanocrystals can be varied between 6 nm and 30 nm with size distribution about 5%~ 10%. The preparations of other magnetic metal oxides nanocrystals can be done by simply substituting different metal precursors for iron. The thermal decomposition of (η^5-

$C_5H_5)CoFe_2(CO)_9$ with oleic acid in octyl ether followed by oxidizing by trimethylamine N-oxide ($(CH_3)_3NO$) can form $CoFe_2O_4$ nanocrystals.[94] Through controlling the molar ratio of precursor to oleic acid and the carbon chain length of carboxylic acids, the size of $CoFe_2O_4$ nanocrystals can be varied from 4 nm to 9 nm. When using $Co(acac)_2$ and $Fe(acac)_3$ as metal precursors, the thermal decomposition of these precursors in a solution of oleic acid, oleylamine, 1,2-hexadecandiol and phenyl ether can yield 4 nm monodispersed $CoFe_2O_4$ nanocrystals. The size of $CoFe_2O_4$ nanocrystals can be controlled by a seed-mediated growth up to 20 nm. Similarly, $MnFe_2O_4$ nanocrystals are produced by using $Mn(acac)_2$ and $Fe(acac)_3$ or $Mn_2(CO)_{10}$ and $Fe(CO)_5$ as precursors.[95]

The shape of many magnetic metal oxides nanocrystals is commonly spherical. Only until recently that the nonhydrolytic synthesis of cubic $CoFe_2O_4$[96] and $MnFe_2O_4$[97] nanocrystals have been reported.

1.5 Some Potential Applications of Magnetic Nanoparticles

The history of applications of magnetic materials could be retrospect to ancient China more than two thousand years ago, where ancient Chinese people used a natural mineral magnetite (Fe_3O_4) as a navigational compass.[98] Nowadays, magnetic materials are ubiquitous and indispensable in our daily life. In the past decades, in response to the booming of a wide range applications of computers and various portable electronic devices, the pursuit of reliable ultrahigh-density and low-cost magnetic recording media provide the major fundamental and technological driving forces for the exploration of magnetic nanoparticles. IBM developed the first commercial hard disk drive (HDD) in 1956, which could store a whopping 5 MB of data. Today, one can get a 3.5-inch drive

that stores 500 GB of data.[5] The growth of storage has exploded largely because of the ability to push the information bits size smaller and spacing closer, which dramatically increases the areal density. Two common recording techniques, longitudinal and perpendicular recording, are currently used to fabricate HDDs as shown in Figure 1.9. For perpendicular recording media, the further increase in areal density is being approached to its limitation of 1 Terabit (TB) per square inch. Beyond longitudinal and perpendicular recording, various possible methods are being proposed and explored. However, there are limits to how small the bits may be made, known as superparamagnetic limitation. To counterbalance it, permanent metal alloy FePt nanocrystals with higher uniaxial anisotropy and coercivity have been extensively investigated and demonstrated that it is possible to break through this superparamagnetic limit and ultimately increase the achievable recording media density to single particle limit at ~ 40 - 50 TB/in^2, as shown in Figure 1.10.[3,99,Chao Liu, Private Communication]

There are a number of potential biomedical applications for magnetic nanoparticles, including the probing, labeling and magnetic separation of biological molecules, magnetic guided targeting drug delivery, magnetic resonance imaging (MRI) contrast enhancement, and hyperthermia treatment. In general, iron oxides, in particular magnetite and maghemite (γ-Fe_2O_3) nanoparticles, are used in these applications as they are more biocompatible and more amenable to the buffered aqueous solution present in biological systems. In MRI, magnetic resonance imaging contrast is the result of the different signal magnitude or intensity produced in response to a particular sequence of applied radiofrequency (RF) pulses and is not only dependent on the concentration of hydrogen

atoms in a specific volume, but is also dependent upon the rate of relaxation of the spin of the protons T1 (the exponential decay constant in the longitudinal relaxation of the spins)

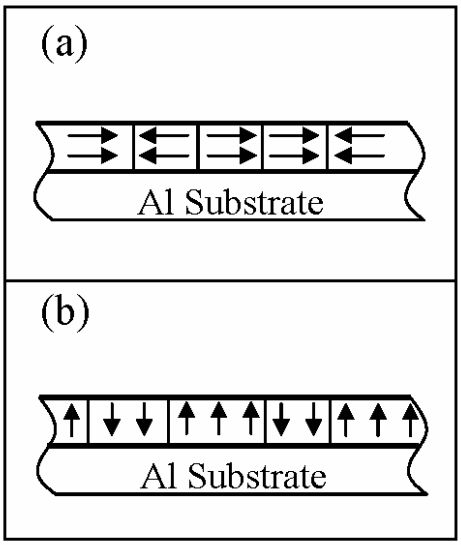

Figure 1.9 Schematic of longitudinal (a) and perpendicular (b) recording models.

and T2 (the exponential relaxation constant in the dephasing (transversal) of the spins).[101] Both T1 and T2 are subject to modification by the magnetic contrast enhancers such as iron oxides nanoparticles, while since T2 relaxation occurs primarily by magnetic interactions of protons with neighboring magnetic nanoparticles, the addition of magnetic field by superparamagnetic nanoparticles has a very strong effect upon T2 and relatively

less influence on T1, so superparamagnetic nanoparticles are generally considered to be T2 contrast enhancement agents.

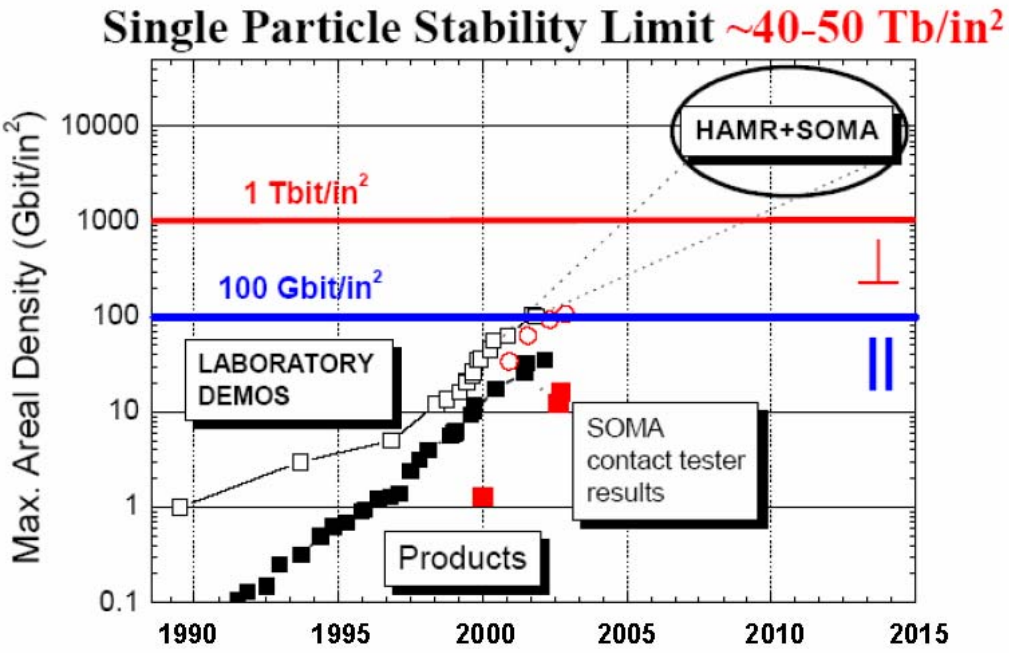

Figure 1.10 Progress in the areal density (bits/in^2) in commercial hard drive disks in the past ten years. ∥ represents longitudinal recording, ⊥ is the perpendicular recording. (Courtesy of Dr. Chao Liu, Seagate)

Recent developments of bioconjugated magnetic nanoparticles have been demonstrated in a multitude of biomedical applications. For example, superparamagnetic iron oxides nanoparticles are coated with poly(ethylene oxide) as blood-pool contrast enhancement agents. Another common approach to biomodification of superparamagnetic iron oxides nanoparticles is to coat nanoparticles with dextran to increase the cell uptake (endocytosis) of nanoparticles and consequently enhance the cell imaging. A remarkable result of application of iron oxides nanoparticles in cancer diagnosis has been recently reported, which the size of prostate cancer as small as 2mm can be distinguishably identified in MRI scan by using superparamagnetic iron oxides as contrast enhancers compared to conventional MRI.[11] In addition, various other methods have also been reported in cancer and tumor diagnosis, gene expression, T-cell migration, DNA and cell purification and sorting.[8,102-107]

A further application of magnetic nanoparticles is based on hyperthermia, which a medical treatment depends on locally heating tissue over 42 °C for a short period of time to destroy the tissue, especially tumors. In hyperthermia, the heat is produced by the hysteresis of magnetic materials. For superparamagnetic nanoparticles, the hysteresis is typically lack on the timescale of magnetic measurements. However, in a relatively high-frequency ac magnetic field, the magnetization lags the magnetic field, giving rise to a complex susceptibility. Thus, the magnetic energy will be dissipated as heat as a result of the out of phase and loss susceptibility.[108] Superparamagnetic nanoparticles with higher saturation magnetization and lower anisotropy would be an ideal hyperthermia system, if considering the limitations of injection dose and ac magnetic field strength that can be applied in hyperthermia treatments.

Besides in magnetic recording media and biomedical applications, magnetic nanoparticles are also used as highly active catalysts due to the higher surface-to-volume aspect ratios. More stable and active catalysts based on NiPt and CoPt nanoparticles have been developed in the fabrication of fuel cells,[109,110] and chemical decomposition of toxic compounds in ground water such as halogenated alkanes and nitroaromatics.[111-117] Finally, some magnetic nanoparticles of Fe, Ni, Co, and FeMo have also been used in control synthesis of carbon nanotubes via a variety of chemical vapor deposition processes.[118-121]

1.6 References

(1) Weller, D.; Moser, A. *IEEE Trans. Magn.* **1999**, *35*, 4423.

(2) Weller, D.; Moser, A.; Folks, L.; Best, M. E.; Lee, W.; Toney, M. F.; Schwickert, M.; Thiele, J.-U.; Doerner, M. F. *IEEE Trans. Magn.* **2000**, *36*, 10.

(3) Sun, S.; Murray, C. B.; Weller, D.; Folks, L.; Moser, A. *Science* **2000**, *287*, 1989.

(4) Weller, D.; Doerner, M. F. *Annu. Rev. Mater. Sci.* **2000**, *30*, 611.

(5) Herzer, G.; Vazquez, M.; Knobel, M.; Zhukov, A.; Reininger, T.; Davies, H. A.; Groessinger, R.; Sanchez Ll, J. L. *J. Magn. Magn. Mater.* **2005**, *294*, 252.

(6) Knobel, M.; Ferrari, E. F.; Silva, F. C. S. *Mater. Sci. Forum* **1999**, *302-303*, 169.

(7) Knobel, M.; Vazquez, M.; Kraus, L. *Handbook of Magnetic Materials* **2003**, *15*, 497.

(8) Pankhurst, Q. A.; Connolly, J.; Jones, S. K.; Dobson, J. *J. Phys. D: Appl. Phys.* **2003**, *36*, R167.

(9) McMichael, R. D.; Shull, R. D.; Swartzendruber, L. J.; Bennett, L. H.; Watson, R. E. *J. Magn. Magn. Mater.* **1992**, *111*, 29.

(10) Liou, S. H.; Huang, S.; Klimek, E.; Kirby, R. D.; Yao, Y. D. *J. Appl. Phys.* **1999**, *85*, 4334.

(11) Harisinghani, M.; Barentsz, J.; Weissleder, R. *New England Journal of Medicine* **2003**, *349*, 1186.

(12) Shen, T.; Weissleder, R.; Papisov, M.; Bogdanov, A., Jr.; Brady, T. J. *Magnetic Resonance in Medicine* **1993**, *29*, 599.

(13) Weissleder, R.; Bogdanov, A.; Neuwelt, E. A.; Papisov, M. *Advanced Drug Delivery Reviews* **1995**, *16*, 321.

(14) Zhao, M.; Josephson, L.; Tang, Y.; Weissleder, R. *Angew. Chem., Int. Ed.* **2003**, *42*, 1375.

(15) Häfeli, U., Schütt, W.; Teller,J.; Zborowski, M. *Scientific and Clinical Applications of Magnetic Carriers*; Plenum Press: New York, 1997.

(16) Ederer, C.; Spaldin, N. A. *Nature Materials* **2004**, *3*, 849.

(17) Raj, K.; Moskowitz, B.; Casciari, R. *J. Magn. Magn. Mater.* **1995**, *149*, 174.

(18) Morrish, A. H. *The Physical Principles of Magetism*; John Wiley & Sons, Inc.: New York, 1965.

(19) Cullity, B. D. *Introduction to Magnetic Materials*; Addison-Wesley Publishing: Reading, 1972.

(20) Jakubovics, J. P. *Magnetism and Magnetic Materials*; The Institute of Metals: London, 1987.

(21) Jiles, D. *Introduction to Magnetism and Magnetic Materials*; Chapman & Hall: London, 1990.

(22) Spaldin, N. A. *Magnetic Materials: Fundamentals and Device Applications*; Cambridge University Press: Cambridge, 2003.

(23) O'Handley, R. C. *Morden Magnetic Materials: Principles and Applications*; John Wiley & Sons Inc.: New York, 2000.

(24) Giorgio, B. *Hysteresis in Magnetism: For Physicists, Materials Scientists, and Engineers*; Academic Press: San Diego, 1998.

(25) Neel, L. *Journal de Physique et le Radium* **1954**, *15*, 225.

(26) Kodama, R. H.; Berkowitz, A. E.; McNiff, E. J., Jr.; Foner, S. *Phys. Rev. Lett.* **1996**, *77*, 394.

(27) Kodama, R. H.; Berkowitz, A. E.; McNiff, E. J., Jr.; Foner, S. *Mater. Sci. Forum* **1997**, *235-238*, 643.

(28) Kodama, R. H.; Berkowitz, A. E. *Physical Review B: Condensed Matter and Materials Physics* **1999**, *59*, 6321.

(29) Bean, C. P.; Jacobs, I. S. *J. Appl. Phys.* **1956**, *27*, 1448.

(30) Bean, C. P.; Livingston, J. D. *J. Appl. Phys.* **1959**, *30*, 120S.

(31) Stoner, E. C.; Wohlfarth, E. P. *Trans. Roy. Soc.* **1948**, *A240*, 599.

(32) Murty, B. S.; Ranganathan, S. *Inter. Mater. Rev.* **1998**, *43*, 101.

(33) Kruis, F. E.; Fissan, H.; Peled, A. *J. Aerosol Sci.* **1998**, *29*, 511.

(34) Murray, C. B.; Kagan, C. R.; Bawendi, M. G. *Annu. Rev. Mater. Sci.* **2000**, *30*, 545.

(35) Peng, X.; Wickham, J.; Alivisatos, A. P. *J. Am. Chem. Soc.* **1998**, *120*, 5343.

(36) Peng, Z. A.; Peng, X. *J. Am. Chem. Soc.* **2002**, *124*, 3343.

(37) LaMer, V. K.; Dinegar, R. H. *J. Am. Chem. Soc.* **1950**, *72*, 4847.

(38) Peng, X. *Adv. Mater.* **2003**, *15*, 459.

(39) Park, S.-J.; Kim, S.; Lee, S.; Khim, Z. G.; Char, K.; Hyeon, T. *J. Am. Chem. Soc.* **2000**, *122*, 8581.

(40) Dumestre, F.; Chaudret, B.; Amiens, C.; Renaud, P.; Fejes, P. *Science* **2004**, *303*, 821.

(41) Puntes, V. F.; Zanchet, D.; Erdonmez, C. K.; Alivisatos, A. P. *J. Am. Chem. Soc.* **2002**, *124*, 12874.

(42) Dumestre, F.; Chaudret, B.; Amiens, C.; Fromen, M.-C.; Casanove, M.-J.; Renaud, P.; Zurcher, P. *Angew. Chem., Int. Ed.* **2002**, *41*, 4286.

(43) Dumestre, F.; Chaudret, B.; Amiens, C.; Respaud, M.; Fejes, P.; Renaud, P.; Zurcher, P. *Angew. Chem., Int. Ed.* **2003**, *42*, 5213.

(44) Sun, S.; Murray, C. B. *J. Appl. Phys.* **1999**, *85*, 4325.

(45) Murray, C. B.; Sun, S.; Doyle, H.; Betley, T. *MRS Bulletin* **2001**, *26*, 985.

(46) Dinega, D. P.; Bawendi, M. G. *Angew. Chem., Int. Ed.* **1999**, *38*, 1788.

(47) Samia, A. C. S.; Hyzer, K.; Schlueter, J. A.; Qin, C.-J.; Jiang, J. S.; Bader, S. D.; Lin, X.-M. *J. Am. Chem. Soc.* **2005**, *127*, 4126.

(48) Cordente, N.; Respaud, M.; Senocq, F.; Casanove, M.-J.; Amiens, C.; Chaudret, B. *Nano Lett.* **2001**, *1*, 565.

(49) Petit, C.; Taleb, A.; Pileni, M. P. *Adv. Mater.* **1998**, *10*, 259.

(50) Nelson, J. A.; Bennett, L. H.; Wagner, M. J. *J. Am. Chem. Soc.* **2002**, *124*, 2979.

(51) Sun, S.; Anders, S.; Thomson, T.; Baglin, J. E. E.; Toney, M. F.; Hamann, H. F.; Murray, C. B.; Terris, B. D. *J. Phys. Chem. B* **2003**, *107*, 5419.

(52) Elkins, K. E.; Vedantam, T. S.; Liu, J. P.; Zeng, H.; Sun, S.; Ding, Y.; Wang, Z. L. *Nano Lett.* **2003**, *3*, 1647.

(53) Liu, C.; Wu, X.; Klemmer, T.; Shukla, N.; Yang, X.; Weller, D.; Roy, A. G.; Tanase, M.; Laughlin, D. *J. Phys. Chem. B* **2004**, *108*, 6121.

(54) Teng, X.; Yang, H. *J. Am. Chem. Soc.* **2003**, *125*, 14559.

(55) Liu, C.; Wu, X.; Klemmer, T.; Shukla, N.; Weller, D.; Roy, A. G.; Tanase, M.; Laughlin, D. *Chem. Mater.* **2005**, *17*, 620.

(56) Teng, X.; Black, D.; Watkins, N. J.; Gao, Y.; Yang, H. *Nano Lett.* **2003**, *3*, 261.

(57) Chen, M.; Liu, J. P.; Sun, S. *J. Am. Chem. Soc.* **2004**, *126*, 8394.

(58) Ely, T. O.; Pan, C.; Amiens, C.; Chaudret, B.; Dassenoy, F.; Lecante, P.; Casanove, M. J.; Mosset, A.; Respaud, M.; Broto, J. M. *J. Phys. Chem. B* **2000**, *104*, 695.

(59) Dassenoy, F.; Casanove, M. J.; Lecante, P.; Verelst, M.; Snoeck, E.; Mosset, A.; Ely, T. O.; Amiens, C.; Chaudret, B. *J. Chem. Phys.* **2000**, *112*, 8137.

(60) Shevchenko, E. V.; Talapin, D. V.; Rogach, A. L.; Kornowski, A.; Haase, M.; Weller, H. *J. Am. Chem. Soc.* **2002**, *124*, 11480.

(61) Shevchenko, E. V.; Talapin, D. V.; Rogach, A. L.; Kornowski, A.; Haase, M.; Weller, H. *J. Am. Chem. Soc.* **2002**, *124*, 13958.

(62) Shevchenko, E. V.; Talapin, D. V.; Schnablegger, H.; Kornowski, A.; Festin, O.; Svedlindh, P.; Haase, M.; Weller, H. *J. Am. Chem. Soc.* **2003**, *125*, 9090.

(63) Sapieszko, R. S.; Matijevic, E. *J. Colloid Interface Sci.* **1980**, *74*, 405.

(64) Regazzoni, A. E.; Matijevic, E. *Corrosion* **1982**, *38*, 212.

(65) Regazzoni, A. E.; Matijevic, E. *Colloids Surf.* **1983**, *6*, 189.

(66) Tamura, H.; Matijevic, E. *J. Colloid Interface Sci.* **1982**, *90*, 100.

(67) Matijevic, E. *Langmuir* **1994**, *10*, 8.

(68) Sugimoto, T. *Adv. Colloid Interface Sci.* **1987**, *28*, 65.

(69) Kan, S.; Yu, S.; Peng, X.; Zhang, X.; Li, D.; Xiao, L.; Zou, G.; Li, T. *J. Colloid Interface Sci.* **1996**, *178*, 673.

(70) Si, S.; Li, C.; Wang, X.; Yu, D.; Peng, Q.; Li, Y. *Cryst, Growth & Design* **2005**, *5*, 391.

(71) Moumen, N.; Pileni, M. P. *Chem. Mater.* **1996**, *8*, 1128.

(72) Tang, Z. X.; Sorensen, C. M.; Klabunde, K. J.; Hadjipanayis, G. C. *J. Colloid*

Interface Sci. **1991**, *146*, 38.

(73) Shafi, K. V. P. M.; Koltypin, Y.; Gedanken, A.; Prozorov, R.; Balogh, J.; Lendvai, J.; Felner, I. *J. Phys. Chem. B* **1997**, *101*, 6409.

(74) Shafi, K. V. P. M.; Gedanken, A.; Prozorov, R.; Balogh, J. *Chem. Mater.* **1998**, *10*, 3445.

(75) Ulman, A.; Shafi, K. V. P. M.; Yn, X.; Yang, N.-L.; Estournes, C. *Polym. Mater. Sci. Eng.* **2001**, *84*, 789.

(76) Vestal, C. R.; Zhang, Z. J. *International Journal of Nanotechnology* **2004**, *1*, 240.

(77) Chen, Q.; Zhang, Z. J. *Appl. Phys. Lett.* **1998**, *73*, 3156.

(78) Chen, Q.; Rondinone, A. J.; Chakoumakos, B. C.; Zhang, Z. J. *J. Magn. Magn. Mater.* **1999**, *194*, 1.

(79) Liu, C.; Zhang, Z. J. *Chem. Mater.* **2001**, *13*, 2092.

(80) Liu, C.; Zou, B.; Rondinone, A. J.; Zhang, Z. J. *J. Phys. Chem. B* **2000**, *104*, 1141.

(81) Liu, C.; Zou, B.; Rondinone, A. J.; Zhang, Z. J. *J. Am. Chem. Soc.* **2000**, *122*, 6263.

(82) Han, M.; Vestal, C. R.; Zhang, Z. J. *J. Phys. Chem. B* **2004**, *108*, 583.

(83) Anderson, R. M.; Vestal, C. R.; Samia, A. C. S.; Zhang, Z. J. *Appl. Phys. Lett.* **2004**, *84*, 3115.

(84) Vestal, C. R.; Zhang, Z. J. *Chem. Mater.* **2002**, *14*, 3817.

(85) Kahn, M. L.; Zhang, Z. J. *Appl. Phys. Lett.* **2001**, *78*, 3651.

(86) He, T.; Chen, D.; Jiao, X. *Chem. Mater.* **2004**, *16*, 737.

(87) He, T.; Chen, D.; Jiao, X.; Wang, Y.; Duan, Y. *Chem. Mater.* **2005**, *17*, 4023.

(88) Rockenberger, J.; Scher, E. C.; Alivisatos, A. P. *J. Am. Chem. Soc.* **1999**, *121*, 11595.

(89) Hyeon, T.; Lee, S. S.; Park, J.; Chung, Y.; Na, H. B. *J. Am. Chem. Soc.* **2001**, *123*, 12798.

(90) Sun, S.; Zeng, H. *J. Am. Chem. Soc.* **2002**, *124*, 8204.

(91) Jana, N. R.; Chen, Y.; Peng, X. *Chem. Mater.* **2004**, *16*, 3931.

(92) Park, J.; An, K.; Hwang, Y.; Park, J.-G.; Noh, H.-J.; Kim, J.-Y.; Park, J.-H.; Hwang, N.-M.; Hyeon, T. *Nature Materials* **2004**, *3*, 891.

(93) Yu, W. W.; Falkner, J. C.; Yavuz, C. T.; Colvin, V. L. *Chem. Commun.* **2004**, 2306.

(94) Hyeon, T.; Chung, Y.; Park, J.; Lee, S. S.; Kim, Y.-W.; Park, B. H. *J. Phys. Chem. B* **2002**, *106*, 6831.

(95) Sun, S.; Zeng, H.; Robinson, D. B.; Raoux, S.; Rice, P. M.; Wang, S. X.; Li, G. *J. Am. Chem. Soc.* **2004**, *126*, 273.

(96) Song, Q.; Zhang, Z. J. *J. Am. Chem. Soc.* **2004**, *126*, 6164.

(97) Zeng, H.; Rice, P. M.; Wang, S. X.; Sun, S. *J. Am. Chem. Soc.* **2004**, *126*, 11458.

(98) Livingston, J. D. *Driving Force: The Natural Magic of Magnets*; Harvard University Press: Cambridge, 1996.

(99) Weller, D.; Sun, S.; Murray, C.; Folks, L.; Moser, A. *IEEE Trans. Magn.* **2001**, *37*, 2185.

(100) Chao Liu, Private Communication

(101) Weishaupt, D.; Kochli, V. D.; Marincek, B. *How Does MRI Work? An Introduction to the Physics and Function of Magnetic Resonance Imaging*; Springer: New York, 2003.

(102) Berry, C. C.; Curtis, A. S. G. *J. Phys. D: Appl. Phys.* **2003**, *36*, R198.

(103) Hoegemann, D.; Ntziachristos, V.; Josephson, L.; Weissleder, R. *Bioconjugate Chemistry* **2002**, *13*, 116.

(104) Mykhaylyk, O.; Cherchenko, A.; Ilkin, A.; Dudchenko, N.; Ruditsa, V.; Novoseletz, M.; Zozulya, Y. *J. Magn. Magn. Mater.* **2001**, *225*, 241.

(105) Dodd, C. H.; Hsu, H. C.; Chu, W. J.; Yang, P.; Zhang, H. G.; Mountz, J. D.; Zinn, K.; Forder, J.; Josephson, L.; Weissleder, R.; Mountz, J. M. *J. Immunol. Methods* **2001**, *256*, 89.

(106) Chatterjee, J.; Haik, Y.; Chen, C. J. *J. Magn. Magn. Mater.* **2001**, *225*, 21.

(107) Roger, J.; Pons, J. N.; Massart, R.; Halbreich, A.; Bacri, J. C. *European Physical Journal: Applied Physics* **1999**, *5*, 321.

(108) Rosensweig, R. E. *J. Magn. Magn. Mater.* **2002**, *252*, 370.

(109) Zhang, X.; Chan, K.-Y. *J. Mater. Chem.* **2002**, *12*, 1203.

(110) Park, K.-W.; Choi, J.-H.; Kwon, B.-K.; Lee, S.-A.; Sung, Y.-E.; Ha, H.-Y.; Hong, S.-A.; Kim, H.; Wieckowski, A. *J. Phys. Chem. B* **2002**, *106*, 1869.

(111) Hofstetter, T. B.; Schwarzenbach, R. P.; Haderlein, S. B. *Environ. Sci. Technol.* **2003**, *37*, 519.

(112) Hofstetter, T. B.; Heijman, C. G.; Haderlein, S. B.; Holliger, C.; Schwarzenbach, R. P. *Environ. Sci. Technol.* **1999**, *33*, 1479.

(113) Singh, J.; Comfort, S. D.; Shea, P. J. *Environ. Sci. Technol.* **1999**, *33*, 1488.

(114) Devlin, J. F.; Klausen, J.; Schwarzenbach, R. P. *Environ. Sci. Technol.* **1998**, *32*, 1941.

(115) Matheson, L. J.; Tratnyek, P. G. *Environ. Sci. Technol.* **1994**, *28*, 2045.

(116) Bandstra, J. Z.; Miehr, R.; Johnson, R. L.; Tratnyek, P. G. *Environ. Sci. Technol.* **2005**, *39*, 230.

(117) Agrawal, A.; Tratnyek, P. G. *Environ. Sci. Technol.* **1996**, *30*, 153.

(118) Cheung, C. L.; Kurtz, A.; Park, H.; Lieber, C. M. *J. Phys. Chem. B* **2002**, *106*, 2429.

(119) Li, Y.; Liu, J.; Wang, Y.; Wang, Z. L. *Chem. Mater.* **2001**, *13*, 1008.

(120) Lee, Y. T.; Park, J.; Choi, Y. S.; Ryu, H.; Lee, H. J. *J. Phys. Chem. B* **2002**, *106*, 7614.

(121) Kim, N. S.; Lee, Y. T.; Park, J.; Ryu, H.; Lee, H. J.; Choi, S. Y.; Choo, J. *J. Phys. Chem. B* **2002**, *106*, 9286.

CHAPTER 2

SPINEL FERRITES AND INSTRUMENTATION

2.1 Spinel Ferrites

2.1.1 Crystal Structure and Magnetic Ordering of Spinel Ferrites

The crystal structure for many important magnetic oxides is based on spinel structure, which is named after the mineral spinel $MgAl_2O_4$. The unit cell of spinel is a large cube and corresponds to the space group O_h^7 (F3dm). The ideal spinel structure consists of the cubic close packing (*ccp*) of oxygen anions with the tetrahedral (A site) and octahedral (B site) holes available for metal cation occupancy. Different charge combinations of metal cations are possible in spinel structure. In the present research, spinel ferrites, MFe_2O_4 ($M = Mn^{2+}$, Fe^{2+}, Co^{2+}, Ni^{2+}, Cu^{2+}, Mg^{2+}, Zn^{2+}, etc.) are the experimental system for the investigations of magnetic properties. A crystal model of spinel ferrite is presented in Figure 2.1. The crystallographic parameters of several spinel ferrites are given in Table 2.1[1].

An important yet complicating issue relevant to the studies of magnetic properties of spinel ferrites is that the cation distribution may vary. Two extreme cases may be distinguished. In *Normal* spinel ferrite, the cations occupy sites as M^{2+} in tetrahedral sites and Fe^{3+} in octahedral sites. $ZnFe_2O_4$ is an example of normal spinel ferrite. In *Inverse*

spinel ferrite, half of Fe^{3+} cations occupy tetrahedral sites, leaving the remaining Fe^{3+} and all of M^{2+} in octahedral sites. Examples of inverse spinels are Fe_3O_4 and $CoFe_2O_4$.

In addition to normal and inverse spinel ferrites, a complete range of cation distributions is possible. In general, cation distributions in spinel ferrites are determined by several factors, including the site preferences of cations in terms of size, bonding effects and crystal stabilization energies, and reaction conditions such as synthetic method, reaction temperature and post heat treatments and aging effects.

As far as the magnetic ordering in spinel ferrites is concerned, since the metal cations in spinel ferrites are mutually separated by larger oxygen anions, the direct interactions between cations are at least very weak. Alternatively, an indirect exchange, so called superexchange interaction as originally proposed by Néel[2], becomes strong enough to order the magnetic moments. The magnetic moments for all metal cations in A sites are orientated parallel with respect to each other and the magnetic moments for all cations in B sites are aligned parallel with one another as well. The magnetic moment orientation of cations between A and B sites, however, is antiparallel to each other in spinel ferrite. As there are twice as many of B sites as A sites, a net magnetic moment results. Therefore, the magnetic structure of spinel ferrite is ferrimagnetic ordering. A magnetic ordering model of spinel ferrite is schematically shown in Figure 2.2. In addition, the superexchange interaction is also strongly dependent on the geometry of arrangement such as distance and angles of cations in A and B sites. There are three major superexchange interactions, $\boldsymbol{j}_{AB}$, $\boldsymbol{j}_{AA}$, and $\boldsymbol{j}_{BB}$ in spinel ferrites as illustrated in Figure 2.3. Again, the magnetic properties of some spinel ferrites are listed in Table 2.2[1].

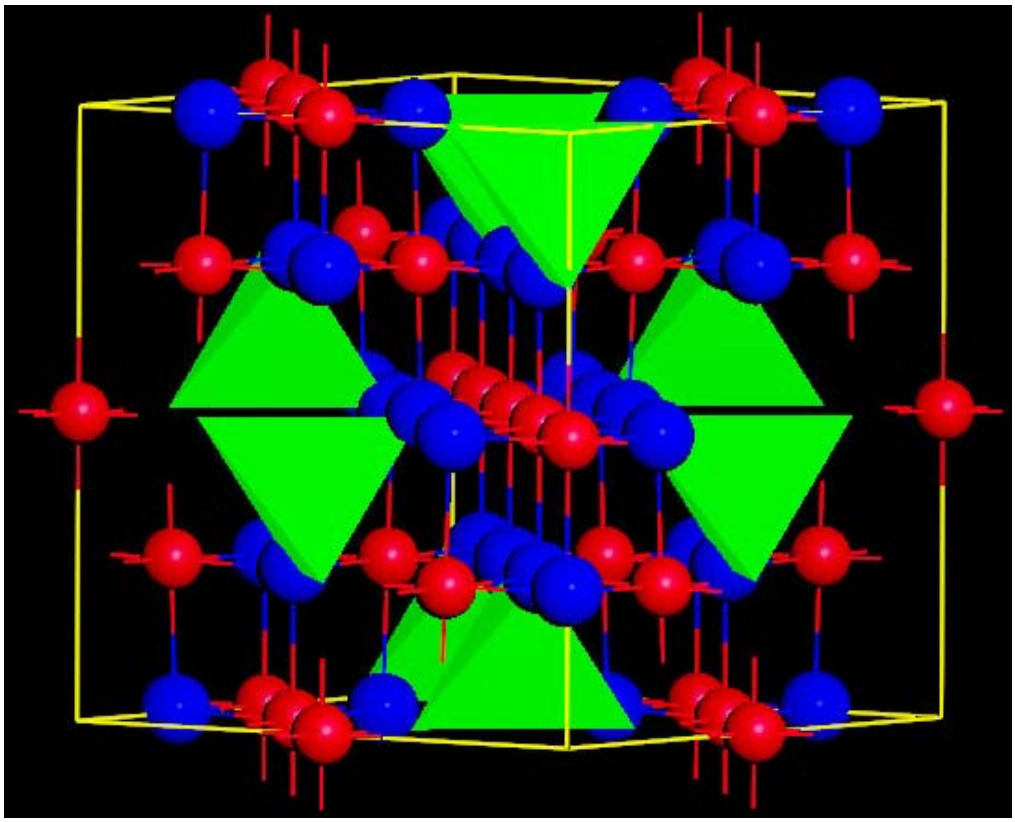

Figure 2.1 The crystal model of the unit cell for spinel ferrite structure. The green colored tetrahedrals are the A sites. The red balls represent the B sites. The blue balls show the cubic close packed oxygen.

Table 2.1 Crystallographic parameters of some spinel ferrites.

Ferrite	Lattice Parameter (Å)	Cation Distribution*	Density (g/cm^3)
Fe_3O_4	8.398	$Fe^{3+}[Fe^{2+}Fe^{3+}]$ (I)	5.193
$CoFe_2O_4$	8.381	$Co_xFe_{1-x}[Co_{1-x}Fe_{1+x}]$ (I) $0.07<x<0.24$	5.924
$MnFe_2O_4$	8.525	$Mn_{1-x}Fe_x[Mn_xFe_{2-x}]$ (M) $0.07<x<0.23$	4.94
$NiFe_2O_4$	8.337	Fe[NiFe] (I)	5.38
$CuFe_2O_4$	8.382 (cubic)	$Cu_{0.33}Fe_{0.67}[Cu_{0.67}Fe_{1.33}]$ (M)	5.39
$ZnFe_2O_4$	8.443	Zn[Fe] (N)	5.32
$MgFe_2O_4$	8.372	$Mg_xFe_{1-x}[Mg_{1-x}Fe_{1+x}]$ (I) $0.14<x<0.26$	4.53

* N: Normal, I: Inverse, M: Intermediate.

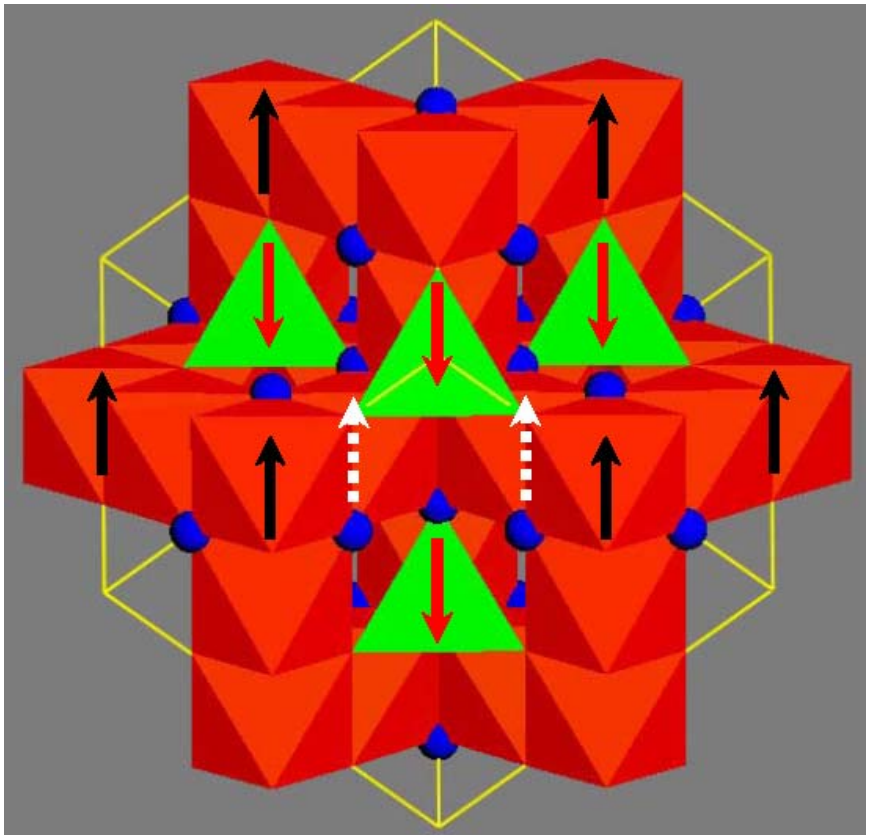

Figure 2.2 The magnetic structure model of spinel ferrite. The four red arrows are the spins in A sites. The six black solid arrows and two white dished arrows represent the spins in B sites. The projection direction is along [111].

Table 2.2 Magnetic properties of some spinel ferrites.

Ferrite	T_C (K)	M_S (300K) (G cm^3/g)	K_1 (x 10^5) (erg/cm^3)	Easy axis	Hard axis
Fe_3O_4	860	95.5	-1.2	[111]	[100]
$CoFe_2O_4$	790	80-94	+18, +30	[100)	[111]
$MnFe_2O_4$	550-620	80	-0.25	[111]	[100]
$NiFe_2O_4$	860-870	56	-0.68	[111]	[100]
$CuFe_2O_4$	725-775	20-35	-0.6 (cubic)	[111]	[100]
$ZnFe_2O_4$	10-15	-	-	-	-
$MgFe_2O_4$	605-710	31-62	-0.25-0.45	[111]	[100]

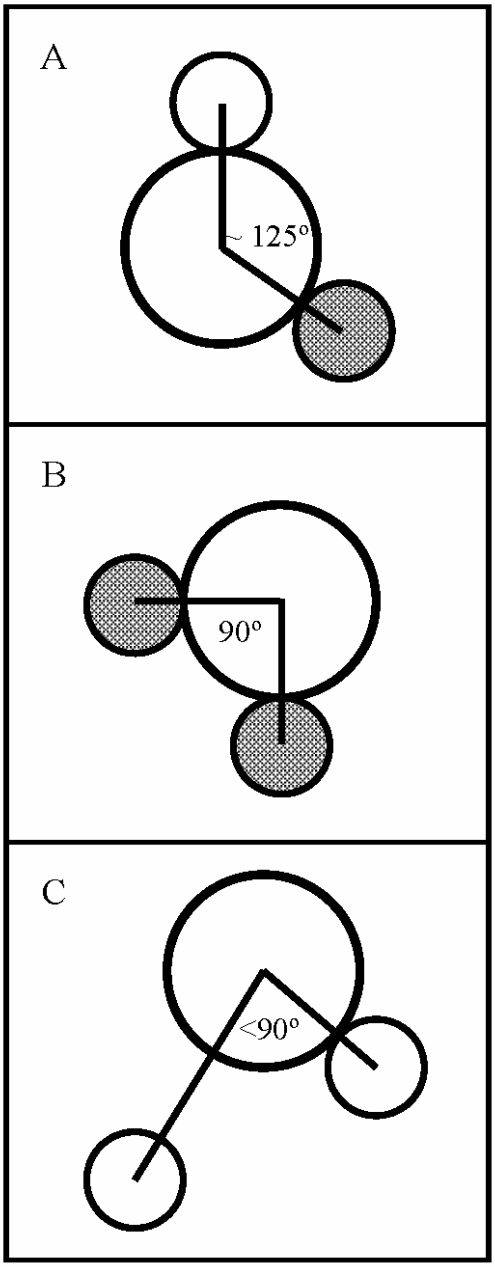

Figure2.3 Three major types of superexchange interactions in spinel ferrites are $\boldsymbol{j}_{AB}$, $\boldsymbol{j}_{BB}$ and $\boldsymbol{j}_{AA}$, shown in panel A, B and C, respectively. The small empty circle is A site, the small solid circle is B site, and the large empty circle is oxygen anion.

2.1.2 A General Method for Size and Shape Controlled Synthesis of Spinel Ferrites

In a general concept, the synthesis of nanomaterials has been classified into 'top-down' and 'bottom-up' methodologies. A wide variety of preparation procedures to the synthesis of different spinel ferrite nanoparticles include mechanic milling, gas condensation, aerosol, coprecipitation, sol-gel processing, hydrothermal treatment, and normal or reverse microemulsion method. However, the quality of the nanoparticles in terms of size control, size distribution is very frequently not good. In many cases of these procedures, a very broad size distribution and even the loss of size control are reported. More importantly, for all of these procedures, the capability to control the shapes of spinel ferrite is rarely possible.

In order to establish the correlation of size and shape effects with the variation in magnetic properties, it is critical to develop a general synthetic method that allows for control over both the size and shape of nanoparticles and produces nanoparticles with a narrow size distribution. Recent advances on the synthesis of colloidal semiconductor nanocrystals have demonstrated that size and shape controlled synthesis of nanocrystals can be achieved by thermal decomposition of molecular precursors in high temperature organic solvents in the presence of proper surfactants. The size and shape of nanocrystals can be precisely controlled by manipulating reaction variables such as molecular precursors, concentration, temperature and growth rate, types of surfactant and solvent. Stimulated by the strategies and knowledge in the synthesis of semiconductor colloidal nanocrystals, we have developed a general synthetic method for spinel ferrites with both size and shape control capability. The developed method is based on a combination of high temperature thermal decomposition of molecular precursors with a seed-mediated

growth process. This method has been successfully used in the synthesis of $CoFe_2O_4$, Fe_3O_4, $MnFe_2O_4$ and the core shell structured spinel ferrites nanocrystals. Generally, by adjusting the molar ratio of seeds to molecular precursors, the size of these spinel ferrites can be varied from 3 nm to 14 nm. By precisely controlling the temperature and growth rate, the shape of $CoFe_2O_4$ nanocrystals can be reversibly interchanged from spherical to cubic. A schematic diagram presented in Figure 2.4 shows the correlation of growth rate and temperature with the shape evolution of cobalt spinel ferrite nanocrystals.

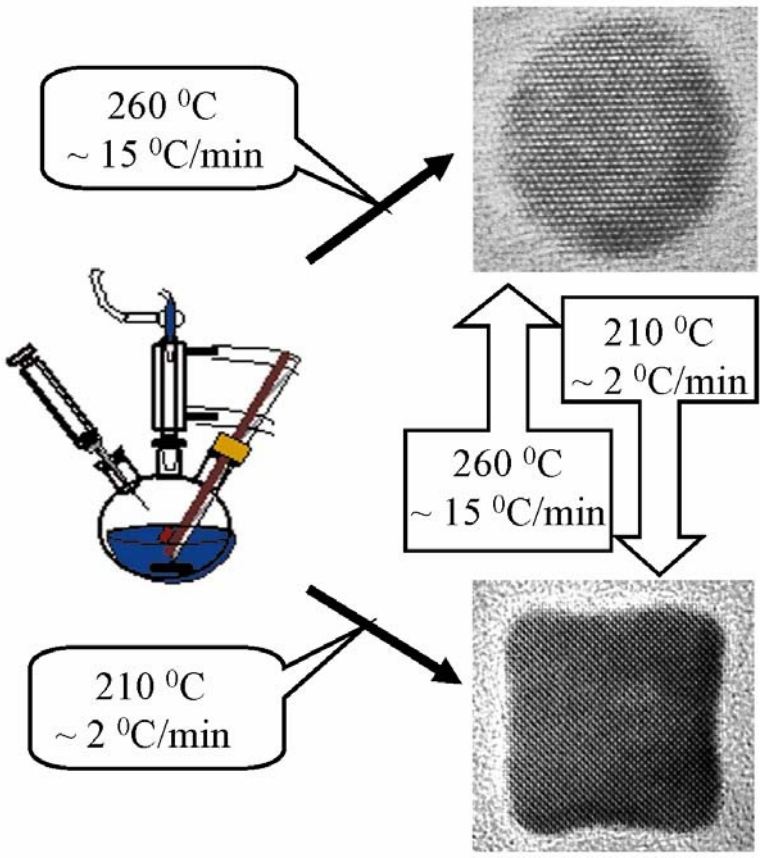

Figure 2.4 The Schematic of size and shape controlled synthesis of spinel ferrites.

2.2 Instrumentation

2.2.1 Powder X-ray Diffraction[3-5]

The interaction of x-ray radiation with crystalline sample is governed by Bragg's law, which indicates a relationship among the diffraction angle (Bragg angle), x-ray wavelength, and interplanar spacing. According to Bragg, the x-ray diffraction can be visualized as x-rays reflecting from a series of crystallographic planes as shown in Figure 2.5. The path differences introduced between a pair of waves traveled through the neighboring crystallographic planes are determined by the interplanar spacing. As the total path difference is equal to nλ (as n being an integer and λ being the wavelength), the constructive interference will occur and a group of diffraction peaks can be observed and give rise to x-ray patterns. The quantitative account of Bragg's law can be expressed as:

$$n\lambda = 2d_{hkl} \sin\theta \qquad (2.1)$$

where d is the interplanar spacing for a given set of *hkl*, λ is the wavelength, and θ is the Bragg angle shown in Figure 2.5.

The intensity of powder diffraction peaks is in principal determined by the structural factor, $\mathbf{F}_{hkl}$ as expressed in equation (2.2), which depends on the crystal structures including relative positions of atoms in the unit cell, types of unit cells and other characteristics such as thermal motion and population parameters.

$$\mathbf{F}_{hkl} = \sum_{i=1}^{n} g^i t^i(s) f^i(s) \exp[2\pi i(hx^i + ky^i + lz^i)] \qquad (2.2)$$

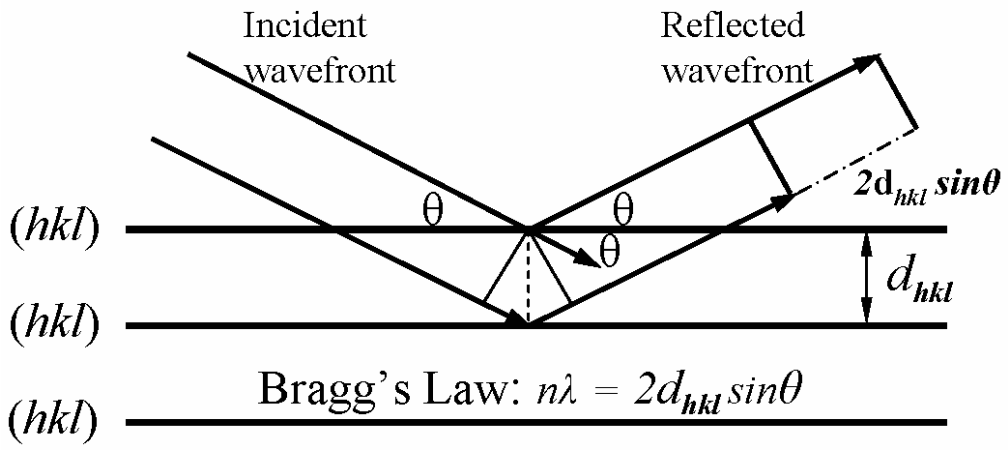

Figure 2.5 Geometrical illustrations of crystal planes and Bragg's law.

where f^{i}(s) is the atomic scattering factor, g^{i} is the population factor of i^{th} atom, t^{i}(s) is the temperature factor, *hkl* are the Miller indices, and xyz are the fractional coordinates of i^{th} atom in the unit cell.

In addition to the primary structural factors, the intensity of diffraction is dependent on other factors, which are not only relevant to sample effects such as its shape and size, grain size and distribution *etc.*, but also with the instruments including detector, slit and / or monochromator geometry.

For all X-ray diffraction experiments presented in this research, a Bruker D8 Advance X-ray diffractometer with Cu Kα (λ = 1.54187 Å) radiation was employed and

operated at applied voltage of 45 kV and filament current of 40 mA. The spinel phase identification for all as-synthesized samples reported here was performed by matching the peak positions and intensities in the experimental diffraction patterns to those patterns in the JCPDS (Joint Committee on Powder Diffraction Standards) database.[6]

One of the more frequent applications of XRD analysis is to determine the crystalline size and lattice strain in nanocrystalline materials. The peak broadening in x-ray diffraction patterns for nanomaterials is the result of the finite size effect. For a finite size nanocrystal, the number of x-ray radiation reflected from successive lattice planes that add up to produce constructive or destructive interference becomes finite and therefore they can not reinforce or cancel out completely. Additionally, some other factors such as inhomogeneous lattice strains, variations in the lattice constants from one crystallite to another and structural faults can also yield the broadening of the diffraction peaks.

The size of nanomaterials can be derived from the peak broadening and calculated by using the Scherrer equation (2.3), provided that the nanocrystalline size is less than 100nm.

$$d = K\lambda / (\beta \cos \theta) \qquad (2.3)$$

where d is the average crystalline dimension perpendicular to the reflecting phases, λ is the x-ray wavelength, θ is the Bragg angle, and β is the finite size broadening. K is a constant close to unity that is related both to the crystalline shape and to the way β is

defined, i.e., either as the full width at half-maximum (FWHM) or as the integral breadth i.e. the ratio of the peak area to peak maximum.

2.2.2 Transmission Electron Microscopy

Modern Transmission Electron Microscopy (TEM) has become a versatile and indispensable tool in exploration of nanomaterials. The complementary imaging, diffraction and spatial resolution microanalysis techniques in TEM provide the information on chemical composition, crystal structure, electronic and /or magnetic structure, size and shape of nanomaterials.

The versatility of transmission electron microscopy for the analysis of materials primarily originates from the various interactions when electron beams undergo within the solid specimen as shown schematically in Figure 2.6. For example, the transmitted electrons are used to visualize the internal crystal structure by bright and dark field imaging and orientation and identification of crystals in selected area electron diffractions. The elemental and chemical information can be simultaneously derived from the analysis of the characteristic x-ray radiations. In light of the fact that the diffraction physics and the principles of imaging can be found in detail from the literature and TEM textbooks[7-10], the following discussion is mainly focused on the energy dispersive x-ray spectroscopy (EDS).

The generation of characteristic x-ray radiation in EDS analysis is generally from an inelastic inner-shell electron excitation process by high energy incident electron beams and can be understood from Figure 2.7. The characteristic x-rays are produced during the deexcitation of an atom following the ejection of an inner-shell electron caused by the

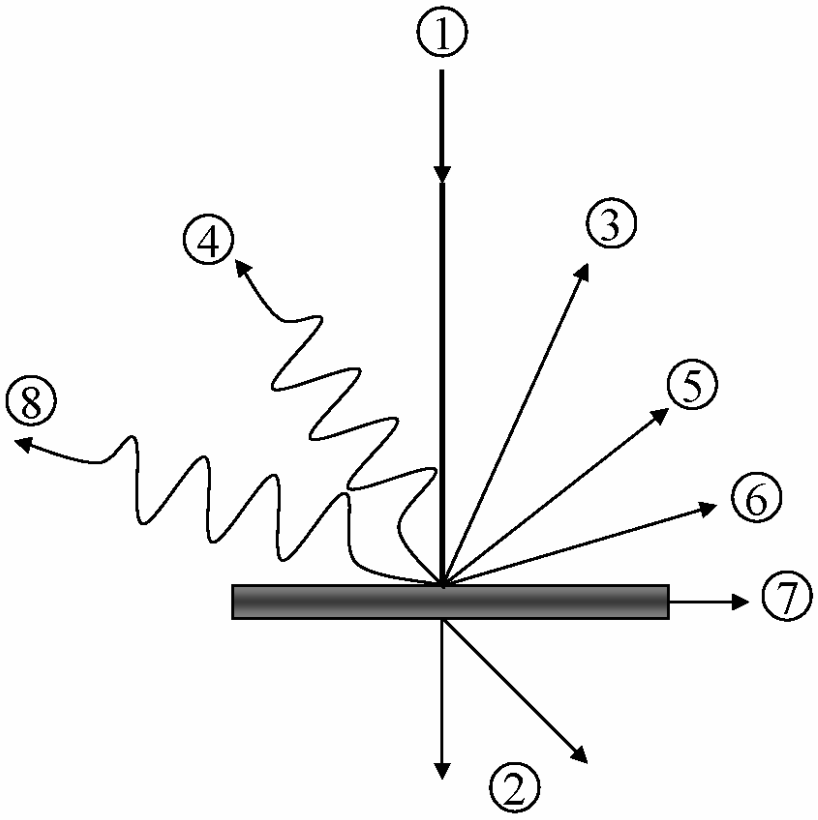

Figure 2.6 The schematic of interactions between beam electrons and specimen. 1, electron beam, 2, transmitted electron, 3, backscattered electron, 4, characteristic x-rays, 5, secondary electron, 6, Auger electron, 7, Absorbed current, 8, cathodeluminescence.

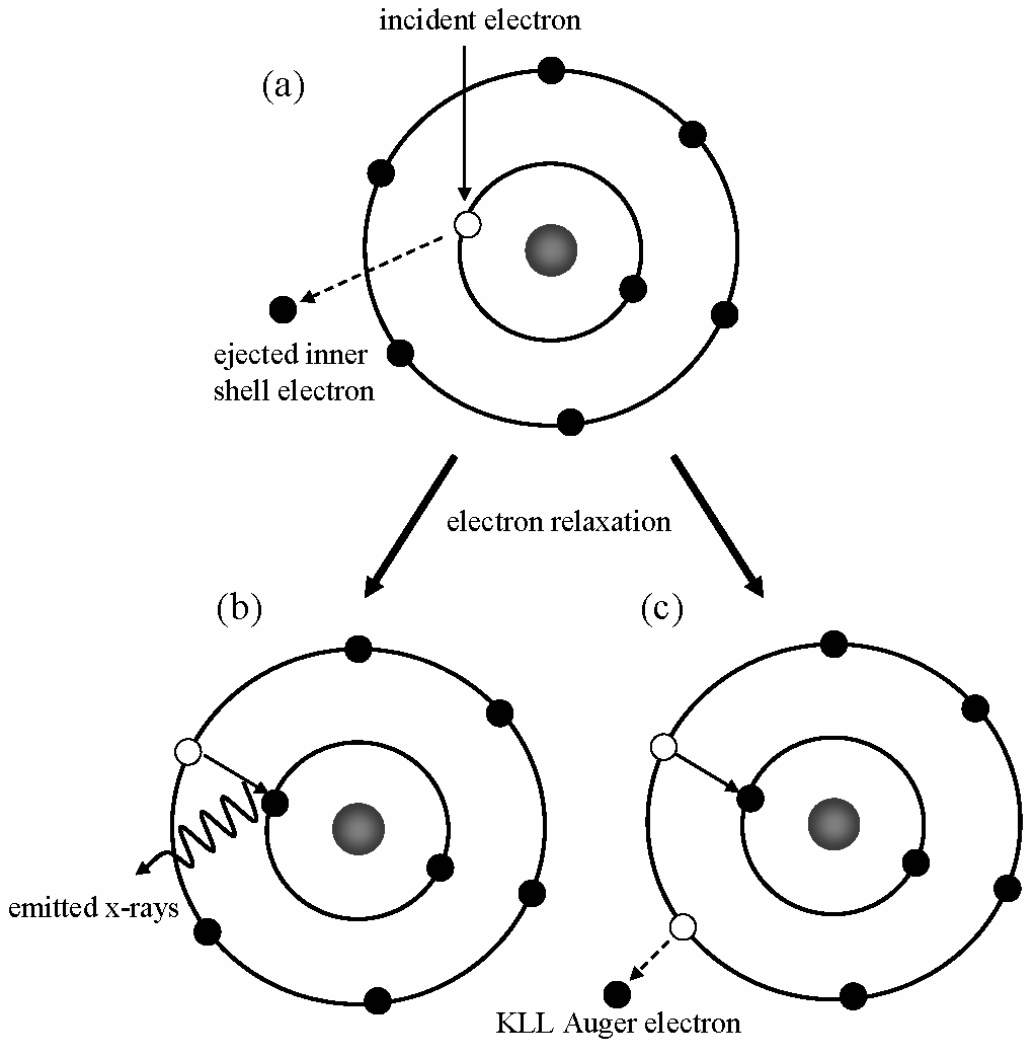

Figure 2.7 Schematic illustration of the process of the inner-shell electron excitation (a) and subsequent deexcitation by emission of characteristic x-rays (b) and Auger electron emission (c).

interaction of an energetic beam electron. A sufficiently energetic beam electron may eject an inner-shell electron, K, L, or M, leaving the atom in an excited state. Subsequent relaxation to its ground state occurs by the transitions of electrons from one shell to another and the emission of *characteristic x-rays* (Figure 2.7 b) or excitation of another outer shell electron and the emission of *Auger electrons* (Figure 2.7c).

The characteristic x-rays are the fingerprint of elements and are determined by the atomic energy level, critical ionization energy, families of x-ray emission energies, and intensities, which provide the fundamental basis of energy dispersive x-ray spectroscopy. The quantitative determination of the chemical composition of a small region at high spatial resolution by EDS can be expressed in equation (2.4), provided that the experiments are under nonchanneling and weak diffracting conditions.

$$I_A = I_0 n_A \acute{\omega}_A \sigma_A a_A d \gamma_A A_b t \qquad (2.4)$$

where I_A is the rate of incident electrons, n_A is the number of A element per unit volume, $\acute{\omega}_A$ is the fluorescent yield, σ_A is the ionization cross-section of the inner shell, a_A is the fraction of the K, L, or M line intensity measured by the detector, d is the specimen thickness, γ_A is the detector efficiency, A_b is the absorption factor, and t is the acquisition time.

In this dissertation, all low magnification TEM images were recorded by JEOL 100 C operating at 100 kV. All high-resolution TEM studies were performed on JEOL 4000

EX TEM with point-to-point image resolution at 0.18 nm, objective lens (Cs = 1.0 mm, Cc = 1.7 mm) and acceleration voltage at 400 kV, respectively. The EDS analyses were conducted on Hitachi field emission 2000 FE TEM operating at 200 kV.

2.2.3 SQUID Magnetometer[11-14]

Superconducting QUantum Interference Devices (SQUIDs) are the most sensitive devices for measuring magnetic flux. SQUIDs have being widely used in a variety of measurements including current, voltage, magnetic field, gravitational field, and magnetic susceptibility. Fundamentally, the SQUIDs consist of a superconducting ring with one or two Josephson junctions. Nowadays, the most common type of SQUIDs is probably the DC SQUID with two resistively-shunted Josephson junctions as schematically shown in Figure 2.8.

In order to operate the DC SQUID, a constant bias current is fed through the superconducting ring. If this current is higher than the critical current of the SQUID, a voltage appears across the two Josephson junctions in Figure 2.9. When a variation in magnetic flux caused by a sample occurs, an additional supercurrent starts to run through the ring in an attempt to compensate the change in flux, giving rise to a higher voltage across the SQUID. Since the magnetic flux is quantized as it passes through a superconducting ring, the average voltage across SQUID becomes a periodic function of the change in magnetic flux. Thus, the DC SQUID is a magnetic flux-to-voltage converter. Similarly, the DC SQUID may be operated by applying a constant voltage and measuring the current as a function of magnetic flux.

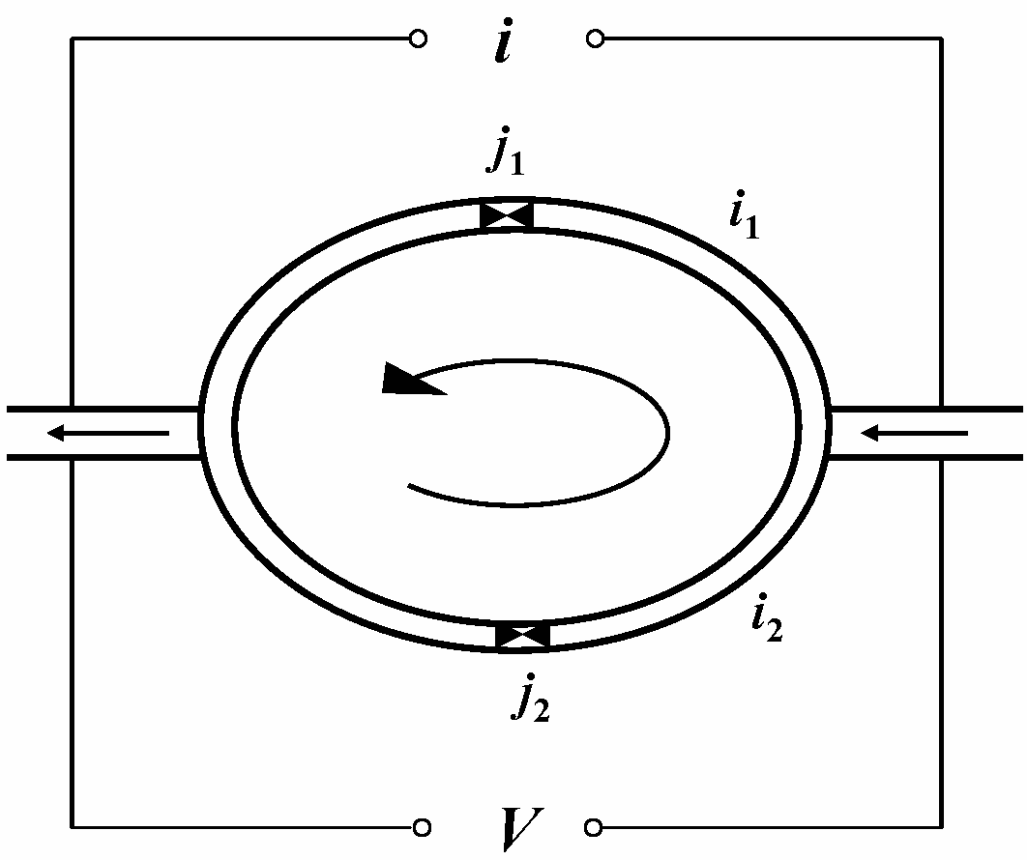

Figure 2.8 The schematic diagram of superconducting ring with two Josephson junctions (j_1 and j_2) in DC SQUIDs.

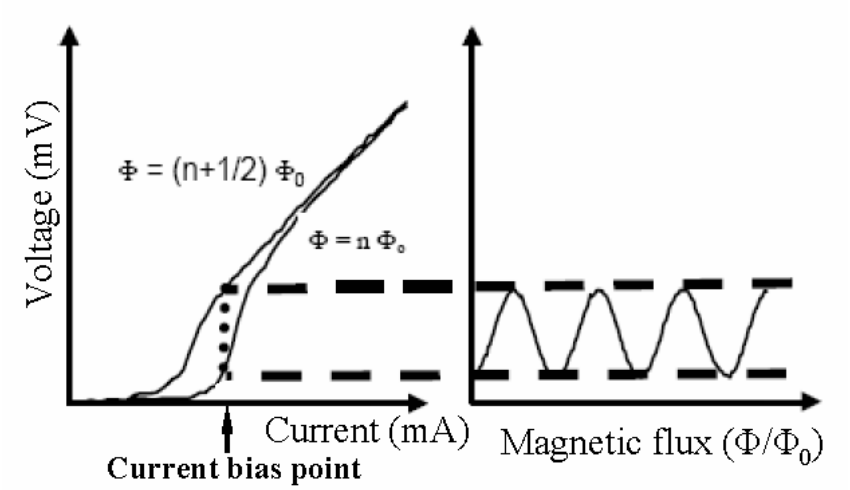

Figure 2.9 The voltage-current and voltage-magnetic flux curves of SQUID. The voltage across SQUID is modulated by the magnetic flux at a period of one quantum of flux Φ_0.

The detection of the variation in magnetic flux in the SQUIDs is coupled to a superconducting wire wound detection coil through induction. For the DC SQUID, the detection coil consists of a set of three superconducting wire wound coils configured as a second-derivative gradiometer, as shown in Figure 2.10. Such gradiometer configuration not only reduces the noise caused by the fluctuations in the large magnetic field of the superconducting magnet, but it can also minimize the background noise and fluctuation due to the relaxation of the magnetic field of superconducting magnet. However, the magnetic moment of a sample is still measurable because the gradiometer coil set measures the local variations in magnetic flux density induced by the dipole field of the sample. Conventionally, a measurement procedure in DC SQUID is performed by moving a sample through superconducting gradiometer at a certain temperature and magnetic field. Any differentiation in the magnetic flux in gradiometer coils generates a proportional variation in the persistent current. Since the SQUID is a highly linear current and voltage converter, any change in the current produces the corresponding variation in voltage, which is essentially proportional to the magnetic moment of the sample. Therefore, the magnitude of magnetic moment of the sample can be determined by the measurement of the variations in voltage in SQUID.

The routine measurements in SQUID magnetometers can be performed in two ways. The first measurement is the field dependence of magnetization at constant temperature M (H), and the second is the temperature dependence of the magnetic materials under constant magnetic field M (T). According to the cooling process, the temperature dependent measurements can be further performed by zero-field-cooling (ZFC) and field-cooling (FC), respectively. In zero-field-cooling measurements, the magnetic sample is

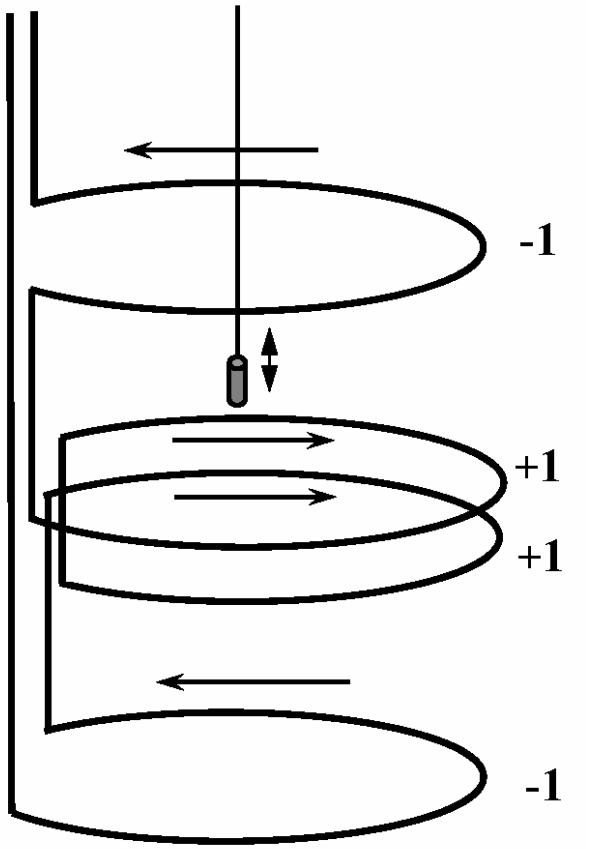

Figure 2.10 The schematic configuration of second-derivative gradiometer superconducting detection coils.

cooled from room temperature without a magnetic field. On the other hand, the field-cooling measurements, the sample is cooled from room temperature in the presence of a magnetic field.

In this research, the magnetic measurements are carried out on a Quantum Design MPMS-5S SQUID magnetometer. The temperature ranges from 5 K to 400 K for temperature dependent magnetic studies, and the magnetic field is from 5 T to -5 T in the field dependent measurements.

2.2.4 Thermal Analysis[15,16]

There are two types of thermal analysis methods performed simultaneously in this research – thermogravimetric analysis and differential scanning calorimetry.

Thermogravimetric analysis (TGA) is a branch of the thermal analysis methods, which detects the mass change of a sample as a function of temperature. For many thermal events including desorption, absorption, sublimation, vaporization, oxidation, reduction, and decomposition, the thermogravimetric analysis is an essential tool for providing important information about the thermal properties of samples. In general, the TGA curves are plotted with the mass change expressed as a percentage against temperature. A schematic representation of a one-stage thermal decomposition process in temperature scanning mode is given in Figure 2.11. The thermal event is characteristic of two temperatures, T_i and T_f, which are referred to as the procedural decomposition temperature and the final temperature, respectively. Simply, T_i stands for the lowest temperature at which the onset of a mass change can be detected under the given

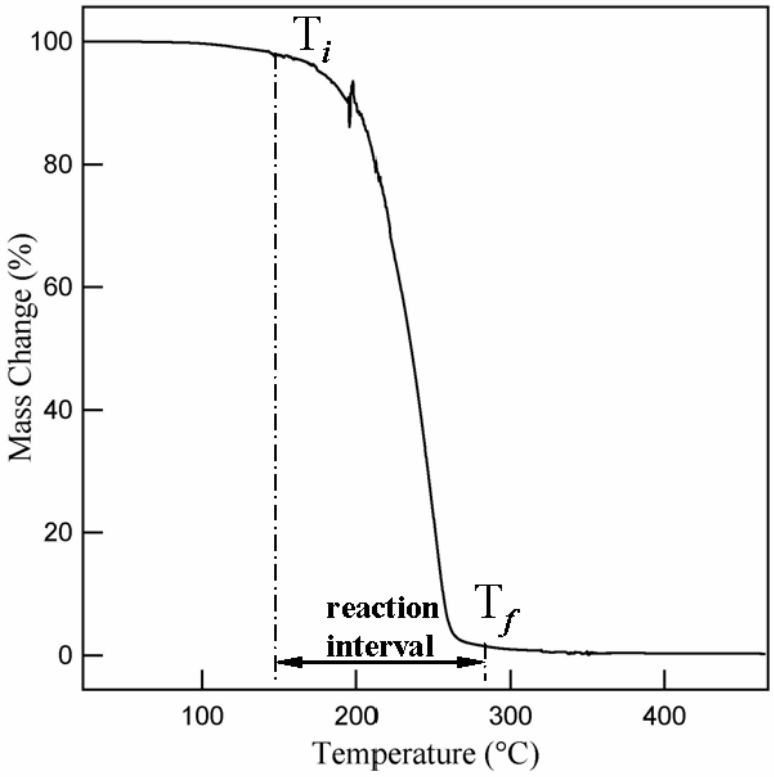

Figure 2.11 One-stage thermal decomposition curve in TGA. T_i and T_f are initial and final reaction temperature, respectively.

experimental conditions. Similarly, T_f represents the lowest temperature by which the thermal process responsible for the mass change is completed.

In parallel with TGA, differential scanning calorimetry (DSC) is another versatile thermal analysis technique, which is characterized by the detection of any variation in energy taking place in the reaction of sample. Two techniques are designed in detection of energy change in DSC measurements, one is heat flux DSC and the other is power compensation DSC. In heat flux DSC experiments, the signal is derived from the temperature difference between the sample and reference, whereas in power compensation measurements, the instrument signal is derived from the differential heat supplied to the sample and reference to maintain the same temperatures. Information about endothermic and exothermic reaction process can be determined from these two types of DSC measurements.

The thermal analysis experiments and results reported here were conducted on Netzsch Luxx STA 409 PG, a type of simultaneous TGA-DSC equipment. The heating rate was controlled at 10 °C/min under highly pure N_2 gas flow for all experiments.

2.3 References

(1) Buschow, K. H. J.; Ed. *Handbook of Magnetic Materials: Volume 8*; Elsevier: Amsterdam, 1995. p197, p212.

(2) Neel, L. *Ann. Phys*. **1948**, *3*, 137

(3) Cullity, B. D. *Elements of X-Ray Diffraction*; 2 ed.; Addison-Wiley Publishing Company: Reading, 1978.

(4) Giacovazzo, C., Ed. *Fundamentals of Crystallography*; 2 ed.; Oxford University Press: Oxford, 2002.

(5) Pecharsky, V. K., Zavalij, Peter Y. *Fundamentals of Powder Diffraction and Structural Characterization of Materials*; Kluwer Academic Publishers: Boston, 2003.

(6) JCPDS numbers are $MnFe_2O_4$: 10-0319, Fe_3O_4: 19-0629, $CoFe_2O_4$: 22-1084, respectively.

(7) Goldstein, J. I.; Newbury, D. E.; Echlin, P.; Joy, D. C.; Fiori, C.; Lifshin, E. *Scanning Electron Microscopy and X-Ray Microanalysis*, 1981.

(8) Williams, D. B., Carter, C. B. *Transmission Electron Microscopy*; Plenum Press: New York, 1996.

(9) Wang, Z. L. *Elastic and Inelastic Scattering in Electron Diffraction and Imaging*; Plenum Press: New York, 1995.

(10) Wang, Z. L. *Adv. Mater.* **1998**, *10*, 13.

(11) Gallop, J. C. *SQUIDs, the Josephson Effects and Superconducting Electronics*; Adam Hilger: Bristol, 1991.

(12) Weinstock, H.; Editor *SQUID Sensors: Fundamentals, Fabrication and Applications.*; Kluwer Academic: Dordrecht, 1996.

(13) Rondinone, A. J.; Zhang, Z. J. *Handbook of Nanophase and Nanostructured Materials* **2003**, *2*, 252.

(14) McElfresh, M. *Fundamentals of Magnetism and Magnetic Measurements*; Quantum Design: San Diego, 1994.

(15) Charsley, E. L., Warrington, S. B., Ed. *Thermal Analysis: Techniques and Applications*; Royal Society of Chemistry: Cambridge, 1992.

(16) Hatakeyama, T., Quinn, F. X. *Thermal Analysis: Fundamentals and Applications to Polmer Science*; 2 ed.; John Wiley & Sons Ltd: Chichester, 1999.

CHAPTER 3

SIZE AND SHAPE CONTROLLED SYNTHESIS AND ASSOCIATED SUPERPARAMAGNETIC PROPERTIES STUDIES

Abstract

By combining nonhydrolytic reaction with seed-mediated growth, high-quality and monodispersed spinel cobalt ferrite, $CoFe_2O_4$, nanocrystals can be synthesized with a highly controllable shape of nearly spherical or almost perfectly cubic. The shape of the nanocrystals can also be reversibly interchanged between spherical and cubic morphologies through control of nanocrystal growth rate. Furthermore, the magnetic studies show that the blocking temperature, saturation, and remanent magnetization of nanocrystals are solely determined by the size regardless fo shape. However, the shape of nanocrystals is a dominating factor for the coercivity of nanocrystals due to the effect of surface anisotropy. Such magnetic nanocrystals with distinct shapes possess tremendous potentials in fundamental understanding of magnetism and in technological applications of magnetic nanocrystals for ultrahigh-density information storage.

3.1 Introduction

The unique and novel size dependent chemical and physical properties displayed by metal and semiconductor nanocrystals have initiated the current wide range of intensive research on nanomaterials[1-6]. Recently, keen interests have been expanded into controlling the shape of nanomaterials and also into understanding the correlations between material properties and its shape. The shape of nanomaterials can be as vital as the size in determining the uniqueness and novelty of material properties[7-11]. Moreover, a large part of the societal impact by nanomaterials surely will be realized in a variety of devices consisting of nanomaterial components. Assembly of nano-components is a key process in building devices, and the shape of nano-building blocks and related properties will be crucial for the assembly and device designs. Shape-controlled synthesis of nanocrystals surely is an experimental challenge[12,13]. Successes in shape control of nanocrystals have been reported in the syntheses of metals[9,11,14-17] and semiconductors[18]. Clearly, it is desirable to develop strategies for shape controlled syntheses of complex metal oxides possessing rich properties, especially the magnetic characteristics. Monodispersed metal oxides nanocrystals have been synthesized by several nonhydrolytic methods using precursors of organometallic and coordination compounds[19-21]. The shape of these nanocrystals typically is spherical. In addition, it has been demonstrated that the seed-mediated growth is an effective route for size controlled synthesis of magnetite[22,23] and gold[24,25] nanocrystals.

Magnetic properties of a material usually are very sensitive to its shape due to the dominating role of anisotropy in magnetism. This chapter reports that by using a seed-mediated growth approach, monodisperse spinel cobalt ferrite, $CoFe_2O_4$, nanocrystals can

grow into a nearly spherical shape or an almost perfect cube in a highly controllable manner. The shape of the nanocrystals can also be reversibly interchanged between spherical and cubic shape by controlling nanocrystal growth rate and temperature. Furthermore, the magnetic studies show that the blocking temperature, saturation, and remanent magnetization of nanocrystals are solely determined by the volume regardless of the spherical or cubic shape. However, the shape of the nanocrystals is a dominating factor for the coercivity of magnetic nanocrystals. Such magnetic nanocrystals with distinct shapes possess tremendous potentials in technological applications of magnetic nanocrystals for high-density information storage and also in fundamental understanding of magnetism. The cubic nanocrystals should greatly facilitate the theoretical modeling for understanding magnetic properties since their morphology offers well-defined crystallographic surfaces and easily recognizable magnetization axes.

3.2 Experimental Section

3.2.1 Synthesis of Magnetic Nanocrystals

Monodispersed $CoFe_2O_4$ nanocrystals were synthesized by using a combination of a nonhydrolytic process and seed-mediated growth. The general strategy is using coordination compounds of iron (III) and cobalt (II) acetylacetonate, $Fe(acac)_3$ and $Co(acac)_2$, as precursors in a nonhydrolytic process to synthesize $CoFe_2O_4$ spherical nanocrystals with a mean diameter of 5 nm. These nanocrystals then serve as seeds to grow larger spherical or cubic magnetic nanocrystals in the seed-mediated growth process.

In a typical synthesis, a mixture of 2 mmol of $Co(acac)_2$, 40 mL of phenyl ether, 20 mmol of 1,2-hexadecandiol, 10 mL of oleic acid, and 10 mL of oleylamine was heated to 140 °C followed by a dropwise addition of 4 mmol $Fe(acac)_3$ in 20 mL of phenyl ether. The temperature of the mixture was kept at reflux for 30 min before being cooled down to room temperature. After addition of ethanol and centrifugation, spherical $CoFe_2O_4$ nanocrystals with a diameter of 5 nm were obtained.

Such 5 nm spherical nanocrystals were used as seeds to grow 8 or 9 nm spherical nanocrystals in the solution of $Co(acac)_2$ and $Fe(acac)_3$ precursors. For instance, to produce 8 nm spherical nanocrystals, 100 mg of 5 nm nanocrystal seeds was employed in a particle growth solution consisting of 1 mmol of $Co(acac)_2$, 2 mmol of $Fe(acac)_3$, 10 mmol of 1-octadecanol, 5 mL of oleic acid, and 5 mL oleylamine in a 20 mL phenyl ether. Then, the solution temperature was raised to 260 °C at a rate of 10 ~ 15 °C/min and kept at reflux at 260 °C for 30 min. The nanocrystals precipitated out after ethanol was added. The nanocrystals can be easily dispersed in nonpolar organic solvents such as hexane and toluene.

3.2.2 Characterizations

X ray diffraction data were collected with a Bruker D8 ADVANCE X-ray diffractometer using Cu Kα radiation. Transmission electron microscopy (TEM) and high resolution Transmission Electron Microscopy (HRTEM) analyses have been performed using JEOL 100C operating at 100 kV and JEOL 4000EX operating at 400 kV, respectively. Magnetic nanocrystals were dispersed onto the amorphous carbon-coated

cupper grids for TEM studies. The nanocrystal size distributions were determined by manually counting over 400 nanocrystals followed by a lognormal fitting.

Magnetic measurements were carried out with a Quantum Design MPMS-5S Superconductor Quantum Interference Devices (SQUID) magnetometer with temperature ranging from 5 K to 400 K and magnetic field up to ± 5 Tesla. Zero field cooled (ZFC) susceptibility measurements were conducted by cooling the samples from room temperature to 5 K under no applied magnetic field. Then, a field of 100 G was applied and the change in magnetization recorded as the temperature was programmed to increase. Field cooled (FC) susceptibility experiments were performed by applying 100 G fields during sample cooling procedure to 5 K. Hysteresis measurements were carried out at 5 K in the applied fields up to ± 5 Tesla. Before hysteresis measurements at 5 K, the powder samples were completely dispersed in eicosane ($C_{20}H_{42}$, Aldrich, 99%) matrix in order to prevent from physical shifting of nanocrystals and reduction of interparticle interaction effect.

3.3 Results and Discussion

From the first step of nonhydrolytic thermal decomposition process, spherical $CoFe_2O_4$ nanocrystals with a diameter of 5 nm were produced. X-ray diffraction and selected area electron diffraction (SAED) studies confirmed such magnetic nanocrystals and all other subsequently obtained nanocrystals possessing a cubic spinel structure. The representative X-ray and electron diffraction patterns are shown in Figure 3.1 and 3.2, respectively. Chemical analysis using the inductively coupled plasma atomic emission

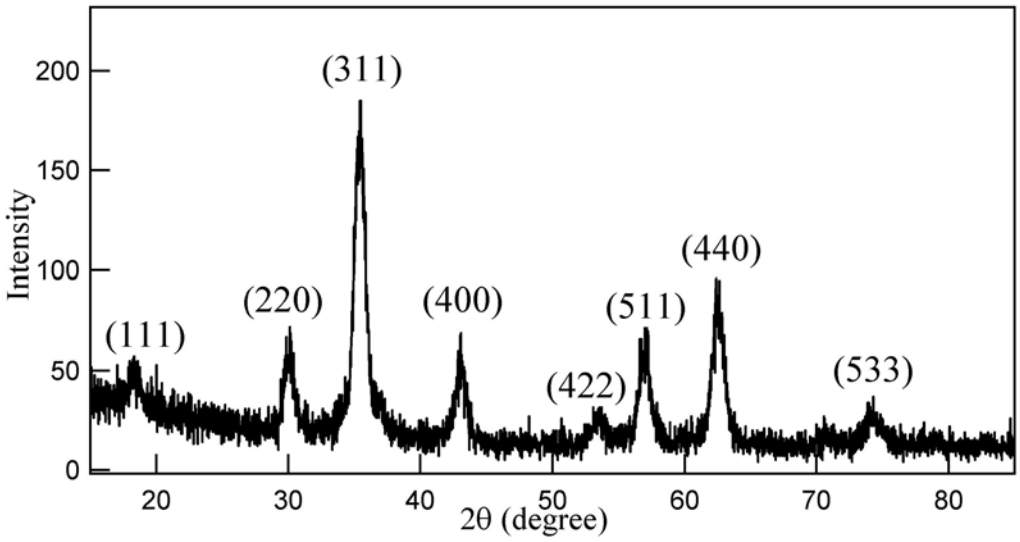

Figure 3.1 A typical X-ray diffraction patterns of $CoFe_2O_4$ nanocrystals.

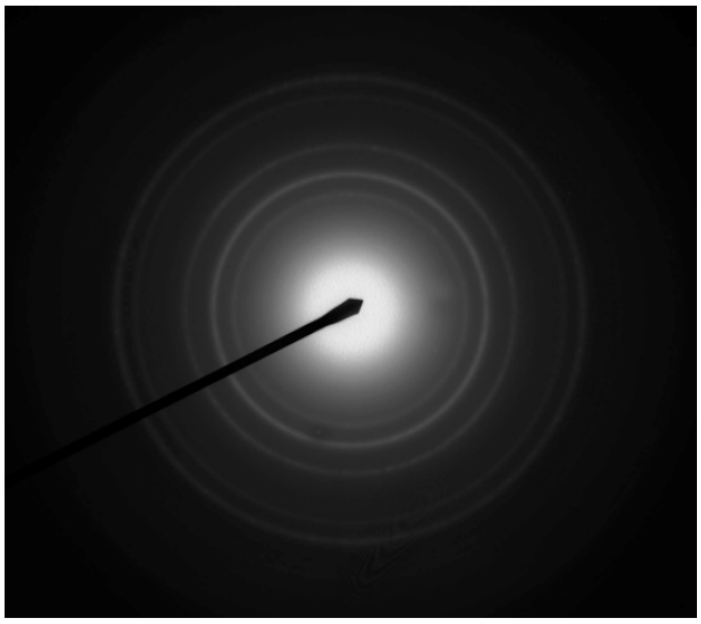

Figure 3.2 A typical selective area electron diffraction (SAED) of $CoFe_2O_4$ nanocrystals.

spectroscopy (ICP-AES) method showed Co and Fe having a closed 1:2 molar ratio in all of as-synthesized $CoFe_2O_4$ nanocrystals.

To make larger spherical $CoFe_2O_4$ nanocrystals, the 5 nm nanocrystals served as the seeds for the seed-mediated growth as the second step of the synthesis for nanocrystals with a diameter of 8 nm, as shown in Figure 3.3 a and 3.3 b, respectively. The size of the nanocrystals was controlled through the ratio between the amount of nanocrystal seeds and the amount of precursors in the solution for seed-mediated growth. The growth procedures described in the Experimental Section have generated a sample consisting of 8 nm spherical nanocrystals with size distribution less than 7% by counting over 400 nanocrystals. Highly monodispersed nanocrystals with a 9 nm diameter can also be obtained using the same procedures but with increased concentration of precursors in the seed-mediated growth process. The typical histograms of size distribution for $CoFe_2O_4$ nanocrystals with a diameter of 5 nm, 8 nm, and 12 nm are shown in Figure 3.4 a, b and c, respectively, indicating the quality of spherical $CoFe_2O_4$ nanocrystals is very high in terms of size distribution.

Although nanocrystals with even larger diameter can also be produced with 5 nm seeds, the quality of nanocrystals in terms of size distribution usually deteriorated. Therefore, monodisperse nanocrystals with bigger diameters were typically synthesized by incrementally increasing the size of nanocrystal seeds. For example, 8 nm $CoFe_2O_4$ nanocrystals were used in seed-mediated growth process to make monodispersed $CoFe_2O_4$ nanocrystals with a diameter of 10 nm or 12 nm, as shown in Figure 3.3 c and 3.3 d, respectively.

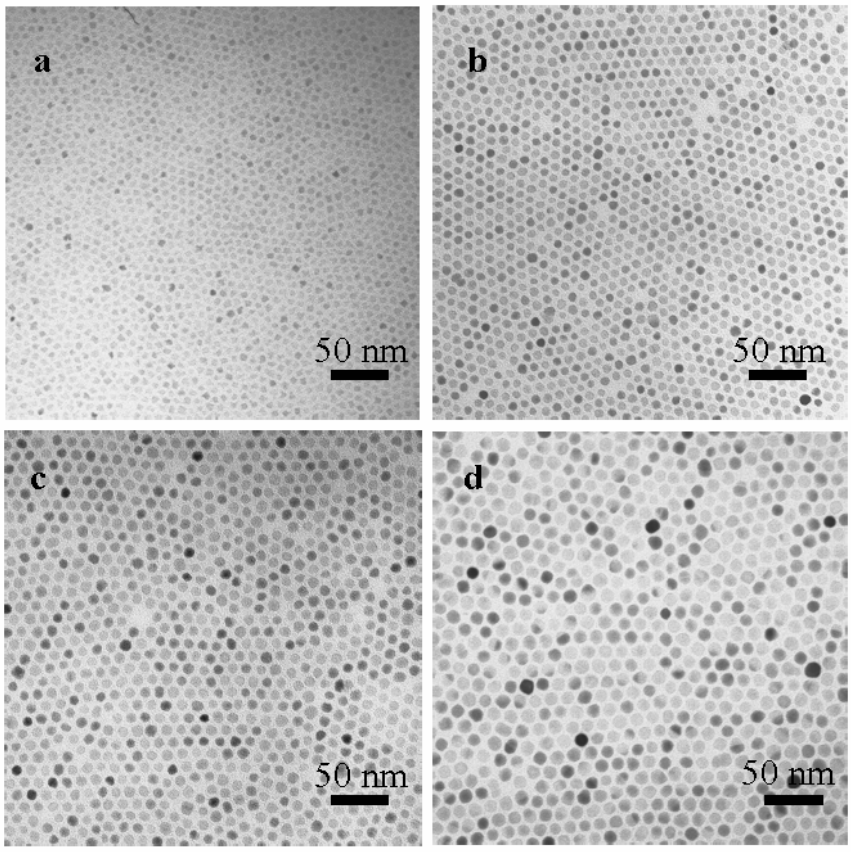

Figure 3.3 The typical TEM micrographs for spherical $CoFe_2O_4$ nanocrystals with a diameter of 5 nm (a), 8 nm (b), 10 nm (c), and 12 nm (d), respectively.

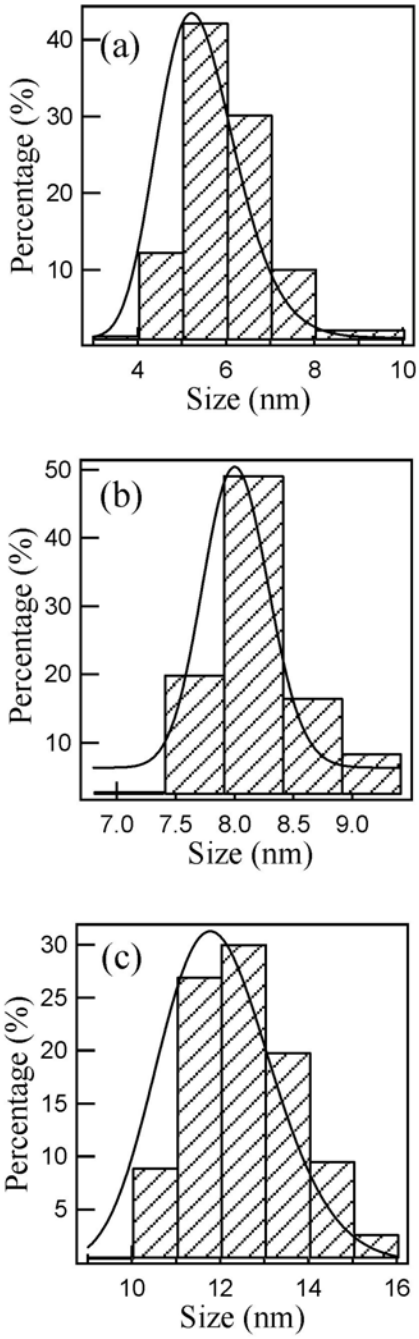

Figure 3.4 The representative histograms of size distribution for spherical $CoFe_2O_4$ nanocrystals (a) 5 nm, (b) 8 nm, and (c) 12 nm, respectively.

It is very intriguing that the shape of $CoFe_2O_4$ nanocrystals can be tuned to cubic during the seed-mediated growth process. Growth reaction parameters such as heating rate, temperature, reaction time, ratio of seed to precursors, and ratio of oleic acid to oleylamine have been systematically studied for the control of size and shape of nanocrystals. The experimental results indicated that heating rate and growth temperature control the shape of $CoFe_2O_4$ nanocrystals. For example, using the same 5 nm spherical seeds and the same growth solution as for the preparation of 9 nm spherical nanocrystals, cubic $CoFe_2O_4$ nanocrystals were produced with an edge length of 8 nm when the temperature was raised only to 210 °C at a rate of 2 ~ 3 °C/min. The product was mainly monodisperse nanocubes with a very tiny fraction of the product consisting of ~ 6 nm spherical nanocrystals, which can be easily separated by addition of acetone into the hexane suspension. To grow longer edge cubes, larger spherical nanocrystals are desirable. For instance, if using 8 nm spherical nanocrystals as seeds, nanocubes with edge length of 10 nm or 12 nm have been produced by simply increasing the amount of precursors. The TEM results of such nanocubes with different edge lengths are presented in Figure 3.5. Figure 3.6 a and 3.6 b are high-resolution TEM (HRTEM) images of ~ 8 nm spherical and ~ 12 nm cubic $CoFe_2O_4$ nanocrystals , indicating that both spherical and cubic $CoFe_2O_4$ nanocrystals are highly single nanocrystalline. It is also very interesting to observe some local short range self assembly formed by cubic nanocrystals as illustrated in Figure 3.6 c and 3.6 d. The quality of cubic $CoFe_2O_4$ nanocrystals is very high. Figure 3.7 displays the histograms from TEM studies showing a narrow size distribution of nanocubes with an almost uniform cube shape. More than 80% of the nanocubes possess an aspect ratio between 1 and 1.05 as illustrated in Figure 3.7 d.

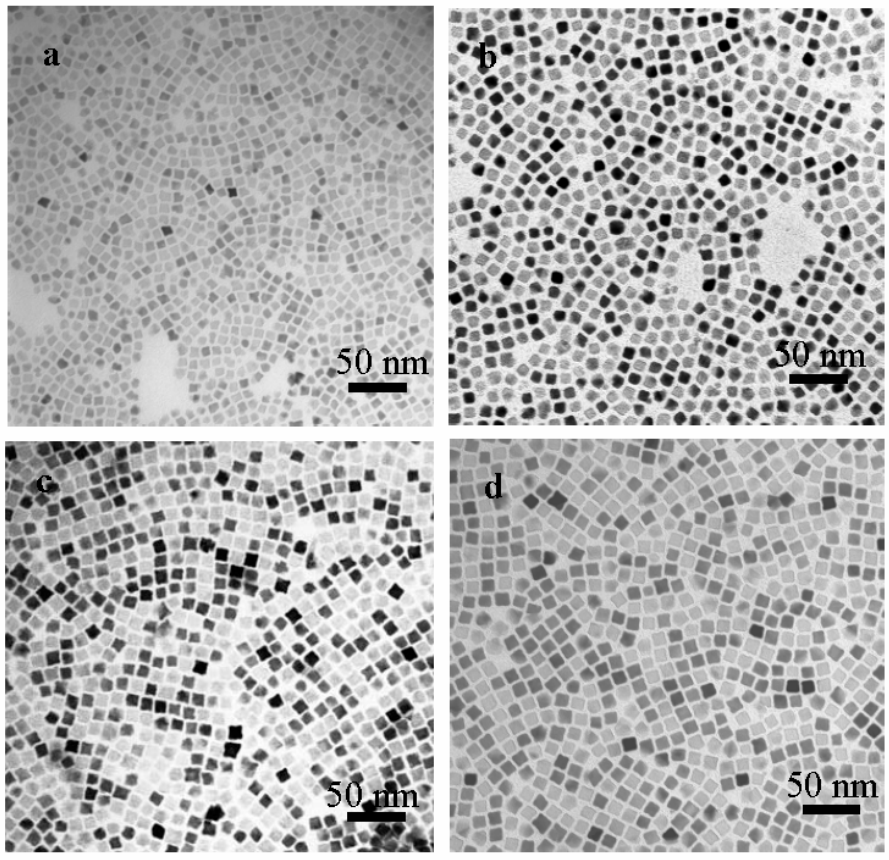

Figure 3.5 The typical TEM micrographs for cubic $CoFe_2O_4$ nanocrystals with cubic edge length at 8 nm (a), 9 nm (b), 10 nm (c), and 12 nm (d), respectively.

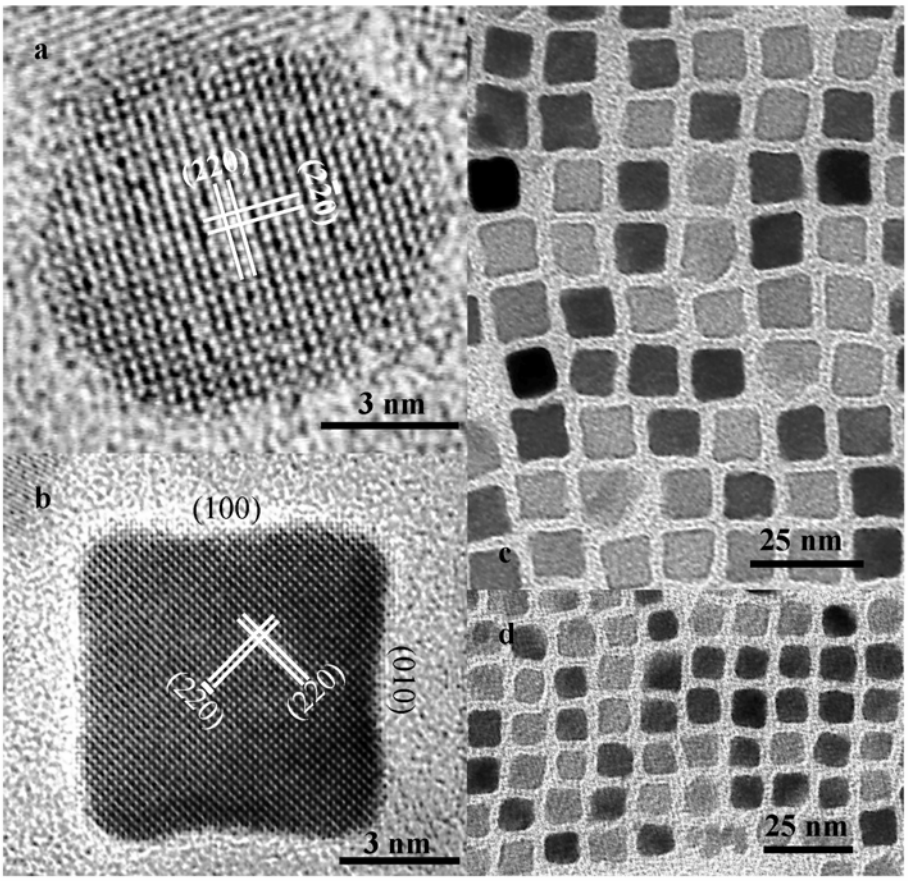

Figure 3.6 HRTEM images of spherical (a) and cubic (b) $CoFe_2O_4$ nanocrystals. Panels (c) and (d) show some local short range ordering in ~ 11 nm and ~ 9 nm nanocubes assemblies.

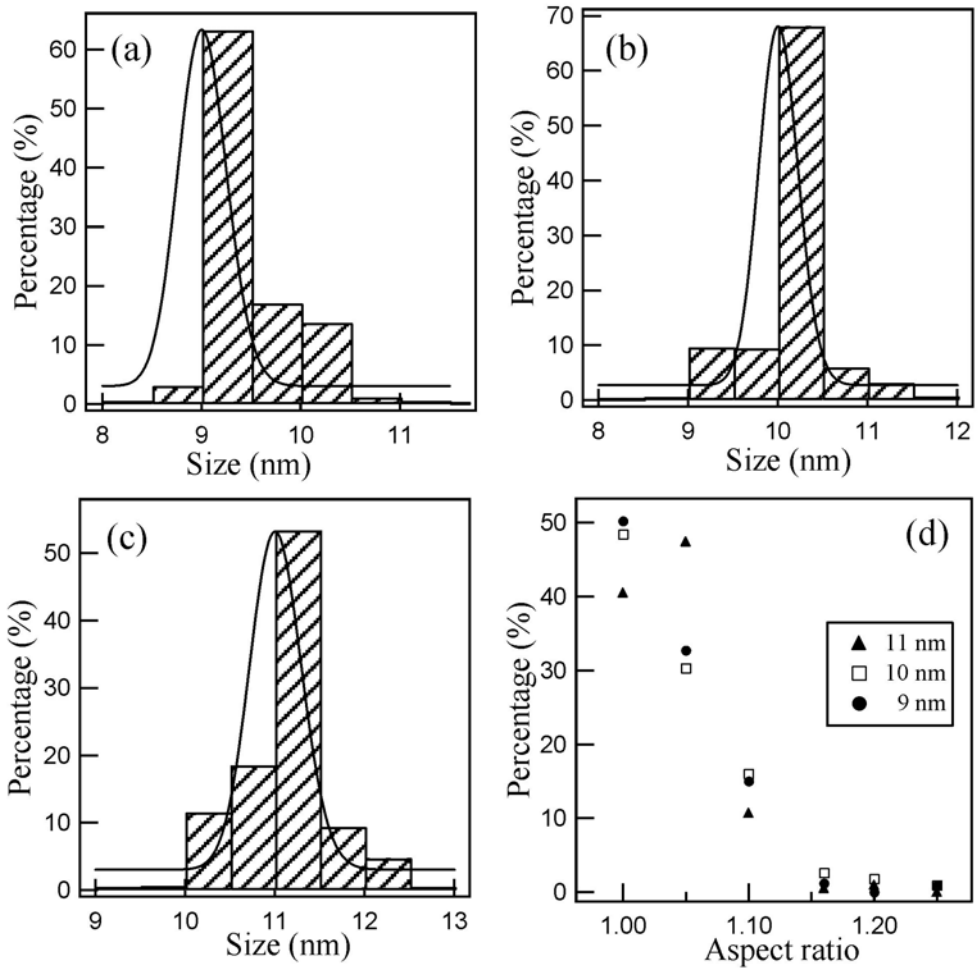

Figure 3.7 The histograms of size distribution of cubic $CoFe_2O_4$ nanocrystals with edge length at (a) 9 nm, (b) 10 nm, and (c) 11 nm. Panel (d) displays the aspect ratios of cubic nanocrystals in panels (a), (b), and (c).

Due to the decisive effect of heating rate and growth temperature on shape control of nanocrystal, Figure 3.8 shows that from 5 nm spherical $CoFe_2O_4$ nanocrystals, nearly cubic nanocrystals with 8 nm edge length can be produced, further such nanocube seeds with an 8 nm edge length can be transformed into almost spherical monodisperse $CoFe_2O_4$ nanocrystals with a 12 nm diameter. Such a reversible shape formation clearly demonstrated that the shape of $CoFe_2O_4$ nanocrystals can be precisely controlled through the temperature and heating growth rate.

The nanocrystal growth rate is the key in shape control. The precursor molecules have a decomposition temperature around 190 °C. As a surfactant, oleic acid stabilized the as synthetic nanocrystals. Oleylamine was used to provide an active and basic condition essential for the formation of spinel ferrite oxides. The long chain alcohol also was essential in nucleation and growth processes since it probably made ferrous cations available, which peculiarly always facilitated the formation of $CoFe_2O_4$ nanocrystals[26,27]. A slow heating rate kept a lower concentration of available active metal monomers from the decomposition of precursors, which combined with the low growth temperature, gave a slow rate in crystal growth. The growth of cubic $CoFe_2O_4$ nanocrystals was terminated at {100} planes, as indicated in Figure 3.6 b, which were predicated to have the lowest surface energy[28,29]. When a much faster heating rate was employed, a high concentration of active metal monomers was present. A faster growth rate at a higher temperature with plenty of active metal monomers available resulted in the crystals growth much less selective in directions and hence produced spherical $CoFe_2O_4$ nanocrystals.

The magnetic properties of $CoFe_2O_4$ nanocrystals with different shapes can provide great insight into the fundamentals of nanomagnetism. The zero-field-cooling (ZFC)

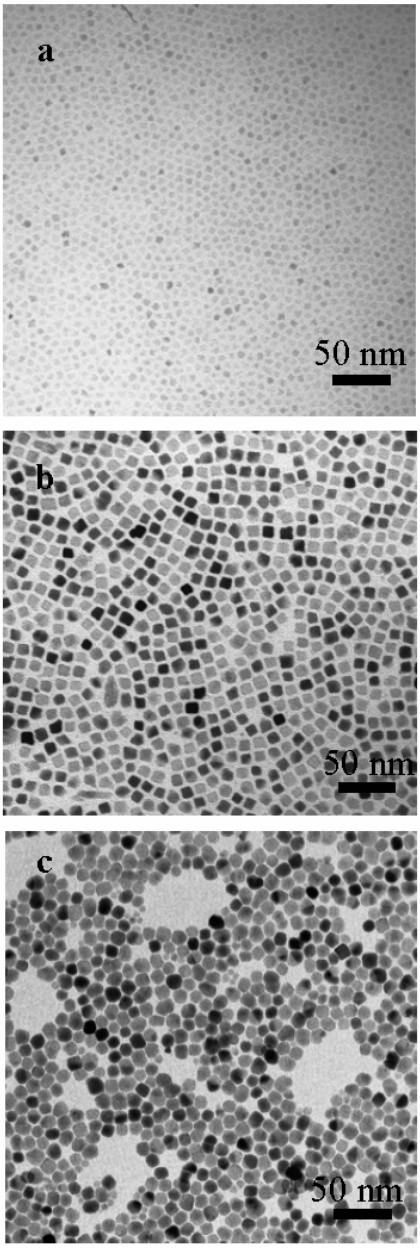

Figure 3.8 The TEM images for the shape interchanges between spherical and cubic nanocrystals. (a) 5 nm sphere, (b) 8 nm cube, and (c) 12 nm sphere.

magnetization measurements of spherical and cubic nanocrystals are shown in Figure 3.9. The values of blocking temperature for both spherical and cubic $CoFe_2O_4$ nanocrystals are plotted against the volumes of nanocrystals in Figure 3.10. Clearly, the blocking temperature T_B increases with increasing the volumes of nanocrystals and falls into the same line for both spherical and cubic shapes. The field dependences of magnetization for spherical and cubic nanocrystals are presented in Figure 3.11 and 3.12, respectively. Although the saturation magnetization (M_S) and remanent magnetization (M_R) show volume dependences in both shapes, the spherical or cubic shape of nanocrystals does not make much difference, as shown in Figure 3.13. As the volume increases, the coercivity (H_C) displays almost the same trend for spherical and cubic nanocrystals. However, the coercivity of nanocubes is drastically lower than the spheres having the same volume in Figure 3.14.

The correlation between blocking temperature and the volume of nanocrystals is well consistent with the Stoner-Wohlfarth theory[30,31], which expresses that the magnetocrystalline anisotropy (E_A) of a nanocrystal is proportional to its volume (V) as

$$E_A = KV \sin^2\theta \qquad (3.1)$$

where K is anisotropy constant and θ is the angle between the easy axis and magnetization direction. Magnetic anisotropy (E_A) serves as an energy barrier for blocking the superparamagnetic relaxation of nanocrystals, and blocking temperature represents the temperature required to overcome this energy barrier by thermal activation.

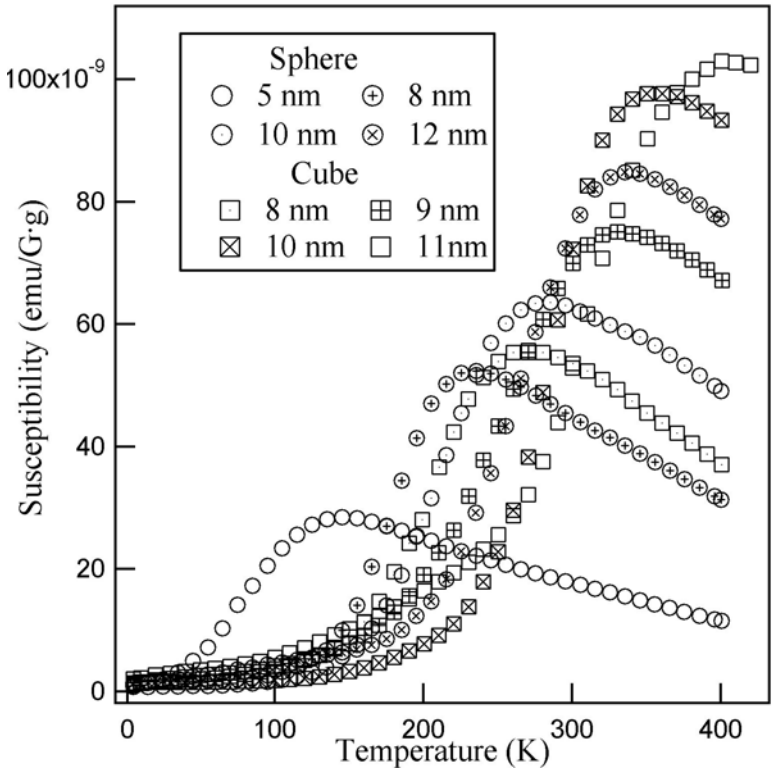

Figure 3.9 Zero-field-cooling magnetization measurements (ZFC) of spherical and cubic $CoFe_2O_4$ nanocrystals under 100 G applied magnetic field.

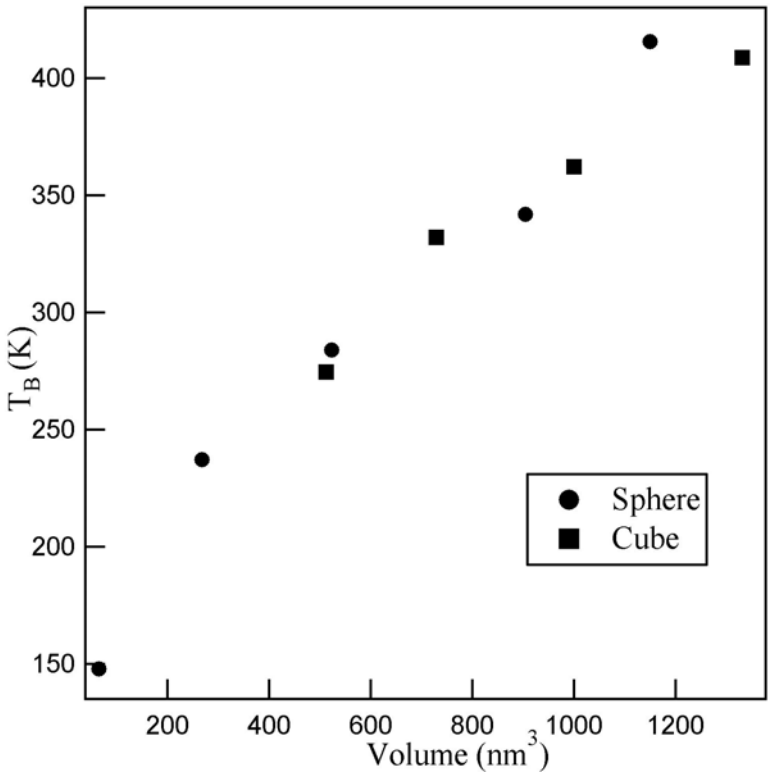

Figure 3.10 The volume dependency of blocking temperatures of spherical and cubic nanocrystals.

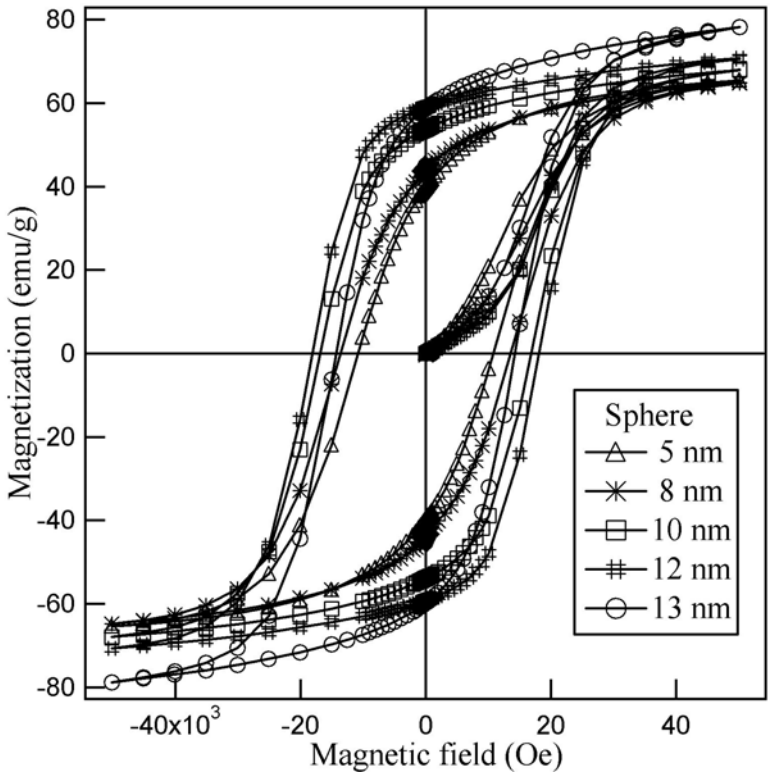

Figure 3.11 The field dependent magnetization measurements of spherical $CoFe_2O_4$ nanocrystals at 5 K.

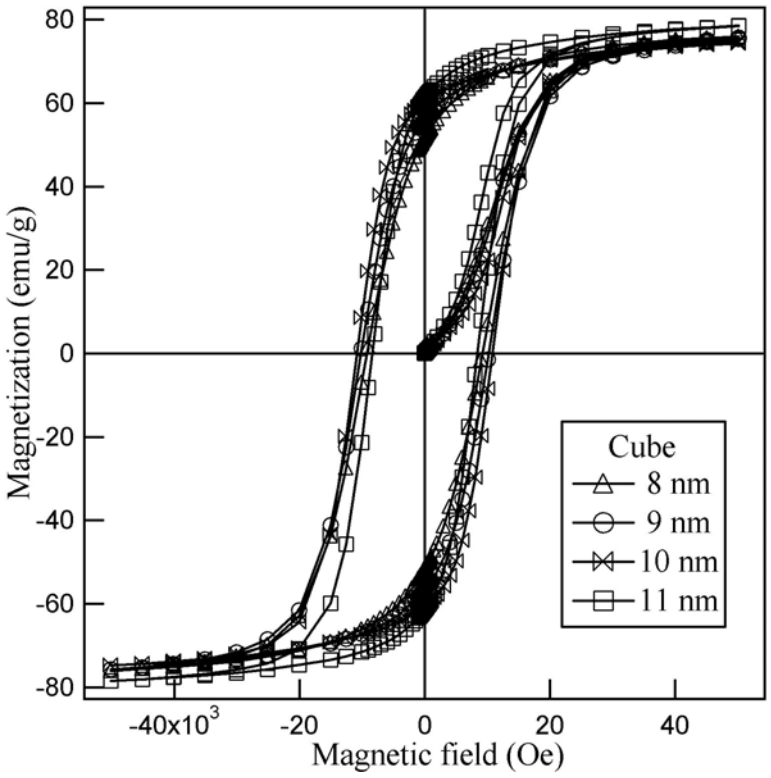

Figure 3.12 The field dependent magnetization measurements of cubic $CoFe_2O_4$ nanocrystals at 5 K.

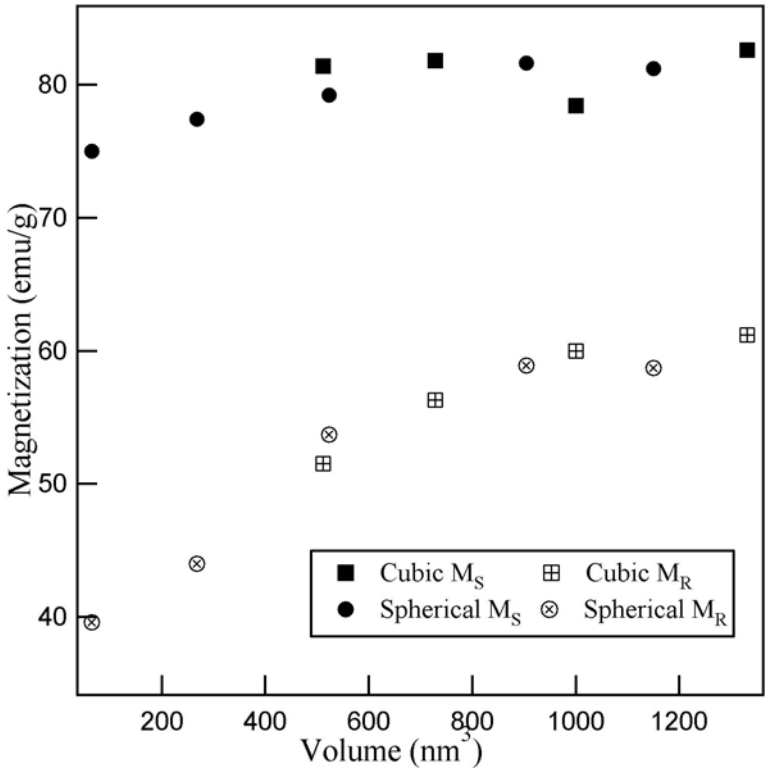

Figure 3.13 The volume dependency of saturation and remanent magnetizations of spherical and cubic $CoFe_2O_4$ nanocrystals.

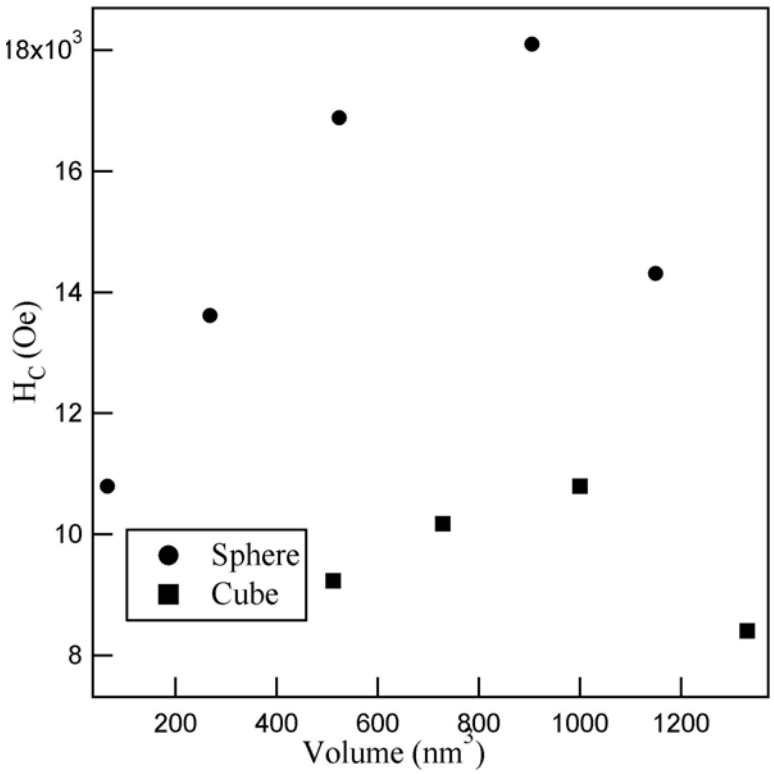

Figure 3.14 The variation of coercivity as a function of the volumes of spherical and cubic $CoFe_2O_4$ nanocrystals.

Thus, the blocking temperature increases as the volume of nanocrystals increases, as shown in Figure 3.10.

The increase in coercivity initially with increasing volume has been considered due to the increase in magnetic anisotropy since an applied field at a given temperature should be able to overcome the energy barrier and change the orientation of magnetization. The eventual decrease in coercivity is usually attributed to a switch of magnetization process from coherent to curling. The coercivity of nanocrystals from Stoner-Wohlfarth theory is determined by anisotropy constant and saturation magnetization:

$$H_C = 2K/\mu_0 M_S \qquad (3.2)$$

where μ_0 is universal constant of permeability in free space. Judging from the blocking temperature and saturation magnetization studies, K and M_S essentially should be the same in equal volume spherical and cubic nanocrystals. Certainly, the dramatic difference in coercivity between the equal volume spherical and cubic nanocrystals strongly implies that this model alone cannot fully address the fundamental issues in field-induced magnetic reversals of nanocrystals.

Cubic morphology with an aspect ratio of almost 1 is magnetically quasi-isotropic, and hence, magnetic shape anisotropy should not have any influence in cubic nanocrystals. Coercivity has to be considered together with the surface pinning of

magnetic moments and the resulting surface anisotropy[32]. The surface magnetic disorder and spin pinning originate from missing coordinating oxygen atom around surface metal cations. When the coordination of surface metal cations has a closer similarity to the coordination symmetry of the metal cations in the core of a nanocrystal, the surface anisotropy should be lower[33]. Compared to the curved topology of spherical nanocrystals, the flat surfaces of cubic nanocrystals enable the surface metal cations to possess a more symmetric coordination and fewer missing coordinating oxygen atoms. Therefore, the surface anisotropy should be much smaller in cubic nanocrystals than the one in spheres. Consequently, cubic nanocrystals show a much lower coercivity than the spherical nanocrystals having the same volume. Clearly, the surface anisotropy shows the dominance in determining the coercivity over the core anisotropy, which is proportional to the volume.

The saturation and remnant magnetization have shown an increase with the increasing volume. Such increases have usually been attributed to a decreasing proportion of the pinned surface magnetic moments in overall magnetization as the nanocrystals grow in size. The nanocrystals with different shapes have demonstrated the distinctly different coercivity that implies different surface pinning. However, the saturation and remnant magnetization display indifference toward the spherical or cubic shape of nanocrystals. This inconsistency surely calls for systematic studies to specifically address the fundamental issues on such important properties as saturation and remanent magnetization. Furthermore, it would be important to know why surface anisotropy does not seem to affect the blocking temperature and what the fundamental difference is between thermally and magnetically overcoming the anisotropy energy barriers.

3.4 Conclusions

The nonhydrolytic synthesis has been developed to produce high-quality and monodisperse $CoFe_2O_4$ nanocrystals. The shape of the nanocrystals is remarkably controlled through adjusting the crystal growth rate. This synthetic method is possibly applicable to the synthesis of different spinel ferrite and other metal oxides nanocrystals though the precursors may need to be chemically modified. A comparison of the magnetic properties possessed by spherical and cubic nanocrystals offers rich insights on the fundamentals of nanomagnetism. Addressing the interesting and important fundamental issues raised by these size and shape-dependent studies surely promises further advancement in the understanding and application of magnetism in the nanometer regime. Furthermore, the assembly of these cubic nanocrystals may results in a breakthrough toward using nanocrystal as one particle one bit magnetic media to achieve ultrahigh-density data storage. Instead of numerous possible crystallographic orientations for each nanocrystal and therefore completely disordered magnetization in a 2D assembly of sphere, a cube would only have six possible crystallographic orientations in an assembly. If the magnetic anisotropy of the cubic material is cubic, all such six directions are magnetically identical, and hence the magnetically ordered assembly is greatly simplified.

3.5 References

(1) Brus, L. *J. Phys. Chem.* **1986**, *90*, 2555.

(2) Steigerwald, M. L.; Brus, L. E. *Acc. Chem. Res.* **1990**, *23*, 183.

(3) Alivisatos, A. P. *J. Phys. Chem.* **1996**, *100*, 13226.

(4) Alivisatos, A. P. *Science* **1996**, *271*, 933.

(5) Heath, J. R. *Acc. Chem. Res.* **1999**, *32*, 388.

(6) Murray, C. B.; Kagan, C. R.; Bawendi, M. G. *Annu. Rev. Mater. Sci.* **2000**, *30*, 545.

(7) Hu, J.; Odom, T. W.; Lieber, C. M. *Acc. Chem. Res.* **1999**, *32*, 435.

(8) Pan, Z. W.; Dai, Z. R.; Wang, Z. L. *Science* **2001**, *291*, 1947.

(9) Puntes, V. F.; Krishnan, K. M.; Alivisatos, A. P. *Science* **2001**, *291*, 2115.

(10) Puntes, V. F.; Zanchet, D.; Erdonmez, C. K.; Alivisatos, A. P. *J. Am. Chem. Soc.* **2002**, *124*, 12874.

(11) Dumestre, F.; Chaudret, B.; Amiens, C.; Renaud, P.; Fejes, P. *Science* **2004**, *303*, 821.

(12) Peng, X. *Adv. Mater.* **2003**, *15*, 459.

(13) Xia, Y.; Yang, P. *Adv. Mater.* **2003**, *15*, (Special issue for nanowire), all review articles relevant to shape controlled synthesis of nanocrystals.

(14) Ahmadi, T. S.; Wang, Z. L.; Green, T. C.; Henglein, A.; El-Sayed, M. A. *Science* **1996**, *272*, 1924.

(15) Jin, R.; Cao, Y.; Mirkin, C. A.; Kelly, K. L.; Schatz, G. C.; Zheng, J. G. *Science* **2001**, *294*, 1901.

(16) Jana, N. R.; Gearheart, L.; Murphy, C. J. *Chem. Commun.* **2001**, 617.

(17) Jin, R.; Cao, Y. C.; Hao, E.; Metraux, G. S.; Schatz, G. C.; Mirkin, C. A. *Nature* **2003**, *425*, 487.

(18) Peng, X.; Manna, U.; Yang, W.; Wickham, J.; Scher, E.; Kadavanich, A.; Allvisatos, A. P. *Nature* **2000**, *404*, 59.

(19) Rockenberger, J.; Scher, E. C.; Alivisatos, A. P. *J. Am. Chem. Soc.* **1999**, *121*,

11595.

(20) Hyeon, T.; Lee, S. S.; Park, J.; Chung, Y.; Na, H. B. *J. Am. Chem. Soc.* **2001**, *123*, 12798.

(21) Hyeon, T.; Chung, Y.; Park, J.; Lee, S. S.; Kim, Y.-W.; Park, B. H. *J. Phys. Chem. B* **2002**, *106*, 6831.

(22) Sun, S.; Zeng, H. *J. Am. Chem. Soc.* **2002**, *124*, 8204.

(23) Sun, S.; Zeng, H.; Robinson, D. B.; Raoux, S.; Rice, P. M.; Wang, S. X.; Li, G. *J. Am. Chem. Soc.* **2004**, *126*, 273.

(24) Jana, N. R.; Gearheart, L.; Murphy, C. J. *Adv. Mater.* **2001**, *13*, 1389.

(25) Jana, N. R.; Gearheart, L.; Murphy, C. J. *Chem. Mater.* **2001**, *13*, 2313.

(26) Rondinone, A. J.; Samia, A. C. S.; Zhang, Z. J. *J. Phys. Chem. B* **1999**, *103*, 6876.

(27) Rondinone, A. J.; Samia, A. C. S.; Zhang, Z. J. *Appl. Phys. Lett.* **2000**, *76*, 3624.

(28) Davies, M. J.; Parker, S. C.; Watson, G. W. *J. Mater. Chem.* **1994**, *4*, 813.

(29) Fang, C. M.; Parker, S. C.; De With, G. *J. Am. Ceram. Soc.* **2000**, *83*, 2082.

(30) Stoner, E. C.; Wohlfarth, E. P. *Trans. Roy. Soc.* **1948**, *A240*, 599.

(31) Stoner, E. C.; Wohlfarth, E. P. *IEEE Trans. Magn.* **1991**, *27*, 3475.

(32) Neel, L. *J. Phys. Radium* **1954**, *15,* 225.

(33) Vestal, C. R.; Zhang, Z. J. *J. Am. Chem. Soc.* **2003**, *125*, 9828.

CHAPTER 4

COMPARATIVE STUDIES ON SUPERPARAMAGNETIC PROPERTIES BETWEEN COBALT FERRITE AND MAGNETITE NANOCRYSTALS

Abstract

The systematic comparison between the superparamagnetic properties of $CoFe_2O_4$ and Fe_3O_4 nanocrystals has been made. The discrepancy in superparamagnetic properties between the similar sized spherical $CoFe_2O_4$ and Fe_3O_4 spinel ferrite nanocrystals is correlated to the magnitude of magnetocrystalline anisotropy, which is determined by the strength of electron spin – orbital angular momentum coupling (L-S). Compared to Fe_3O_4 nanocrystals, due to a strong electron spin-orbital interaction from Co^{2+} cations, the value of blocking temperature of $CoFe_2O_4$ nanocrystals is at least 100 K higher than that of the same sized Fe_3O_4 nanocrystals. Additionally, the coercivity of Fe_3O_4 nanocrystals is as a minimum as 50 times smaller than the same sized $CoFe_2O_4$ nanocrystals at 5K. These results clearly demonstrate that the superparamagnetic properties of spinel ferrites nanocrystals can be tailored by adjusting the chemical composition through controlling the magnetic couplings at atomic level.

4.1 Introduction

Magnetic properties of nanostructured materials have been investigated extensively for both fundamental interest and technological applications[1-6]. As the size of magnetic material shrinks into nanoscale regime, each of magnetic nanocrystal becomes single magnetic domain in virtue of the unfavorable energy compensation to form multiple domains. The magnetic behavior begins to elucidate the unique superparamagnetic character as a consequence of the magnetic anisotropy energy that separates two distinct stable states is compatible with the thermal energy. Such magnetic anisotropy energy is essentially controlled by the magnetocrystalline anisotropy energy, which originates fundamentally from the quantum couplings including the electron spin-spin coupling (S-S coupling) and spin-orbital angular momentum coupling (L-S coupling). Thus, magnetic nanocrystals provide an idea research system for the fundamental investigations on the relationship between superparamagnetism and magnetic couplings at atomic level. An elucidating example is the correlation between the L-S coupling and the superparamagnetic properties of magnetic nanocrystals through the modulation of magnetic anisotropy energy.

Superparamagnetism of magnetic nanocrystals is unique and plays different roles on various technological applications. To overcome the ‘superparamagnetic limit’ has been becoming a critical issue in fabrication of ultrahigh information storage media by self assembly of magnetic nanocrystals[7,8]. On the contrary, it is essential for the magnetic nanocrystals to stay at the superparamagnetic state in a wide variety of medical and clinical applications such as magnetic cell sorting and DNA separation[9-11], contrast-enhancement magnetic resonance imaging (MRI) and site-specific magnetic drug

carriers[12-14]. Moreover, the better understanding on the correlation of superparamagnetic properties with magnetic anisotropy energy offers an effective approach to rational design the magnetic nanocrystals in fulfilling different or even controversy imperatives through well-controlled magnetic anisotropy energy. For example, when using magnetic nanoparticles as site-specific targeting magnetic drug carriers, it requires that the magnetic nanoparticles should remain in the circulation for a sufficiently long time to allow them to reach their targets without being destroyed or evacuated. Recent studies have been demonstrated that the circulation time is inversely proportional to the particle size. However, the studies on magnetic properties indicate that the magnetization of magnetic nanocrystals is usually decreasing as the size of magnetic nanocrystal attenuation. Thus, a smaller sized magnetic nanocrystal possessing enhanced magnetic properties is desirable. Nevertheless, to satisfy each of the specific technical and biomedical applications, it depends on the systematic studies of the superparamagnetism in various types of magnetic nanocrystals on the basis of the manipulation of magnetic couplings at atomic level.

Although various synthetic procedures to different spinel ferrites nanoparticles have been reported[15-21], with few exceptions[22], the systematically comparative investigations on different spinel ferrites are still limited, in particular, the comparison between iron oxides such as magnetite and other spinel ferrites including cobalt ferrite. Moreover, in most of previous studies, it is rather difficult and sometimes not reliable to make a clear comparison, because of the broad size distribution and the lack of consistency on the synthetic procedures for different spinel ferrites nanoparticles. With recent advance on the synthesis of colloidal nanocrystals, monodispersed magnetite[23] along with other

spinel ferrites such as $CoFe_2O_4$ nanocrystals[24] can be synthesized under the same reaction conditions. Therefore, it is feasible to comparatively investigate the superparamagnetic properties on different types of spinel ferrites nanocrystals.

In present chapter, various sized $CoFe_2O_4$ and Fe_3O_4 nanocrystals with a typical size distribution less than 7% have been synthesized by using a non-hydrolysis process with a seed-mediated growth. The relationship between the superparamagnetic properties and the magnetic coupling, specifically the L-S coupling has been established by the comparative studies of the same sized spherical cobalt spinel ferrite and magnetite nanocrystals. The results that at least 100 degree higher on blocking temperature and 50 times larger on coercivity of $CoFe_2O_4$ nanocrystals than those of the same sized Fe_3O_4 nanocrystals are well consistent with a larger magnetocrystalline anisotropy energy constant of $CoFe_2O_4$, which comes from a strong L-S coupling in Co^{2+} lattice sites. Such study also suggests that magnetic $CoFe_2O_4$ nanocrystals may be a promising candidate in biomedical applications such as magnetic cell sorting and DNA separation.

4.2 Experimental Section

4.2.1 Synthesis of $CoFe_2O_4$ and Fe_3O_4 Nanocrystals

Spherical $CoFe_2O_4$ nanocrystals with size from 5 to 12 nm and spherical 4 to 10 nm Fe_3O_4 nanocrystals used in this chapter have been synthesized by high temperature non-hydrolysis process combined with seed-mediated growth [24]. All chemicals were purchased from Aldrich Chemicals Inc. and used without further treatment. To synthesize Fe_3O_4 nanocrystals, a mixture of 20 mL phenyl ether, 1 mmol iron (III) acetylacetonate

(Fe (acac)$_3$), 5 mmol 1,2 hexadecanediol, 1.4 mL oleic acid and 1.9 mL oleylamine were heated up to 260 °C and kept for 30 min.. After cooled to room temperature, 10 mL ethanol was added and black precipitates were collected by centrifugation. The size of Fe_3O_4 nanocrystals is about 4 nm in diameter. Other sized Fe_3O_4 nanocrystal samples used in this chapter were prepared by adjusting the molar ratios of seeds to iron precursors in the similar synthetic procedure. For example, to make 7 nm Fe_3O_4 nanocrystals, 70 mg of 4 nm Fe_3O_4 nanocrystals was mixed with 1 mmol Fe (acac)$_3$, 5 mmol 1-octadecanol, 1.4 mL oleic acid and 1.9 mL oleylamine in 30 mL phenyl ether. The solution was headed up to 260 °C and kept for 30 min, after the solution was cooled to room temperature, a black precipitate can be obtained by the addition of ethanol. The as-synthesized nanocrystals were usually washed with hexane and precipitated by acetone alternatively for one or two times and the dry samples were stored under vacuum before the magnetic measurements.

The synthesis of $CoFe_2O_4$ nanocrystals is the same as the procedure for Fe_3O_4 with an exception, which both Co(acac)$_2$ and Fe(acac)$_3$ are the precursors with the molar ratio of 1 to 2, instead of only Fe(acac)$_3$.

4.2.2 Transmission Electron Microscopy

TEM images and the selected area electron diffraction (SAED) patterns were recorded by using JEOL JEM 100C operated at 100 kV. The samples were prepared by slowly evaporating a drop of nanocrystal suspension in hexane on amorphous carbon-coated copper grids at room temperature.

4.2.3 Magnetic Measurements

Both temperature and magnetic field dependent magnetization measurements were carried out on superconducting quantum interference devices (SQUID) magnetometer (Quantum Design MPMS-5S) with a magnetic field up to ± 5 Tesla and temperature ranging from 5 K to 400 K. All samples for the magnetic measurements were prepared by fully dispersed an appropriate amount of dry powder nanocrystals in eicosane ($C_{20}H_{42}$, Aldrich, 99%) in order to minimize the magnetic interparticle interactions.

4.3 Results and Discussion

The monodispersed Fe_3O_4 nanocrystals with size varying from 4 to 10 nm and $CoFe_2O_4$ nanocrystals with size ranging between 5 and 12 nm have been synthesized from the combination of non-hydrolysis procedure with a seed-mediated growth process. The representative TEM images of 10 nm Fe_3O_4 and 12 nm $CoFe_2O_4$ spherical nanocrystals are shown in Figure 4.1a and 4.1b, respectively. Clearly, it can be seen that both Fe_3O_4 and $CoFe_2O_4$ nanocrystals are highly monodispersed and the typical size distribution is less than 7%. The crystal structure for as-synthesized Fe_3O_4 and $CoFe_2O_4$ nanocrystals is confirmed to be cubic spinel by selected area electron diffraction (SAED) studies as illustrated in Figure 4.2 a and b for $CoFe_2O_4$ and Fe_3O_4, respectively.

Figure 4.3 shows the zero-field-cooling magnetization measurements for both Fe_3O_4 and $CoFe_2O_4$ nanocrystals with size at 5 and 10 nm. The magnetizations are normalized

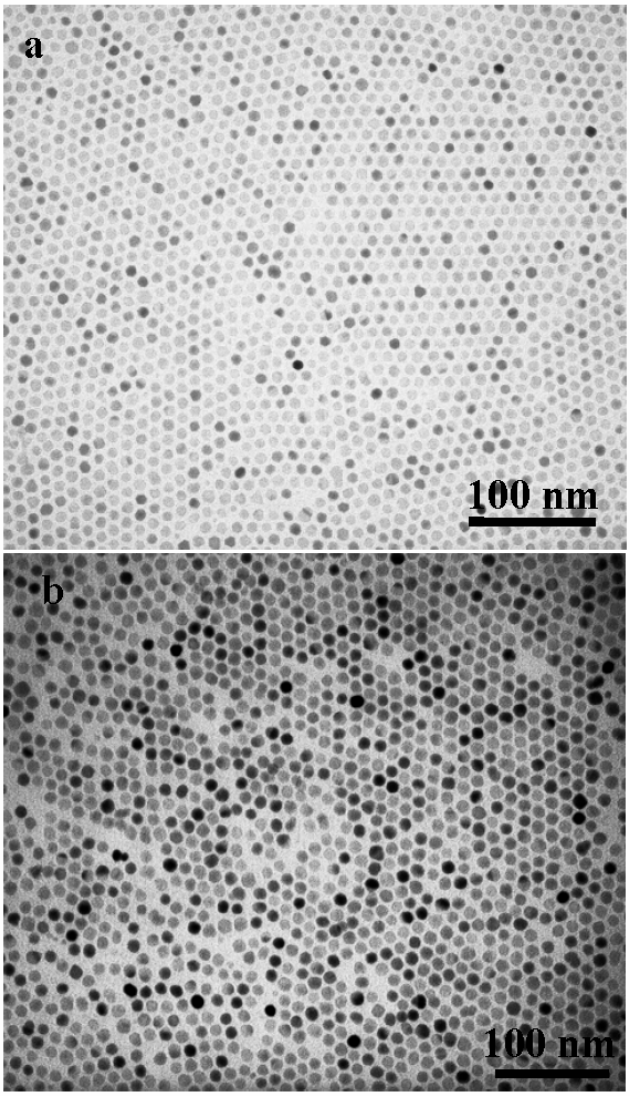

Figure 4.1 Panel a and b are the representative TEM images of 10 nm Fe_3O_4 and 12 nm $CoFe_2O_4$ nanocrystals, respectively.

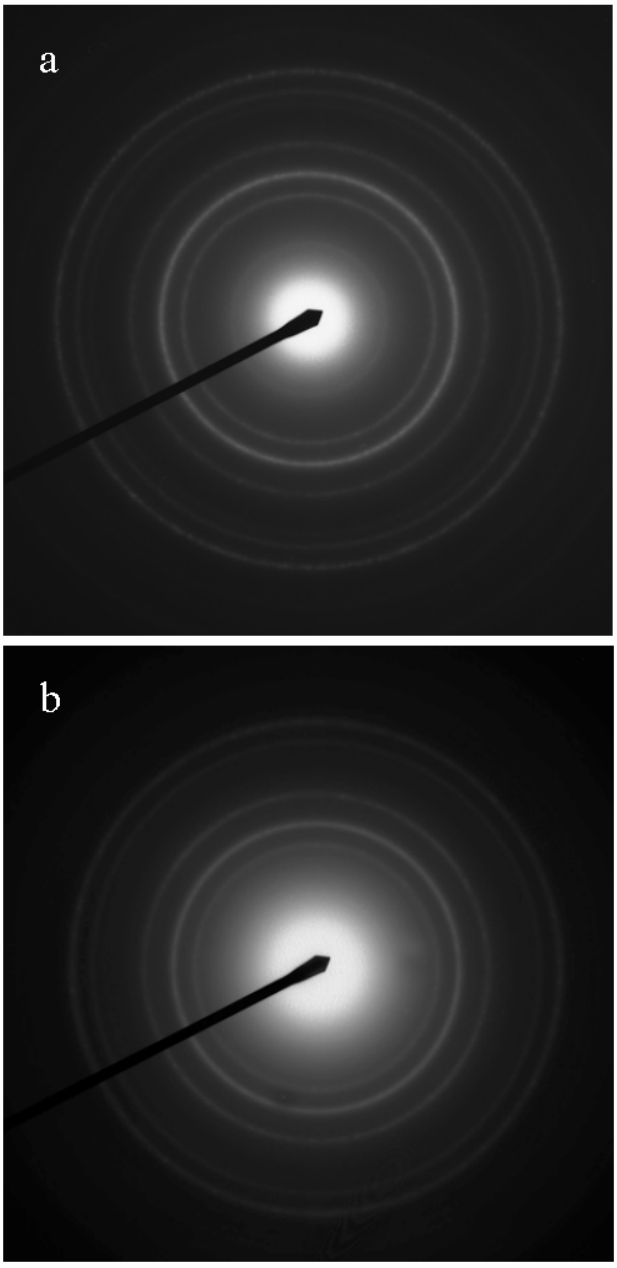

Figure 4.2 Selected area electron diffraction (SAED) patterns for (a) 10 nm Fe_3O_4 nanocrystals and (b) 12 nm $CoFe_2O_4$ nanocrystals

for all measurements in order to make a clear comparison. Clearly, regardless the size of nanocrystals, as the temperature increases, the magnetization shows a maximum value at certain temperature. Afterward, the magnetization begins to reduce and shows the paramagnetic character. The temperature at which the magnetization shows the maximum value is defined as the blocking temperature (T_B). For both Fe_3O_4 and $CoFe_2O_4$ nanocrystals, the blocking temperature increases as the size of nanocrystals increasing. However, there is a dramatic discrepancy in blocking temperature for the same sized Fe_3O_4 and $CoFe_2O_4$ nanocrystals. For example, as shown in Figure 4.4, the blocking temperature of 5 nm Fe_3O_4 is at least 100 K less than that of 5 nm $CoFe_2O_4$ nanocrystals. Furthermore, such divergence in the blocking temperature becomes larger and larger as the size of nanocrystals increases.

The field dependent magnetization measurements at 5 K are in Figure 4.5. The insert plots display the enlargement of partial hysteresis curves for 5 and 10 nm Fe_3O_4 nanocrystals, respectively. The coercivity (H_C), saturation (M_S) and remanent (M_R) magnetizations as a function of the size of nanocrystals are in Figure 4.6, 4.7 and 4.8, respectively. Clearly, the values of these magnetic parameters for $CoFe_2O_4$ nanocrystals are greatly larger than those of the same sized Fe_3O_4 nanocrystals. The typical coercivity of $CoFe_2O_4$ nanocrystals is on the range of tens of thousand, whereas for Fe_3O_4 nanocrystals, it is only several hundreds in magnitude. As shown in Figure 4.6, for example, the coercivity of 5 nm Fe_3O_4 nanocrystals is only 214 Oe. On the other hand, for 5 nm $CoFe_2O_4$ nanocrystals, it is over 10.8 kOe, which is more than 50 times larger than that of Fe_3O_4 nanocrystals. As for the saturation and remanent magnetization, first, the tendency that both of them increase as size being increased is observed. In addition,

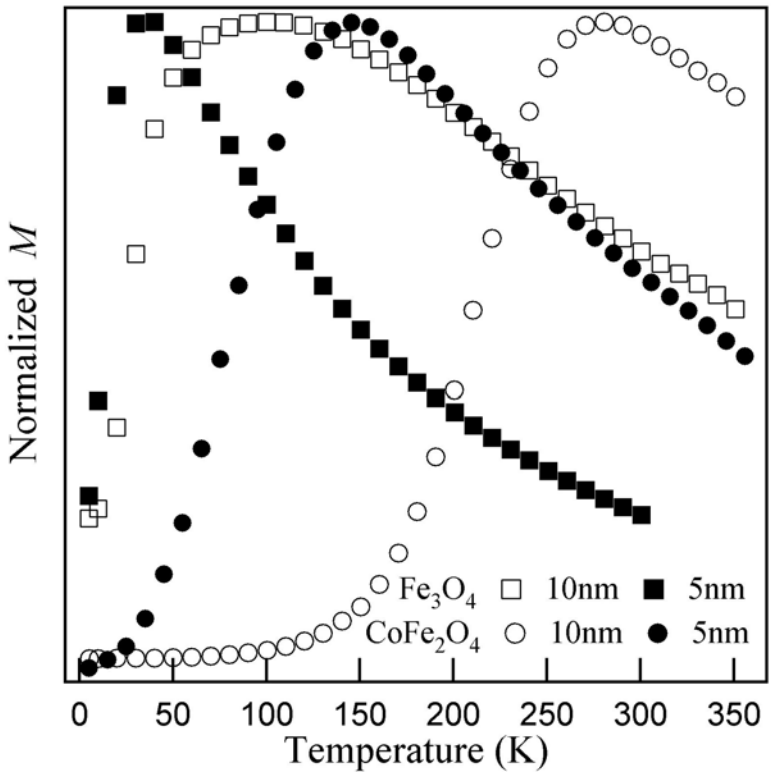

Figure 4.3 The zero-field-cooling (ZFC) magnetization measurements of 5 and 10 nm Fe_3O_4 and the same sized $CoFe_2O_4$ nanocrystals in100 Oe magnetic field. Note that the magnetizations of all samples are normalized.

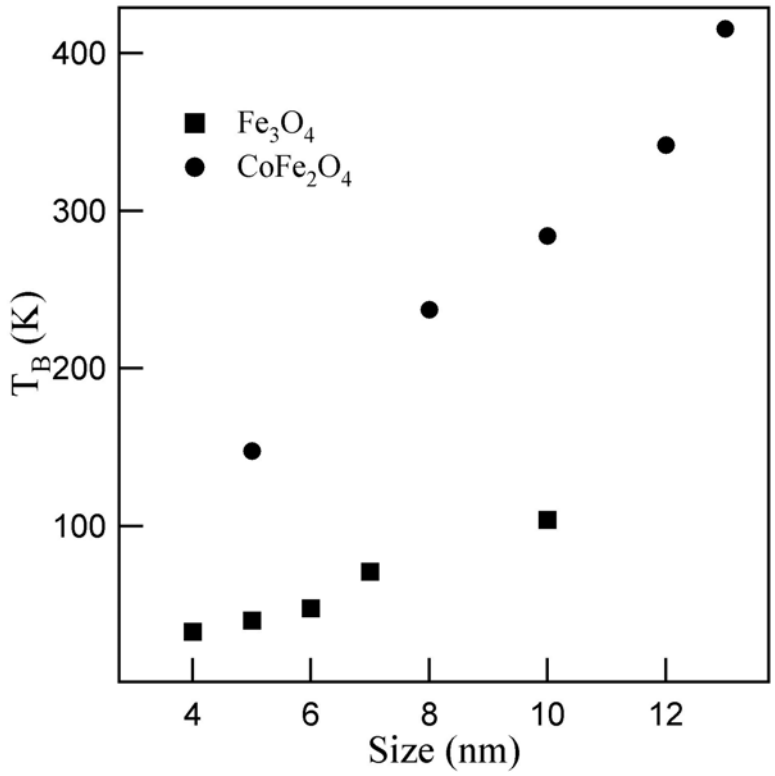

Figure 4.4 The variation of blocking temperature as a function of sizes of Fe_3O_4 and $CoFe_2O_4$ nanocrystals.

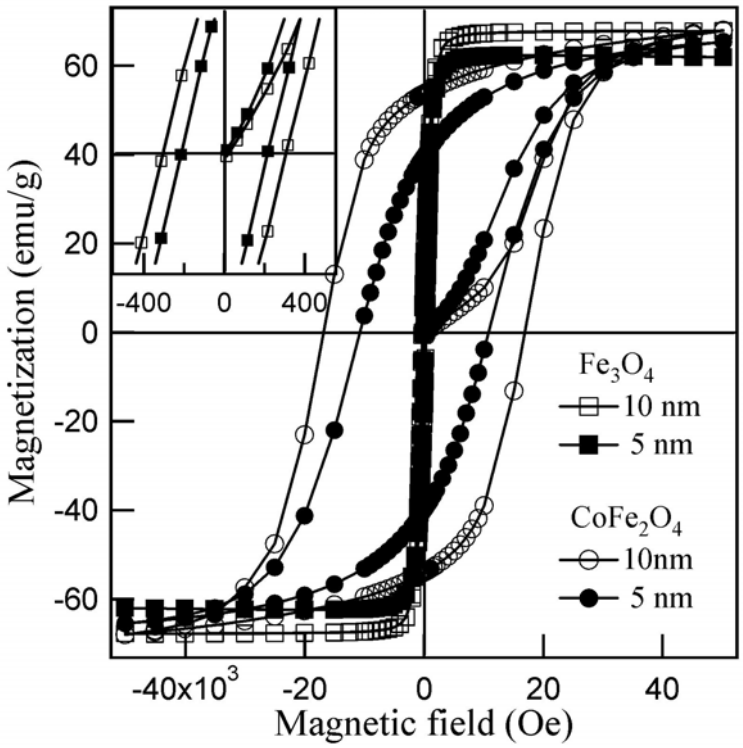

Figure 4.5 The field dependent magnetization measurements of 5 and 10 nm Fe_3O_4 and the same sized $CoFe_2O_4$ nanocrystals at 5 K. The insert plots show the enlarged partial hysteresis curves for 5 and 10 nm Fe_3O_4 nanocrystals, respectively.

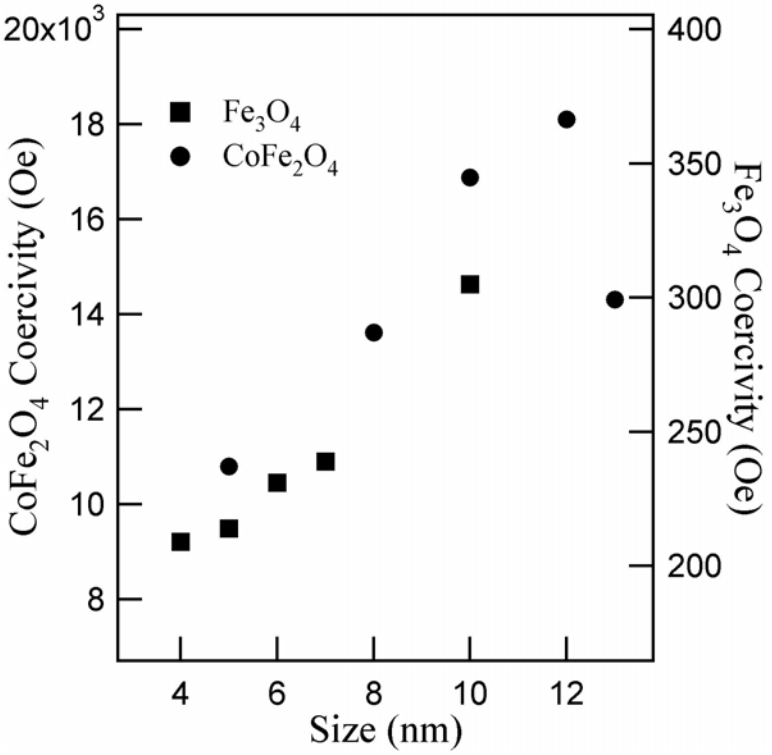

Figure 4.6 The coercivity varies as a function of sizes of Fe_3O_4 and $CoFe_2O_4$ nanocrystals.

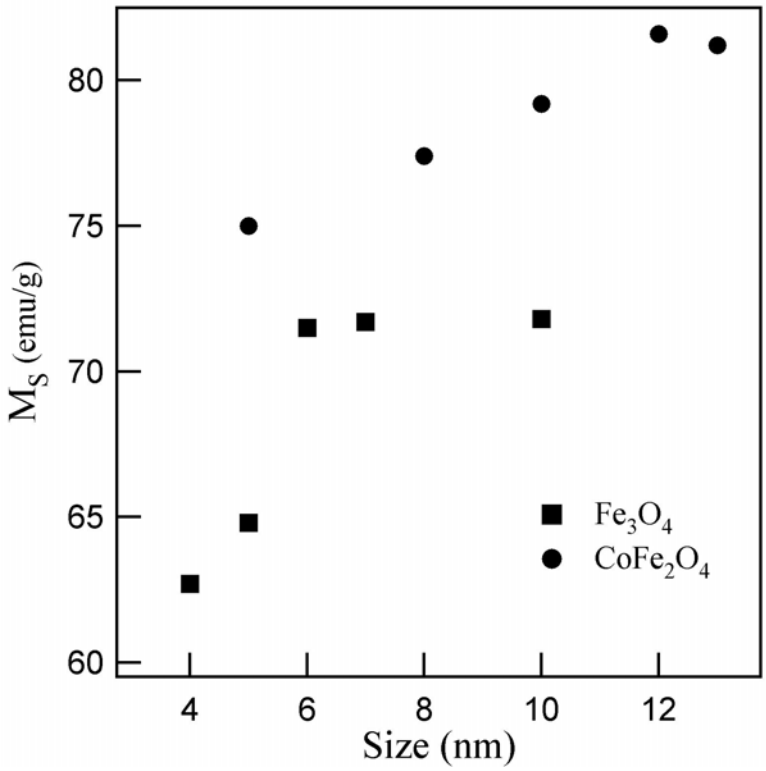

Figure 4.7 The saturation magnetization (M_S) changes as a function of sizes of Fe_3O_4 and $CoFe_2O_4$ nanocrystals.

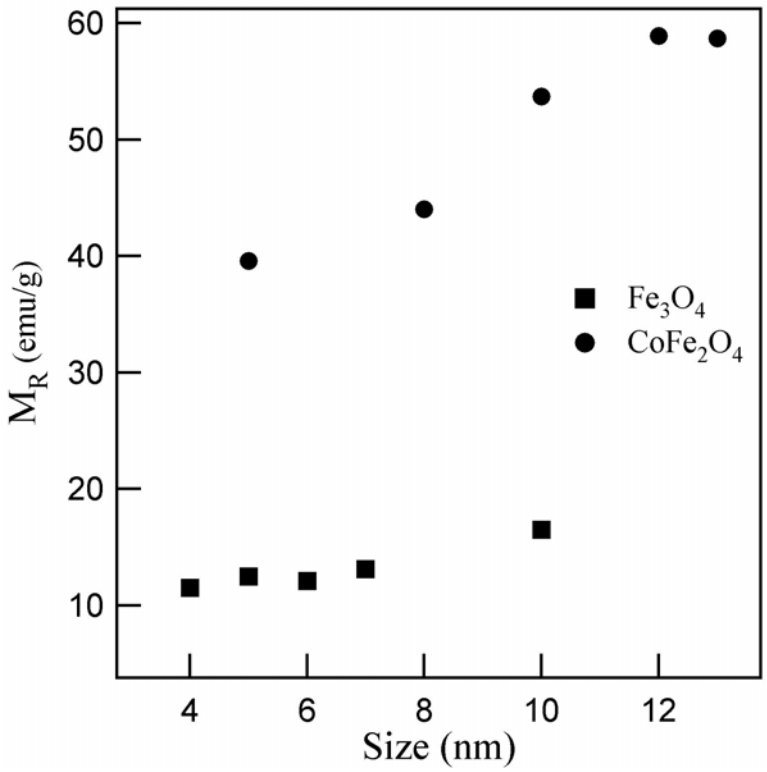

Figure 4.8 The variation of remanence magnetization (M_R) as a function of sizes of Fe_3O_4 and $CoFe_2O_4$ nanocrystals.

after certain size, the saturation magnetization is flat out and approaches to the values of the corresponding bulk materials [25]. An average 10 emu/g larger on M_S of $CoFe_2O_4$ nanocrystals is observed when comparing to Fe_3O_4 nanocrystals, and it also shows that the smaller the size is, the bigger the difference in M_S.

The superparamagnetic properties of $CoFe_2O_4$ and Fe_3O_4 nanocrystals clearly show that the magnetocrystalline anisotropy energy plays a decisive role. According to Stoner-Wohlfarth single domain theory[26], the magnetocrystalline anisotropy energy (E_A) for non-interacting single domain nanocrystal is determined by:

$$E_A = KV \sin^2\theta \qquad (4.1)$$

where K is the magnetocrystalline anisotropy constant, V is the volume of nanocrystal, and θ is the angle between the ease axis of nanocrystal and the magnetization direction. The magnetocrystalline anisotropy energy services as a potential barrier to prevent the spin flipping from the blocking state to the superparamagnetic state. Generally, the magnetic moment can be agitated by thermal energy, k_BT with k_B as Boltzmann constant. The measure of E_A determines the temperature threshold at which the thermal activation can surpass the magnetic anisotropy energy barrier, and consequently the magnetic nanocrystals are in the superparamagnetic relaxation state. As expressed in equation (4.1), both the magnetocrystalline anisotropy constant (K) and the volume of nanocrystals are two key parameters on the determination of magnetocrystalline anisotropy energy. Judging from the higher blocking temperature presented by $CoFe_2O_4$ nanocrystals in Figure 4.4, the magnetic anisotropy energy should be much higher in $CoFe_2O_4$

nanocrystals compared to the same sized Fe_3O_4 nanocrystals. Given the same volume, the higher magnetic anisotropy energy suggests that the magnetocrystalline anisotropy constant is larger in $CoFe_2O_4$ nanocrystals. Since the magnetic properties of materials are fundamentally originated from the electron spin-spin coupling (S-S coupling) and spin-orbital coupling (L-S coupling). As a result, the magnitude of magnetic anisotropy energy is directly associated with the strength of such quantum couplings, in particularly the spin-orbital coupling. Therefore, the correlation between the quantum coupling and the superparamagnetic properties of nanocrystals through the variation of magnetic anisotropy energy can be established.

For magnetic metal oxide with cubic spinel structure, metal cations occupy one of the two types of vacancies formed by face-center-cubic (*fcc*) close packing of oxygen anions, which are referred to tetrahedral (A) sites and octahedral (B) sites. The antiparallel magnetic interaction between tetrahedral sites and octahedral sites in spinel ferrite is the strongest magnetic coupling, leading to an antiferromagnetic ordering. Since both $CoFe_2O_4$ and Fe_3O_4 are typical invert spinel ferrites[25], where Fe^{3+} cations occupy in tetrahedral and octahedral sites and Co^{2+} or Fe^{2+} cations being only in octahedral sites. According to the ligand field theory[27], since the presence of 5 unpaired electrons in the electron configuration $3d^5$ brings about the ground term as ^5S for Fe^{3+} cations, no L-S coupling occurs because of none orbital angular momentum (L=0). Thus, the difference in magnetic anisotropy comes solely from the Co^{2+} and Fe^{2+} cations in octahedral sites due to the different strength of L-S coupling between Co^{2+} and Fe^{2+} cations. The ground term ^4F is the result of the $3d^7$ electronic configuration of Co^{2+} cation with 3 unpaired electrons in a weak spherical ligand field. After further splitting in

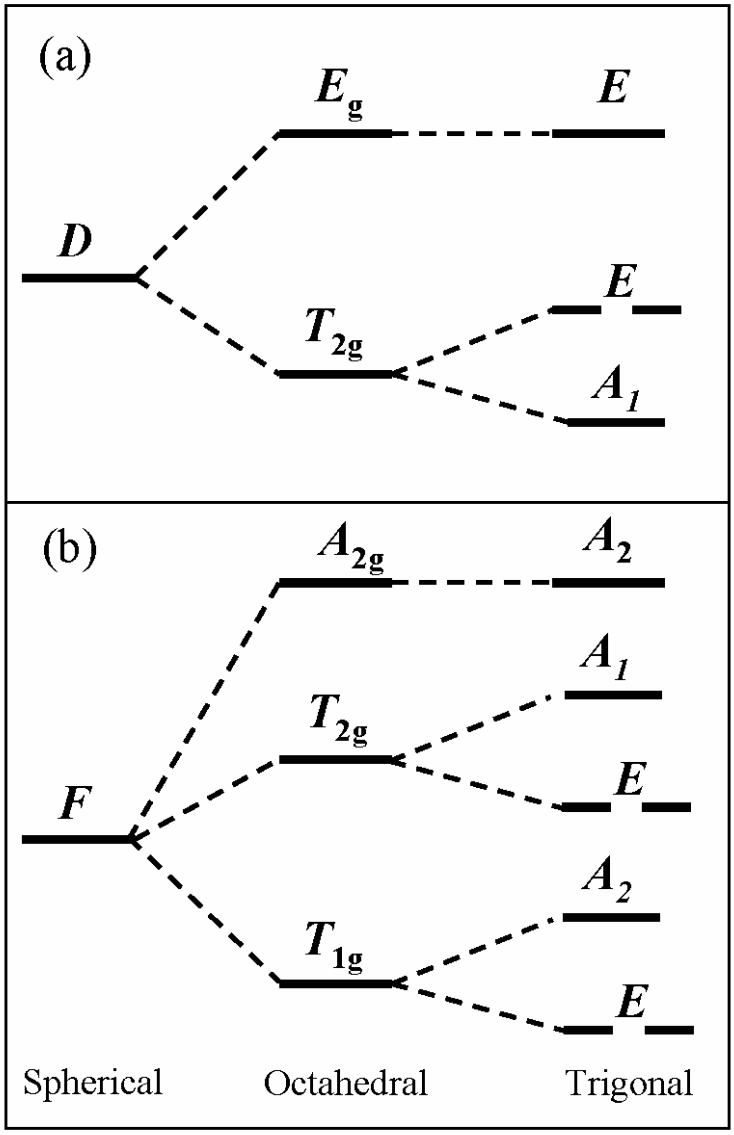

Figure 4.9 The schematic diagrams in (a) and (b) are the splitting of energy levels of D and F terms in spherical, octahedral and trigonal ligand fields, respectively.

octahedral ligand field, a triplet T_{1g} becomes the lowest state. Similarly, for Fe^{2+} cation, the ground sate of ^5D splits into the lowest state T_{2g} in octahedral field. The fact that a local symmetry distortion varies the octahedral field into the trigonal one introduces a discrepant effect on the further splitting of triplet states for Co^{2+} and Fe^{2+} cations[28,29]. As shown in Figure 4.9, a splitting on the triplet T_{1g} of Co^{2+} in trigonal ligand field leaves the doublet E as the lowest ground state. Consequently, the orbital angular momentum can not be completely quenched for Co^{2+} cations, leading to a strong L-S coupling in $CoFe_2O_4$. On the contrary, even though the triplet T_{2g} of Fe^{2+} can still be degenerated into singlet and doublet, it is the singlet that is the lowest ground state. As a result, there is no L-S coupling in magnetite due to the completely quenched orbital angular momentum of Fe^{2+} cation in trigonal ligand field. Therefore, the interaction between spin and orbital angular momentum of Co^{2+} cations in $CoFe_2O_4$ nanocrystals is significantly stronger than that of Fe^{2+} cations in Fe_3O_4 nanocrystals. As a result, a larger value of the magnetocrystalline anisotropy energy for $CoFe_2O_4$ nanocrystals gives rise to a higher blocking temperature compared to the same sized Fe_3O_4 nanocrystals.

A similar argument is also valid for a larger coercivity of $CoFe_2O_4$ nanocrystals observed in field dependent magnetization measurements shown in Figure 4.6. The coercivity from Stoner-Wohlfarth theory for single domain nanoparticle is determined by the magnetocrystalline anisotropy constant (K) and saturation magnetization (M_S), and can be expressed as[26]

$$H_C = 2K/(\mu_0 M_S) \qquad (4.2)$$

where μ_0 is the universal constant of permeability in free space. Thus, a weaker spin-orbital coupling of Fe^{2+} cations in magnetite gives rise to smaller magnetocrystalline anisotropy and consequently the smaller coercivity of Fe_3O_4 nanocrystals. On the same basis, the larger coercivity of $CoFe_2O_4$ can be attributed to the stronger spin-orbital coupling from Co^{2+} cations in cobalt ferrite. In addition, the increase of coercivity in both $CoFe_2O_4$ and Fe_3O_4 nanocrystals with increasing sizes is mainly due to the increase in magnetic anisotropy since the applied magnetic field at given temperature should be able to overcome the energy barrier and reverse the magnetization orientation.

The variation of magnetization as sizes is of great importance for the magnetic nanocrystals in biomedical applications, due to the fact that a smaller size with a larger saturation magnetization is always a desirable magnetic parameter in clinical applications of magnetic nanocrystals. However, as shown in Figure 4.6, it clearly shows that a faster reduction of saturation magnetization as the size of Fe_3O_4 nanocrystals decreases, whereas, for $CoFe_2O_4$ nanocrystals, although the size decreases, the saturation magnetization doesn't loss too much. Such results may indicate that $CoFe_2O_4$ nanocrystals would be a better candidate as the magnetic carriers, because a smaller magnetic nanocrystal with a relative larger saturation magnetization may extend the critical circulation time.

4.4 Conclusions

The systematic characterization and comparison of the superparamagnetic properties of cobalt ferrite and magnetite nanocrystals with similar sizes have been studied. Compared to Fe_3O_4 nanocrystals, the same sized $CoFe_2O_4$ nanocrystals possesses

at least 100 degree higher in blocking temperature and as a minimum as 50 times larger of coercivity as well as an average 10 emu/g enhancement on saturation magnetization. A dramatically stronger electron spin-orbital coupling on Co^{2+} lattice sites leads to such a distinctly greater magnetic anisotropy giving rise to a great discrepancy on magnetic properties between these two spinel ferrites nanocrystals. The comparative studies elucidate that it is possible to introduce the different metal cations having various strength of L-S magnetic coupling in spinel matrix to precisely adjust the magnetic anisotropy, a key factor in understanding and controlling the superparamagnetic properties of magnetic nanocrystals. Certainly, it should also facilitate the technological applications of cobalt spinel ferrite and magnetite nanocrystals, specifically in biomedical applications such as magnetic cell sorting and / or DNA separation and the magnetic carriers for site-specific drug delivery.

4.5 References

(1) Awschalom, D. D.; DiVincenzo, D. P. *Physics Today* **1995**, *48*, 43.

(2) Leslie-Pelecky, D. L.; Rieke, R. D. *Chem. Mater.* **1996**, *8*, 1770.

(3) Awschalom, D. D.; Kawakami, R. K. *Nature* **2000**, *408*, 923.

(4) Sun, S.; Murray, C. B.; Weller, D.; Folks, L.; Moser, A. *Science* **2000**, *287*, 1989.

(5) Puntes, V. F.; Krishnan, K. M.; Alivisatos, A. P. *Science* **2001**, *291*, 2115.

(6) Dumestre, F.; Chaudret, B.; Amiens, C.; Renaud, P.; Fejes, P. *Science* **2004**, *303*, 821.

(7) Weller, D.; Moser, A. *IEEE Trans. Magn.* **1999**, *35*, 4423.

(8) Weller, D.; Doerner, M. F. *Annu. Rev. Mater. Sci.* **2000**, *30*, 611.

(9) Olsvik, O.; Popovic, T.; Skjerve, E.; Cudjoe, K. S.; Hornes, E.; Ugelstad, J.; Uhlen, M. *Clinical microbiology reviews* **1994**, *7*, 43.

(10) Haukanes, B. I.; Kvam, C. *Nature Biotechnology* **1993**, *11*, 60.

(11) Uhlen, M. *Nature* **1989**, *340*, 733.

(12) Berry, C. C.; Curtis, A. S. G. *J. Phys. D: Appl. Phys.* **2003**, *36*, R198.

(13) Mitchell, D. G. *J. Magn. Reson. Imaging* **1997**, *7*, 1.

(14) Weissleder, R.; Bogdanov, A.; Neuwelt, E. A.; Papisov, M. *Advanced Drug Delivery Reviews* **1995**, *16*, 321.

(15) Chen, J. P.; Sorensen, C. M.; Klabunde, K. J.; Hadjipanayis, G. C.; Devlin, E.; Kostikas, A. *Phys. Rev. B* **1996**, *54*, 9288.

(16) Pileni, M. P.; Moumen, N.; Hochepied, J. F.; Bonville, P.; Veillet, P. *J. Phys. IV* **1997**, *7*, C1/505.

(17) Liu, C.; Zou, B.; Rondinone, A. J.; Zhang, Z. J. *J. Phys. Chem. B* **2000**, *104*, 1141.

(18) Liu, C.; Zhang, Z. J. *Chem. Mater.* **2001**, *13*, 2092.

(19) Hyeon, T.; Chung, Y.; Park, J.; Lee, S. S.; Kim, Y.-W.; Park, B. H. *J. Phys. Chem. B* **2002**, *106*, 6831.

(20) Choi, E. J.; Ahn, Y.; Kim, S.; An, D. H.; Kang, K. U.; Lee, B.-G.; Baek, K. S.; Oak, H. N. *J. Magn. Magn. Mater.* **2003**, *262*, L198.

(21) Yu, W. W.; Falkner, J. C.; Yavuz, C. T.; Colvin, V. L. *Chem. Commun.* **2004**, 2306.

(22) Liu, C.; Zou, B.; Rondinone, A. J.; Zhang, Z. J. *J. Am. Chem. Soc.* **2000**, *122*, 6263.

(23) Sun, S.; Zeng, H. *J. Am. Chem. Soc.* **2002**, *124*, 8204.

(24) Song, Q.; Zhang, Z. J. *J. Am. Chem. Soc.* **2004**, *126*, 6164.

(25) Buschow, K. H. J.; Ed. *Handbook of Magnetic Materials: Volume 8*; Elsevier: Amsterdam, 1995. Chapter 3.

(26) Stoner, E. C.; Wohlfarth, E. P. *Trans. Roy. Soc.* **1948**, *A240*, 599.

(27) Figgis, B. N.; Hitchman, M. A. *Ligand Field Theory and Its Applications*; Wiley – VCH: New York, 2000.

(28) Wadas, R. *Magnetism in Spinels, Garnets, and Perovskites*, 1974. p162.

(29) Wohlfarth, E. P.; Editor *Ferromagnetic Materials: A Handbook on the Properties of Magnetically Ordered Substances, Vol. 3*, 1982. p202.

CHAPTER 5

SYNTHESIS AND SUPERPARAMAGNETIC STUDIES OF BIMAGNETIC NANOCRYSTALS WITH CORE SHELL ARCHITECTURE

Abstract

Bimagnetic spinel ferrites core-shell nanocrystals comprising magnetic hard ($CoFe_2O_4$) and soft phases ($MnFe_2O_4$ or Fe_3O_4) were synthesized by a combination of non-hydrolysis of coordination compounds in high temperature organic solvent with a seed-mediated growth process. Core-shell nanocrystals characterized by conventional TEM and high resolution TEM (HRTEM) clearly show that the shell is epitaxially coated on core forming a single nanocrystal. In addition, the chemical element mapping analyzed by energy dispersive X-ray spectroscopy (EDS) undoubtedly confirms the core-shell architecture of as-synthesized magnetic nanocrystals. Moreover, the magnetic studies show that the magnetic properties are linearly correlated to the volume fraction of magnetic soft phase because of the effective exchange coupling between core and shell as the shell thickness varying from 0.5 nm to 3 nm. However, an unexpected enhancement on coercivity, specifically at the initially epitaxial overcoating of soft magnetic spinel ferrites upon hard phase $CoFe_2O_4$ core may be related to the surface effect. The fabrication of such bimagnetic nanocrystals with core-shell architecture represents a rational design approach to fundamental understanding and controlling magnetic properties in a wide variety of technical applications.

5.1 Introduction

Parallel with extensive research on colloidal nanocrystals performed in a wide range of areas due to their novel size and shape dependent chemical and physical properties[1-10], recent research interests on nanocrystals with core shell architecture have been intensified[11-21]. In general, core shell type nanocrystals pave the way for a rational design, fabrication and functionalization of nanomaterials in order to satisfy the desirable property requirements in numerous practical applications. For instance, the creation of core/shell CdSe/ZnS nanocrystals has resulted in an ultrasensitive biological label with much brighter, better photostability and narrower spectral linewidth character [22]. By taking advantage of both the position and intensity of silver surface plasmon band and the stability as well as surface chemistry of gold, Mirkin and co-workers[23] have demonstrated that a fabrication of Ag/Au core/shell nanoparticles can be a robust detection system for various biomolecules such as DNA and proteins. A recent report by Klimov and co-workers[24] also demonstrated that the formation of a semiconductor CdSe shell on a magnetic Co core can lead to a bifunctional nanocomposite with both optical label and magnetic manipulation capability. Moreover, core shell type nanocrystals also provide an effective approach to understanding the fundamental issues in nanoscience. It is well known that surface effect originated from increasing surface to volume ratio is more often one of predominate factors in determination of nanomaterial properties. Nanocrystals with core shell architecture may be a good system in addressing such surface effect. Given a specific core, it is feasible to systematically investigate the surface effect upon the intrinsic properties of core part by precise selection and controlled introduction of shell part, either organic or inorganic. By overcoated a series of organic

molecules with modulated crystal field splitting energy (CFSE) upon different sized $MnFe_2O_4$ spinel ferrite nanoparticles, Zhang and co-workers[25] have systematically studied the surface effect upon magnetism and the results clearly elucidated that a ligand with larger CFSE resulted in a weaker spin-orbital coupling, consequently, a smaller coercivity of nanoparticles due to the reduction of surface anisotropy. Finally, it is the interaction between core and shell that makes core shell structured nanocrystals unique for tailoring the fundamental properties and functions that are constrained in single component nanoscale materials. The studies on ferromagnetic Co nanoparticles coated with an antiferromagnetic shell of CoO not only has given rise to the discovery of a new type of anisotropy, known as exchange anisotropy[26,27], which is a shift of the hysteresis loop along the field axis, but also such magnetic interaction between an antiferromagnetic material and a ferromagnetic material resulted in a considerable improved thermal stability of magnetic nanoparticles to overcome the 'superparamagnetic limit', a critical issue on using magnetic nanoparticles in recording media[28]. Nevertheless, the fabrication of nanomaterials with core shell architecture is an effective strategy to understand, optimize and enhance material optical, electronic, magnetic, catalytic, structural, and surface properties in a reliable and predictable manner on both basic science and a broad range of technical applications.

Various bimagnetic nanocrystals with core shell architecture have been synthesized by different methods in several groups. By deliberately formed a passivating oxide shell, core shell structured nanoparticles of α-Fe @ iron oxides or Co @ CoO have been prepared by evaporation-deposition technique[29,30]. Similarly, the reduction of ferro salts with $NaBH_4$ in reverse micelle followed by surface oxidation in air has also been used to

form α-Fe @ iron oxide and α-Fe @ $Fe_{1-x}B_x$ core shell structured nanoparticles[31,32]. However, based on these synthetic methods, the control of shell thickness and / or sequential variation of chemical compositions of shell are still limited successful. With recent advance on synthesis of colloidal nanocrystals, it has been demonstrated that high quality magnetic nanocrystals can be produced with both size and shape control capability[33-45]. However, the synthesis of bimagnetic core shell typed nanocrystals such as ferrimagnetic – ferrimagnetic structured core-shell nanocrystals is still lack. Moreover, recent studies on magnetic properties of nanostructured materials have mainly focused on chemical composition, size and shape dependency. However, understanding the magnetic properties of core-shell structured nanocrystals is also of fundamental interest and the fabrication of core shell nanocrystals have recently been demonstrated a rational approach to overcoming certain technical obstacles such as magnetic phase transition of FePt nanocrystals in high-density data storage[46] and the improvement of energy product in permanent magnets[47]. Finally, it is well known that spinel ferrite is a type of ferrimagnetic material and there are both magnetic hard phase such as $CoFe_2O_4$ and magnetic soft phases such as Fe_3O_4 and $MnFe_2O_4$ in spinel ferrite materials family. As a result, spinel ferrite can be an ideal experimental system for addressing fundamental issues such as interfacial exchange coupling and surface effect upon magnetic properties through the fabrication of bimagnetic nanocrystals with core shell architecture. Due to the same crystal structure and nearly equal lattice constants, the lattice mismatch among different spinel ferrites is almost negligible. Therefore, it is feasible to epitaxially create various overcoating shell layer upon different core part, instead of the shell formed by tiny polycrystalline as observed in some previous studies[48]. In this chapter, the synthesis

and magnetic properties studies on different bimagnetic spinel ferrites core shell structured nanocrystals are presented. Specifically, the correlations of the shell thickness and different volume ratio of magnetic soft phases with the blocking temperature and coercivity are discussed.

5.2 Experimental Section

5.2.1 Synthesis of Spinel Ferrite Core-Shell Nanocrystals

The detailed synthetic procedures for spinel ferrites nanocrystals have been reported[41,44,45] and were employed to synthesize different types of core-shell structured nanocrystals as followed. First, in a solution containing 30 mL phenyl ether, 10 mmol 1,2-hexadecanediol, 6 mmol oleic acid and 6 mmol oleylamine, 6 nm $CoFe_2O_4$, or Fe_3O_4 nanocrystals were made by slowly heating up a mixture of 1 mmol $Co(acac)_2$ and 2 mmol $Fe(acac)_3$ or solely 2 mmol $Fe(acac)_3$ to 259 ± 2 °C for 45 min, respectively. As for $MnFe_2O_4$ nanocrystals, the reaction temperature was raised to 295 ± 5°C by changing the solvent from phenyl ether to benzyl ether and kept other reagents the same. The epitaxial growth of shell on core was simply repeated the forgoing procedure. For example, to make 6 nm $CoFe_2O_4$ core with 1 nm $MnFe_2O_4$ shell, 60 mg of $CoFe_2O_4$ nanocrystals was added into a mixture of 0.25 mmol $Mn(acac)_2$, 0.5 mmol $Fe(acac)_3$, 5 mmol 1-octadecanol, 2 mmol oleic acid and oleylamine in 30 mL benzyl ether. The solution was then slowly heated up to reflux under N_2 gas protection for 30 min. After the solution was cooled to room temperature, the black precipitates were collected by addition of ethanol. The final black 6 nm $CoFe_2O_4$ core with 1 nm $MnFe_2O_4$ shell ($CoFe_2O_4$@$MnFe_2O_4$)

nanocrystals were dispersed in hexane and re-precipitated by acetone and collected by centrifugation. Similarly, other core-shell spinel ferrites nanocrystals such as $CoFe_2O_4$@Fe_3O_4, $MnFe_2O_4$@$CoFe_2O_4$ and Fe_3O_4@$CoFe_2O_4$ were synthesized in the same procedure. In addition, the chemically doped 6.5 nm $Co_{1-x}Mn_xFe_2O_4$ nanocrystals with the percentage of Mn (x) ranging from 0.02 to 0.7 have also been prepared by such procedure.

5.2.2 Transmission Electron Microscopy Analysis

Low magnification TEM studies were performed using JEOL 100C at 100 kV. High-resolution TEM (HRTEM) studies and energy dispersive X-ray spectroscopy (EDS) microanalysis were carried out on JEOL 4000EX at 400 kV and Hitachi HF-2000 Field Emission TEM at 200 kV, respectively. The samples for TEM analysis were prepared by dispersed a drop of nanocrystals solution on holey carbon-coated copper grids.

5.2.3 Magnetic Characterization

Both temperature and field dependent magnetization measurements were carried out on superconducting quantum interference device (SQUID) magnetometer (Quantum Design MPMS-5S) with a magnetic field up to ± 5 Tesla (T) and temperature ranging from 5 K to 400 K. Susceptibility measurements were conducted from a temperature range of 5 to 400 K in an applied magnetic field of 100 G. Hysteresis measurements were carried out at 5 K under an applied field up to ± 5 T. All samples for field dependent hysteresis measurements were prepared by fully dispersed an appropriate amount of dry

powder nanocrystals in eicosane ($C_{20}H_{42}$, Aldrich, 99%) in order to minimize the effect of magnetic interparticle interactions.

5.3 Results and Discussion

By purposely selection and combination of magnetic hard phase and soft phase from cubic spinel ferrites, four different types of core shell structured bimagnetic nanocrystals $CoFe_2O_4$@$MnFe_2O_4$, $MnFe_2O_4$@$CoFe_2O_4$, $CoFe_2O_4$@Fe_3O_4 and Fe_3O_4@$CoFe_2O_4$ have been synthesized in a non-hydrolysis along with a seed-mediated growth process. The sizes of cores ranged from 5.5 nm to 6.5 nm. The shell thicknesses were controlled by adjusting the molar ratio of seeds to the amount of precursors and varied from 0.5 nm to 3- nm in thickness as determined from TEM images shown in Figure 5.1 to 5.4 for $MnFe_2O_4$@$CoFe_2O_4$, $CoFe_2O_4$@$MnFe_2O_4$, $CoFe_2O_4$@Fe_3O_4 and Fe_3O_4@$CoFe_2O_4$, respectively. The typical size distributions for all these as-synthesized core-shell nanocrystals are less than 7%. From high-resolution TEM (HRTEM) studies as displayed in Figure 5.1F, 5.2F, 5.3F and 5.4F, first, it can be clearly seen that the shell layers were epitaxially overcoated upon the core parts forming a single nanocrystal, because both core and shell belong to the same cubic spinel crystal structure and their lattice constants are so close to each other that the lattice mismatch can be negligible. Additionally, since the numbers of electrons for elemental Mn, Fe and Co are next to each other, HRTEM images showed a weak contrast between core and shell.

To further verify the bimagnetic nanocrystals are truly core shell typed structure, energy dispersive X-ray spectroscopy (EDS) microanalysis has been performed by positioning a fine electron probe (~ 2 - 3 nm) at different parts of large nanocrystals.

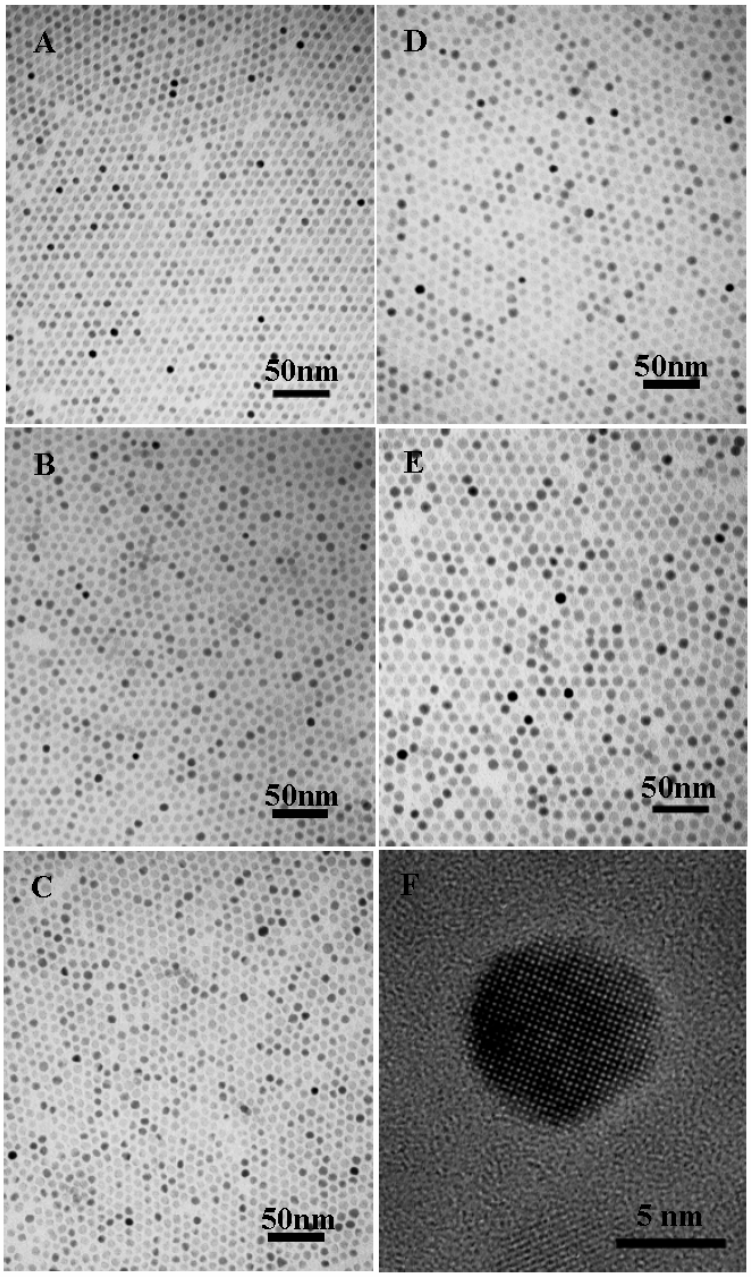

Figure 5.1 TEM micrographs for $MnFe_2O_4$@$CoFe_2O_4$ core shell nanocrystals. (A) 6 nm pure core $MnFe_2O_4$ nanocrystals. The sizes for various core shell nanocrystals are in (B) 7.5 nm, (C) 8 nm, (D) 10 nm, (E) 11 nm, and (F) HRTEM image of 8 nm core shell nanocrystal.

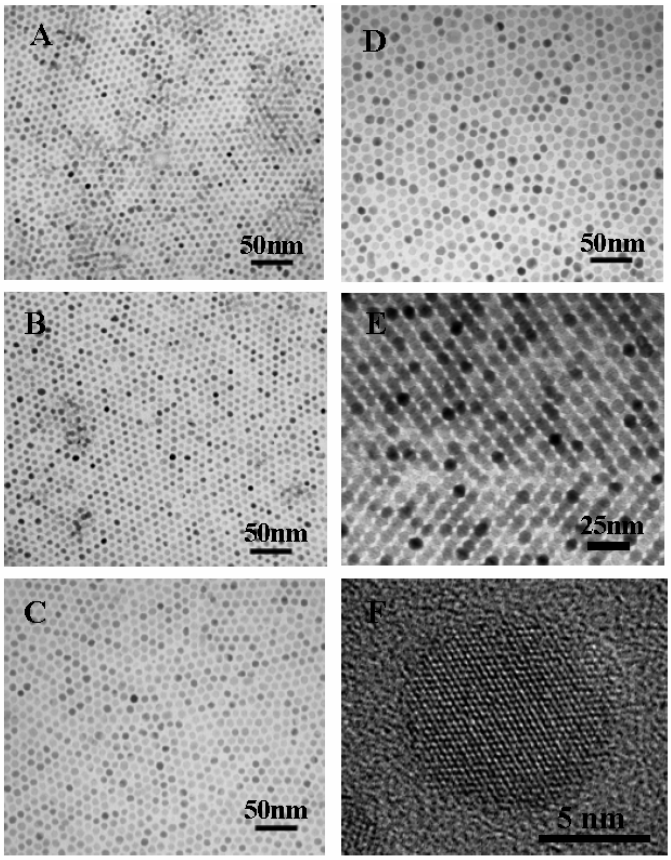

Figure 5.2 TEM micrographs for $CoFe_2O_4$@ $MnFe_2O_4$ core shell nanocrystals. (A) 6.5 nm pure core $CoFe_2O_4$ nanocrystals. The sizes for various core shell nanocrystals are in (B) 7.5 nm, (C) 8.5 nm, (D) 10.5 nm, (E) 12 nm, and (F) HRTEM image of 8.5 nm core shell nanocrystal.

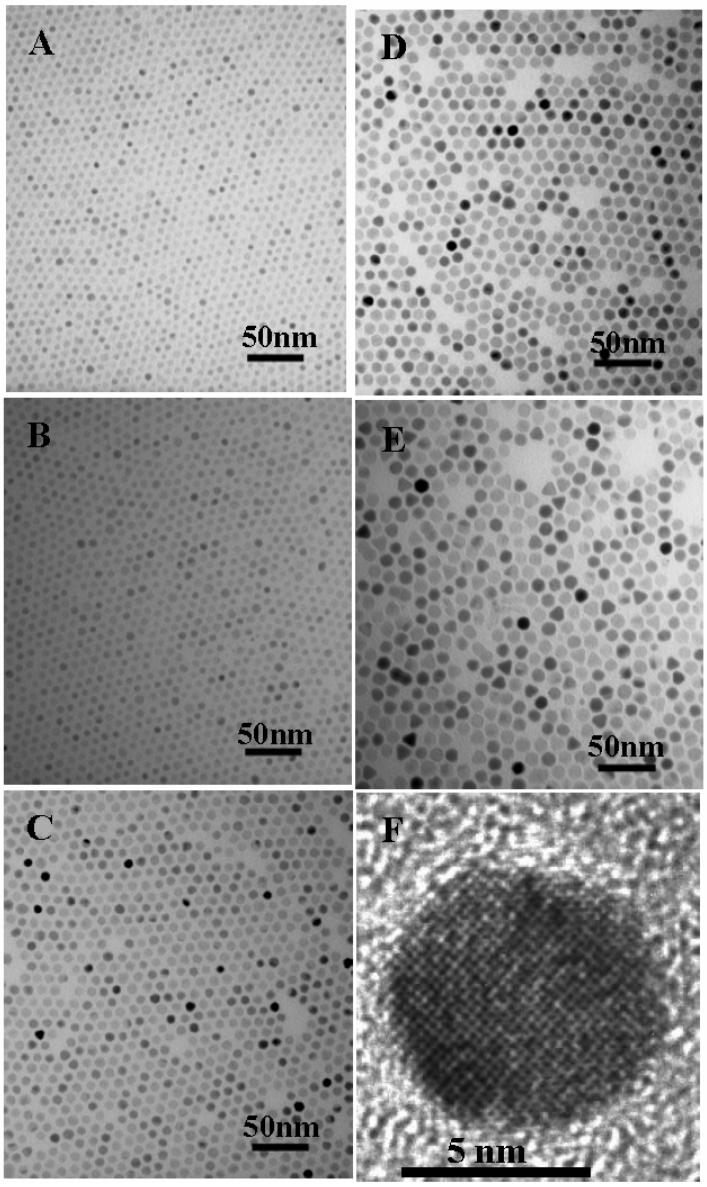

Figure 5.3 TEM micrographs for $CoFe_2O_4$@Fe_3O_4 core shell nanocrystals. (A) 5.5 nm pure core $CoFe_2O_4$ nanocrystals. The sizes for various core shell nanocrystals are in (B) 6.5 nm, (C) 7.5 nm, (D) 9.5 nm, (E) 11.5 nm, and (F) HRTEM image of 9.5 nm core shell nanocrystal.

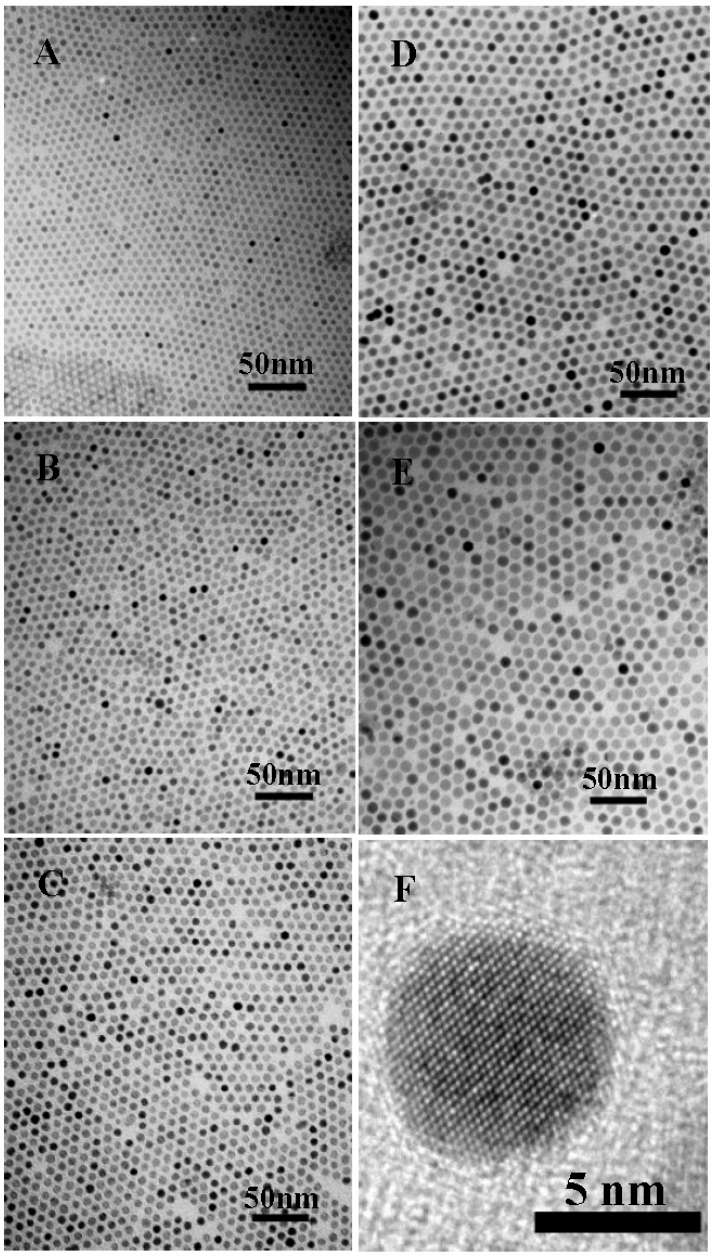

Figure 5.4 TEM micrographs for Fe_3O_4@$CoFe_2O_4$ core shell nanocrystals. (A) 5.5 nm pure core Fe_3O_4 nanocrystals. The total sizes for various core shell nanocrystals are in (B) 6.5 nm, (C) 7.5 nm, (D) 8 nm, (E) 10 nm, and (F) HRTEM image of 8 nm core shell nanocrystal.

Figure 5.5 A and B showed two different EDS spectra for 6 nm $MnFe_2O_4$ core overcoated by 2 nm $CoFe_2O_4$ shell nanocrystals, which were measured by aligning electron probe either through center or edge part of core-shell structured nanocrystals, respectively. As the electron probe passed through the center of such nanocrystal, elements of Mn, Fe, and Co were detected by EDS in Figure 5.5A. In contrast, only elements of Fe and Co were identified when the electron beam was aligned at the edge of nanocrystal, although a negligibly weak signal of Mn was also acquired as indicated in dished circle. In case of 10 nm sized $CoFe_2O_4$ @ $MnFe_2O_4$ core shell nanocrystals as shown in Figure 5.6A and B, EDS results indicated that there were all elements of Mn, Fe and Co presented as electron probe passing through center, whereas no Co signal was detected if electron beam was on shell part as labeled by an arrow in Figure 5.6B. For $CoFe_2O_4$ @ Fe_3O_4 core shell samples, similar EDS results were also obtained from EDS spectra as illustrated in Figure 5.7A and B, respectively. Surely, such EDS studies unambiguously confirm that all of as-synthesized bimagnetic nanocrystals are indeed the core shell structured nanocrystals.

Figure 5.8, 5.9, 5.10 and 5.11 are the temperature dependency of susceptibility χ (T) for various bimagnetic spinel ferrite core shell structured nanocrystals. The magnetization variation as a function of temperature for all core shell bimagnetic nanocrystals shows the single phase magnetic behavior, where the transition from blocking state to superparamagnetic state seems not sensitive to whether hard magnetic material as the core and soft phase being shell or the reversed core shell architecture. The value of blocking temperature of $CoFe_2O_4$ @ $MnFe_2O_4$ and $CoFe_2O_4$ @ Fe_3O_4 core shell nanocrystals is plotted against the thickness of shell in Figure 5.12.

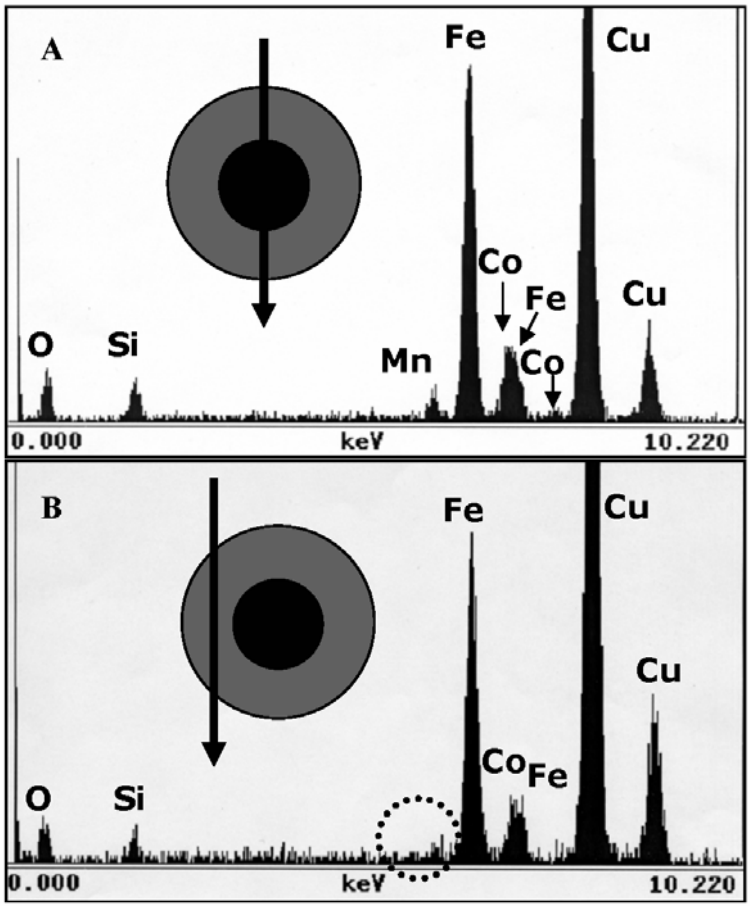

Figure 5.5 EDS spectra for $MnFe_2O_4$@$CoFe_2O_4$ core shell nanocrystals. The schematic in (A) and (B) indicates where the electron beam is aligned as the EDS spectra are acquired.

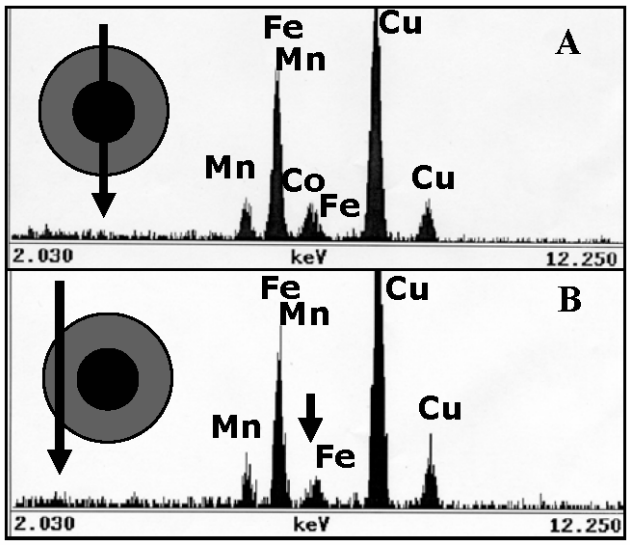

Figure 5.6 EDS spectra for $CoFe_2O_4$@$MnFe_2O_4$ core shell nanocrystals. The schematic in (A) and (B) indicates where the electron beam is aligned as the EDS spectra are acquired.

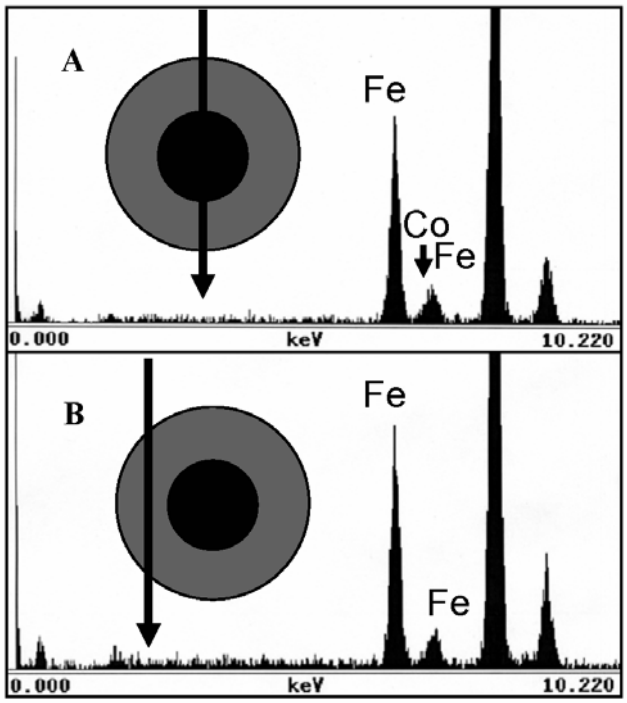

Figure 5.7 EDS spectra for $CoFe_2O_4@Fe_3O_4$ core shell nanocrystals. The schematic in (A) and (B) indicates where the electron beam is aligned as the EDS spectra are acquired.

When the magnetic hard $CoFe_2O_4$ nanocrystals serve as cores, regardless the shell consisting of either $MnFe_2O_4$ or Fe_3O_4, the blocking temperature (T_B) increases as long as the thickness of shell increases. As the core being such magnetic soft phase materials as $MnFe_2O_4$ or Fe_3O_4 nanocrystals and the shell composed of hard phase $CoFe_2O_4$ as shown in Figure 5.13 for $MnFe_2O_4$ @ $CoFe_2O_4$ and Fe_3O_4 @ $CoFe_2O_4$ core-shell nanocrystals, similar trends of blocking temperature as a function of the shell thickness, which is the thicker the shell, the higher the blocking temperature, are remained. The magnitude of increase of blocking temperature, however, is relatively larger for hard phase shell overcoated upon soft core. Clearly, compared to the blocking temperature of pure core nanocrystals, a higher blocking temperature is observed for all bimagnetic nanocrystals with core shell architecture.

The measurements of the field dependence of magnetization for various bimagnetic spinel ferrite core shell structured nanocrystals are shown in Figure 5.14 to 5.17. Clearly, all hysteresis curves show a smooth magnetization reversal against magnetic field, indicating the same single phase magnetic character as that observed by susceptibility measurements. The variation of coercivity as a function of the thickness of shell falls into two contradictory trends. As shown in Figure 5.18, for $MnFe_2O_4$ @ $CoFe_2O_4$ and Fe_3O_4 @ $CoFe_2O_4$ core shell structured nanocrystals, the coercivity increases as the result of the increase of the thickness of shell. On the contrary, the coercivity deceases when the shell becomes thicker and thicker for the core shell structured $CoFe_2O_4$ @ $MnFe_2O_4$ and $CoFe_2O_4$ @ Fe_3O_4 nanocrystals in Figure 5.19. Interestingly, compared with pure $CoFe_2O_4$ core, it is unexpected to observe a strong enhancement of coercivity of core shell structured nanocrystals, in particular, at the initial overcoating of magnetic soft

phase either $MnFe_2O_4$ or Fe_3O_4 shell upon magnetic hard phase core $CoFe_2O_4$ nanocrystals, even though such shell is only 0.5 nm in thickness.

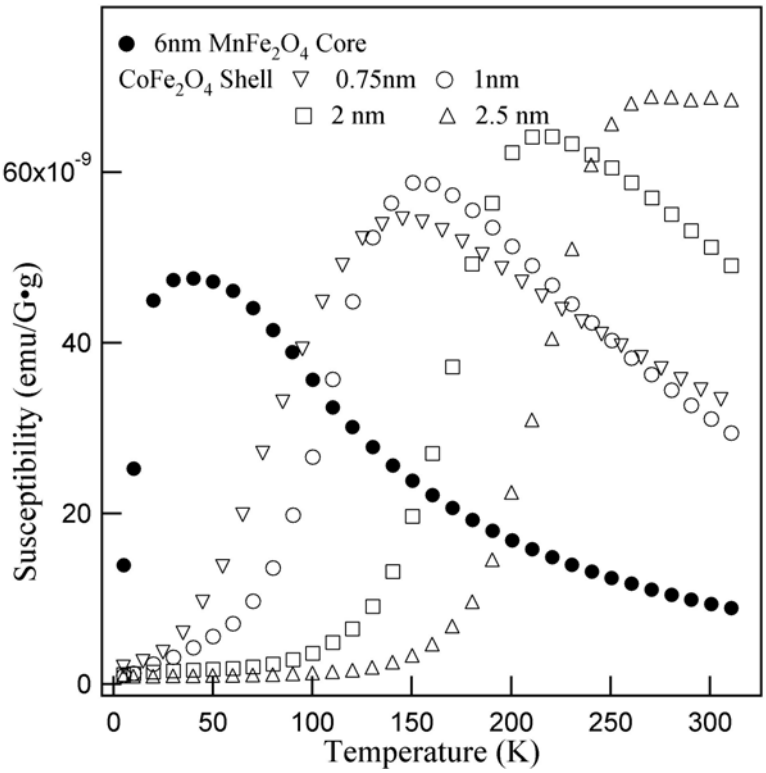

Figure 5.8 The temperature dependent susceptibility measurements for various core shell structured $MnFe_2O_4$@$CoFe_2O_4$ nanocrystals.

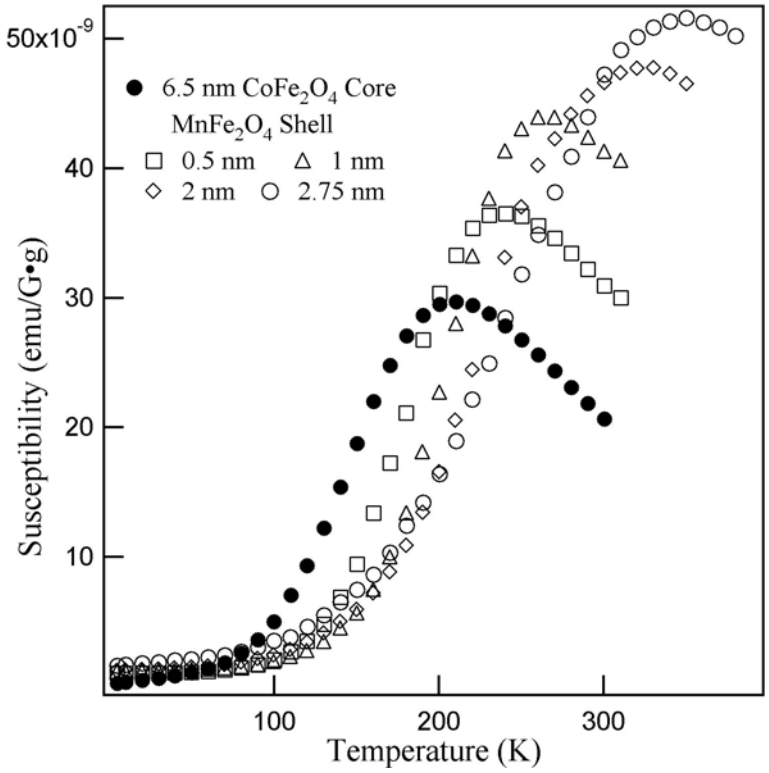

Figure 5.9 The temperature dependent susceptibility measurements for various core shell structured $CoFe_2O_4$@$MnFe_2O_4$ nanocrystals.

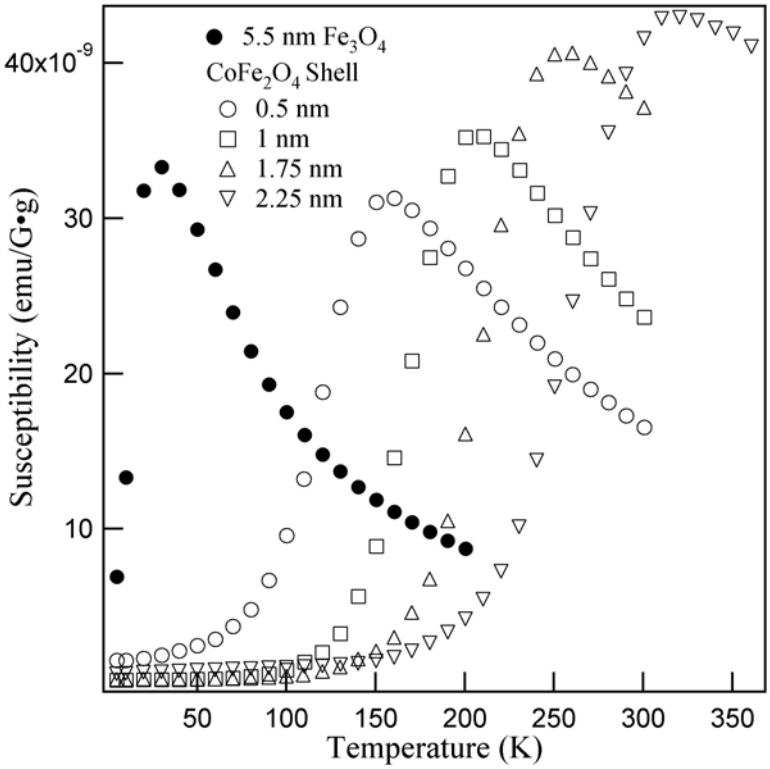

Figure 5.10 The temperature dependent susceptibility measurements for various core shell structured Fe_3O_4@$CoFe_2O_4$ nanocrystals.

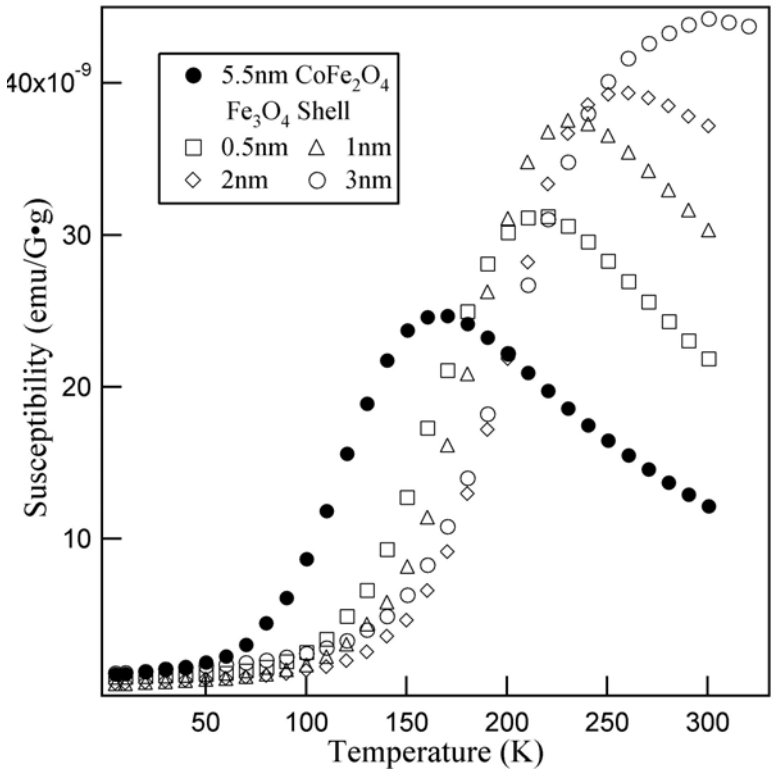

Figure 5.11 The temperature dependent susceptibility measurements for various core shell structured $CoFe_2O_4$@Fe_3O_4 nanocrystals.

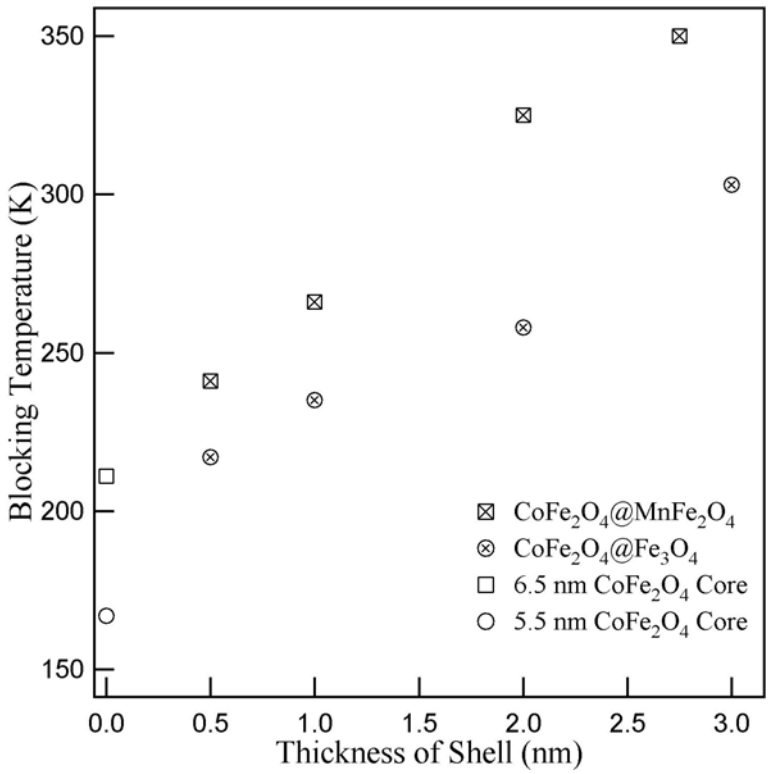

Figure 5.12 The value of blocking temperature as a function of the thickness of shell for $CoFe_2O_4$@$MnFe_2O_4$ and $CoFe_2O_4$@Fe_3O_4 core shell nanocrystals.

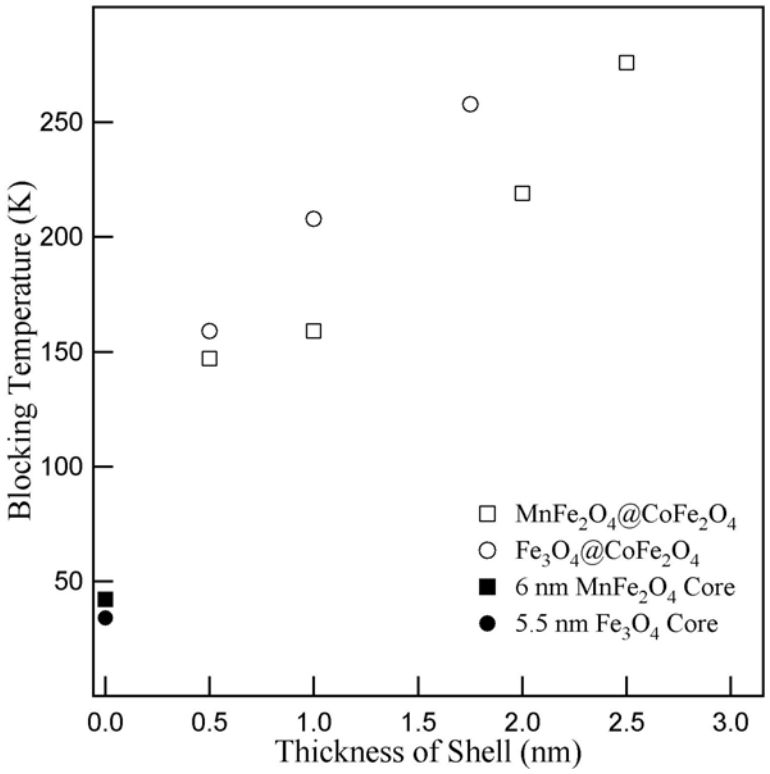

Figure 5.13 The value of blocking temperature as a function of the thickness of shell for $MnFe_2O_4@CoFe_2O_4$ and $Fe_3O_4@CoFe_2O_4$ core shell nanocrystals.

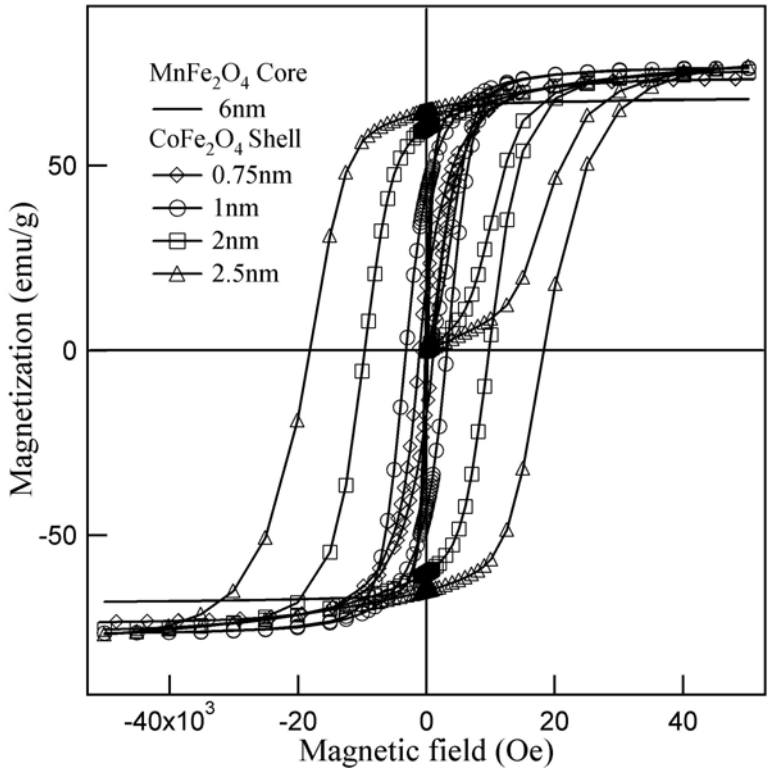

Figure 5.14 The field dependent magnetization measurements for different sized $MnFe_2O_4$@$CoFe_2O_4$ core shell nanocrystals.

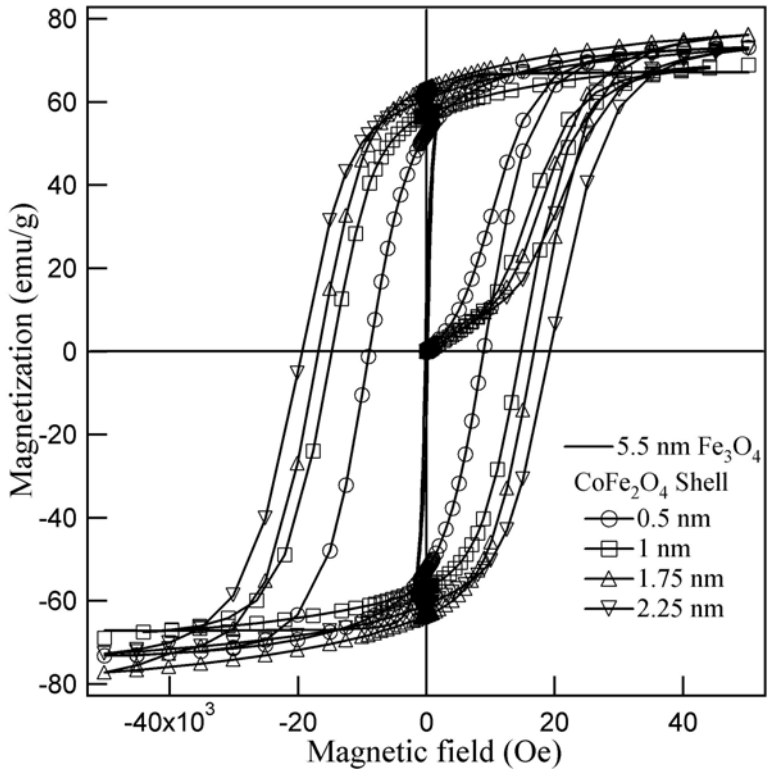

Figure 5.15 The field dependent magnetization measurements for different sized Fe_3O_4@$CoFe_2O_4$ core shell nanocrystals.

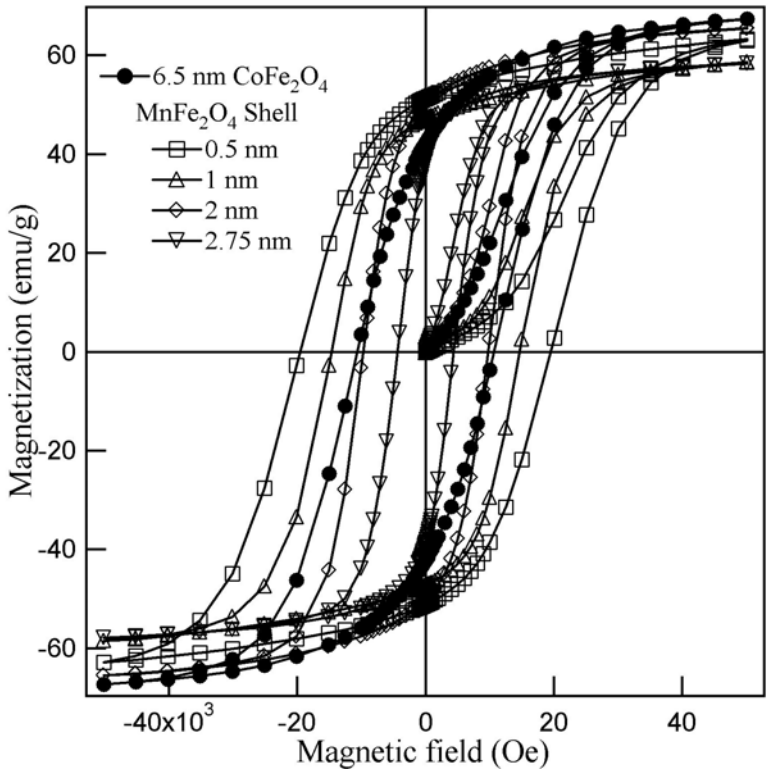

Figure 5.16 The field dependent magnetization measurements for different sized $CoFe_2O_4$@$MnFe_2O_4$ core shell nanocrystals.

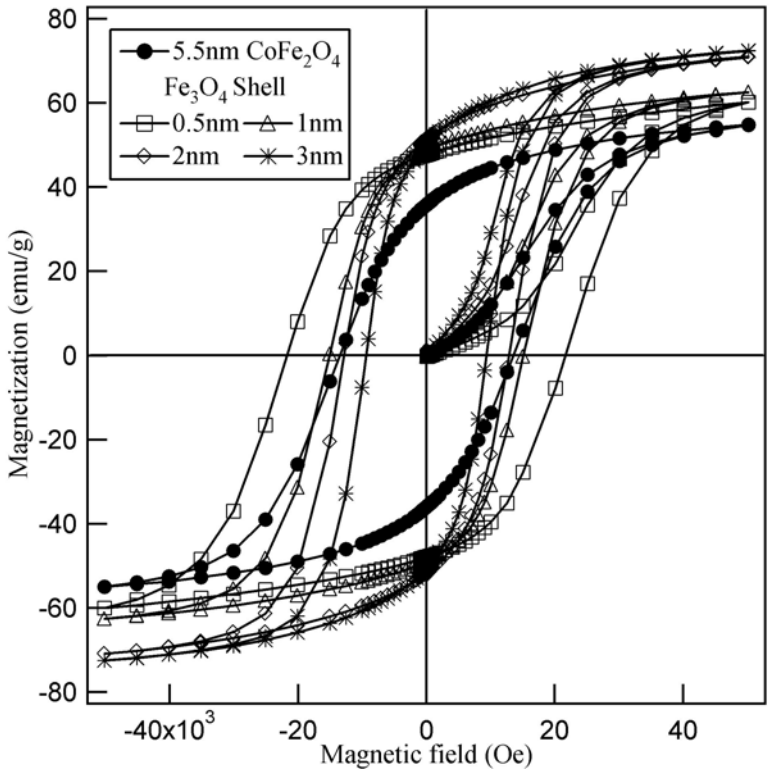

Figure 5.17 The field dependent magnetization measurements for different sized $CoFe_2O_4$@Fe_3O_4 core shell nanocrystals.

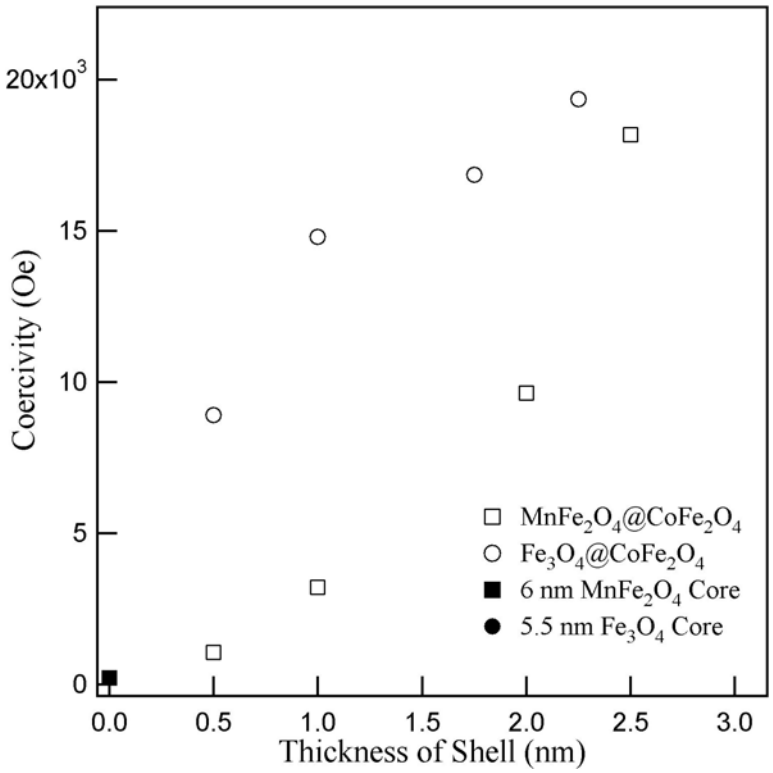

Figure 5.18 The coercivity variation as a function of the thickness of shell for $MnFe_2O_4@CoFe_2O_4$ and $Fe_3O_4@CoFe_2O_4$ core shell nanocrystals.

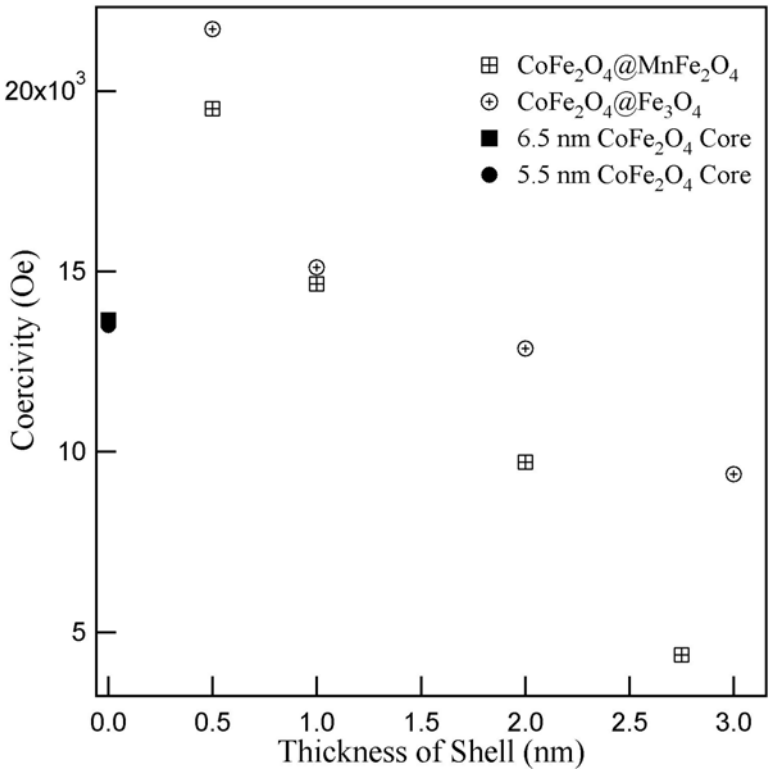

Figure 5.19 The coercivity variation as a function of the thickness of shell for $CoFe_2O_4$@$MnFe_2O_4$ and $CoFe_2O_4$@Fe_3O_4 core shell nanocrystals.

Toward fully understand the uniqueness of magnetic properties exclusively presented by bimagnetic nanocrystals with core-shell architecture rather than other structures. Several mechanical mixtures composing of pure hard phase $CoFe_2O_4$ and pure soft phase $MnFe_2O_4$ nanocrystals and the chemically doped $Co_{1-x}Mn_xFe_2O_4$ ($0.02 \leq x \leq 0.7$) nanocrystals have been prepared. The results of the temperature and field dependent magnetization measurements for the mechanical mixtures of $CoFe_2O_4$ and $MnFe_2O_4$ nanocrystals are in Figure 5.20 and 5.21, respectively. Clearly, both susceptibility curves and hysteresis loops show the characteristic two-phase magnetic behavior, which is incompatible with the single phase magnetic character as a result of the bimagnetic core shell structured nanocrystals. Such two-phase magnetic behavior is also consistent with no or weak exchange-coupled magnetic system consisting of both hard and soft phase as predicted theoretically by Kenller *et al*.[49]. In case of the same sized chemically doped $Co_{1-x}Mn_xFe_2O_4$ nanocrystals, TEM results are shown in Figure 5.22. The temperature dependent magnetization measurements for the molar percentage (x) of Mn varying from 0.02 to 0.7 are presented in Figure 5.23. The value of the blocking temperature as a function of the molar percentage of Mn is plotted in Figure 5.24. Surely, the trend of the blocking temperature of such chemically doped $Co_{1-x}Mn_xFe_2O_4$ nanocrystals is completely opposite to those of core shell structured nanocrystals (Figure 5.12 and 5.13), although the definite single phase magnetic behavior still can be seen from temperature dependent magnetization measurements. Equally, the diversity of coercivity variation between chemically doped $Co_{1-x}Mn_xFe_2O_4$ nanocrystals and core-shell structured bimagnetic nanocrystals can be drawn based on the results of hysteresis measurements and coercivity values in Figure 5.25 and 5.26, respectively. Thus, one can exclude the

possibilities that the fabrication and magnetic properties of bimagnetic core shell nanocrystals could originate from either a mechanical mixture of hard and soft phases or a chemically doped nanoparticulate system.

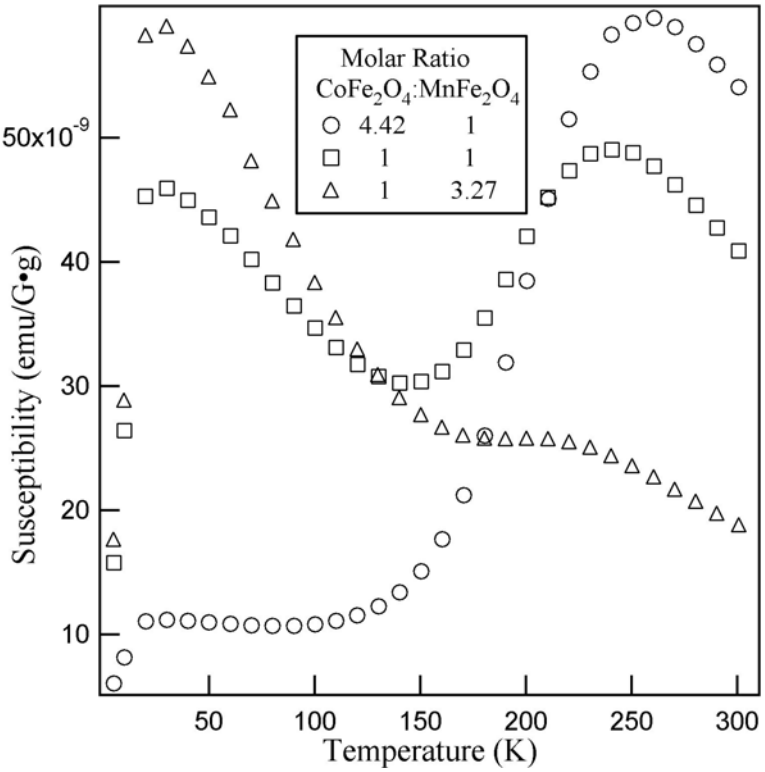

Figure 5.20 The susceptibility measurements of three mechanically mixtures consisting of pure $CoFe_2O_4$ and $MnFe_2O_4$ nanocrystals at different molar ratios.

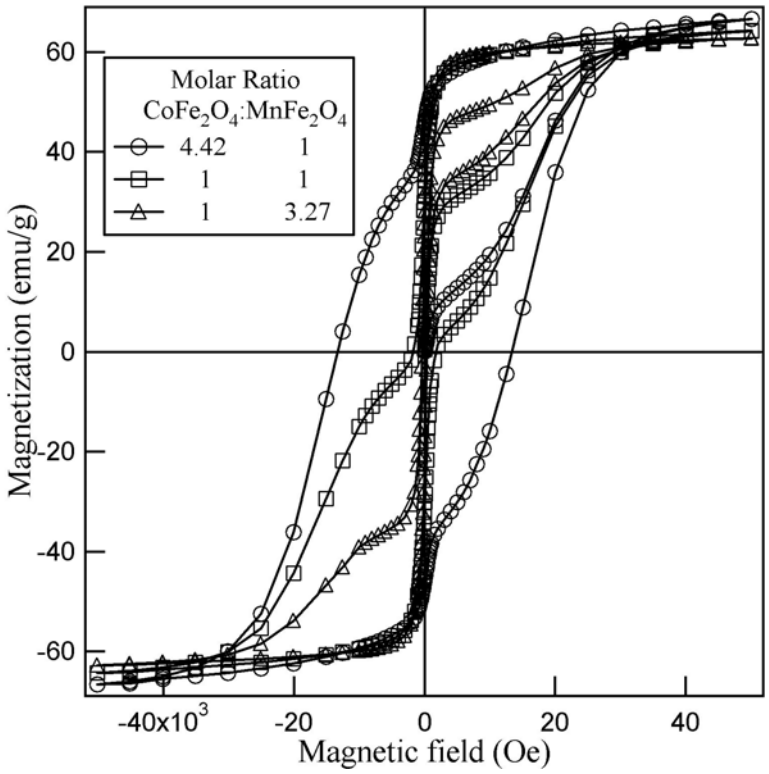

Figure 5.21 The hysteresis measurements of three mechanically mixtures consisting of pure $CoFe_2O_4$ and $MnFe_2O_4$ nanocrystals at different molar ratios.

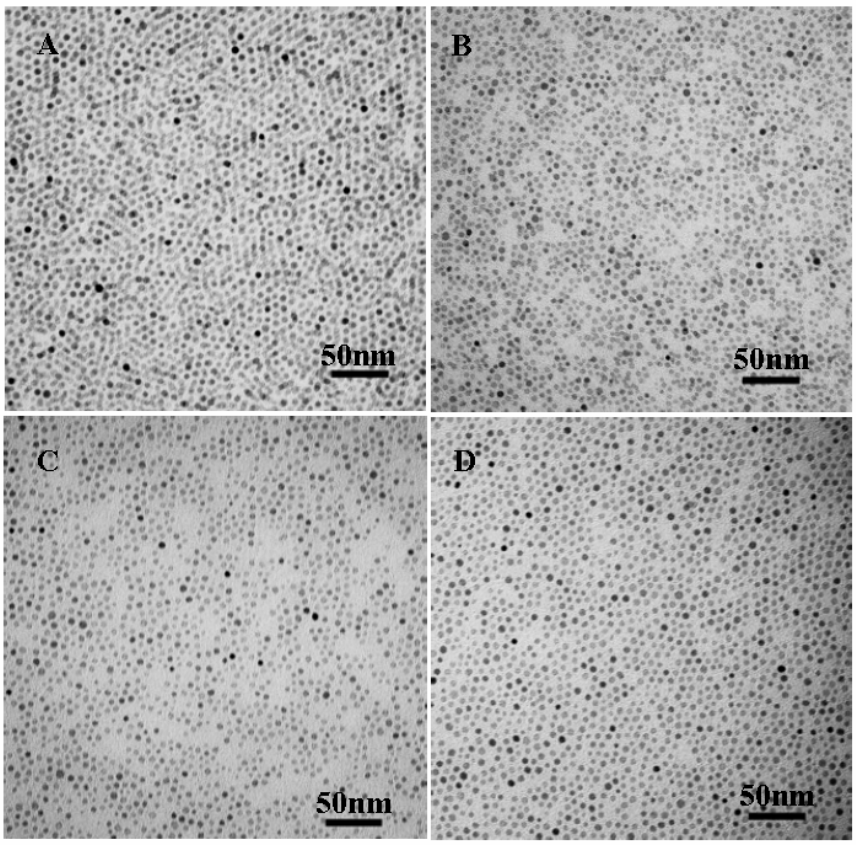

Figure 5.22 TEM micrographs for similar sized chemically doped $Co_{1-x}Mn_xFe_2O_4$ nanocrystals. The size is about 6.5 nm with a 10% size distribution.

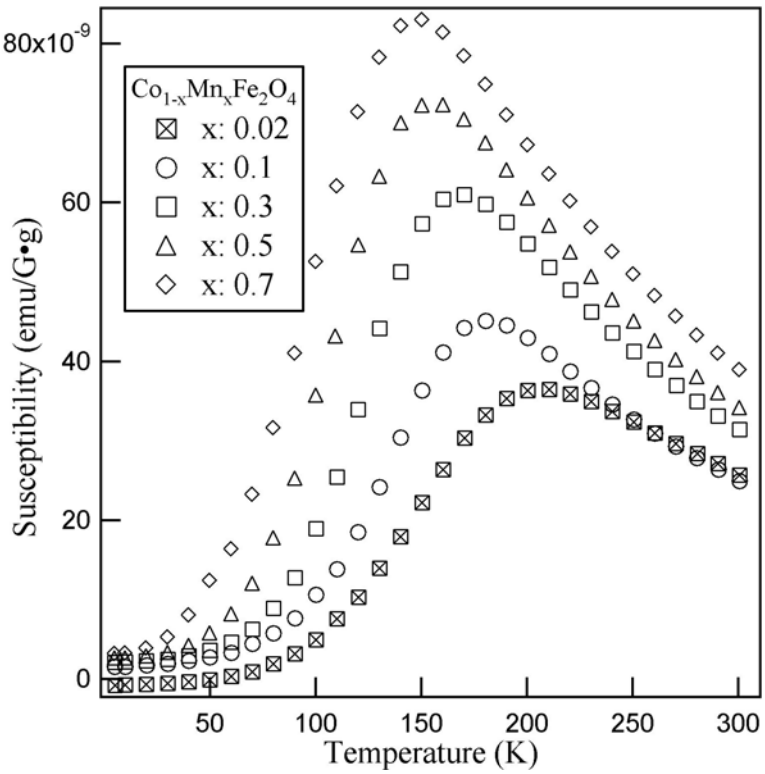

Figure 5.23 The temperature dependent magnetization measurements of chemically doped $Co_{1-x}Mn_xFe_2O_4$ with different molar percentage of Mn ($0.02 \leq x \leq 0.7$).

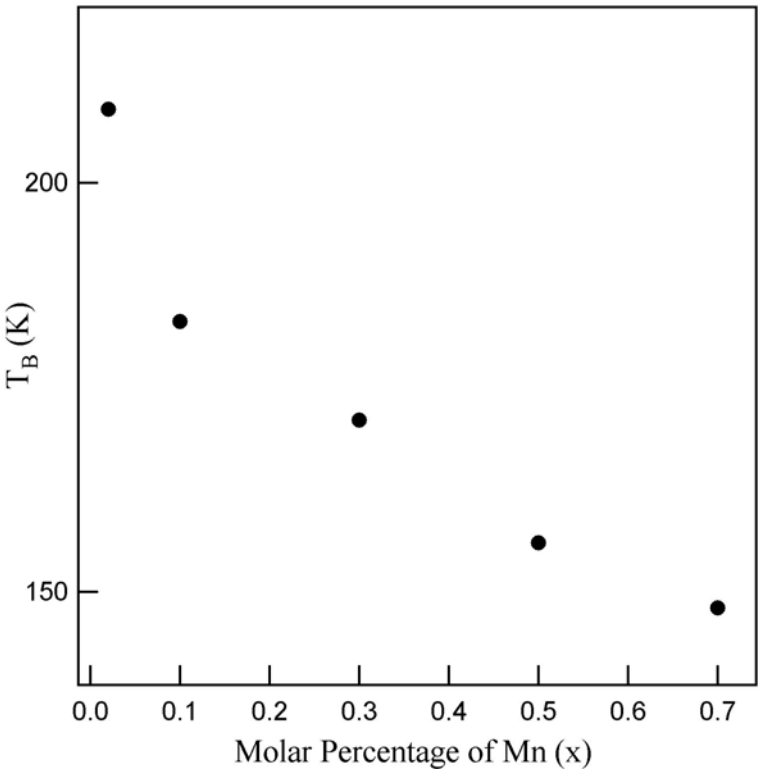

Figure 5.24 The blocking temperature of chemically doped $Co_{1-x}Mn_xFe_2O_4$ nanocrystals varying with the molar percentage of Mn.

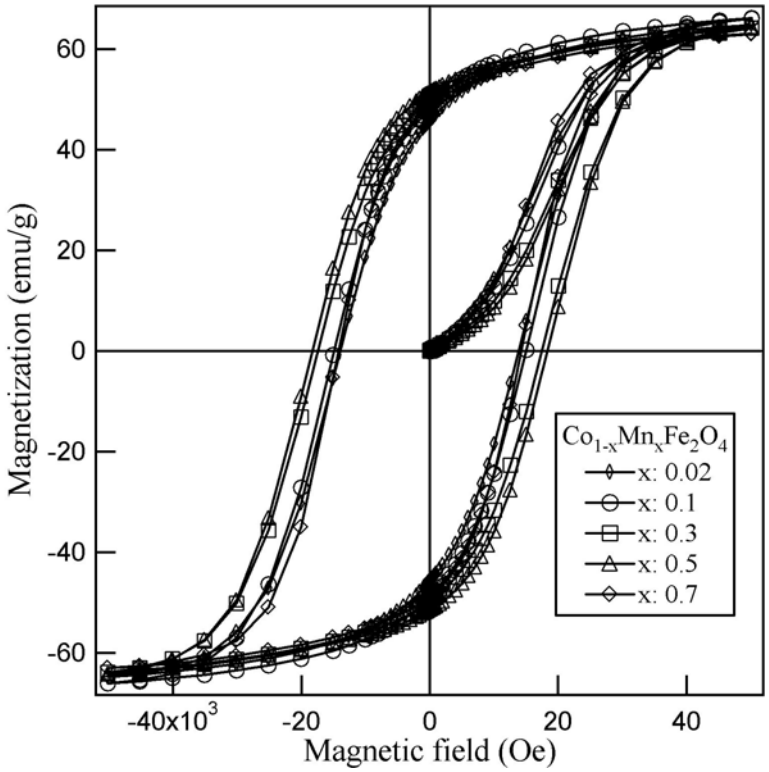

Figure 5.25 The hysteresis curves of chemically doped $Co_{1-x}Mn_xFe_2O_4$ with different molar percentage of Mn ($0.02 \leq x \leq 0.7$).

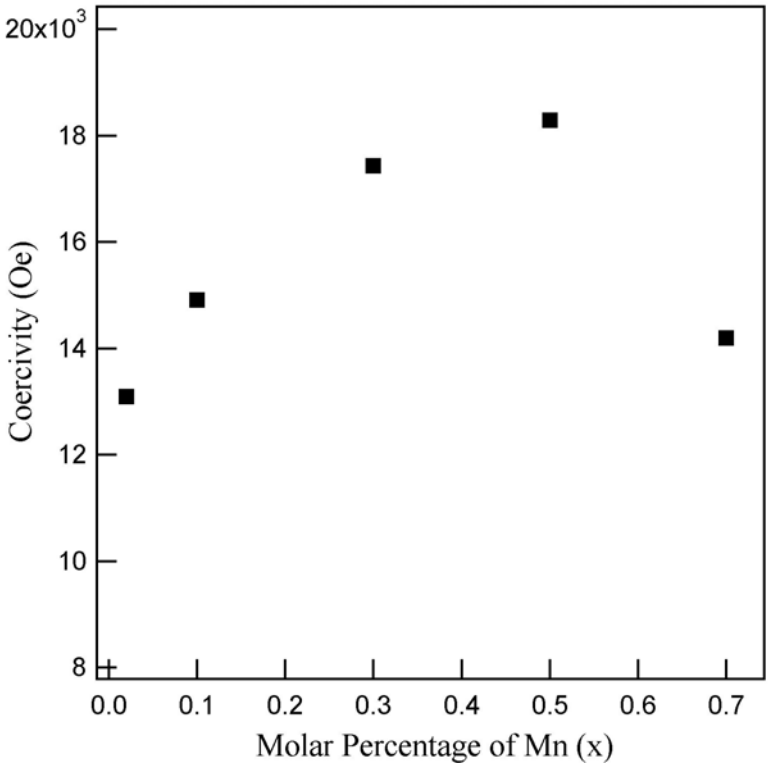

Figure 5.26 The coercivity of chemically doped $Co_{1-x}Mn_xFe_2O_4$ nanocrystals varying as a function of the molar percentage of Mn.

The magnetic properties of bimagnetic nanocrystals with core shell architecture can shine the insightful light into the fundamental understanding of nanomagnetism. The blocking temperature variation of core shell structured nanocrystals is essentially consistent with the single domain Stoner-Wohlfarth theory[50,51], although it was originally derived from a non-interacting single phase magnetic system. The further reason for extending Stoner-Wohlfarth theory to core shell typed nanocrystal is because the shell is epitaxially overcoated upon core forming a single nanocrystal. As a result, an effective exchange coupling between magnetic hard and soft phase induces the core-shell nanocrystal cooperatively acting as a single phase material, as shown in Figure 5.8 to 5. 11. In the frame of Stoner-Wohlfarth theory, the superparamagnetic state occurs when the magnetic anisotropy energy E_A of nanoparticulate system is overcome by thermal energy. The defined magnetic anisotropy energy E_A can be expressed as

$$E_A = KV \sin^2\theta \qquad (5.\ 1)$$

where K is the anisotropy energy constant, V is the volume of the nanoparticle, and θ is the angle between the magnetization direction and the ease axis of nanoparticle. Magnetic anisotropy energy serves as an energy barrier for blocking the superparamagnetic relaxation of nanocrystals. The blocking temperature, T_B, represents the threshold of thermal activation and can be used as an indication of such transition to the superparamagnetic state. Thus, one can control the anisotropy energy and further the blocking temperature of nanoparticle by precisely modulating the anisotropy energy constant K and /or adjusting the volume of nanoparticle. For bimagnetic nanocrystals

with core shell architecture studied here, the general trend of the blocking temperature increasing with the thickness of shell can be attributed to the enhancement of the effective anisotropy energy constant and the increase of the volume of core shell structured nanocrystal. Given the same sized core and the same thickness of shell, for example, 5.5 nm core @ 0.5 nm shell for $CoFe_2O_4$ @ Fe_3O_4 and Fe_3O_4 @ $CoFe_2O_4$, the higher magnetic anisotropy constant of $CoFe_2O_4$ (18×10^5 erg/cm^3) than that of Fe_3O_4 (1.2×10^5 erg/cm^3)[52] gives rise to a larger increasing of effective anisotropy constant for Fe_3O_4 @ $CoFe_2O_4$ core shell typed nanocrystals. As a result, the larger magnitude of increase of blocking temperature is observed (Figure 5.12 and 5.13). The influence of volume, on the other hand, may become a dominating factor on the blocking temperature for the core-shell structured nanocrystals with $CoFe_2O_4$ being core and $MnFe_2O_4$ or Fe_3O_4 as shell, because the magnetic anisotropy constants of $MnFe_2O_4$ and Fe_3O_4 are over an order of magnitude less than that of $CoFe_2O_4$. Therefore, the increasing of the blocking temperature as the thickness of shell increases for such core shell structured bimagnetic nanocrystals is a general trend.

The single-phase magnetization reversal of core-shell bimagnetic nanocrystals with magnetic field has been considered due to a strong effective exchange coupling between hard phase and soft phase. In the nanostructured two-phase magnet model proposed by Skomski and Coey[53,54], assuming the hard and soft phase are intimate contact with crystallographic alignment of their ease axes and consequently a strong hard-soft exchange coupling, the coercivity (H_C) of nanostructured exchange-coupled two-phase magnet is determined by the volume fraction weighted magnetocrystalline anisotropy and saturation magnetization.

$$\mu_0 H_C = 2(f_S K_S + f_H K_H)/(f_S M_S + f_H M_H) \qquad (5.2)$$

where μ_0 is a universal constant of permeability in free space, K the magnetocrystalline anisotropy constant, M the saturation magnetization, f the volume fraction, and the subscripts H and S refer to the hard and soft phases, respectively. Judging from the fact that the magnetocrystalline anisotropy constant of $CoFe_2O_4$ is much larger than those of $MnFe_2O_4$ and Fe_3O_4, whereas the value of saturation magnetization is relatively equal to each other[52], the equation (5.2) can be simplified and transformed to equations (5.3) and (5.4) without introducing significant error:

$$\mu_0 H_C = 2(K_H / M_H)\,(1\text{-}f_S) \qquad (5.3)$$

$$\mu_0 H_C = 2 f_H K_H / M_H \qquad (5.4)$$

The coercivity of various core shell structured nanocrystals as a function of volume fractions of hard and soft phases as well as the linear fittings derived from equation (5.3) and (5.4) are plotted in Figure 5.27 and 5.28. It is worth to note that a reverse coordinate is used for the volume fraction of hard phase $CoFe_2O_4$ in Figure 5.27 and 5.28. Clearly, one can find a good agreement between experimental results and theoretical model. Furthermore, instead of the size or shell thickness dependency, it is volume fraction that the coercivity depends on for core shell structured bimagnetic nanocrystals, which is either linearly decreases with increasing the volume fraction of soft phase or is linearly proportional to the volume fraction of hard phase.

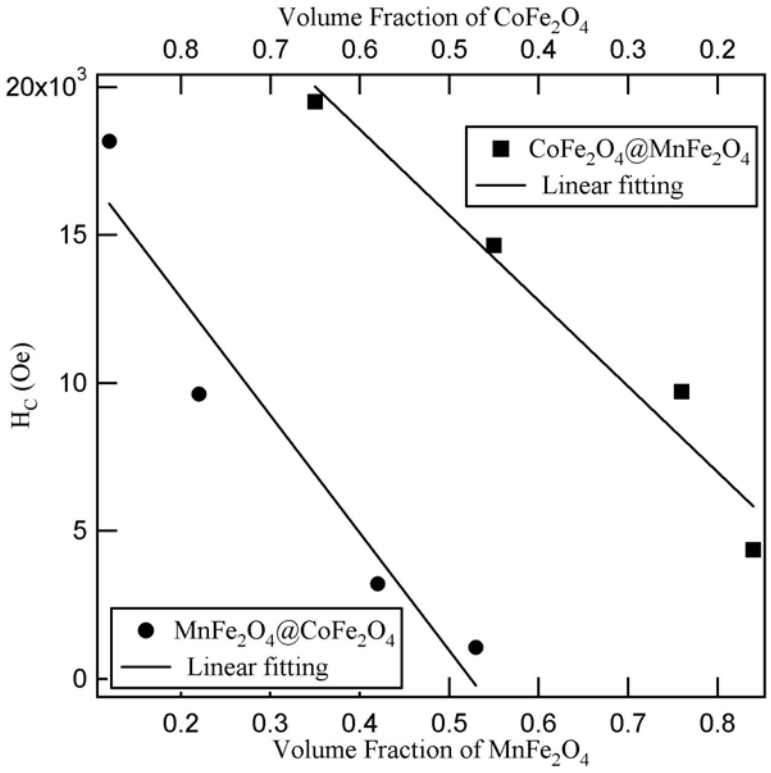

Figure 5.27 The coercivity of $CoFe_2O_4$@$MnFe_2O_4$ and $MnFe_2O_4$@$CoFe_2O_4$ plotted against the volume fraction of $MnFe_2O_4$ and $CoFe_2O_4$. The solid lines are the linear fittings. Note that a reversed coordinate is used for the volume fraction of $CoFe_2O_4$.

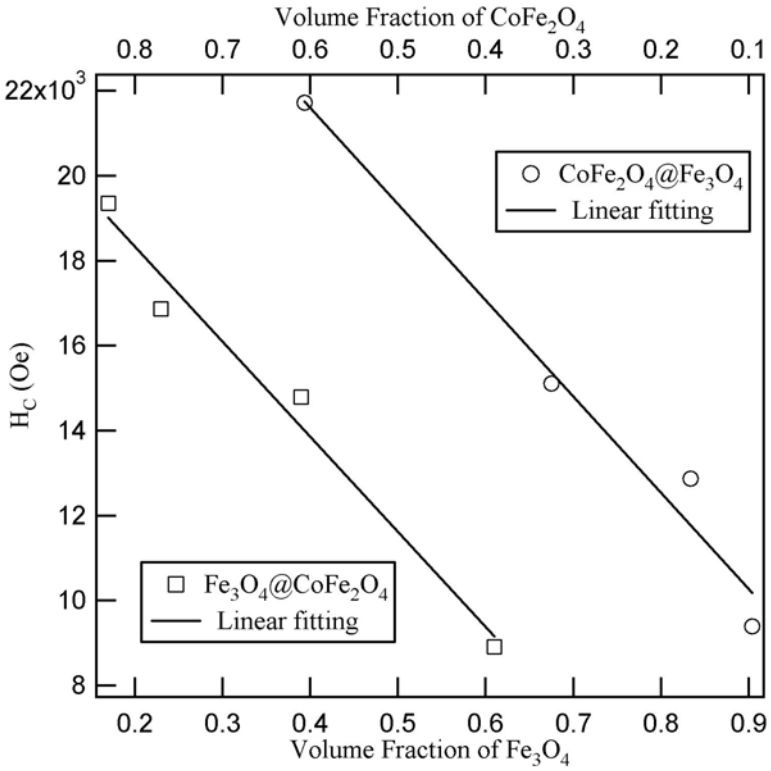

Figure 5.28 The coercivity of $CoFe_2O_4$@Fe_3O_4 and Fe_3O_4@$CoFe_2O_4$ plotted against the volume fraction of Fe_3O_4 and $CoFe_2O_4$. The solid lines are the linear fittings. Note that a reversed coordinate is used for the volume fraction of $CoFe_2O_4$.

It is equally important to note the discrepancy in coercivity variation between experimental results and theoretical predication, especially the enhancement of coercivity at the initial overcoating of soft phase upon hard $CoFe_2O_4$ core in Figure 5.19. The possible reason for such difference may be related to the surface effect, which was not taken into account in the two-phase magnet theory model used above. The coercivity of bulk magnetic material can be improved by the introduction of pinning centers and consequently inhibited the propagation of the reversed nucleus. In case of nanocrystals, the surface pinning or spin canting occurs much frequently than bulk materials[55-57], leading to an extra enhancement on coercivity as shown in Figure 5.19. Moreover, only is a half of core shell structured nanocrystals studied here restrictively fulfilled the geometrical configuration requirement of the originally theoretical model, where the calculation was based on a soft phase included in a hard phase. Our experimental results, along with other recent reports[58], however, indicates that this model could be still valid for other geometrical configurations consisting of two-phase nanocomposites such as hard magnetic material coated by soft ones, as long as the magnetic properties, specifically coercivity, are dramatically different. Definitely, more experimental results and theoretical studies are desired before any solid conclusion can be drawn with in this respect.

5.4 Conclusions

Various bimagnetic nanocrystals with core shell architecture have been synthesized by a combination of non-hydrolysis process with a seed-mediated growth. The core shell structure has been confirmed by both HRTEM and energy dispersive X-ray spectroscopy microanalysis. The magnetic characterizations on the mechanical mixture of pure hard and soft phase and chemically doped $Co_{1-x}Mn_xFe_2O_4$ nanocrystals supplied further evidence on supporting the successful fabrication of core shell structured bimagnetic nanocrystals. Moreover, the magnetic studies on such core shell nanocrystals reveal a strong exchange coupling between hard and soft phase leading to a single phase magnetic behavior on both temperature and field dependent magnetization. The increase of blocking temperature of core shell nanocrystals as the thickness of shell increasing is the general trend. The coercivity, on the other hand, shows the linear dependency on the volume fraction of either soft phase or hard phase, which is well consistent with the previous theory model, although the unexpected enhancement on coercivity due to surface effect can not be explained. The unique magnetic properties of core shell structured nanocrystals clearly demonstrate that the fabrication of core shell magnetic nanocomposites is an effective approach to precisely customizing material properties for a wide variety of technical applications.

5.5 References

(1) Brus, L. *J. Phys. Chem.* **1986**, *90*, 2555.

(2) Murray, C. B.; Norris, D. J.; Bawendi, M. G. *J. Am. Chem. Soc.* **1993**, *115*, 8706.

(3) Alivisatos, A. P. *Science* **1996**, *271*, 933.

(4) Heath, J. R. *Acc. Chem. Res.* **1999**, *32*, 388.

(5) Murray, C. B.; Kagan, C. R.; Bawendi, M. G. *Annu. Rev. Mater. Sci.* **2000**, *30*, 545.

(6) Peng, X.; Wickham, J.; Alivisatos, A. P. *J. Am. Chem. Soc.* **1998**, *120*, 5343.

(7) Peng, X.; Manna, U.; Yang, W.; Wickham, J.; Scher, E.; Kadavanich, A.; Allvisatos, A. P. *Nature* **2000**, *404*, 59.

(8) Sun, S.; Murray, C. B.; Weller, D.; Folks, L.; Moser, A. *Science* **2000**, *287*, 1989.

(9) El-Sayed, M. A. *Acc. Chem. Res.* **2004**, *37*, 326.

(10) Burda, C.; Chen, X.; Narayanan, R.; El-Sayed, M. A. *Chemical Reviews* **2005**, *105*, 1025.

(11) Peng, X.; Schlamp, M. C.; Kadavanich, A. V.; Alivisatos, A. P. *J. Am. Chem. Soc.* **1997**, *119*, 7019.

(12) Dabbousi, B. O.; Rodriguez-Viejo, J.; Mikulec, F. V.; Heine, J. R.; Mattoussi, H.; Ober, R.; Jensen, K. F.; Bawendi, M. G. *J. Phys. Chem. B* **1997**, *101*, 9463.

(13) Cao, Y.; Banin, U. *J. Am. Chem. Soc.* **2000**, *122*, 9692.

(14) Pastoriza-Santos, I.; Koktysh, D. S.; Mamedov, A. A.; Giersig, M.; Kotov, N. A.; Liz-Marzan, L. M. *Langmuir* **2000**, *16*, 2731.

(15) Caruso, F. *Adv. Mater.* **2001**, *13*, 11.

(16) Schneider, J. J. *Adv. Mater.* **2001**, *13*, 529.

(17) Vestal, C. R.; Zhang, Z. J. *J. Am. Chem. Soc.* **2002**, *124*, 14312.

(18) Lu, Y.; Yin, Y.; Li, Z.-Y.; Xia, Y. *Nano Lett.* **2002**, *2*, 785.

(19) Teng, X.; Black, D.; Watkins, N. J.; Gao, Y.; Yang, H. *Nano Lett.* **2003**, *3*, 261.

(20) Zeng, H.; Li, J.; Wang, Z. L.; Liu, J. P.; Sun, S. *Nano Lett.* **2004**, *4*, 187.

(21) Jeong, U.; Kim, J.-U.; Xia, Y.; Li, Z.-Y. *Nano Lett.* **2005**, *5*, 937.

(22) Chan, W. C. W.; Nile, S. *Science* **1998**, *281*, 2016.

(23) Cao, Y.; Jin, R.; Mirkin, C. A. *J. Am. Chem. Soc.* **2001**, *123*, 7961.

(24) Kim, H.; Achermann, M.; Balet, L. P.; Hollingsworth, J. A.; Klimov, V. I. *J. Am. Chem. Soc.* **2005**, *127*, 544.

(25) Vestal, C. R.; Zhang, Z. J. *J. Am. Chem. Soc.* **2003**, *125*, 9828.

(26) Meiklejohn, W. H.; Bean, C. P. *Physical Review* **1957**, *105*, 904.

(27) Meiklejohn, W. H. *J. Appl. Phys.* **1962**, *33*, 1328.

(28) Skumryev, V.; Stoyanov, S.; Zhang, Y.; Hadjipanayis, G.; Givord, D.; Nogues, J. *Nature* **2003**, *423*, 850.

(29) Gangopadhyay, S.; Hadjipanayis, G. C.; Shah, S. I.; Sorensen, C. M.; Klabunde, K. J.; Papaefthymiou, V.; Kostikas, A. *J. Appl. Phys.* **1991**, *70*, 5888.

(30) Gangopadhyay, S.; Hadjipanayis, G. C.; Sorensen, C. M.; Klabunde, K. J. *J. Appl. Phys.* **1993**, *73*, 6964.

(31) Duxin, N.; Stephan, O.; Petit, C.; Bonville, P.; Colliex, C.; Pileni, M. P. *Chem. Mater.* **1997**, *9*, 2096.

(32) Carpenter, E. E.; Calvin, S.; Stroud, R. M.; Harris, V. G. *Chem. Mater.* **2003**, *15*, 3245.

(33) Murray, C. B.; Kagan, C. R.; Bawendi, M. G. *Science* **1995**, *270*, 1335.

(34) Ahmadi, T. S.; Wang, Z. L.; Green, T. C.; Henglein, A.; El-Sayed, M. A. *Science* **1996**, *272*, 1924.

(35) Peng, Z. A.; Peng, X. *J. Am. Chem. Soc.* **2001**, *123*, 1389.

(36) Peng, Z. A.; Peng, X. *J. Am. Chem. Soc.* **2002**, *124*, 3343.

(37) Jin, R.; Cao, Y.; Mirkin, C. A.; Kelly, K. L.; Schatz, G. C.; Zheng, J. G. *Science* **2001**, *294*, 1901.

(38) Jana, N. R.; Gearheart, L.; Murphy, C. J. *Adv. Mater.* **2001**, *13*, 1389.

(39) Puntes, V. F.; Krishnan, K. M.; Alivisatos, A. P. *Science* **2001**, *291*, 2115.

(40) Hyeon, T.; Lee, S. S.; Park, J.; Chung, Y.; Na, H. B. *J. Am. Chem. Soc.* **2001**, *123*, 12798.

(41) Sun, S.; Zeng, H. *J. Am. Chem. Soc.* **2002**, *124*, 8204.

(42) Sun, Y.; Xia, Y. *Science* **2002**, *298*, 2176.

(43) Manna, L.; Milliron, D. J.; Meisel, A.; Scher, E. C.; Alivisatos, A. P. *Nature Materials* **2003**, *2*, 382.

(44) Sun, S.; Zeng, H.; Robinson, D. B.; Raoux, S.; Rice, P. M.; Wang, S. X.; Li, G. *J. Am. Chem. Soc.* **2004**, *126*, 273.

(45) Song, Q.; Zhang, Z. J. *J. Am. Chem. Soc.* **2004**, *126*, 6164.

(46) Liu, C.; Wu, X.; Klemmer, T.; Shukla, N.; Weller, D.; Roy, A. G.; Tanase, M.; Laughlin, D. *Chem. Mater.* **2005**, *17*, 620.

(47) Zeng, H.; Li, J.; Liu, J. P.; Wang, Z. L.; Sun, S. *Nature* **2002**, *420*, 395.

(48) Hadjipanayis, G. C.; Siegel, R. W.; Ed. *Nanophase Materials: Synthesis, Properties, Applications.* Kluwer Academic: London, 1994. p573.

(49) Kneller, E. F.; Hawig, R. *IEEE Trans. Magn.* **1991**, *27*, 3588.

(50) Stoner, E. C.; Wohlfarth, E. P. *Trans. Roy. Soc.* **1948**, *A240*, 599.

(51) Stoner, E. C.; Wohlfarth, E. P. *IEEE Trans. Magn.* **1991**, *27*, 3475.

(52) Buschow, K. H. J.; Ed. *Handbook of Magnetic Materials: Volume 8*; Elsevier: Amsterdam, 1995. Chapter 3.

(53) Skomski, R.; Coey, J. M. D. *Phys. Rev. B*. **1993**, *48*, 15812.

(54) Skomski, R.; Coey, J. M. D. *IEEE Trans. Magn.* **1994**, *30*, 607.

(55) Dimitrov, D. A.; Wysin, G. M. *Phys. Rev. B*. **1994**, *50*, 3077.

(56) Kodama, R. H.; Berkowitz, A. E.; McNiff, E. J., Jr.; Foner, S. *Phys. Rev. Lett.* **1996**, *77*, 394.

(57) Kodama, R. H.; Berkowitz, A. E.; McNiff, E. J., Jr.; Foner, S. *Mater. Sci. Forum* **1997**, *235-238*, 643.

(58) Zeng, H.; Sun, S.; Li, J.; Wang, Z. L.; Liu, J. P. *Appl. Phys. Lett.* **2004**, *85*, 792.

CHAPTER 6

SELF ASSEMBELY OF ANISOTROPIC SHAPED MAGNETITE NANOCRYSTALS

Abstract

A mixture of magnetite (Fe_3O_4) nanocrystals with distinctive anisotropic shapes has been synthesized by seed-mediated growth method. Complementary analyses using bright-field and dark-field TEM as well as high resolution transmission electron microscopy (HRTEM) and selected area electron diffraction (SAED) techniques unambiguously reveal that the anisotropic shapes of Fe_3O_4 nanocrystals are tetrahedral platelet (TP) (nanoprisms), truncated tetrahedral platelet (TTP) (nanodisks), truncated octahedral (TO) and octahedral (OT) (nanocompass), respectively. Three types of self assembled 3D superstructures formed by such anisotropic nanocrystals, hexagonal columnar, primitive cubic, and body center cubic-like (*bcc*) have been observed. The self assembled 3D superlattices of such anisotropic shaped Fe_3O_4 nanocrystals are characterized by highly orientational ordering and shape-selective fractional microphase segregation. The experimental observations, which the crystallization of orientational ordering in each 3D superlattice is strongly dependent on the shapes of nanocrystal, are in general consistent with Onsager entropic effect theory, although both attractive van der Waals interaction, and in particular for magnetic nanocrystals studied here, magnetic

dipolar interaction should also be taken into account of the formation of such orientational ordering in 3D superstructures. Self-assembly of magnetic nanocrystals with anisotropic shape and orientational ordering is crucial for the fundamental understanding of collective magnetic coupling in assembled nanoparticle arrays and for the potential applications such as the control of magnetic moment orientational alignments in ultrahigh density magnetic recording media.

6.1 Introduction

Self assembly is defined as a process in which a spontaneous and reversibly organization of preexisting components forms ordered aggregates by means of non-covalent or weak covalent attractive and/or repulsive interactions[1]. Although the concept of self assembly is historically originated from the investigations of molecular processes[2], it is no longer limited to molecules and its focus has been expanded and directed toward nanoscopic, mesoscopic and macroscopic components[3]. During the past few decades, tremendous research effort has been devoted to the exploration of understanding self assembly by functional nanoscale materials[4-8], because self assembly process shows a promise of playing an indispensable role in assembly of functional nano-building blocks into macroscopic structures and novel devices. In addition, self assembly is probably the only possible effective approach to the fabrication of three dimensional (3D) microstructures by functional nanoscale building blocks, where the length scale is smaller than those conveniently accessible by 'top-down' lithographic methods. Recently, remarkable progress in the synthesis of colloidal nanocrystals has been achieved in the preparation of different high quality nanomaterials with controllable crystal structures, chemical compositions, surface properties, sizes, and shapes[9,10]. Numerous approaches and techniques have been employed to fabricate the self assembled ordered microstructures from noble metals[11-17], semiconductors[18,19], and metal oxides[20] nanocrystals. However, the shape of nanocrystals in self assembly arrays is very frequently limited in spherical and only until recently extended to some anisotropic shapes such as nanorods[21-25], partially due to the fact that rather than the spherical or rod shapes, the synthesis of nanocrystal with anisotropic shapes is remained an experimental

challenge. Moreover, shape is not only a fundamental property from microscopic to macroscopic objects, but also shape is one of the key components of nanoscale building blocks in self assembly. Therefore, to systematic investigate and fully understand what the shape, specifically anisotropic shape effects upon self assembly of functional nanometer building blocks into 3D superstructures is of scientific interest such as collective electronic and optical properties in quantum dots arrays, and magnetic interparticle interaction in magnetic nanocrystals assemblies and technological importance including the control of magnetic moment orientational ordering in ultrahigh magnetic recording media.

The control of positional ordering is probably a major goal of self assembly. However, the control of spatial orientation ordering in self assembly of nanocrystals may be more interesting and significant, yet more difficult to achieve, in nanofabrication. Recent studies on millimeter scaled objects[26-28] suggest that the encoding nanoscale building blocks with rational designed shapes may provide a more effective approach to controlling the translational and spatial orientation ordering in self assembly. Generally, for spherical nanocrystals, due to its highly symmetrical (infinite) character in nature and isotropic interparticle interactions, the spatial orientation ordering in the self assemblies formed by spherical nanocrystals is barely reserved, and only translational or positional ordering in such superstructures can be achieved. In contrast, for nanocrystals encoded with anisotropic shape, the vertexes, edges and faces point along crystallographic axes of the native crystal structure of material. As a consequence, the desired orientational ordering in 3D superstructures can be well conserved, that is, the nanocrystal axes are cooperatively co-oriented with respect to each other and generally also directed along the

crystallographic axes of crystal lattice. Therefore, it is desirable to establish the correlation between the orientational ordering of self assembled 3D structures and the distinctly non-spherical, polyhedral shape of individual nanocrystal.

The self assembly of preexisting components is essentially a phase transition between disorder and order states. The involved energies or interactions in this phase transition are non-covalent in nature, including van der Waals, electrostatic, entropic, capillary, hydrophobic, magnetic dipolar, or hydrogen bonding *et al*. From the studies on the growth of complex structures from spherical particles with size ranging from several nanometers to micrometers in a wide variety of materials[5,29], both size, size distribution and size ratios are the dominant factors on the determination of structures through controlling the nature, strength, range and direction of particle interactions for the thermodynamically stabilized 2D or 3D superstructures formed by self assembled nanocrystals. For example, Ohara *et al*.[30] reported that 2D crystallization of polydispersed gold nanocrystals formed size dependent segregation and was attributed such size selective phase transition to the size dependent attractive van der Waals interaction. On the other hand, Kiely *et al.*[13] observed an ordered AB_2 2D structure as well as hexagonal close packed and random positioned segregated phases from the bimodal gold nanocrystals. These authors concluded that such size selective phase segregation highly likely arises from the entropy-driven crystallization. Similarly, for 3D superstructures formed from binary spherical nanocrystals mixtures, Murray *et al.*[8] have demonstrated that by precisely controlled the size ratios of nanocrystals as well as the evaporation rates, the self assembly of PbSe and γ-Fe_2O_3 nanocrystals can be crystallized into AB_{13} or AB_2 superlattices as long as the size ratio is close to 0.58. Although the authors did not

explained the reason for the formation mechanism of such ordered superlattices, these 3D complex ordered superstructures are not only consistent with other previous experimental observations arising from the crystallization of a binary mixture of hard spherical polymethylmethacrylate (PMMA) colloids[31], but also well compatible with the theoretical predication and computer simulations based on the entropy-driven superlattice formation[32,33]. As the shape varies from isotropic sphere to anisotropic morphologies, interactions likely depend on a new set of factors such as shape itself including geometric symmetries and facets, aspect ratios, and polydispersity in shape *etc*. Recent studies on the self assembly of non-spherical, anisotropic nanocrystals such as rod[21,23,25] and plate-like[34-37] nanocrystals have demonstrated that the self assembly of anisotropic shaped nanocrystals differs dramatically from that of the spherical nanocrystals. Moreover, the interactions such as van der Waals attraction, electrostatic force, and dipolar interaction[38-40] have been proposed to be more important on translational ordering and orientational orderings in the self assemblies, despite the fact that the counterintuitive ordering entropy seems to remain the key contribution to the thermodynamic stability from disorder to order transition[41]. In addition, the influence of shapes, polydispersity, and aspect ratio on the phase separation have been investigated theoretically by computer simulations[42-45]. Nevertheless, since current progress on the self assemblies of nanocrystals with distinctly anisotropic shapes into 3D orientational ordered structures has only been limited successful, it is worthwhile to devote more research efforts toward understanding the effect of anisotropic shapes on self assembled superstructures.

The focus in this chapter is on the self assembly of anisotropic shaped Fe_3O_4 nanocrystals. First, a mixture of anisotropic shaped Fe_3O_4 nanocrystals were synthesized

by a combination of nonhydrolysis procedure with seed-mediated growth. Then, the complementary analyses by high resolution transmission electron microscopy (HRTEM) and low-magnification dark field imaging techniques were conducted to determine the shapes of Fe_3O_4 nanocrystals, which are tetrahedral platelet (TP) (nanoprism), truncated tetrahedral platelet (TTP) (nanodisk), truncated octahedral (TO) and octahedral (OT) (nanocompass). More interesting and important, the assembly of the anisotropic shaped Fe_3O_4 nanocrystals gives rise to three distinctive shape selective 3D superstructures, as being hexagonal columnar, primitive cubic, and body center cubic-like (*bcc*). The experimental observations clearly reveal that the construction of anisotropic shaped nanocrystals into 3D self assembled superstructures is characteristic of both highly orientational ordering and shape-selective fractional phase segregation. Finally, the shape evolution and magnetic properties of anisotropic Fe_3O_4 nanocrystals are discussed.

6.2 Experimental Sections

Hexane, acetone, toluene, ethanol, and isopropanol were purchased from Fisher Scientific Inc., and except isopropanol was distilled, others were used as received. Octane (98%), dodecane (99+%), phenyl ether (99%), benzyl ether (99%), oleic acid (90%), oleylamine (tech. 70%), iron (III) acetylacetonate ($Fe(acac)_3$) (97%), 1,2-hexadecandiol (tech. 90%), and 1-octadecanol (99%) were purchased from Aldrich Chemical Inc., and were used without further treatment.

6.2.1 Synthesis of Spherical Fe_3O_4 Nanocrystals as Seeds

A typical synthesis included two steps, the spherical seed formation and seed-mediated grow process. All reactions were under N_2 protection. In seed formation step, a mixture of 30 mL phenyl ether, 2 mmol $Fe(acac)_3$, 10 mmol 1,2- hexadecandiol, 3 mL oleic acid and 3 mL oleylamine was relatively quickly heated up to 260 ºC, and kept solution reflux for 30 min., and then cooled down to room temperature. After the addition of excess of ethanol, a black precipitates can be collected by either centrifugation or a permanent magnet. After two more times washing with ethanol, the precipitates was redispersed in hexane and reprecipitated by acetone. The size of Fe_3O_4 nanocrystals is about 4 nm. To make larger Fe_3O_4 nanocrystals, seed-mediated growth was applied. For example, combining 80 mg of 8 nm seeds with 1 mmol $Fe(acac)_3$, 5 mmol 1-octadecanol, 3 mL oleic acid and 3 mL oleylamine in 30 mL phenyl ether, 10 nm Fe_3O_4 nanocrystals were formed. The shape of nanocrystals is mainly spherical under such reaction conditions.

6.2.2 Synthesis of Anisotropic Shaped Fe_3O_4 Nanocrystals

Different sizes of spherical Fe_3O_4 nanocrystals were used as seeds and the procedure was similar to that of making spherical ones except the growth rate was controlled to be slower and reaction temperature was lower than that for making spherical ones. For example, very slowly heated up a solution to 220 ºC, where 60 mg of 10 nm seeds and 2 mmol $Fe(acac)_3$ were mixed with 30 mL phenyl ether, 10 mmol 1-octadecanol, 3 mL oleic acid, and 3 mL oleylamine, and kept reaction for 2 hours. Instead

of single shape, four different shapes of Fe_3O_4 nanocrystals were obtained in such reaction conditions.

6.2.3 Characterization

Powder X-ray diffraction patterns were recorded using D8 Advance diffractometer (Bruke AXS Inc.) with Cu Kα radiation (λ = 1.54056 Å). Both bright field and dark field transmission electron microscopy (TEM) studies were carried out on JEOL 100C under 100 kV. The selected area electron diffraction (SAED) and high resolution imaging (HRTEM) were conducted on JEOL 4000EX at 400 kV. The samples for TEM analysis were prepared by either dispersed a drop of concentrated (~ 3mg/mL) or diluted (~ 0.1mg/mL) hexane (0.1 ~ 0.2% v/v, oleic acid) nanocrystals solution on amorphous carbon-coated copper grids and dried at room temperature.

The studies on magnetic properties were carried out on SQUID MPMS-5S magnetometer (Quantum Design Inc.) with magnetic field up to ± 5T and temperature range from 5 K to 300 K. The samples for SQUID measurements were prepared by fully dispersed dry powder Fe_3O_4 nanocrystals in eicosane ($C_{20}H_{42}$, 99%, Aldrich Inc.) matrix.

6.3 Results and Discussion

The representative TEM image of monolayer self-assembly of 12 ~ 14 nm anisotropic shaped Fe_3O_4 nanocrystals is shown in Figure 6.1a. The TEM image of monolayer self-assembly of 10 nm spherical Fe_3O_4 nanocrystals and the typical electron diffraction pattern of anisotropic shaped Fe_3O_4 nanocrystals are presented in Figure 6.1b and 6.1c, respectively.

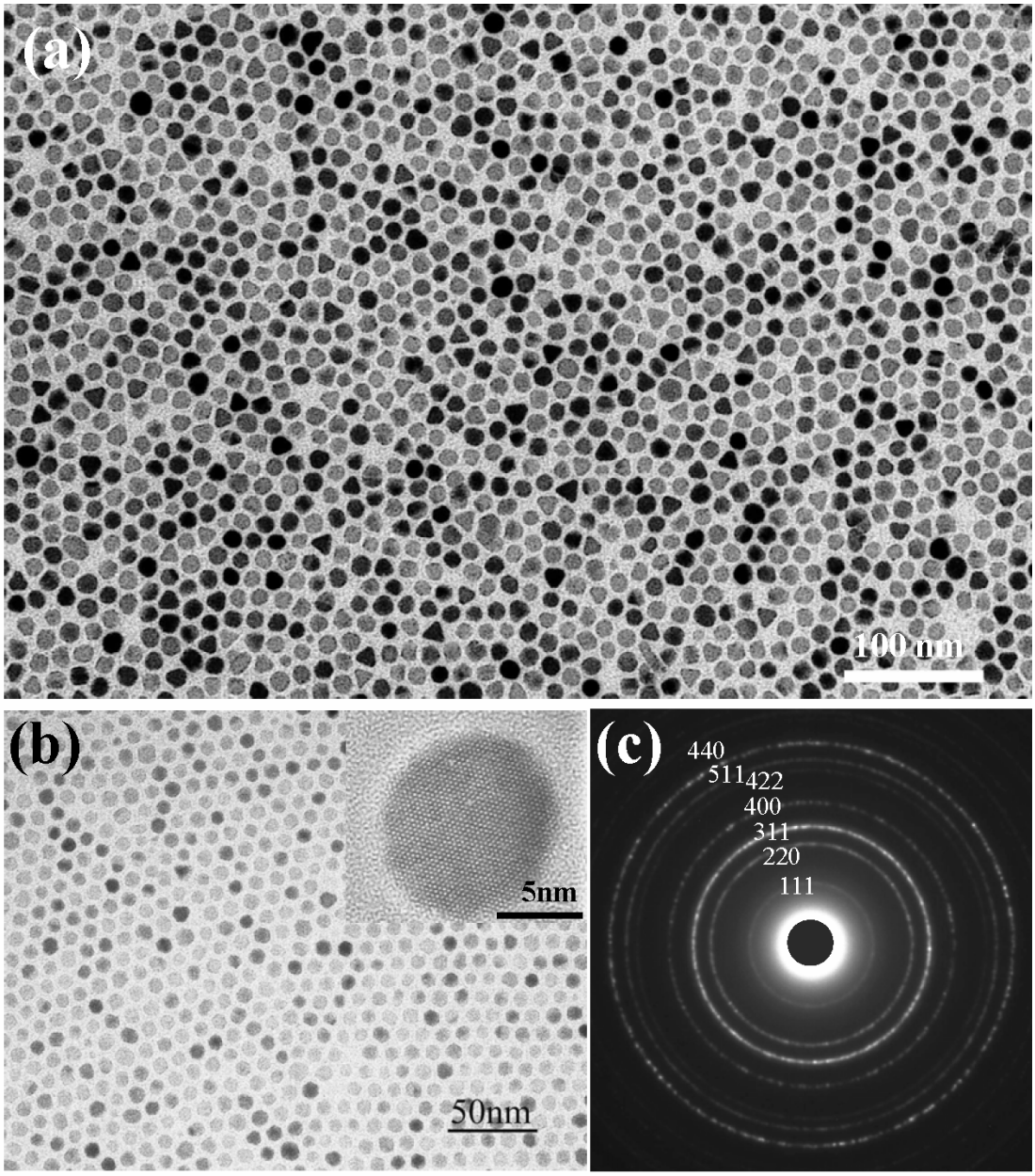

Figure 6.1 Typical TEM micrographs are (a) the anisotropic shaped Fe_3O_4 monolayer with size 12 ~ 14 nm, (b) 10 nm spherical Fe_3O_4 2D monolayer. The inset is the HRTEM imaging. (c) is the SAED patterns of anisotropic shaped Fe_3O_4 nanocrystals. The characteristic ring pattern indicates the random orientation of individual nanocrystal.

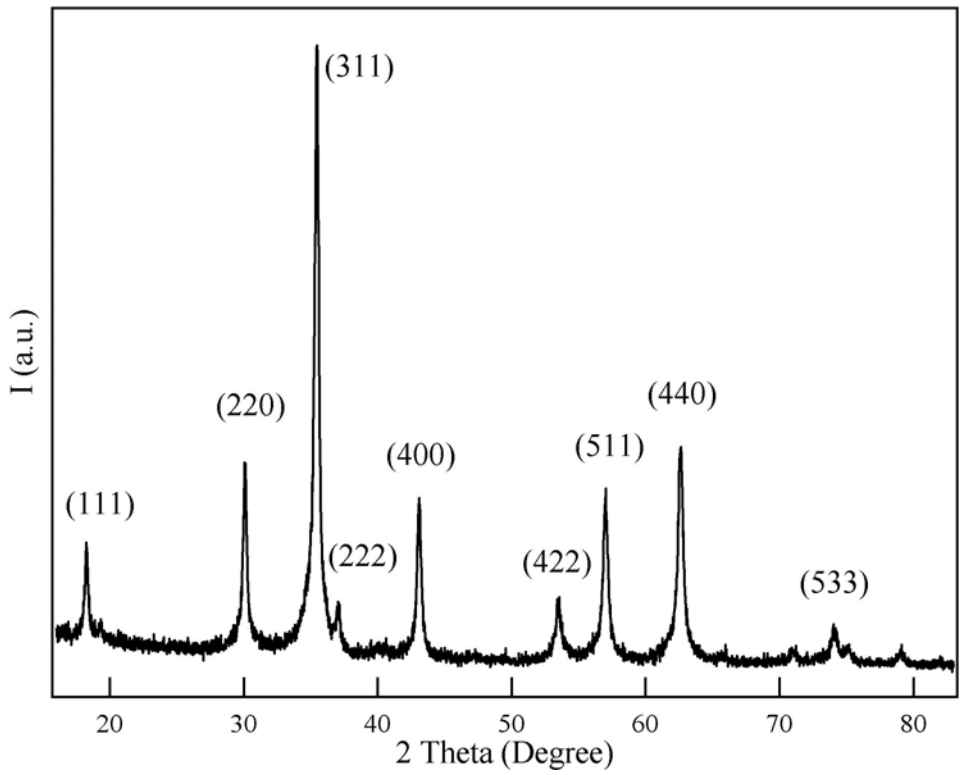

Figure 6.2 X-ray diffraction patterns of anisotropic shaped Fe_3O_4 nanocrystals.

First, one can clearly see that the spherical Fe_3O_4 nanocrystals form hexagonal close packing, indicating the size distribution is monodispersed. In addition, the anisotropic shaped Fe_3O_4 nanocrystals also form the self-assembly structure at lower volume fraction (~ 0.1mg/mL). The powder X-ray diffraction shown in Figure 6.2 in conjunction with selected area electron diffraction patterns (Figure 6.1c) confirms that the crystal structure of both spherical and anisotropic shaped Fe_3O_4 nanocrystals is cubic spinel structure. It is worth to point out that the SAED pattern is characteristic of the ring pattern feature,

indicating that each individual nanocrystal is randomly oriented in these monolayer self-assemblies.

Figure 6.3 shows three different types of self assembled 3D superstructures or superlattices with highly translational and orientational ordering formed by anisotropic shaped Fe_3O_4 nanocrystals. The mean length scale of such anisotropic shaped Fe_3O_4 nanocrystals is about 12 nm ~ 14 nm in longitudinal direction and the aspect ratio for octahedral shape is about 1.27 to 1.3. Another sample of mixed Fe_3O_4 nanocrystals with size around ~ 8 nm and the aspect ratio from 1.12 to 1.14 for octahedral shape has also been observed the formation of the same types of self assembled 3D superstructures shown in Figure 6.4. The overall size distribution for these two samples is less than 10%, and for each specific shape the size distribution is less than 7%. It is worth to note that it may be difficult to determine the size distribution for entire sample, due to the fact that the as-synthesized samples are a mixture of four anisotropic shapes and there is currently no quantitative variable to measure the polydispersity on shape.

Type I is hexagonal columnar structure as shown in Figure 6.5a. The electron diffraction patterns in Figure 6.5b are characterized by six-fold symmetry spots, which can be indexed as [111] diffraction pattern in a face-center cubic structure, suggesting all nanocrystals within 3D self assembled superstructures preferentially co-orient with respect to each other and parallel with the same single crystallographic axis, which is along [111] axis. It is noteworthy that the stacking sequence in hexagonal columnar is uniquely constructed by each single hexagonal shaped nanocrystal orientational aligning

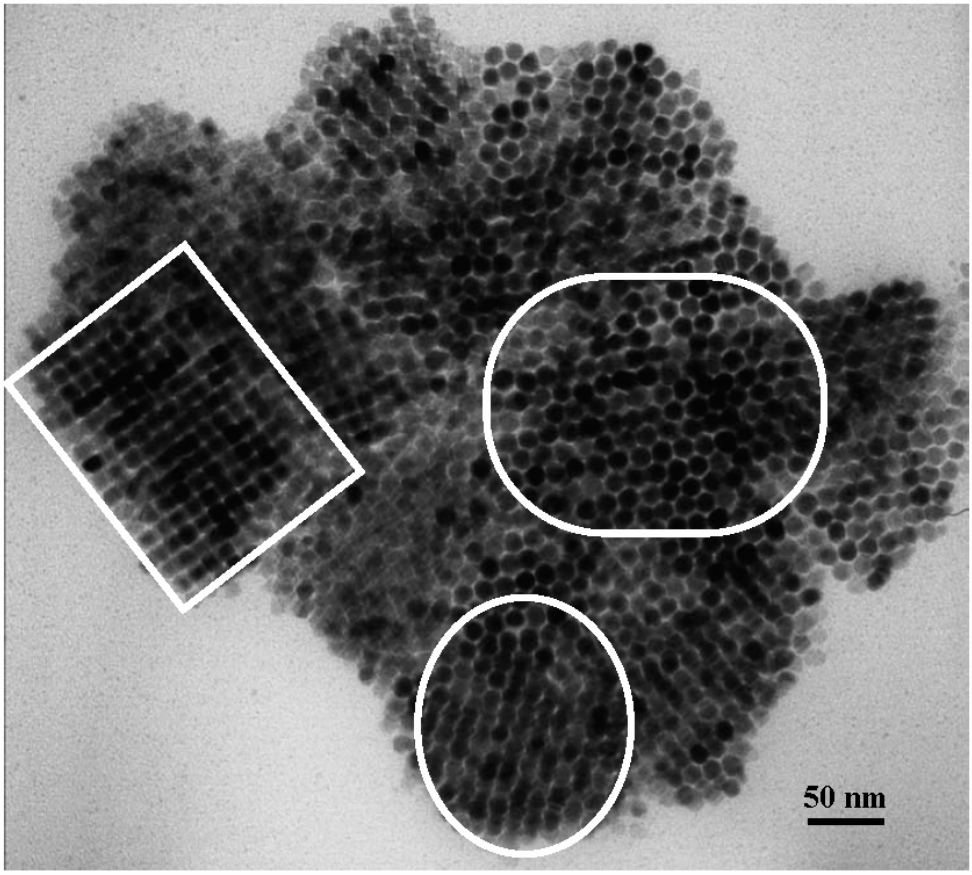

Figure 6.3 TEM micrograph shows different shapes of 12 ~ 14 nm Fe_3O_4 nanocrystals self assembled to form the shape selective 3D superstructures.

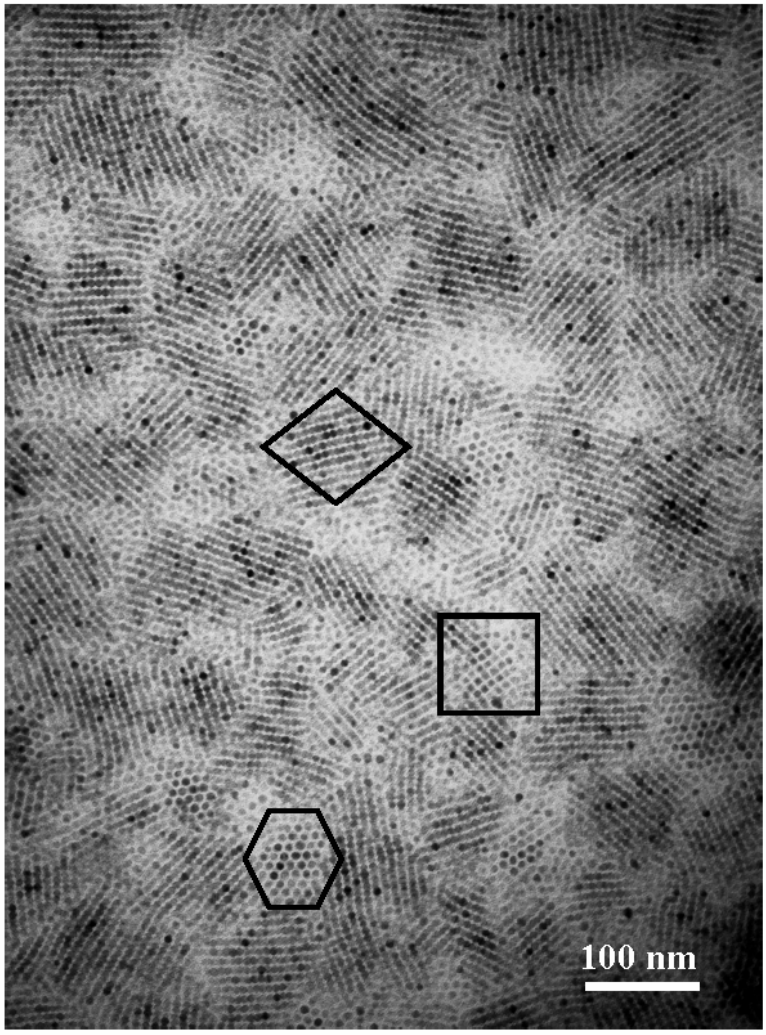

Figure 6.4 TEM micrograph shows different shapes of ~ 8 nm Fe_3O_4 nanocrystals self assembled to form the shape selective 3D superstructures.

itself directly along the normals of the nanocrystal faces, that is, nanocrystals stack along columns face-to-face, instead of moving laterally to occupy the interstitial sites formed by three neighboring nanocrystals. Clearly, hexagonal columnar stacking differs from the common hard-sphere hexagonal-close-packing (*hcp*). The 2D projection image as illustrated by HRTEM in Figure 6.5c is hexagonal shape. However, it is because of the similarity in 2D HRTEM projected images between tetrahedral and truncated tetrahedral shaped platelet (disk-like), the low magnification dark-field TEM (DF-TEM) analysis was used in order to distinguish them from each other as shown in Figure 6.5d inset. The results unambiguously verify that the shape of individual nanocrystal within hexagonal columnar superstructure is indeed the truncated tetrahedral platelet (TTP) faceted by {111} planes as two bases. Accordingly, the schematic models for both individual TTP nanocrystal and the top-view 3D superlattices are presented in Figure 6.5d, respectively. Although the perfect triangular 2D projected shape is also observed and determined to be the tetrahedral platelet (TP) by HRTEM and DF-TEM studies as well as intensity histograms recorded across three diagonal directions as shown in Figure 6.6a and b, respectively, these TP shaped nanocrystals are almost completely excluded from the construction of the hexagonal columnar superstructures by TTP nanocrystals.

The unit building blocks in Type II self assembled superstructure, as judging from HRTEM image shown in Figure 6.7c, is the truncated octahedral (TO) Fe_3O_4 nanocrystals, in which two {100} facets setup the TO top and bottom bases and all other terminal facets are closed alternatively by other four {100} and eight {111} planes. The 2D and 3D TO models are schematically plotted in Figure 6.7d. Based on TEM image in Figure 6.7a and a set of characteristic four-fold symmetry SAED spots pattern in Figure

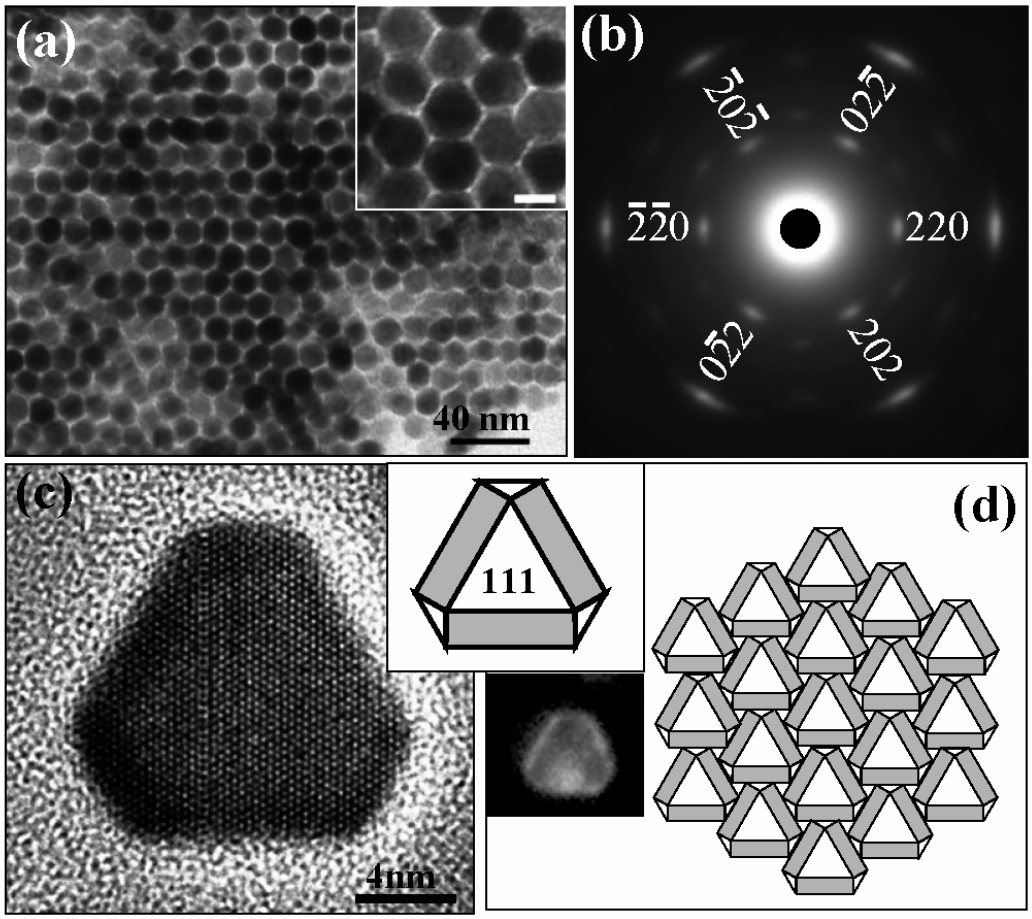

Figure 6.5 (a) is the hexagonal columnar 3D superstructure formed by TTP Fe_3O_4 nanocrystals. The inset is a part of enlargement. (b) is the SAED patterns with a set of six-fold symmetry spots character, indicating all nanocrystals co-orient along [111] direction. (c) is the HRTEM image of TTP shape Fe_3O_4 nanocrystal, the zone axis is along [111]. (d) shows a low magnification dark-field image of TTP shaped nanocrystal as well as the single nanocrystal and top-view 3D superstructure models.

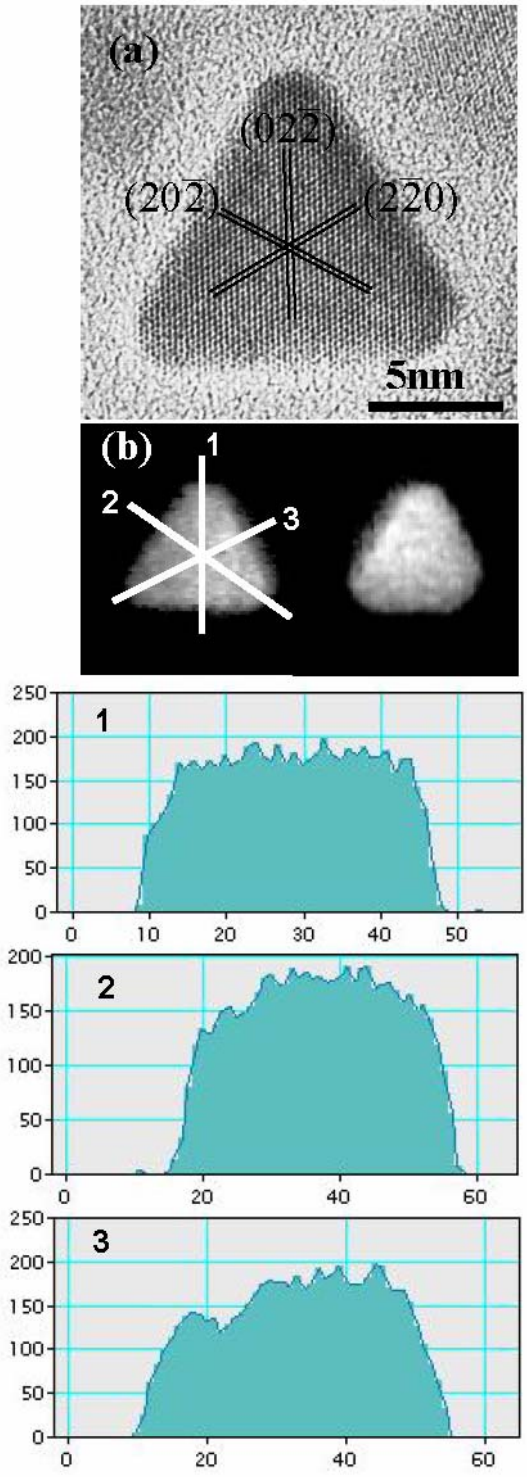

Figure 6.6 (a) is HRTEM image of TP shaped Fe_3O_4 nanocrystal. (b) is the low magnification dark-field image of TP shaped Fe_3O_4 nanocrystals. 1, 2 and 3 are the corresponding histograms of intensity as labeled in (b), respectively.

6.7b, the structure of Type II self assembled superstructure is indicative of a primitive cubic type, and the preferential orientation is determined to be along [100] direction. A schematic 2D top-view of Type II superstructure is displayed in Figure 6.7e. It should be pointed out that the frequency on occurrence of primitive cubic superstructure is the lowest among three self assemblies, which may imply that a possible least population of truncated octahedral shaped Fe_3O_4 nanocrystals in mixture is present or the shape of TO is likely an inhibitive shape to create 3D self assembled superstructure, in spite of high order symmetry associated with truncated octahedral shape.

An interesting and unexpected observation among three superstructures is from Type III, a self assembled construction of octahedral (OT) Fe_3O_4 nanocrystals into a body center cubic-like (*bcc*) superstructure, as shown in Figure 6.8a. To the best of our knowledge, so far, such orientational ordered superstructure built by OT nanocrystals has not been reported yet. From the TEM image, one can clearly see that all of the OT Fe_3O_4 nanocrystals are collectively co-aligned along [011] crystallographic direction, as indicated by a series of two-fold symmetry spots on SAED pattern in Figure 6.8b. The HRTEM image and its 3D model, as shown in Figure 6.8c and 6.8d, clearly demonstrate that the shape of Fe_3O_4 is octahedral (OT) with all terminal facets being exclusively the {111} planes. The representative top-view and side-view models for 3D superstructure are depicted in Figure 6.8e and 6.8f, respectively.

The fact that three self assembled 3D superstructures by anisotropic shaped Fe_3O_4 nanocrystals are characteristic of preferential orientation ordering and shape-selective microphase segregation ambiguously elucidates that the shape of nanocrystals is a crucial component on the control of structures and orientations of self assemblies. Theoretically,

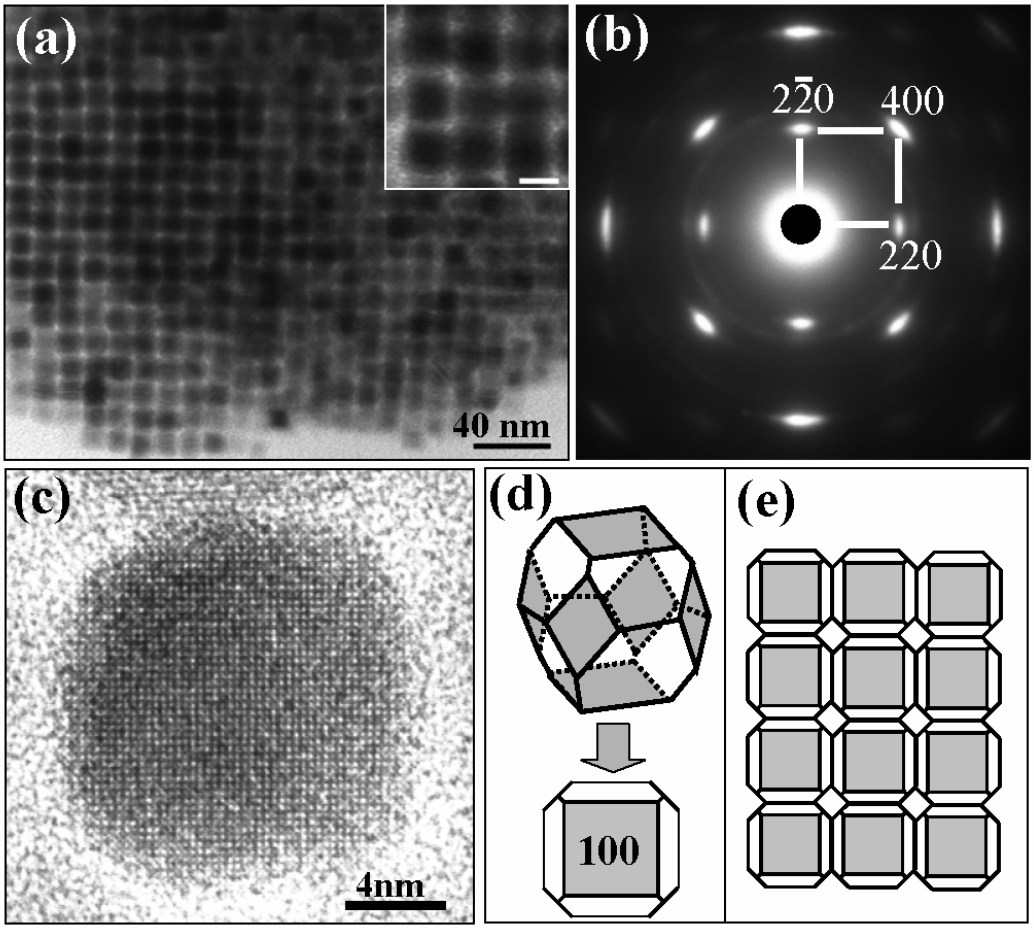

Figure 6.7 (a) is the primitive cubic-like 3D superstructure formed by TO shaped Fe_3O_4 nanocrystals. The inset is a part of enlargement. (b) is the SAED patterns, which is characterized by a set of four-fold symmetry spots, indicating the orientation is along [001]. (c) is the HRTEM image of TO shaped Fe_3O_4 nanocrystal. (d) shows 3D and 2D models of individual nanocrystal. (e) the top-view of 3D superstructure model.

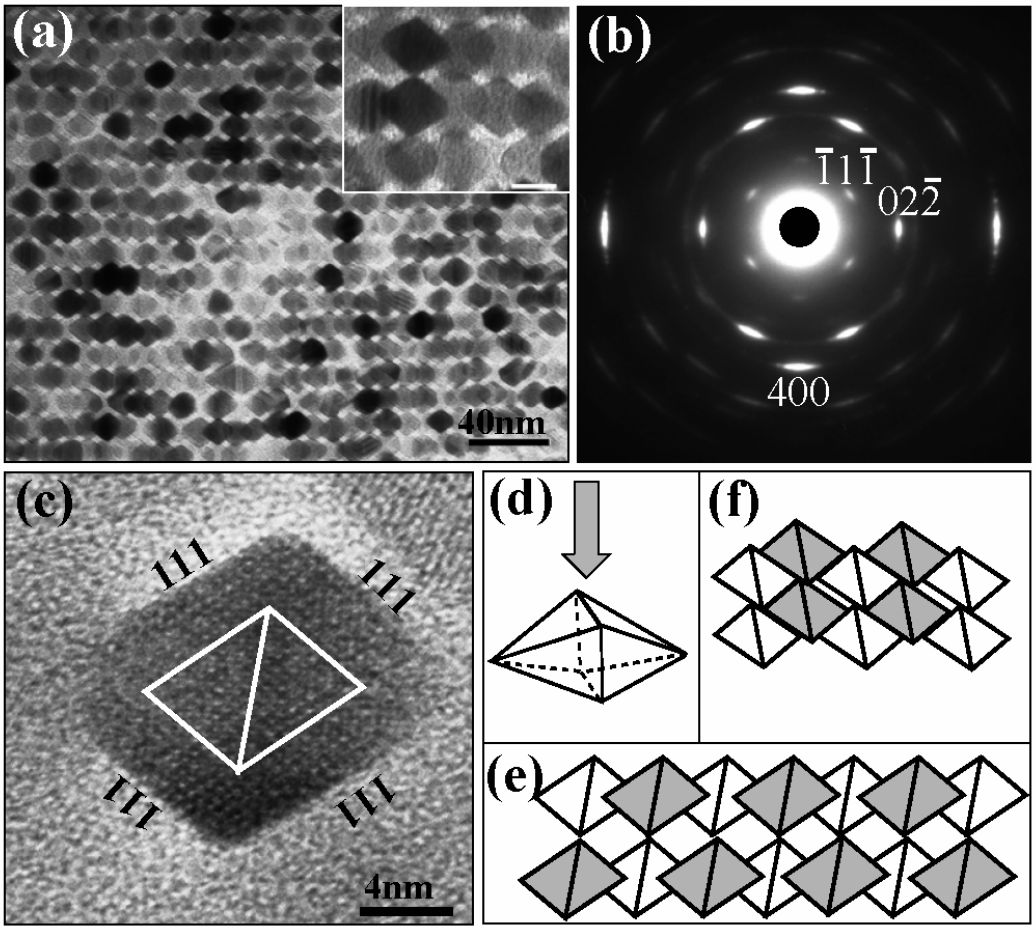

Figure 6.8 (a) is the body center cubic-like 3D superstructure formed by OT shaped Fe_3O_4 nanocrystals. The inset is a part of enlargement. (b) is the SAED patterns, which is characterized by a set of two-fold symmetry spots, indicating the orientation is along [011]. (c) is the HRTEM image of OT shaped Fe_3O_4 nanocrystal. (d) is the 3D model of individual nanocrystal. (e) and (f) are the top-view and side-view of 3D superstructure models, respectively.

the experimental phenomena are, in general, compatible with Onsager theory[46], a counterintuitive entropy concept, in which the loss of entropy associated with the translational, orientational ordering and mixing state is more than compensated for by the gain in entropy associated with the increase in free volume in the orientationally ordered state. As solvent evaporation and concentration increasing, the shape-selective microphase fractionation is the result of an effective attraction among like-components, which resembles the *"likes dissolve likes"* molecular behavior[47], and the well-known phenomenon, so-called "macromolecular crowing" in biology and "depletion attraction" in chemistry and physics[48-50].

The phase transitions of hexagonal platelet nanoparticles suspension have been investigated experimentally on 90 nm nickel (II) hydroxide[36] and 168 nm gibbsite plate-like particles suspensions[35], and theoretically by computer simulations. When the volume fraction is high, the columnar structure can occur due to a size segregation effect as predicated by computer simulation [43], which the size distribution of plate-like nanoparticles in ordered state is further narrowed compared to the mixing state. The computer simulation of shape effect on phase transition[44] also suggested that the effective diameter of different plate-like shapes is different, provided that the different plate-like shapes have the same facial area. Compared to the effective diameter of hexagonal platelet, the effective diameter is smaller for triangular platelet. As a consequence, size segregation effect leads to all of triangular platelet Fe_3O_4 nanocrystals (TP) being excluded from the construction of hexagonal columnar 3D superstructure in Type I self assembly (see Figure 6.5).

The truncated octahedral in Type II superstructure and octahedral in Type III are essentially the biaxial shape, the concept of effective diameter derived from platelet shaped nanoparticles is not applicable. A recent "soft sphere" model proposed by Korgel *et al*.[39] suggests that the facets or faces of nanocrystals such as truncated octahedral give rise to a stronger effective van der Waals attraction as the separation distance between neighbor nanocrystals decreases, and thus can induce face-to-face packing sequence and the preferential orientation ordering in superstructure. In addition, the dipolar interaction, either induced or permanent, can further boost the attractive interparticle interaction. Since Fe_3O_4 is magnetic and the magnetic dipolar is generally aligned along longitudinal direction, we presume that magnetic dipolar interaction plays an important role on the orientation ordering of Type III self assembled superstructure. In fact, the permanent dipolar moment and magnetic dipolar interaction have been taken into account of the formation of smectic A ordering in CdSe nanorods arrays[25] and Co nanorods bundles[51], respectively.

The shape evolution of anisotropic shaped Fe_3O_4 nanocrystals can be understood as follows. Without other reaction parameters variation, when a relatively faster growth rate is controlled and the temperature keeps at 260 ºC, most Fe_3O_4 nanocrystals are spherical. On the contrary, the shaped Fe_3O_4 nanocrystals are present predominately if the growth rate is adjusted to be slower with temperature maintaining at 220 ºC. Such results suggest that there is a strong correlation between the shape evolution and the growth rates as well as temperature in seed-mediated growth process. In cubic spinel structure, the surface energy associated with {100}, {110}, and {111} facets are the lowest ones, although a specific value for each of these facets may not be the same for different compounds[52-54].

Accordingly, when a faster growth rate and higher temperature are applied, a homogeneous growth on all crystallographic directions is favorable as a consequence of more energy is available. Therefore, the most stable morphology of nanocrystals would be the sphere due to the lowest total surface energy associated with spherical shape. On the other hand, as the reaction is kept at slower growth rate and lower temperature, the discrepancy in surface energies on different facets begins to play a dominant role in shape evolution. As the less iron cations are present in the solution, the tendency of minimizing the total surface energy induces iron cations selectively accumulate on the higher surface energy facets. As a result, anisotropic shaped nanocrystals are produced. Moreover, the reason that the observed shapes of Fe_3O_4 nanocrystals in final products comprise of four different anisotropic morphologies can be attributed to the fact that the basis shapes of Fe_3O_4 nanocrystals are tetrahedral and octahedral and the dominated terminal facets of observed Fe_3O_4 nanocrystals are {111} planes are well consistent with the general character of tetrahedral and octahedral shapes, which the {111} facets are the exclusive terminal planes. Finally, it is worth to note that the morphologies of Fe_3O_4 nanocrystals are dramatically different from the previously reported cubic $CoFe_2O_4$ nanocrystals, where the facets of nanocube are exclusively the {100} planes[55]. Certainly, this discrepancy in shape evolution between Fe_3O_4 and $CoFe_2O_4$ is enormous yet interesting, if taking into account of both Fe_3O_4 and $CoFe_2O_4$ possess the same invert cubic spinel structure and the synthetic reaction conditions are similar to each other. This might suggest that the surface energy for the same set of facets could be considerably sensitive to the chemical compositions of materials.

The investigation of magnetic properties on various anisotropic shapes of nanocrystals can provide great insights into the fundamental understanding of nanomagnetism. Figure 6.9 shows the field dependent magnetization for spherical and

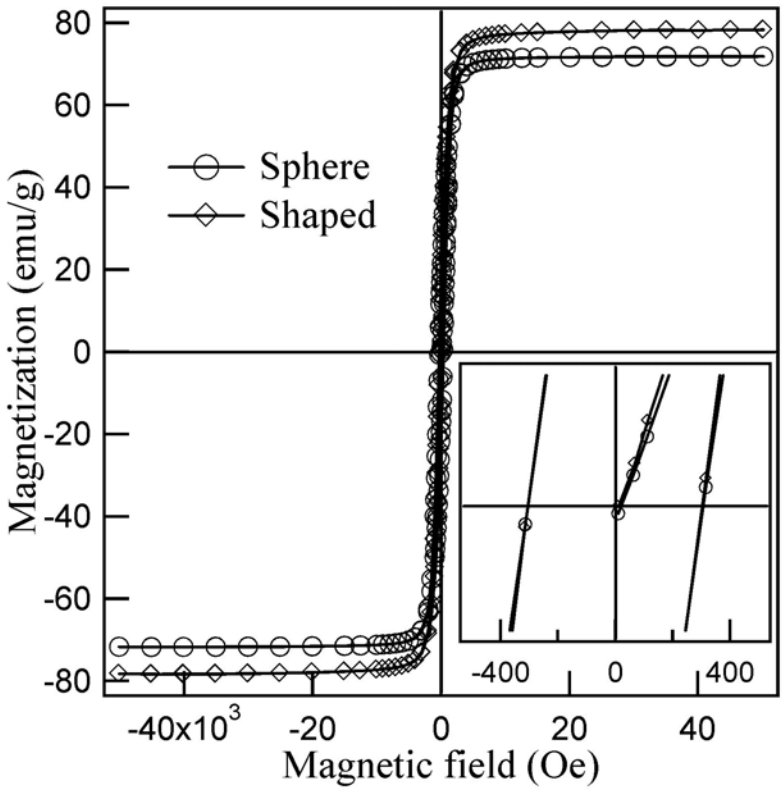

Figure 6.9 Field dependent magnetization measurements of 10 nm spherical and mixed anisotropic shaped 12 ~ 14 nm Fe_3O_4 nanocrystals at 5 K.

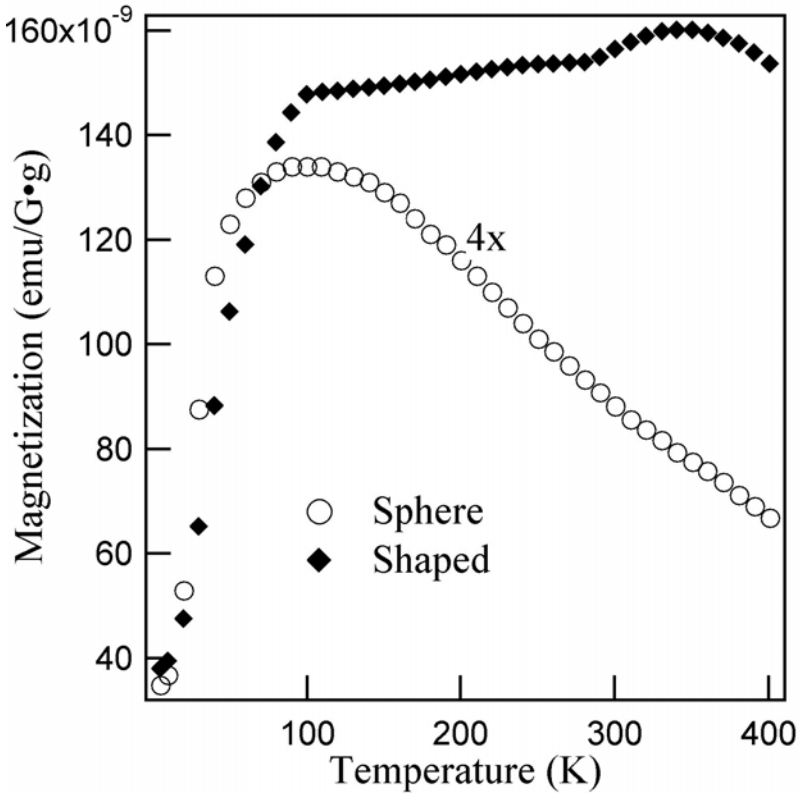

Figure 6.10 Zero field cooling (ZFC) magnetization measurements of 10 nm spherical and mixed anisotropic shaped 12 ~ 14 nm Fe_3O_4 nanocrystals under applied 100G magnetic field.

mixed anisotropic shaped Fe_3O_4 nanocrystals at 5 K. The enlarged inset plots clearly display the hysteresis behavior for both spherical and shaped nanocrystals. No significant difference is observed for the saturation magnetization (M_S), remanent magnetization (M_R), and coercivity (H_C) as the morphology varies from spherical to anisotropic shapes. Judging from our previous results on the magnetic properties of spherical and cubic $CoFe_2O_4$ nanocrystals [55], the almost equal values of coercivity for spherical and anisotropic shaped Fe_3O_4 nanocrystals can be attributed to the surface anisotropy effect.

The zero-field-cooling magnetization measurements of spherical and anisotropic shaped Fe_3O_4 nanocrystals are presented in Figure 6.10. It is not particularly surprised that as temperature increasing, the magnetization of mixed anisotropic shaped Fe_3O_4 nanocrystals first increases quickly and then progressively covers a broad range of temperature, and no clear-cut maximum point can be derived from thermally superparamagnetic relaxation.

According to Stoner-Wohlfarth single domain theory[56,57], the anisotropy energy (E_A) of nanocrystal can be expressed as

$$E_A = KV \sin^2\theta \qquad (6.\ 1)$$

where K is the magnetocrystalline anisotropy constant, V is the volume of nanocrystal, and θ is the angle between ease axis of nanocrystal and magnetization direction. From equation (1), the anisotropy energy (E_A) depends on magnetocrystalline anisotropy constant (K) and the volume (V) of nanocrystal. Because the as-synthesized Fe_3O_4 nanocrystals are composed of different anisotropic shapes, the anisotropy constant values

are varied due to the shape anisotropy. Similarly, the progressive variation of geometric volumes associated with different polyhedral shapes also can contribute the modification to the anisotropy energy. As a result, a series of anisotropy energy barriers need to be overcome in order to flip the magnetic moments of nanocrystals from the blocking state to the superparamagnetic one as the temperature is steadily increasing. Therefore, an unusual broad flattened curve, instead of a single narrow peak is shown in zero-field-cooling magnetization measurements.

6.4 Conclusions

Magnetite nanocrystals with truncated tetrahedral platelet, truncated octahedral and octahedral shapes have been synthesized by seed-mediated growth method. Highly oriented 3-D superlattices formed by such shaped Fe_3O_4 nanocrystals have been determined to be hexagonal columnar, primitive cubic-like, and body center cubic-like by the complementary analyses using bright and dark field TEM, HRTEM and SAED techniques. Shape-selective phase demixing or microphase segregation and highly orientational ordering are striking features in three types of 3D self assembled superstructures. The results clearly elucidate that the shapes of nanocrystals indeed play a vital role in the self assembly and the orientational ordering of superlattices are strongly dependent on the anisotropic shapes of nanocrystals. Although the entropic effect is in principle the driving force for the formation of 3D self assembled superstructures, the van der Waals attractive interaction in face-to-face stacking sequence and magnetic dipolar interaction along longitudinal direction may also provide contribution to the orientational ordering. The ability to control the shapes of nanocrystals and understanding the

relationship between shape and complex structures certainly facilitate the applications of magnetic nanocrystals as building blocks for high density data storage.

6.5 References

(1) Whitesides, G. M.; Grzybowski, B. *Science* **2002**, *295*, 2418.

(2) Whitesides, G. M.; Mathias, J. P.; Seto, C. T. *Science* **1991**, *254*, 1312.

(3) Whitesides, G. M.; Boncheva, M. *Proc. Natl. Acad. Sci. U. S. A.* **2002**, *99*, 4769.

(4) Heath, J. R. *Acc. Chem. Res.* **1999**, *32*, 388.

(5) Murray, C. B.; Kagan, C. R.; Bawendi, M. G. *Annu. Rev. Mater. Sci.* **2000**, *30*, 545.

(6) Bowden, N. B.; Weck, M.; Choi, I. S.; Whitesides, G. M. *Acc. Chem. Res.* **2001**, *34*, 231.

(7) Huang, Y.; Duan, X.; Wei, Q.; Lieber, C. M. *Science* **2001**, *291*, 630.

(8) Redl, F. X.; Cho, K. S.; Murray, C. B.; O'Brien, S. *Nature* **2003**, *423*, 968.

(9) Xia, Y.; Yang, P. *Adv. Mater.* **2003**, *15*, 351.

(10) Burda, C.; Chen, X.; Narayanan, R.; El-Sayed, M. A. *Chemical Reviews* **2005**, *105*, 1025.

(11) Whetten, R. L.; Khoury, J. T.; Alvarez, M. M.; Murthy, S.; Vezmar, I.; Wang, Z. L.; Stephens, P. W.; Cleveland, C. L.; Luedtke, W. D.; Landman, U. *Adv. Mater.* **1996**, *8*, 428.

(12) Wang, Z. L.; Harfenist, S. A.; Vezmar, I.; Whetten, R. L.; Bentley, J.; Evans, N. D.; Alexander, K. B. *Adv. Mater.* **1998**, *10*, 808.

(13) Kiely, C. J.; Fink, J.; Brust, M.; Bethell, D.; Schiffrin, D. J. *Nature* **1998**, *396*, 444.

(14) Sun, S.; Murray, C. B.; Weller, D.; Folks, L.; Moser, A. *Science* **2000**, *287*, 1989.

(15) Murray, C. B.; Sun, S.; Doyle, H.; Betley, T. *MRS Bulletin* **2001**, *26*, 985.

(16) Courty, A.; Fermon, C.; Pileni, M.-P. *Adv. Mater.* **2001**, *13*, 254.

(17) Shevchenko, E. V.; Talapin, D. V.; Rogach, A. L.; Kornowski, A.; Haase, M.; Weller, H. *J. Am. Chem. Soc.* **2002**, *124*, 11480.

(18) Murray, C. B.; Kagan, C. R.; Bawendi, M. G. *Science* **1995**, *270*, 1335.

(19) Talapin, D. V.; Shevchenko, E. V.; Kornowski, A.; Gaponik, N.; Haase, M.;

Rogach, A. L.; Weller, H. *Adv. Mater.* **2001**, *13*, 1868.

(20) Bentzon, M. D.; Van Wonterghem, J.; Moerup, S.; Tholen, A.; Koch, C. J. W. *Philos. Mag. B* **1989**, *60*, 169.

(21) Kim, F.; Kwan, S.; Akana, J.; Yang, P. *J. Am. Chem. Soc.* **2001**, *123*, 4360.

(22) Li, L.-s.; Walda, J.; Manna, L.; Alivisatos, A. P. *Nano Lett.* **2002**, *2*, 557.

(23) Li, L.-S.; Alivisatos, A. P. *Adv. Mater.* **2003**, *15*, 408.

(24) Jana, N. R. *Angew. Chem., Int. Ed.* **2004**, *43*, 1536.

(25) Talapin, D. V.; Shevchenko, E. V.; Murray, C. B.; Kornowski, A.; Foerster, S.; Weller, H. *J. Am. Chem. Soc.* **2004**, *126*, 12984.

(26) Clark, T. D.; Tien, J.; Duffy, D. C.; Paul, K. E.; Whitesides, G. M. *J. Am. Chem. Soc.* **2001**, *123*, 7677.

(27) Oliver, S. R. J.; Clark, T. D.; Bowden, N.; Whitesides, G. M. *J. Am. Chem. Soc.* **2001**, *123*, 8119.

(28) Clark, T. D.; Ferrigno, R.; Tien, J.; Paul, K. E.; Whitesides, G. M. *J. Am. Chem. Soc.* **2002**, *124*, 5419.

(29) Xia, Y.; Editor *Special Issue: Photonic Crystals. Adv. Mater.*, 2001; Vol. 13.

(30) Ohara, P. C.; Leff, D. V.; Heath, J. R.; Gelbart, W. M. *Phys. Rev. Lett.* **1995**, *75*, 3466.

(31) Bartlett, P.; Ottewill, R. H.; Pusey, P. N. *Phys. Rev. Lett.* **1992**, *68*, 3801.

(32) Frenkel, D.; Louis, A. A. *Phys. Rev. Lett.* **1992**, *68*, 3363.

(33) Eldridge, M. D.; Madden, P. A.; Frenkel, D. *Nature* **1993**, *365*, 35.

(34) van der Kooij, F. M.; Lekkerkerker, H. N. W. *J. Phys. Chem. B* **1998**, *102*, 7829.

(35) van der Kooij, F. M.; Kassapidou, K.; Lekkerkerker, H. N. W. *Nature* **2000**, *406*, 868.

(36) Brown, A. B. D.; Clarke, S. M.; Rennie, A. R. *Langmuir* **1998**, *14*, 3129.

(37) Brown, A. B. D.; Ferrero, C.; Narayanan, T.; Rennie, A. R. *Eur. Phys. J. B* **1999**, *11*, 481.

(38) McGrother, S. C.; Gil-Villegas, A.; Jackson, G. *Mol. Phys.* **1998**, *95*, 657.

(39) Korgel, B. A.; Fullam, S.; Connolly, S.; Fitzmaurice, D. *J. Phys. Chem. B* **1998**, *102*, 8379.

(40) Lalatonne, Y.; Richardi, J.; Pileni, M. P. *Nature Materials* **2004**, *3*, 121.

(41) Frenkel, D.; Lekkerkerker, H. N. W.; Stroobants, A. *Nature* **1988**, *332*, 822.

(42) Bates, M. A.; Frenkel, D. *J. Chem. Phys.* **1998**, *109*, 6193.

(43) Bates, M. A.; Frenkel, D. *J. Chem. Phys.* **1999**, *110*, 6553.

(44) Bates, M. A. *J. Chem. Phys.* **1999**, *111*, 1732.

(45) Auer, S.; Frenkel, D. *Nature* **2001**, *413*, 711.

(46) Onsager, L. *Ann. N. Y. Acad. Sci.* **1949**, *51*, 627.

(47) Israelachvili, J. N. *Intermolecular and Surface Forces*; 2nd ed.; Academic Press: New York, 1992.

(48) Lekkerkerker, H. N. W.; Stroobants, A. *Nature* **1998**, *393*, 305.

(49) Adams, M.; Dogic, Z.; Keller, S. L.; Fraden, S. *Nature* **1998**, *393*, 349.

(50) Anderson, V. J.; Lekkerkerker, H. N. W. *Nature* **2002**, *416*, 811.

(51) Dumestre, F.; Chaudret, B.; Amiens, C.; Respaud, M.; Fejes, P.; Renaud, P.; Zurcher, P. *Angew. Chem., Int. Ed.* **2003**, *42*, 5213.

(52) Fang, C. M.; Parker, S. C.; De With, G. *Key Eng. Mater.* **2002**, *206-213*, 543.

(53) Fang, C. M.; Parker, S. C.; De With, G. *J. Am. Ceram. Soc.* **2000**, *83*, 2082.

(54) Davies, M. J.; Parker, S. C.; Watson, G. W. *J. Mater. Chem.* **1994**, *4*, 813.

(55) Song, Q.; Zhang, Z. J. *J. Am. Chem. Soc.* **2004**, *126*, 6164.

(56) Stoner, E. C.; Wohlfarth, E. P. *Trans. Roy. Soc.* **1948**, *A240*, 599.

(57) Stoner, E. C.; Wohlfarth, E. P. *IEEE Trans. Magn.* **1991**, *27*, 3475.

CHAPTER 7

PRECURSOUR DESIGN, SIZE CONTROLLED SYNTHESIS AND SUPERPARAMAGNETIC PROPERTIES STUDIES OF MANGANESE FERRITE NANOCRYSTALS

Abstract

By deliberately substituted ligand benzoylacetone (bzac) for acetylacetone (acac) in coordination compounds of manganese (II) acetylacetonate, $Mn(acac)_2$ and iron (III) acetylacetonate, $Fe(acac)_3$, the thermal stabilities of these molecular precursors show a well-matched onset thermal decomposition temperature characterized by the thermogravimetic analysis and differential scanning calorimetry. High quality manganese ferrite, $MnFe_2O_4$ nanocrystals with tunable size have been synthesized by using these substituted molecular precursors in a non-hydrolysis seed-mediated growth process. The crystal structure, sizes and size distributions of as-synthesized $MnFe_2O_4$ nanocrystals have been characterized by X-ray diffraction, low magnification TEM and high resolution transmission electron microscopy (HRTEM). Moreover, the studies on magnetic properties clearly indicate that the superparamagnetic properties such as blocking temperature and coercivity are dependent on the size of $MnFe_2O_4$ nanocrystals, which is well consistent with Stoner-Wohlfarth single domain theory.

7.1 Introduction

Nanoscale magnetic materials have been extensively investigated due to their novel fundamental size dependent chemical and physical properties and a wide range of technological applications such as magnetic data storage, target drug delivery, magnetic resonance imaging (MRI) contrast enhancement and ferrofluids[1-8]. Recent advances in synthesis of colloidal nanocrystals have demonstrated that high temperature thermal decomposition of molecular precursors such as coordination compounds or organometallic compounds in organic solvents is an effective approach to the synthesis of high quality colloidal nanocrystals in terms of crystal structures, sizes and size distributions[9-13]. Molecular precursors have become one of the most important parameters on the size control of nanocrystals in the thermal decomposition reaction system. In particular, for magnetic metal oxides, various molecular precursors have been extensively exploited in the syntheses of different magnetic nanomaterials. For example, different single metal molecular precursors including $FeCup_3$, $Fe(CO)_5$, $Fe(acac)_3$, and iron carboxylate complexes have been successfully used to prepare iron oxides nanoparticles[14-17]. However, to produce complex multi-metal oxides such as spinel ferrites, MFe_2O_4 (M = Mn, Co, Ni, Cu, Zn) nanocrystals, the applicability of the single molecular precursor having different metals is formidably limited by the availability of such type precursors and the flexibility of chemical composition control of nanocrystals. An effective alternative depends on multiple single precursors for a given spinel ferrite. Therefore, the thermal stability of molecular precursor becomes a vital role on the size-controlled synthesis of nanocrystals. Herein, by deliberately substituted benzoylacetone (bzac) for acetylacetone (acac) in coordination compounds of $Mn(acac)_2$ and $Fe(acac)_3$,

the effect of thermal stability on the size-controlled synthesis of $MnFe_2O_4$ nanocrystals is addressed. The systematic studies on the thermal properties show that the thermal stability of molecular precursors specifically the onset thermal decomposition temperature can be precisely controlled by manipulation of inductive electron effect and steric effect of ligands.

By using these new $Mn(bzac)_2$ and $Fe(bzac)_3$ molecular precursors, high quality manganese ferrite, $MnFe_2O_4$ nanocrystals with tunable size from 4.5 nm to 12 nm have been synthesized by a non-hydrolysis seed-mediated growth method. The magnetic studies of these $MnFe_2O_4$ nanocrystals show the typical size-dependent superparamagnetic properties. The blocking temperature and coercivity are clearly dependent on the size of $MnFe_2O_4$ nanocrystals. The blocking temperature and the coercivity at 5 K increase from 32 K to 123 K and from 171 Oe to 447 Oe, respectively, as the nanocrystal size increasing. The superparamagnetic behaviors of these $MnFe_2O_4$ nanocrystals are consistent with the Stoner-Wohlfarth single domain theory. Such interesting and important size dependent superparamagnetic properties certainly facilitate the $MnFe_2O_4$ nanocrystals in various technological applications, including magnetocaloric refrigeration[18], image contrast enhancement agents in magnetic resonance imaging (MRI) technologies[19], magnetic carriers for site-specific targeting drug delivery[4], and very recent spin valve biomolecules detection systems[20-22].

7.2 Experimental Sections

7.2.1 Molecular Precursors Synthesis

1-benzoylacetone (99%) and manganese acetate tetrahydrate (99+%) were purchased from Aldrich Inc. Iron nitrate (98+%) and sodium acetate (99%) were purchased from Fisher Scientific Inc.. All chemicals were used as received without any further treatment.

The preparations of coordination compounds of Mn (II) benzoylacetonate, $Mn(bzac)_2$ and iron (III) benzoylacetonate, $Fe(bzac)_3$, were followed by a reported method[23,24]. In brief, under N_2 gas protection, a freshly-made 100 mL of 0.4 M 1-benzoylacetone alcoholic solution with 5g sodium acetate was added dropwise into 100 mL of 0.2 M manganese acetate solution, and the yellowish precipitates were formed. After stirring for 8 hours, the yellow precipitates were filtrated and washed with ethanol and ether alternatively, and dried in a vacuum oven at 40 °C for 8 hours. The dry powder of $Mn(bzac)_2$ was stored in a glove box for subsequent use. A similar synthetic procedure was used to prepare $Fe(bzac)_3$.

7.2.2 Size-Controlled Synthesis of $MnFe_2O_4$ Nanocrystals

To make $MnFe_2O_4$ nanocrystals, the following procedure was used. A mixture of 30 mL phenyl ether, 1 mmol $Mn(bzac)_2$, 2 mmol $Fe(bzac)_3$, 10 mmol 1,2 hexadecandiol, 3 mL oleic acid and 3 mL oleylamine was heated up to 260 ºC, and kept reflux at 260ºC for 30 min. After the solution was cooled to room temperature, 20 mL ethanol was added, a black precipitates were collected by either centrifugation or using a permanent magnet. This black precipitates were re-dispersed in hexane and re-precipitated by addition of

acetone. The size of as-synthesized $MnFe_2O_4$ nanocrystals is about 4 nm. To prepare larger $MnFe_2O_4$ nanocrystals, the seed mediated growth process was employed. By adjusting the amount of seed and precursors, the size of $MnFe_2O_4$ nanocrystals can be tuned up to 12 nm. For example, in the presence of 30 mL phenyl ether, 1 mmol $Mn(bzac)_2$ and 2 mmol $Fe(bzac)_3$, 10 mmol 1-octadecanol, 3 mL oleic acid and 3 mL oleylamine, 8 nm $MnFe_2O_4$ nanocrystals were produced by using 60 mg of 4 nm $MnFe_2O_4$ nanocrystals as seeds. To further increase the size of $MnFe_2O_4$ nanocrystals, the above synthetic procedure is repeatedly used.

7.2.3 Characterization

The X-ray diffraction experiments were carried out on a Bruker D8 Advance X-ray diffractometer with Cu *Kα* radiation. Transmission electron microscopy (TEM) was conducted on JEOL 100C operating at 100 kV and high resolution transmission electron microscopy (HRTEM) analyses were performed on a JEOL 4000 EX at 400 kV, respectively. The thermogravimetic analysis (TGA) and differential scanning calorimetry (DSC) were collected at a heating rate of 10 °C/min to 400 °C or 700 °C using a Netzsch Luxx STA 409 PG. The Superconductor Quantum Interference Devices (SQUID) (Quantum Design MPMS - 5S) magnetometer was used to conduct magnetic measurements with magnetic field up to ± 5 Tesla and temperature ranging from 5 K to 400 K. All samples for magnetic measurements were prepared by dispersing dry powdered $MnFe_2O_4$ nanocrystals in an eicosane ($C_{20}H_{42}$, 99%, Aldrich) matrix to minimize the interparticle interaction effect.

7.3 Results and Discussion

The TGA and DSC curves recorded simultaneously for $Fe(bzac)_3$ at a rate of 10 °C/min in a dynamic atmosphere of nitrogen are shown in Figure 7.1a. The thermal decomposition of $Fe(bzac)_3$ is characteristic of a continue weight loss of 55% in TGA curve and two closed exothermic conjugated with one endothermic events occurring at onset temperatures of 221 °C, 228 °C and 344 °C respectively in DSC curve. Similarly, the TGA and DSC curves of $Mn(bzac)_2$ in Figure 7.1b show an endothermic 5% mass loss from 30 °C to 120 °C that is characteristic of the loss of absorbed water. The subsequently small exothermic peak without mass loss at 142 °C indicates a melting event, which is in agreement with previous result[23,25]. Further 50% weight loss associated with a combination of exothermic and endothermic peaks occurring at onset temperature of 234 °C is indicative of thermal decomposition of $Mn(bzac)_2$. Similarly, Figure 7.2a shows the TGA and DSC curves for $Fe(acac)_3$. The thermal decomposition of $Fe(acac)_3$ first occurs at 186 °C, which is characterized by a sharp exothermic peak and a 25% weight loss. The subsequent decomposition is a steady weight loss with one tiny and one large and broad exothermic peak. The TGA and DSC analyses for $Mn(acac)_2$ are plotted in Figure 7.2b. It can be seen that a sharp 30% exothermic weight loss occurring at onset temperature of 249 °C is a clear identification of thermal decomposition of $Mn(acac)_2$. This decomposition remains up to 800 °C by a series of exothermic peaks and the continue weight loss. These results are consistent with other reported results[25].

Due to the fact that the synthesis of $MnFe_2O_4$ nanocrystals requires a simultaneously thermal decomposition of two molecular precursors, a closer, if not identical, of onset thermal decomposition temperature of molecular precursors is

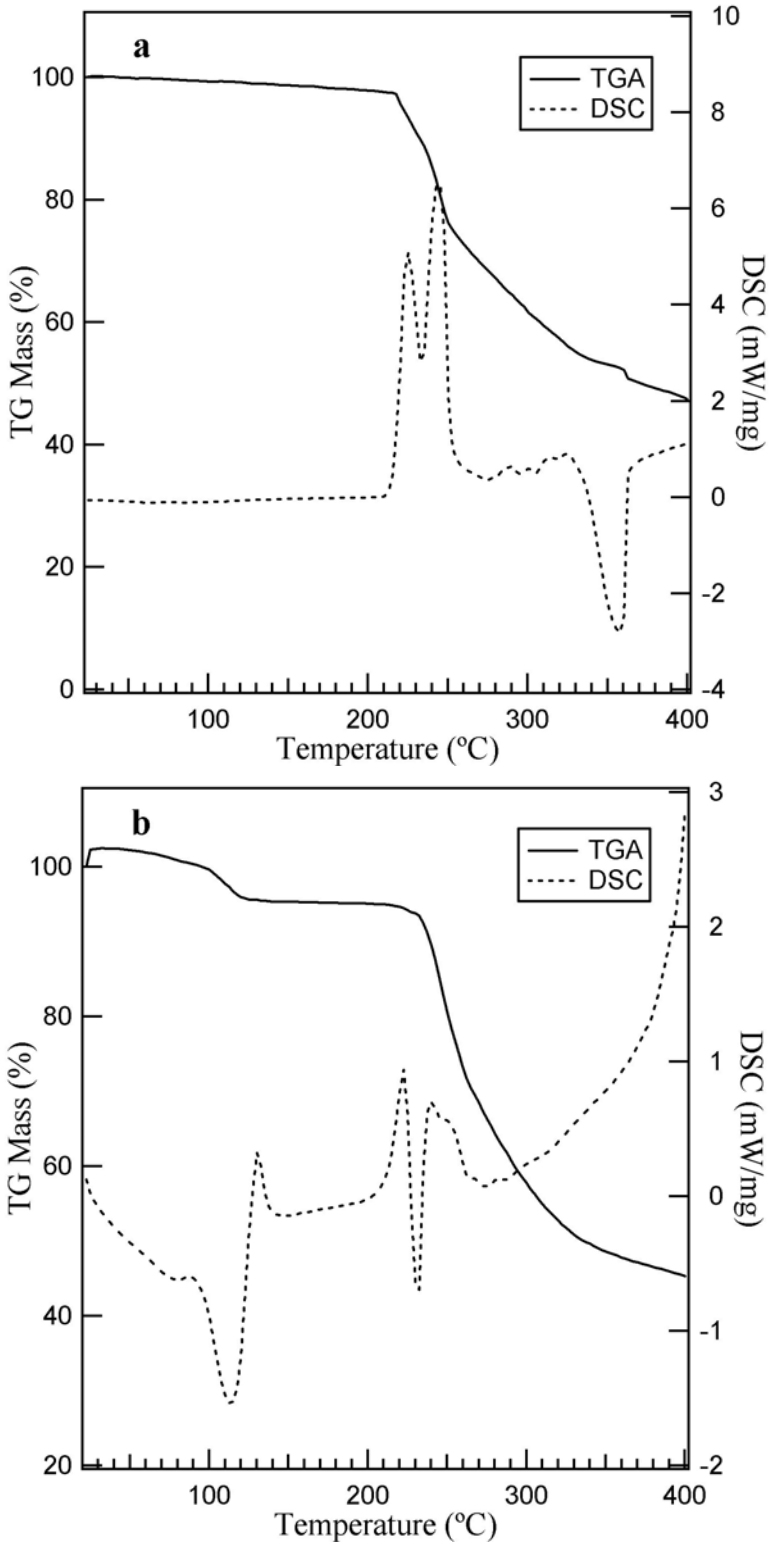

Figure 7.1 The TGA and DSC curves for (a) $Fe(bzac)_3$ and (b) $Mn(bzac)_2$, respectively.

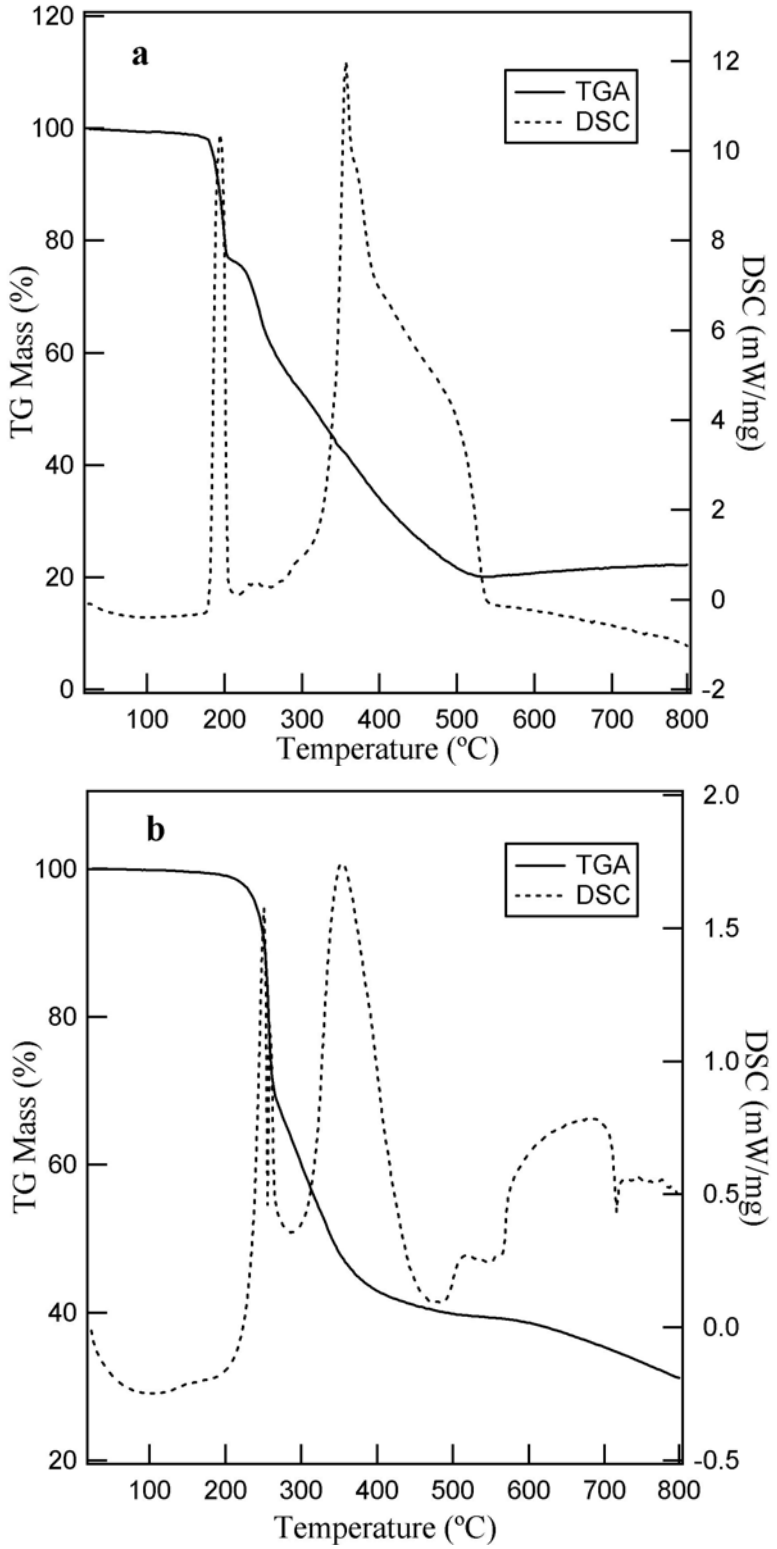

Figure 7.2 The TGA and DSC curves for (a) $Fe(acac)_3$ and (b) $Mn(acac)_2$, respectively.

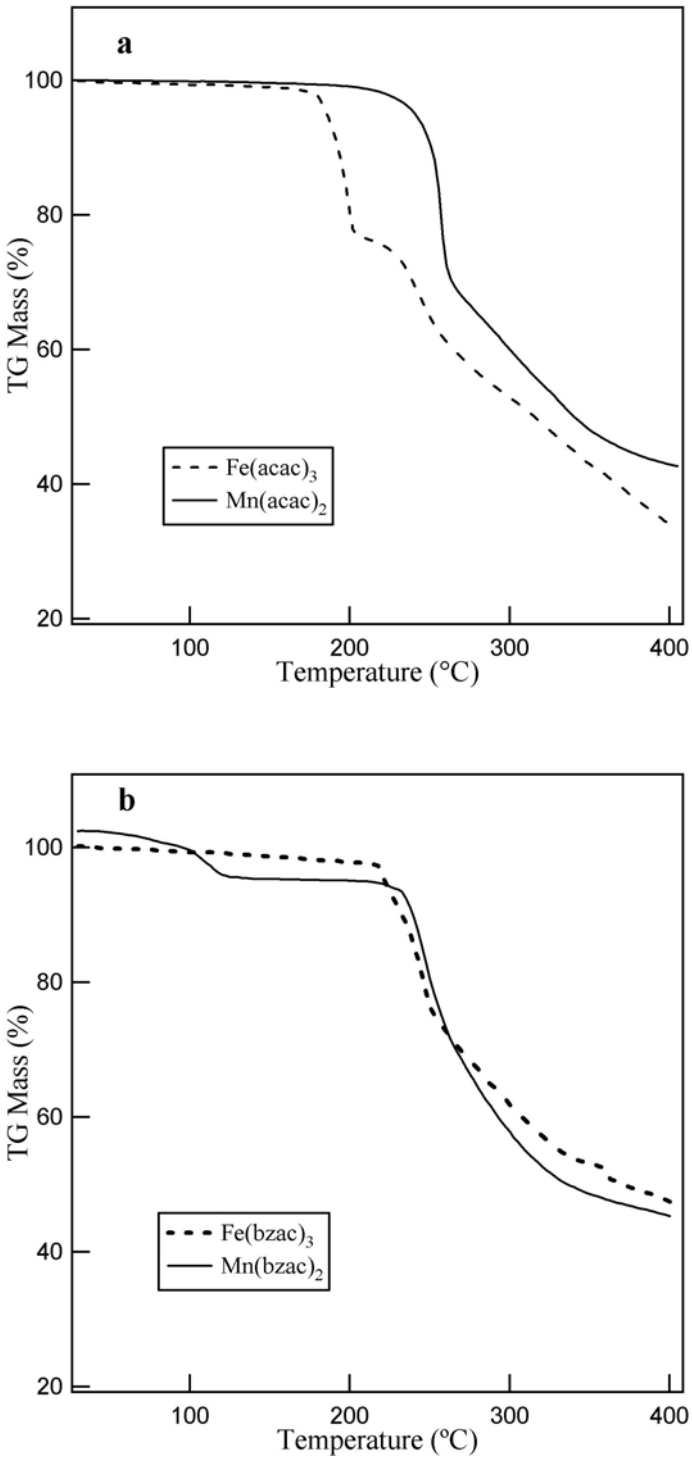

Figure 7.3 The comparison of TGA results (a) $Fe(acac)_3$ and $Mn(acac)_2$, (b) $Fe(bzac)_3$ and $Mn(bzac)_2$.

desirable. From the re-plotted TGA curves for $Fe(acac)_3$ and $Mn(acac)_2$ in Figure 7.3 a, it clearly shows that the onset thermal decomposition of $Fe(acac)_3$ is more than 60 °C different from that of $Mn(acac)_2$. In contrast, by purposely substitution of phenyl group for methyl group in acac ligand, the TGA curves for $Fe(bzac)_3$ and $Mn(bzac)_2$ in Figure 7.3b evidently show that $Fe(bzac)_3$ and $Mn(bzac)_2$ possess a well-matched thermal decomposition temperature relative to those of $Fe(acac)_3$ and $Mn(acac)_2$. Thus, such results unambiguously indicate that $Fe(bzac)_3$ and $Mn(bzac)_2$ are the better molecular precursors for the synthesis of $MnFe_2O_4$. The variation of thermal stabilities of $Fe(bzac)_3$ and $Mn(bzac)_2$ can be attributed to the cooperative electronic effect and steric effect of phenyl group[26], as the phenyl group is a weak electron acceptor relative to the methyl group, causing a small variation of thermal stability for both $Mn(bzac)_2$ and $Fe(bzac)_3$. On the other hand, the phenyl group is a bulky group and consequently introduces a steric effect by holding the oxygen atoms in bzac ligand close together compared to the distance of oxygen atoms in acac ligand[27-29]. As a result, for the larger cation Mn^{2+} in tetrahedral configuration, the thermal stability of $Mn(bzac)_2$ decreases, while for smaller Fe^{3+} in octahedral configuration, the thermal stability of $Fe(bzac)_3$ is less susceptible to such steric effect. Therefore, the decrease in thermal stability of $Mn(bzac)_2$ and enhancement in thermal stability of $Fe(bzac)_3$ result in an almost identical onset thermal decomposition temperature between $Mn(bzac)_2$ and $Fe(bzac)_3$.

By using $Mn(bzac)_2$ and $Fe(bzac)_3$ as molecular precursors, $MnFe_2O_4$ nanocrystals can be synthesized and the quality in terms of chemical composition and size distribution, in particular, for smaller $MnFe_2O_4$ nanocrystals can be greatly improved. As shown in

Figure 7.4, microscaled self assembled superlattice can be easily formed by simply drop-casting concentrated 4.5 nm $MnFe_2O_4$ nanocrystals suspension on TEM grids, indicating

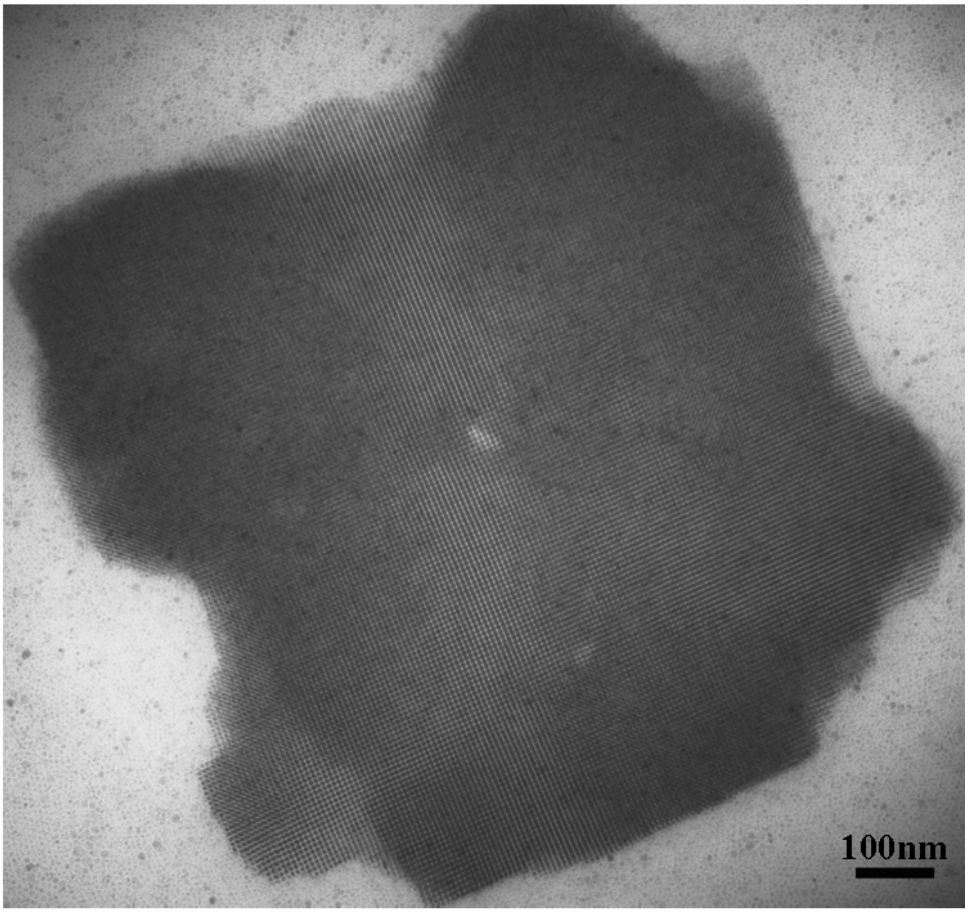

Figure 7.4 Micrometer scale superlattice formed by 4.5 nm spherical $MnFe_2O_4$ nanocrystals.

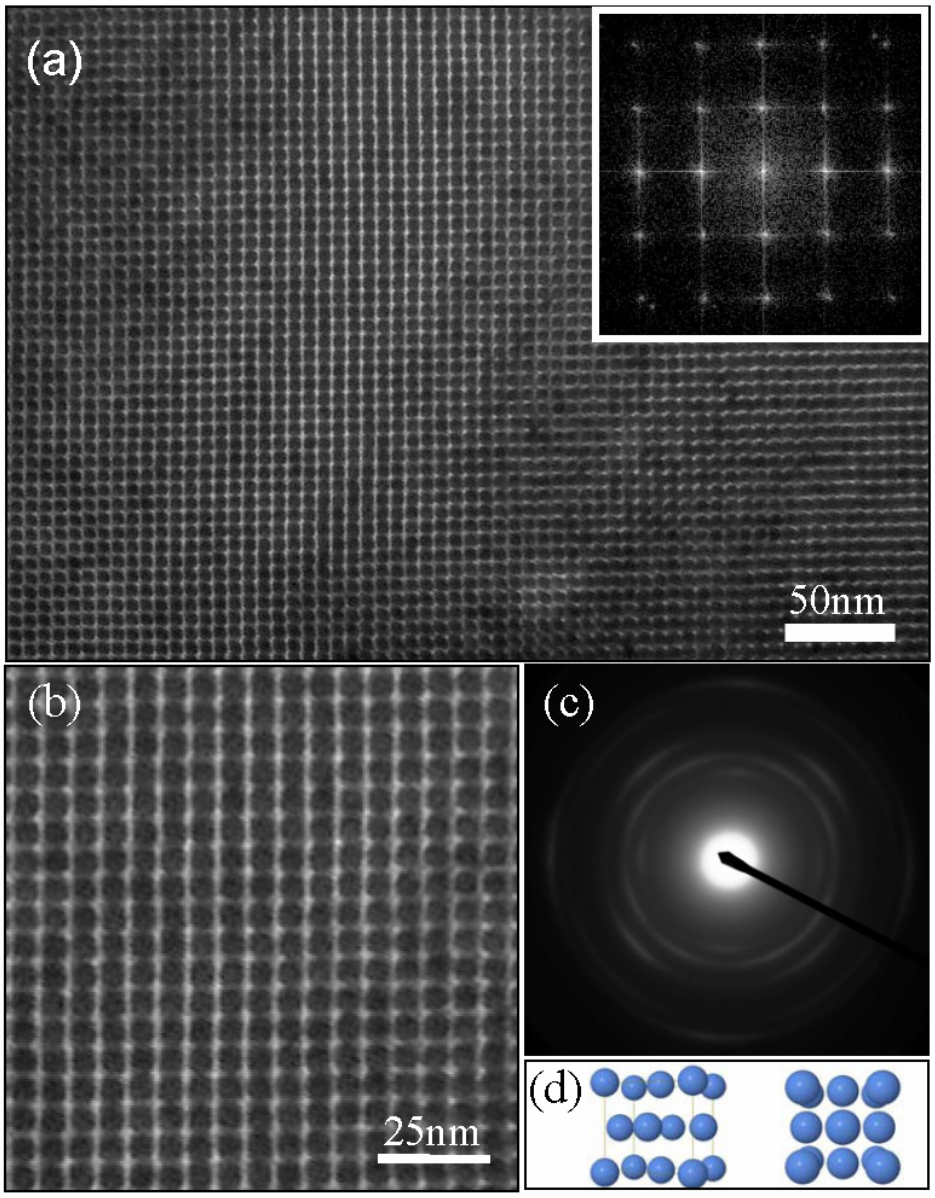

Figure 7.5 (a) face-center-cubic (*fcc*) superlattice. The inset shows FFT image with four-fold symmetry. (b) partial enlargement of (a). (c) SAED patterns show a series of spots instead of ring patterns, indicating partial orientation ordering in superlattice. (d) fcc structure model (left) and projection view along [001] direction (right).

a very narrow size distribution. The partial enlargements of this superlattice, inset fast Fourier Transformation (FFT) image, selected area electron diffraction patterns (SAED) and *fcc* models are displayed in Figure 7.5a, b, c and d, respectively. Clearly, these results reveal that the superlattice is a face-center-cubic (*fcc*) structure with orientation along [001] direction. Some interesting superlattices formed by various sized $MnFe_2O_4$ nanocrystals are shown in Figure 7.6. Additionally, the typical low magnification TEM and HRTEM images of 12 nm $MnFe_2O_4$ nanocrystals synthesized by seed-mediated growth are shown in Figure 7.7, which verify these $MnFe_2O_4$ nanocrystals are highly crystallized single crystals due to the clear atomic lattice fringes in HRTEM image. Moreover, the crystal structure of as-synthesized $MnFe_2O_4$ nanocrystals is indexed to be the cubic spinel structure by SAED in Figure 7.5c and X-ray diffraction patterns in Figure 7.8.

The temperature dependent magnetization measurements of $MnFe_2O_4$ nanocrystals with size ranging from 4.5 nm to 12 nm are shown in Figure 7.9a. The values of blocking temperatures (T_B) are plotted against sizes in Figure 7.9b. The blocking temperatures of $MnFe_2O_4$ nanocrystals are observed linearly dependent on the sizes of nanocrystals. The field dependent magnetization measurements of different sized $MnFe_2O_4$ nanocrystals at 5 K are presented in Figure 7.10a. From the inset enlarged part of hysteresis curves, it can be clearly seen that all $MnFe_2O_4$ nanocrystals show hysteresis behavior. The values of coercivity as a function of nanocrystal sizes are in Figure 7.10b. Clearly, as the size of $MnFe_2O_4$ nanocrystals increases, the coercivity of $MnFe_2O_4$ nanocrystals increases.

The correlation between the superparamagnetic properties of $MnFe_2O_4$ nanocrystals and their size is consistent with the size dependence of the magnetocrystalline anisotropy

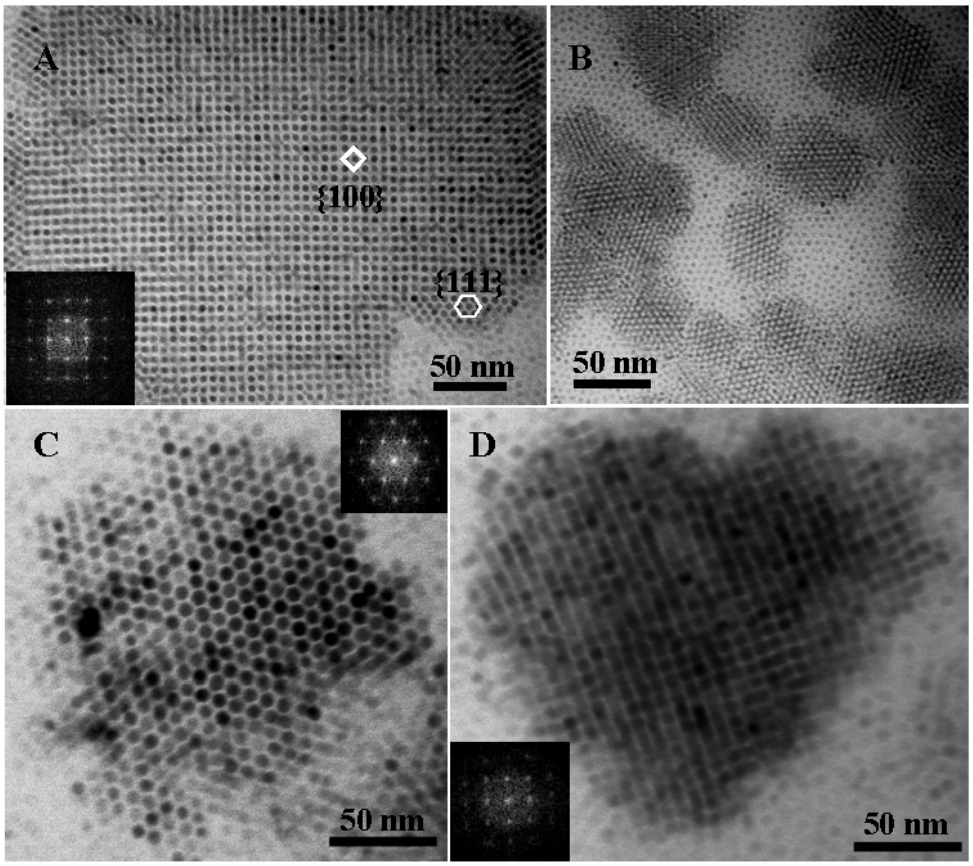

Figure 7.6 Various superlattices formed by different sized $MnFe_2O_4$ nanocrystals. (a) 5 nm, the inset FFT shows four-fold symmetry, (b) 3 nm, (c) hexagonal close packing (*hcp*) by 8 nm spherical $MnFe_2O_4$ nanocrystals, the inset FFT shows six-fold symmetry, (d) an interesting heart-shaped superlattice with four-fold symmetry as indicated by inset FFT image.

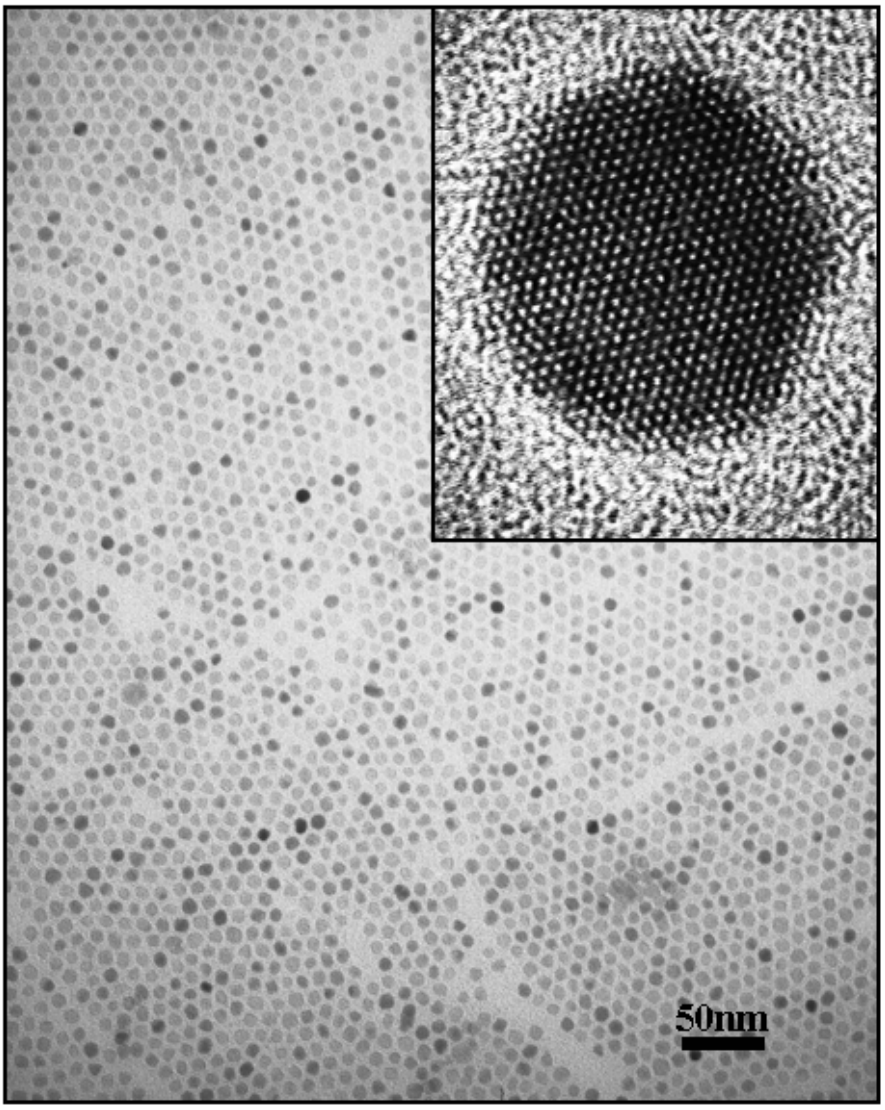

Figure 7.7 The typical TEM and HRTEM (inset) images of 12 nm spherical $MnFe_2O_4$ nanocrystals.

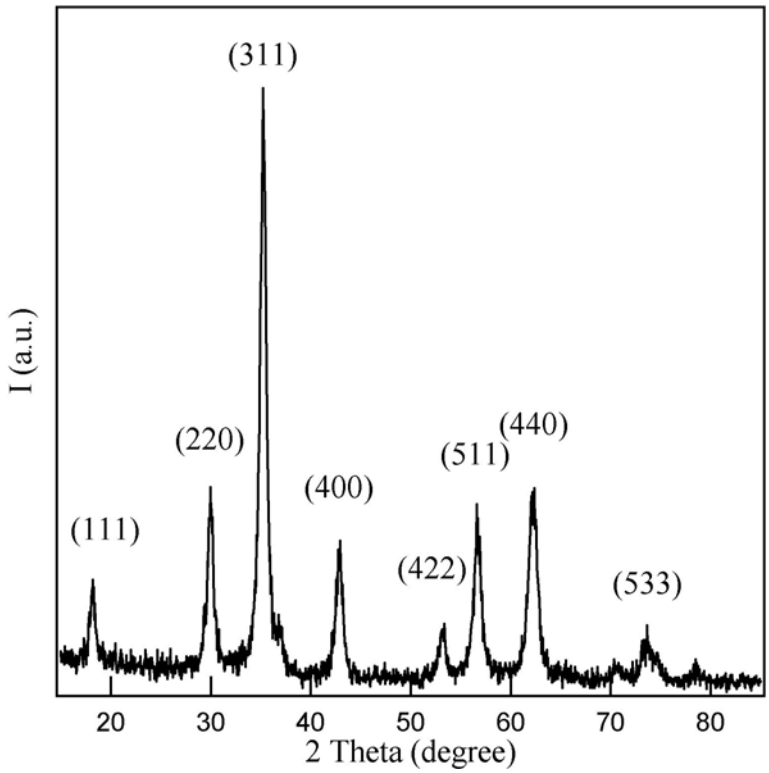

Figure 7.8 The representative XRD patterns of $MnFe_2O_4$ nanocrystals.

in the magnetic nanomaterials. According to the Stoner-Wohlfarth theory[30,31], the magnetocrystalline anisotropy (E_A) of a single domain nanocrystal can be determined by:

$$E_A = KV \sin^2\theta \qquad (7.\ 1)$$

where K is the magnetocrystalline anisotropy constant, V is the volume of nanocrystal, and θ is the angle between the magnetization direction and ease axis of nanocrystal. The

magnetocrystalline anisotropy is an energy barrier to keep magnetization from varying from one direction to the other. When E_A becomes comparable with the thermal energy, k_BT as k_B being the Boltzmann constant, the magnetization direction of nanocrystals is randomly orientated and goes through rapid superparamagnetic relaxation. The blocking temperature is the threshold point of thermal activation. As temperature is higher than blocking temperature, thermal energy overrules the magnetocrystalline anisotropy energy and the orientation of magnetization of each nanocrystal simply aligns the applied magnetic field direction. Consequently, the nanocrystals show paramagnetic properties. When temperature is below the blocking temperature, the magnetization direction of nanocrystal is orientated along nanocrystal own ease axis, instead of the applied magnetic field direction, because the thermal energy is not sufficient enough to overcome the magnetocrystalline anisotropy energy. Larger magnetic nanocrystal possesses higher magnetocrystalline anisotropy energy, and consequently higher thermal energy is required to become superparamagnetic. Therefore, the blocking temperature increases as the size of nanocrystal increasing.

The hysteresis in the field dependent magnetization of $MnFe_2O_4$ nanocrystals below blocking temperature shows that the magnetic anisotropy serves as an energy barrier to prevent the magnetization orientation of nanocrystals from closely following the magnetic field direction. The coercivity (H_C) represents the certain field strength of the magnetic field that is required to overcome the magnetocrystalline anisotropy barrier and to allow the magnetization of nanocrystals aligning in the field direction. The coercivity of magnetic nanocrystal from Stoner Wohlfarth theory can be expressed as:

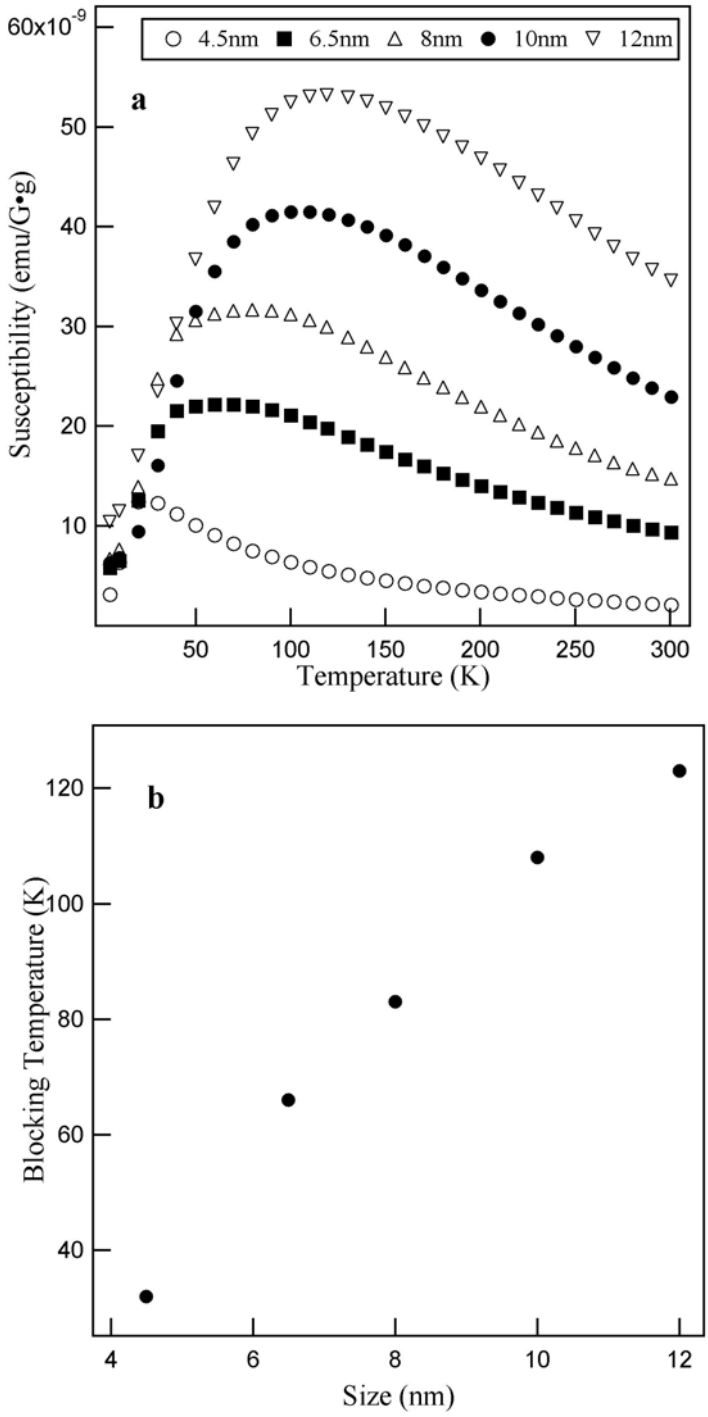

Figure 7.9 (a) Temperature dependent magnetization measurements, (b) The blocking temperatures as a function of sizes of $MnFe_2O_4$ nanocrystals.

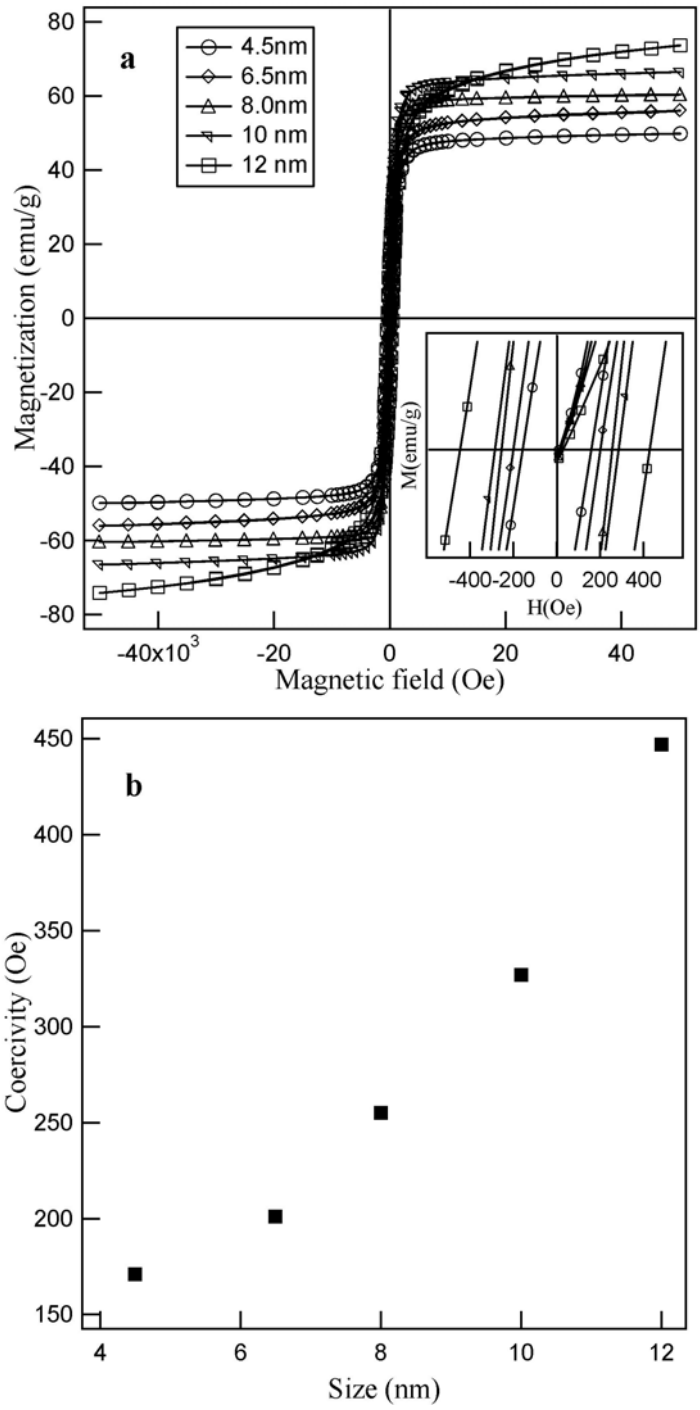

Figure 7.10 (a) Field dependent magnetization measurements, (b) The coercivity as a function of sizes of $MnFe_2O_4$ nanocrystals.

$$H_C = 2K / \mu_0 M_S \qquad (7.\ 2)$$

where μ_0 is a universal constant of permeability in free space and M_S is the saturation magnetization of nanocrystal. As the temperature is below blocking temperature for the given sized nanocrystals, the required coercivity for switching the magnetization direction of the nanocrystals certainly increases as the magnetocrystalline anisotropy increases. Therefore, the coercivity of $MnFe_2O_4$ nanocrystals increases with increasing the nanocrystal size.

7. 4 Conclusions

The success of size-controlled synthesis of $MnFe_2O_4$ nanocrystals demonstrates that the thermal behavior of molecular precursors is a key reaction parameter for the synthesis of complex multiple-metal oxides nanocrystals. Through controlling the inductive electron effect and steric effect of ligand, the thermal properties of molecular precursors can be tailored to satisfy the synthetic requirements. The capabilities of such molecular design of precursor have been extended to the preparation of chemically doped $Co_xMn_{1-x}Fe_2O_4$ and core-shell structured $CoFe_2O_4$@$MnFe_2O_4$ nanocrystals by using these new molecular precursors. The important size dependent superparamagnetic properties of these $MnFe_2O_4$ nanocrystals unambiguously make $MnFe_2O_4$ nanocrystals as promising candidates for various practical applications such as MRI contrast enhancement agents, magnetic probes for biomolecules and magnetically guided drug delivery.

7. 5 References

(1) Alivisatos, A. P. *Science* **1996**, *271*, 933.

(2) Leslie-Pelecky, D. L.; Rieke, R. D. *Chem. Mater.* **1996**, *8*, 1770.

(3) Sun, S.; Murray, C. B.; Weller, D.; Folks, L.; Moser, A. *Science* **2000**, *287*, 1989.

(4) Häfeli, U., Schütt, W.; Teller,J.; Zborowski, M. *Scientific and Clinical Applications of Magnetic Carriers*; Plenum Press: New York, 1997.

(5) Weissleder, R.; Bogdanov, A.; Neuwelt, E. A.; Papisov, M. *Advanced Drug Delivery Reviews* **1995**, *16*, 321.

(6) Weissleder, R. *Nature Biotechnology* **2001**, *19*, 316.

(7) Weissleder, R.; Moore, A.; Mahmood, U.; Bhorade, R.; Benveniste, H.; Chiocca, E. A.; Basilion, J. P. *Nature Medicine* **2000**, *6*, 351.

(8) Raj, K.; Moskowitz, B.; Casciari, R. *J. Magn. Magn. Mater.* **1995**, *149*, 174.

(9) Murray, C. B.; Norris, D. J.; Bawendi, M. G. *J. Am. Chem. Soc.* **1993**, *115*, 8706.

(10) Peng, X.; Wickham, J.; Alivisatos, A. P. *J. Am. Chem. Soc.* **1998**, *120*, 5343.

(11) Qu, L.; Peng, Z. A.; Peng, X. *Nano Lett.* **2001**, *1*, 333.

(12) Murray, C. B.; Kagan, C. R.; Bawendi, M. G. *Annu. Rev. Mater. Sci.* **2000**, *30*, 545.

(13) Peng, Z. A.; Peng, X. *J. Am. Chem. Soc.* **2001**, *123*, 1389.

(14) Rockenberger, J.; Scher, E. C.; Alivisatos, A. P. *J. Am. Chem. Soc.* **1999**, *121*, 11595.

(15) Hyeon, T.; Lee, S. S.; Park, J.; Chung, Y.; Na, H. B. *J. Am. Chem. Soc.* **2001**, *123*, 12798.

(16) Sun, S.; Zeng, H. *J. Am. Chem. Soc.* **2002**, *124*, 8204.

(17) Jana, N. R.; Chen, Y.; Peng, X. *Chem. Mater.* **2004**, *16*, 3931.

(18) McMichael, R. D.; Shull, R. D.; Swartzendruber, L. J.; Bennett, L. H.; Watson, R. E. *J. Magn. Magn. Mater.* **1992**, *111*, 29.

(19) Mitchell, D. G. *J. Magn. Reson. Imaging* **1997**, *7*, 1.

(20) Li, G.; Wang, S. X.; Sun, S. *IEEE Trans. Magn.* **2004**, *40*, 3000.

(21) Robinson, D. B.; Persson, H. H. J.; Zeng, H.; Li, G.; Pourmand, N.; Sun, S.; Wang, S. X. *Langmuir* **2005**, *21*, 3096.

(22) Wang, S. X.; Bae, S.-Y.; Li, G.; Sun, S.; White, R. L.; Kemp, J. T.; Webb, C. D. *J. Magn. Magn. Mater.* **2005**, *293*, 731.

(23) Berg, E. W.; Truemper, J. T. *J. Phys. Chem.* **1960**, *64*, 487.

(24) Berg, E. W.; Truemper, J. T. *Anal. Chim. Acta* **1965**, *32*, 245.

(25) Zhang, Z.; Wong, C. P. *Journal of Applied Polymer Science* **2002**, *86*, 1572.

(26) Martell, A. E.; Hancock, R. D.; Ed. *Metal Complexes in Aqueous Solutions*, 1996.

(27) Camerman, A.; Mastropaolo, D.; Camerman, N. *J. Am. Chem. Soc.* **1983**, *105*, 1584.

(28) Madsen, G. K. H.; Iversen, B. B.; Larsen, F. K.; Kapon, M.; Reisner, G. M.; Herbstein, F. H. *J. Am. Chem. Soc.* **1998**, *120*, 10040.

(29) Boese, R.; Antipin, M. Y.; Blaeser, D.; Lyssenko, K. A. *J. Phys. Chem. B* **1998**, *102*, 8654.

(30) Stoner, E. C.; Wohlfarth, E. P. *Trans. Roy. Soc.* **1948**, *A240*, 599.

(31) Stoner, E. C.; Wohlfarth, E. P. *IEEE Trans. Magn.* **1991**, *27*, 3475.

Vita

Qing Song was born on April 10, 1969 in Shenyang, Liaoning Province, P. R. China to Xiande Song and Jufan Sun. In 1987, he began his undergraduate studies at Jilin University in Changchun, P. R. China and graduated with a B. S. in Package Engineering in 1991. After six years worked in an import and export company, he went back to Jilin University in 1997 to continue his education and preformed studies on the synthesis of TiO_2 nanomaterial and photoelectrochemistry under supervised by professors Yubai Bai and Zichen Wang. He graduated with M. S. in physical chemistry in 2000. In 2001, he joined Dr. Z. John Zhang's research group at School of Chemistry and Biochemistry, Georgia Institute of Technology in Atlanta, Georgia. He graduated with a Ph. D in chemistry in 2005.